

AD 667230

54

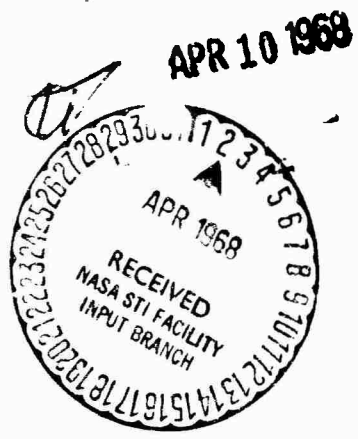


Bulletin 37  
Part 7  
(of 7 Parts)

# THE SHOCK AND VIBRATION BULLETIN

JANUARY 1968

A Publication of  
THE SHOCK AND VIBRATION  
INFORMATION CENTER  
Naval Research Laboratory, Washington, D.C.



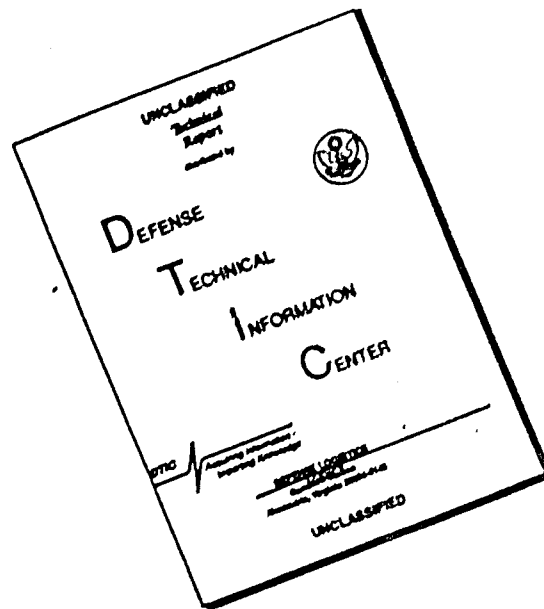
Office of  
The Director of Defense  
Research and Engineering

CLEARINGHOUSE

This document has been approved for public release and sale; its distribution is unlimited

256

# DISCLAIMER NOTICE



THIS DOCUMENT IS BEST QUALITY AVAILABLE. THE COPY FURNISHED TO DTIC CONTAINED A SIGNIFICANT NUMBER OF PAGES WHICH DO NOT REPRODUCE LEGIBLY.

## **SYMPOSIUM MANAGEMENT**

### **THE SHOCK AND VIBRATION INFORMATION CENTER**

William W. Mutch, Director  
Henry C. Pusey, Coordinator  
Rudolph H. Volin, Coordinator  
Katherine G. Jahnel, Administrative Secretary

#### **37th Program Committee**

David Askin, U.S. Army Frankford Arsenal  
Jerry Sullivan, Naval Ship Systems Command Hdq.  
Robert F. Wilkus, Systems Engineering Group, W-PAFB  
Dennis J. Martin, NASA Langley Research Center

#### **Navy Liaison**

Naval Training Device Center

William Powell  
Allan Collier

ACCESSION FOR	
GPST	WRITE SECTION <input checked="" type="checkbox"/>
DOC	EDIT SECTION <input type="checkbox"/>
REMARKS	
DATE	
BY	
REVIEWED BY	
DATE	
BY	
REVIEWED BY	
DATE	
BY	

#### **Bulletin Production**

Graphic Arts Branch, Technical Information Division,  
Naval Research Laboratory

**Bulletin 37**  
**Part 7**  
**(of 7 Parts)**

# **THE SHOCK AND VIBRATION BULLETIN**

**JANUARY 1968**

**A Publication of  
THE SHOCK AND VIBRATION  
INFORMATION CENTER  
Naval Research Laboratory, Washington, D.C.**

The 37th Symposium on Shock and Vibration was held in Orlando, Florida, on 24-26 October 1967. The U.S. Navy was host.

**Office of  
The Director of Defense  
Research and Engineering**



# CONTENTS

## PART 7

### Environmental Data

SURVEY OF THE CARGO-HANDLING SHOCK AND VIBRATION ENVIRONMENT . . . . .	1
F. E. Ostrem, General American Research Division, Niles, Illinois	
A NEW LOOK AT TRANSPORTATION VIBRATION STATISTICS . . . . .	19
J. W. Schiue and W. D. Phelps, Jet Propulsion Laboratory, Pasadena, California	
RECENT SHOCK AND VIBRATION MEASUREMENTS ON THE M-151 (JEEP) VEHICLE . .	39
R. D. Brunner and G. M. Pomonik, Hughes Aircraft Company, Canoga Park, California	
LATERAL IMPACT SHOCK DURING SHIP LOADING OF THE A3 POLARIS MISSILE . . .	67
E. G. Fischer, C. R. Brown, and A. J. Molnar, Westinghouse Electric Corporation, Pittsburgh, Pennsylvania	
*RF-4C VIBRATION AND ACOUSTIC ENVIRONMENT STUDY	
J. F. Dreher, Air Force Flight Dynamics Laboratory, and W. D. Hinegardner, Systems Engineering Group, Wright-Patterson AFB, Ohio	
EMPIRICAL CORRELATION OF FLIGHT VEHICLE VIBRATION RESPONSE . . . . .	77
W. H. Roberts, Martin-Marietta Corporation, Orlando, Florida	
VIBRATION DATA SUMMARY OF MINUTEMAN WING VI FLIGHT TEST MISSILES . . . .	93
R. R. Burnett and R. E. Morse, TRW Systems, Redondo Beach, California	
SPACECRAFT VIBRATION: COMPARISON OF FLIGHT DATA AND GROUND TEST DATA . .	173
G. Kachadourian, General Electric Company, Philadelphia, Pennsylvania	
MEASUREMENT AND ANALYSIS OF GUN FIRING AND VIBRATION ENVIRONMENTS OF THE RIVER PATROL BOAT . . . . .	205
R. S. Reed, Naval Ordnance Laboratory, Silver Spring, Maryland	
*RESPONSE OF THE AIM-9D (SIDEWINDER) MISSILE TO CAPTIVE-FLIGHT VIBRATION	
W. W. Parmenter, Naval Weapons Center, China Lake, California	
SCALE-MODEL WIND-TUNNEL ACOUSTIC DATA . . . . .	221
J. R. Baratono and F. A. Smith, Martin-Marietta Corporation, Denver, Colorado	

### PAPERS APPEARING IN PART 1

Part 1 - Classified  
(Titles Unclassified)

RECENT WORK ON SHOCK AT N.C.R.E.	
A. M. MacIntosh, Naval Construction Research Establishment, Dunfermline, Fife, Scotland	
STATE OF SHOCK IN THE NAVY, 1967	
H. L. Rich, Naval Ship Research and Development Center, Washington, D. C.	
NAVY DYNAMIC DESIGN ANALYSIS METHOD - PANEL SESSION	
SHOCK HARDENING RIVERINE WARFARE CRAFT FOR VIETNAM	
O. H. Porter and F. Weinberger, Naval Ship Research and Development Center, Washington, D. C.	
SHOCK TESTING OF SONAR TRANSDUCERS -- A STATUS REPORT	
G. M. Mayer and C. D. Johnson, Navy Underwater Sound Laboratory, New London, Connecticut	
AN EXPLOSION SHOCK-TESTING METHOD FOR SHIPBOARD EQUIPMENT	
R. R. Higginbotham, Naval Ship Research and Development Center, Portsmouth, Virginia	

\*This paper appears in Shock and Vibration Bulletin 37, Supplement.

RIGID BODY RESPONSE OF NAVAL SURFACE VESSELS TO AIR BLAST  
J. T. Irick, AVCO Corporation, Lowell, Massachusetts, S. Silverman and W. E. Baker,  
Southwest Research Institute, San Antonio, Texas

REACTION OF MILD STEEL TARGETS TO EXPLODING MUNITIONS  
J. W. Appgar, Ballistic Research Laboratories, Aberdeen Proving Ground, Maryland

RESPONSE OF A MISSILE STRUCTURE UNDER HIGH VELOCITY IMPACT  
C. Riparbelli, General Dynamics/Pomona, Pomona, California

AIM4D/F4 CAPTIVE-FLIGHT VIBRATION LOADS AND ENVIRONMENTAL MEASURE-  
MENTS PROGRAM  
C. D. Knauer, Jr. and P. E. McHorney, Hughes Aircraft Company, El Segundo, California

#### PAPERS APPEARING IN PART 2

##### Instrumentation and Analysis

PORTABLE LASER INSTRUMENT FOR VIBRATION ANALYSIS AND TRANSDUCER CALIBRATION  
G. A. Massey and R. R. Carter, Sylvania Electronic Systems, Mountain View, California

HIGH-FREQUENCY MICROPHONE CALIBRATION USING A SUPERSONIC FREE-FLIGHT RANGE  
C. D. Hayes, Jet Propulsion Laboratory, Pasadena, California, and R. C. Binder, University of  
Southern California, Los Angeles, California

METHOD OF MEASURING VIBRATORY DISPLACEMENTS IN TERMS OF A LIGHT WAVELENGTH  
J. L. Goldberg, National Standards Laboratory, Sydney, Australia

CALIBRATION OF ACCELEROMETERS BY IMPULSE EXCITATION AND FOURIER INTEGRAL  
TRANSFORM TECHNIQUES  
J. D. Favour, The Boeing Company, Seattle, Washington

BIDIRECTIONAL SHOCK AND HIGH-IMPACT EFFECTS ON SHOCK TRANSDUCERS  
V. F. DeVost and P. S. Hughes, Naval Ordnance Laboratory, Silver Spring, Maryland

INFLUENCE OF FIXTURE STRESS CONCENTRATIONS ON RING ACCELEROMETERS  
J. A. Nagy and C. E. Henley, Jr., NASA Goddard Space Flight Center, Greenbelt, Maryland

SONAR TRANSDUCER VIBRATION REQUIREMENTS AND MEASUREMENT TECHNIQUES  
G. M. Mayer and E. G. Marsh, Navy Underwater Sound Laboratory, New London, Connecticut

AUTOMATED VIBRATION ANALYSIS  
R. J. Pabich and W. H. Sellers, Raytheon Company, Bedford, Massachusetts

A COMPACT, LOW-COST SHOCK-SPECTRUM ANALYZER  
W. W. Mebane, Naval Ordnance Laboratory, Silver Spring, Maryland

DYNAMIC PHASE PLOTTING  
T. E. Smart, Sandia Corporation, Albuquerque, New Mexico

RANDOM-VIBRATION-INDUCED ERRORS IN A MISSILE CAUSED BY NONLINEAR INERTIAL  
ACCELEROMETERS  
N. A. Leifer, Bell Telephone Laboratories, Inc., Whippany, New Jersey

VIBRATION DISTRIBUTIONS IN MULTIPANEL STRUCTURES: COMPARISON OF MEASURE-  
MENTS WITH STATISTICAL ENERGY PREDICTIONS  
E. E. Ungar and N. Koronaios, Bolt Beranek and Newman Inc., Cambridge, Massachusetts

CONSTANT BANDWIDTH FM DATA SYSTEM DESIGNED FOR SATURN S-IVB/V  
VIBRATION TESTS  
D. F. Redford, Thiokol Chemical Corporation, Brigham City, Utah

DYNAMICS PORTION OF GEMINI AGENT A TARGET VEHICLE ENGINE MODIFICATION AND  
TEST PROGRAM (PROJECT SURTHERRE)  
N. Angelopoulos, Lockheed Missiles & Space Company, Sunnyvale, California

DYNAMIC ANALYSIS OF COMPLEX STRUCTURES  
M. D. Benton, G. K. Hobbs, Hughes Aircraft Company, El Segundo, California, and J. R.  
Dickerson, University of Texas, Austin, Texas

## PAPERS APPEARING IN PART 3

### Vibration Testing

#### ADVANCES IN NUMEROLOGY

J. P. Salter, Royal Armaments Research and Development Establishment, Fort Halstead, Sevenoaks, Kent, England

#### INTERNAL VIBRATION OF ELECTRONIC EQUIPMENT RESULTING FROM ACOUSTIC AND SHAKER INDUCED EXCITATION

A. D. Houston, Lockheed Missiles & Space Company, Sunnyvale, California

#### RANDOM-VIBRATION RESPONSE DATA FOR ORBITING GEOPHYSICAL OBSERVATORY: FLIGHT, ACOUSTIC, AND VIBRATION TEST

W. G. Elsen, NASA Goddard Space Flight Center, Greenbelt, Maryland

#### RANDOM-VIBRATION TEST LEVEL CONTROL USING INPUT AND TEST ITEM RESPONSE SPECTRA

A. J. Curtis and J. G. Herrera, Hughes Aircraft Company, Culver City, California

#### RANDOM-FORCE VIBRATION TESTING

J. V. Otts and N. F. Hunter, Jr., Sandia Corporation, Albuquerque, New Mexico

#### CONTROL POINT AVERAGING FOR LARGE SPECIMEN VIBRATION TESTS

H. R. Berkman, Litton Systems, Inc., Van Nuys, California

#### VIBRATION METHODS FOR MULTIPLE RANDOM EXCITATION

W. E. Noonan, McDonnell Company, St. Louis, Missouri

#### DYNAMIC TESTING OF FULL-SCALE SATURN LAUNCH VEHICLES

B. R. Jacobs, Northrop Nortronics, Huntsville, Alabama

#### BUFFET RESPONSE MEASUREMENTS OF A SEVEN PERCENT AEROELASTICALLY SCALED MODEL OF VARIOUS TITAN III CONFIGURATIONS

J. T. Uchiyama and F. W. Peters, Martin-Marietta Corporation, Denver, Colorado

#### HIGH-FORCE VIBRATION TESTING OF THE SATURN S-IVB STAGE

L. G. Smith, McDonnell Douglas Corporation, Huntington Beach, California

#### SIMPLIFIED METHOD OF CONDUCTING A DUAL RANDOM-VIBRATION INTEGRATED SYSTEM TEST

J. G. Colt, Radio Corporation of America, Burlington, Massachusetts

#### CONTROL STABILIZATION FOR MULTIPLE SHAKER TESTS

N. F. Hunter, Jr., Sandia Corporation, Albuquerque, New Mexico, and J. G. Helmuth, Chadwick-Helmuth Company, Inc., Monrovia, California

#### THE SHIM SPRING ISOLATOR

L. Wallerstein, Jr., Lord Manufacturing Company, Erie, Pennsylvania

### Test Facilities

#### ADVANCED COMBINED ENVIRONMENTAL TEST FACILITY

E. J. Kirchman and C. J. Arcilesi, NASA Goddard Space Flight Center, Greenbelt, Maryland

#### DEVELOPMENT OF SIMULATED AIRCRAFT DELIVERY USING A ROCKET SLED

W. R. Kampfe and K. M. Timmerman, Sandia Corporation, Albuquerque, New Mexico

#### AERODYNAMIC NOISE INVESTIGATION IN A SHORT-DURATION SHOCK TUNNEL

D. H. Ross, Aerospace Corporation, El Segundo, California

#### IMPACT TESTING WITH A FOUR-INCH AIR GUN AND LEAD TARGETS

H. J. Davis, Harry Diamond Laboratories, Washington, D. C.

PAPERS APPEARING IN PART 4

Shock Analysis and Simulation

MEASUREMENT AND ANALYSIS OF SPACECRAFT SEPARATION TRANSIENT RESPONSE FOR MARINER-TYPE SPACECRAFT

P. Barnett, Jet Propulsion Laboratory, Pasadena, California

MECHANICAL SHOCK OF HONEYCOMB STRUCTURE FROM PYROTECHNIC SEPARATION

J. R. Olsen, J. R. West, Jr., H. Himelblau, North American Rockwell Corporation, Los Angeles, California, C. D. Knauer, Jr., and P. E. McHorney, Jr., Hughes Aircraft Company, El Segundo, California

A SIMPLE STRENGTH CONCEPT FOR DEFINING PRACTICAL HIGH-FREQUENCY LIMITS OF SHOCK SPECTRUM ANALYSIS

M. Gertei and R. Holland, Allied Research Associates, Concord, Massachusetts

TRANSIENT VIBRATION SIMULATION

T. E. Fitzgerald and L. C. Kula, The Boeing Company, New Orleans, Louisiana

PREDICTING MECHANICAL SHOCK TRANSMISSION

J. E. Manning and K. Lee, Bolt Beranek and Newman Inc., Cambridge, Massachusetts

SHOCK DAMAGE MECHANISM OF A SIMPLE STRUCTURE

L. T. Butt, Naval Ship Research and Development Center, Portsmouth, Virginia

GENERAL MOTORS ENERGY-ABSORBING STEERING COLUMN AS A COMPONENT OF SHIPBOARD PERSONNEL PROTECTION

J. T. Hawkins and A. E. Hirsch, Naval Ship Research and Development Center, Washington, D. C.

HEAVY WEIGHT SHOCK TEST FIXTURES: DESIGN AND RESULTS

C. G. Schrader, San Francisco Bay Naval Shipyard, San Francisco, California

DERIVATION AND IMPLICATIONS OF THE NAVY SHOCK ANALYSIS METHOD

F. J. Heymann, Westinghouse Electric Corporation, Lester, Pennsylvania

DYNAMIC ANALYSIS OF A TYPICAL ELECTRONIC EQUIPMENT CABINET SUBJECTED TO NUCLEAR-WEAPON-INDUCED SHOCK

J. H. Putukian, Kaman Avidyne, Burlington, Massachusetts

DEVELOPMENT OF A ZERO-G COAST PHASE AIR GUN

S. Rodkin, General Electric Company, Philadelphia, Pennsylvania

DEVELOPMENT OF A MISSILE LAUNCH SHOCK TEST FACILITY FOR SHILLELAGH

R. W. Stevens, Martin-Marietta Corporation, Orlando, Florida

USE OF EXPLODING WIRE APPARATUS FOR LABORATORY SIMULATION OF SHOCK WAVES

F. B. Safford, Mechanics Research Inc., El Segundo, California, and R. C. Binder, University of Southern California, Los Angeles, California

NIKE-X SHOCK TUBE FACILITY

R. G. Donaghy and J. J. Healy, Office of the Chief of Engineers, Department of the Army, Washington, D. C.

DESIGN AND PERFORMANCE OF DUAL MODE SHOCK MACHINE

W. D. Everett, Naval Missile Center, Point Mugu, California

Air Blast and Ground Shock

INFLUENCE OF SHIP MOBILITY ON INTERNAL FORCES PRODUCED BY BLAST

A. Chajes, F. J. Dzialo, and M. P. White, Department of Civil Engineering, University of Massachusetts, Amherst, Massachusetts

DYNAMIC BEHAVIOR OF SHIPBOARD ANTENNA MASTS SUBJECTED TO BLAST-GENERATED OVERPRESSURES

F. A. Britt and R. H. Anderson, Mechanics Research, Inc., El Segundo, California

**\*HARDENED ANTENNA TECHNOLOGY**

D. A. Benson, A. F. Gurdo, R. W. Mair and D. J. Waters, Rome Air Development Center, Griffiss AFB, New York

**ABSOLUTE UPPER AND LOWER BOUNDS FOR THE CRITICAL BLAST LOADING ENVIRONMENT OF TARGET ELEMENTS AND SYSTEMS**

E. Sevin and W. D. Pilkey, IIT Research Institute, Chicago, Illinois

**ELASTIC-PLASTIC COLLAPSE OF STRUCTURES SUBJECTED TO A BLAST PULSE**

W. B. Murfin, Sandia Corporation, Albuquerque, New Mexico

**INTERNAL LOADING OF STRUCTURES BY BLAST WAVES**

J. F. Melichar, Ballistic Research Laboratories, Aberdeen Proving Ground, Maryland

**EFFECTS OF SLIDING ON BLAST LOADS REQUIRED TO OVERTURN STRUCTURES**

C. E. Gebhart, IIT Research Institute, Chicago, Illinois

**USE OF DETONABLE GAS EXPLOSIONS FOR BLAST AND SHOCK STUDIES**

M. R. Johnson and M. J. Balcerzak, General American Research Division, Niles, Illinois

**INCORPORATION OF SHOCK PROTECTION IN EXISTING ABOVEGROUND CYLINDRICAL STRUCTURES SUBJECTED TO NUCLEAR BLAST**

E. Cohen, S. Weissman and L. Sanchez, Ammann and Whitney, New York, New York

**PAPERS APPEARING IN PART 5**

**Large Vibro-Acoustic Test Facilities**

**VIBROACOUSTIC ENVIRONMENTAL SIMULATION FOR AEROSPACE VEHICLES**

K. McK. Eldred, Wyle Laboratories, El Segundo, California

**\*RDT SONIC FATIGUE FACILITY, DESIGN AND PERFORMANCE CHARACTERISTICS**

A. W. Kolb and H. A. Magrath, Air Force Flight Dynamics Laboratory, Wright-Patterson AFB, Ohio

**OPERATIONAL CHARACTERISTICS OF A 100,000 CUBIC FOOT ACOUSTIC REVERBERATION CHAMBER**

F. M. Murray, Wyle Laboratories, Huntsville, Alabama

**CONCEPT, DESIGN, AND PERFORMANCE OF THE SPACECRAFT ACOUSTIC LABORATORY**

R. J. Wren, W. D. Dorland, J. D. Johnston, Jr., NASA Manned Spacecraft Center, Houston, Texas, and K. McK. Eldred, Wyle Laboratories, El Segundo, California

**THEORETICAL STUDY OF ACOUSTIC SIMULATION OF IN-FLIGHT ENVIRONMENTS**

R. W. White, Wyle Laboratories, Huntsville, Alabama

**DATA HANDLING METHODS FOR LARGE VEHICLE TESTING**

D. J. Bozich, Wyle Laboratories, Huntsville, Alabama

**DEVELOPMENT AND VERIFICATION OF THE VIBRATION TEST REQUIREMENTS FOR THE APOLLO COMMAND AND SERVICE MODULES**

D. E. Newbrough, General Electric Company, Houston, Texas, R. A. Colonna, NASA Manned Spacecraft Center, Houston, Texas, and J. R. West, North American Rockwell Corporation, Downey, California

**DEVELOPMENT AND VERIFICATION OF THE APOLLO LUNAR MODULE VIBRATION TEST REQUIREMENTS**

D. E. Newbrough, General Electric Company, Houston, Texas, M. Bernstein and E. F. Baird, Grumman Aircraft Engineering Company, Bethpage, New York

**SATURN S-II, S-IVB, AND INSTRUMENT UNIT SUBASSEMBLY AND ASSEMBLY VIBRATION AND ACOUSTIC EVALUATION PROGRAMS, PARTS 1 AND 2**

R. W. Schock, J. M. Everitt, NASA Marshall Space Flight Center, Huntsville, Alabama, and J. R. Seat, Brown Engineering Company, Huntsville, Alabama

---

\*This paper appears in Shock and Vibration Bulletin 37, Supplement.

DEVELOPMENT OF ACOUSTIC TEST CONDITIONS FOR APOLLO LUNAR MODULE  
FLIGHT CERTIFICATION

W. D. Dorland, R. J. Wren, NASA Manned Spacecraft Center, Houston, Texas, and K. McK.  
Eldred, Wyle Laboratories, El Segundo, California

\*FACILITY SONIC FATIGUE PROOF TESTING

O. F. Maurer, Air Force Flight Dynamics Laboratory, Wright-Patterson AFB, Ohio

VIBROACOUSTIC TEST METHODS FOR VIBRATION QUALIFICATION OF APOLLO  
FLIGHT HARDWARE

R. W. Peverley, General Electric Company, Houston, Texas

ACOUSTICAL QUALIFICATION OF S-IC FIN STRUCTURES

C. J. Beck, Jr., The Boeing Company, Huntsville, Alabama, and D. R. Kennedy, Brown Engi-  
neering Company, Huntsville, Alabama

\*SIMULATION OF ACOUSTIC FATIGUE FAILURE IN THE WIDEBAND NOISE TEST FACILITY  
OF THE AIR FORCE FLIGHT DYNAMICS LABORATORY

R. C. W. van der Heyde, Air Force Flight Dynamics Laboratory, Wright-Patterson AFB, Ohio

REAL-TIME COMBINED ACOUSTIC-VACUUM TESTING OF SPACECRAFT

L. J. Demas, NASA Goddard Space Flight Center, Greenbelt, Maryland

PAPERS APPEARING IN PART 6

Helicopter Environments

HELICOPTER VIBRATIONS

C. D. Roach, U. S. Army Aviation Materiel Laboratories, Fort Eustis, Virginia

HELICOPTER VIBRATION -- A MAJOR SOURCE. ITS PREDICTION AND AN APPROACH TO  
ITS CONTROL

R. P. White, Jr., and F. A. DuWaldt, Cornell Aeronautical Laboratory, Inc., Buffalo, New York

\*IN-FLIGHT VIBRATION AND ACOUSTIC STUDY ON THE UH-1F HELICOPTER

C. E. Thomas and J. T. Ach, Air Force Flight Dynamics Laboratory, Wright-Patterson  
AFB, Ohio

HELICOPTER FUSELAGE VIBRATION PREDICTION BY STIFFNESS MOBILITY METHODS

J. J. Sciarra, The Boeing Company, Morton, Pennsylvania

ISOLATION OF HELICOPTER ROTOR-INDUCED VIBRATIONS USING ACTIVE ELEMENTS

P. C. Calcaterra and D. W. Schubert, Barry Research & Development, Watertown, Massachusetts

HYBRID VIBRATION-ISOLATION SYSTEM FOR HELICOPTERS

D. A. Bies and T. M. Yang, Bolt Beranek and Newman Inc., Los Angeles, California

RECENT ADVANCES IN THE STUDY OF SYNCHRONOUS VIBRATION ABSORBERS

A. V. Srinivasan, Kaman Corporation, Bloomfield, Connecticut

OPTIMIZING THE DYNAMIC ABSORBER TO INCREASE SYSTEM DAMPING

G. K. Jones, NASA Goddard Space Flight Center, Greenbelt, Maryland

APPLICATION OF THE DYNAMIC ANTIRESONANT VIBRATION ISOLATOR TO HELICOPTER  
VIBRATION CONTROL

R. Jones and W. G. Flannelly, Kaman Corporation, Bloomfield, Connecticut

\*This paper appears in Shock and Vibration Bulletin 37, Supplement.

# ENVIRONMENTAL DATA

## SURVEY OF THE CARGO-HANDLING SHOCK AND VIBRATION ENVIRONMENT\*

F. E. Ostrem  
General American Research Division  
Niles, Illinois

A comprehensive literature survey and search was conducted for data and information applicable to the cargo-handling shock and vibration environment. The information compiled is summarized to show the various forms of the available data; where drop height data are available they are presented to show the distribution of drop heights for particular packages, distribution systems, and handling operations. Other information is also presented on the handling environment, such as the number of drops received per package per trip, the distribution of the drops over the faces, edges, and corners, the effect of package size and weight, the effect of the distribution, and the effect of labels and handholds. A case history for paper sacks, which describes the complete drop height history from manufacturer to customer, is also presented.

### INTRODUCTION

The shock and vibration environment encountered by cargo during shipment can be severe enough to cause damage. This, of course, depends upon the levels of the input motions resulting from the shipping environment and upon the fragility rating or ruggedness of the cargo. Packaging and design engineers, faced with the problem of ensuring safe shipment of their product or piece of equipment, must have detailed information concerning the shipping environment (and the fragility rating of the cargo) in determining whether an item requires protection. When it is determined that protection is required, the information can be used for designing protective packaging or isolation systems.

A comprehensive literature survey and search was conducted for information and data describing field measurement programs of the cargo-handling shock and vibration environment. Over 150 reports and articles were reviewed, and over 50 agencies and organizations concerned with problems of this nature were

contacted. A portion of the information compiled is summarized in this paper.

### STATE OF THE ART

The shipping shock and vibration environment includes both the in-transit environment and the handling environment. The in-transit environment includes those motions resulting from movement on transport vehicles (truck, ship, railroad, and aircraft). The handling environment includes those motions resulting from operations such as physical handling, loading and unloading, and movement within storage or warehouse areas.

A summary and discussion of the shock and vibration environment to which items are subjected during transportation by the four major modes is presented in Ref. [1]. In that study the shock and vibration environment was described in terms of cargo floor response, i.e., input to the cargo. This method of describing the environment is adequate, since all packages on a vehicle can be assumed to be subjected

\*Conducted under contract NAS 8-11451 with the George C. Marshall Space Flight Center, National Aeronautics and Space Administration.

to the same levels of shock and vibration (approximately). For handling operations, this is not the case. The load which one unit receives is independent of the loads which others receive (assuming the packages are handled individually), and the packages are only subjected to the same possibility of receiving a shock of a given magnitude. Therefore handling loads should be specified on a statistical basis. An ideal form of data for specifying handling loads is a set of statistics giving magnitudes and frequencies of occurrence of shocks for the various handling operations performed. Since the intensity of the handling shocks is influenced by such factors as the distribution system and the characteristics of the package (size, shape, weight), it would be desirable to have information describing these effects. Unfortunately, few measurement programs have had these goals.

In spite of the fact that there is a great deal of interest in the cargo-handling shock and vibration environment, very few data are currently available. One of the reasons for the scarcity of data is that accurate self-contained instrumentation capable of recording (unattended) for long periods has not been available. Another reason is that successful (although overdesigned) packages have been shipped by conservatively estimating the environment.

Some of the early approaches to package design problems were (a) field trials, (b) comparison tests with proved containers, and (c) laboratory testing. More recently, field measurement programs have been conducted in an attempt to define accurately the cargo-handling environment. These programs have employed both observation (visual and photographic) and instrumentation (instrumented packages) techniques.

#### AVAILABLE DATA

Data describing cargo-handling shock and vibration have been reported in various forms. Depending upon the instrumentation available and the type of information sought, the data have been reported in terms of zones of shock, peak accelerations, drop heights, or shock spectra.

Data reported in terms of zone of shock or peak accelerations provide information on the relative severity of the shocks occurring during shipping but do not provide information on the input shock excitation. Data reported in terms of drop height are considered of most use because of (a) the standard drop height test, and (b) the information provided on the energy to be

absorbed. Data reported in terms of shock spectra are of most use for describing the shock environment of equipment mounted on large structures.

The results of some of the more extensive measurement programs reporting the data in the above forms are reviewed. The instrumentation and/or method of obtaining the data are also described.

#### Zones of Shock

The pioneer investigation of the handling environment was conducted by the National Safe Transit Committee [2]. In that study, commercial impact recorders were mounted in wooden boxes and shipped as ordinary products. The instrument recorded the shocks encountered during shipment by the displacements of spring-mass systems. The spring-mass systems are linked to recording pens which record the deflections on a recording paper driven by a clock mechanism. The pen deflections are recorded in zones of shock from 1 to 5 with zone 5 representing the severest shock. Figure 1 shows the results of numerous test shipments for all modes of transportation. The results point out that the severest environment, regardless of the type of carrier employed, occurs during the handling operations.

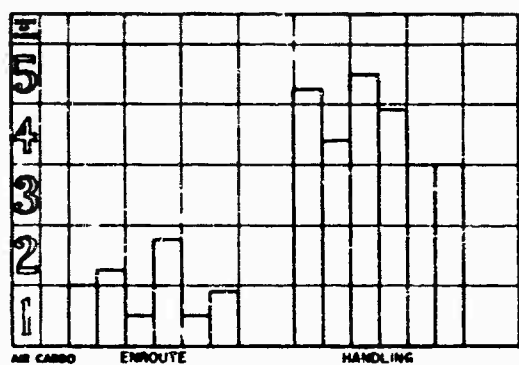
#### Peak Acceleration

Another extensive measurement program employing commercial impact recorders has been reported by Packaging Consultants Incorporated, Washington, D. C. [3]. In this study 33 shipping containers of various shapes and weights were fabricated and instrumented with Impact-O-Graphs. The packages were shipped via air, truck, ship, and air within a radius of 200 miles of Washington. The measured field data are reported in terms of peak accelerations (Table 1). Laboratory tests attempting to correlate instrument peak acceleration reading with drop height showed wide variations.

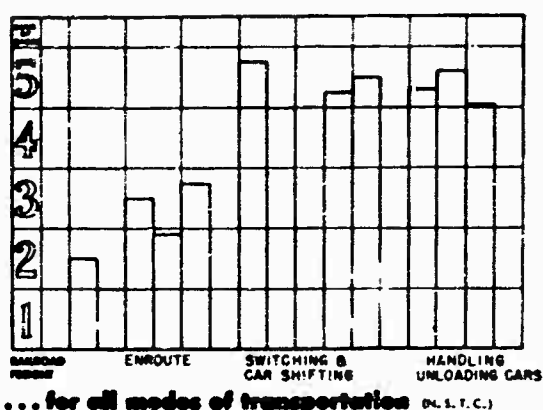
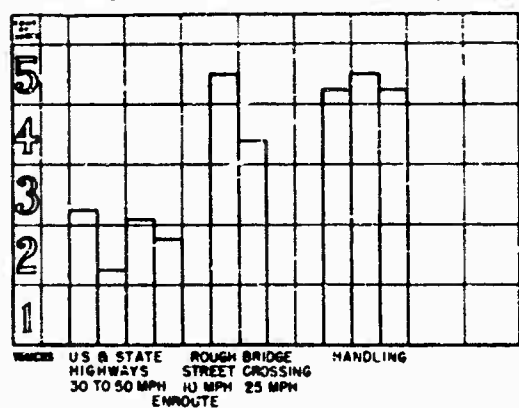
#### Drop Height

The distribution of drop heights has been measured for particular packages, distribution systems, and handling points. Typical data shown below are plotted on log-normal probability paper and present the statistical probability of a package receiving a drop at or above the height indicated, during a trip or handling operation.





Summary of averages for all test shipments



... for all modes of transportation (U.S.T.C.)

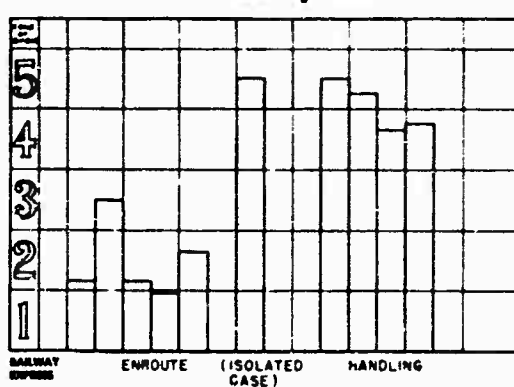


Fig. 1. Summaries of National Safe Transit Committee measurement programs

TABLE 1  
Cargo-Handling Field Test Results: Peak Acceleration (g)

Container Shape Length: Width: Height	Container Weight (lb)			
	Small (60-90)	Medium Small, Skid Mounted (150-250)	Medium, Skid Mounted (250-500)	Large, Skid Mounted (500-1500)
Average (3:2:2)	3-144 (41)	4-131 (31)	3-24 (14)	3-43 (21)
Long (3:1:1)	4-50 (30)	3-38 (20)	4-35 (19)	3-14 (18)
Tall (1:1:2)	3-76 (29)	3-41 (22)	3-50 (17)	3-17 (9)

Note. -- Data presented are ranges, followed by means (in parentheses).

Data for the plywood box of Fig. 2 were obtained from tests conducted by Wright Air Development Center [4]. Instrumentation consisted of a commercial Impact-O-Graph used in conjunction with a cubical spring suspension system. The purpose of the spring suspension system was control of the input to the recording instrument so that the instrument is independent of the type of surface impacted, i.e., of compressibility of the surface. This study was restricted to routes involved in shipments from one air material area to another via Railway Express (although some shipments were made via Air Freight). The data are based on 49 trips involving 13 packages (862 drops were recorded above 3 in.). The data show that only 5 percent of the packages received drops above 21 in.

Data for the fiberboard box of Fig. 3 were obtained from tests conducted by the Packaging and Allied Trades Research Association (PATRA), Surrey, England [5]. The PATRA drop recorder was used in this study. This instrument consists of an arrangement of weights pivoted about an axis perpendicular to a recording chart and so arranged that each is sensitive to shocks along one of the three sensitive axes. Three recording pens record the drops on opposite pairs of faces of the container. Drops are recorded on a waxed paper chart which is driven at a constant speed. On impact, the paper is accelerated by a shock-operated drive. This separates the shock traces and makes it easier to read successive drops. The recorder is mounted inside a package with a 2-in. layer of polyurethane foam around it. The results presented in

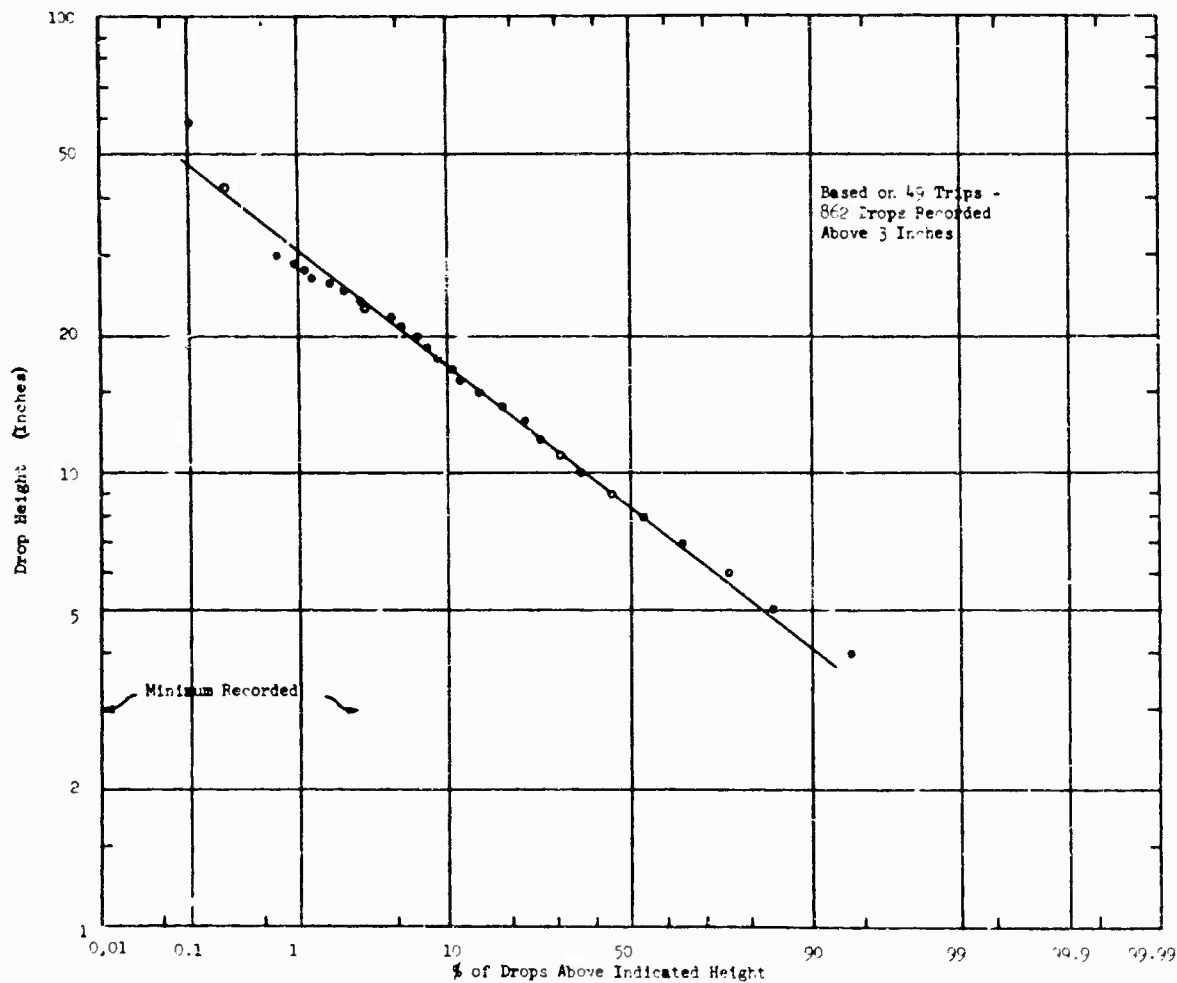


Fig. 2. Drop height. 43-lb cubical cleated plywood box (19 by 19 by 19 in.) sent by Railway Express

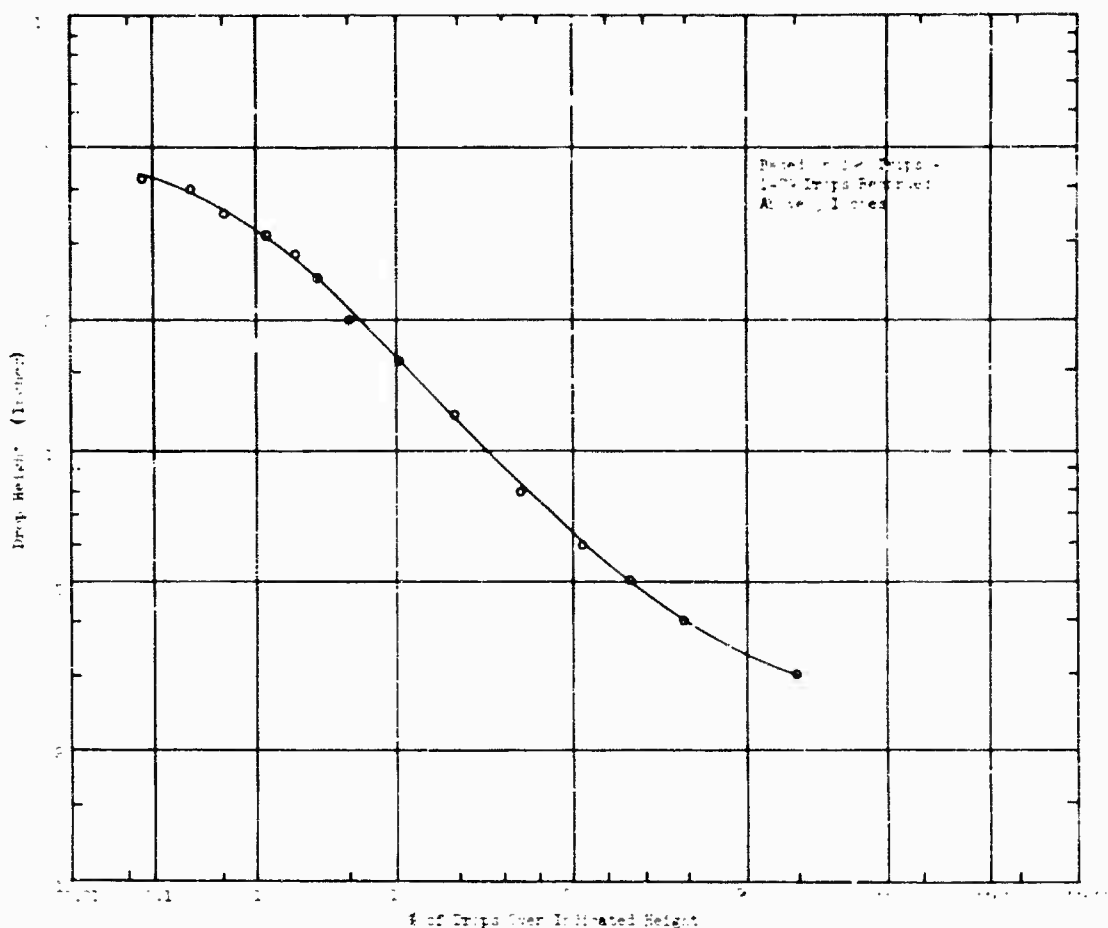


Fig. 3. Drop height: 22-lb corrugated fiberboard box (17.5 by 12 by 11.5 in.) sent by rail (mixed goods)

Fig. 3 were obtained from packages shipped via railroad in mixed-goods consignments. The curve is based on measurements recorded on 192 packages (three out and return trips from a large railroad goods depot).

Figure 4 presents drop height data for two transfer points at a large railroad depot. The data were obtained from observational studies conducted by the Swedish Packaging Research Laboratory, Stockholm, Sweden [6]. Seven handling operations were observed at the depot, which handles express freight weighing less than 80 lb. The severest handling operation (curve 1) consisted of transferring the packages from a conveyor to a handcart. Drop heights were observed only during the loading of the first layer on the cart on the far end. These packages received the highest drops and occurred during 5 percent of the loading time.

A second handling operation was observed in transferring the packages from a railroad car to a handcart (curve 2). Again, packages loaded on the bottom layer received the highest drops, and were the only ones recorded. These two curves demonstrate the effect of horizontal loading distance on drop height.

Other reported PATRA studies include direct observation of the handling operations associated with loading and unloading of a railroad car [3]. The drop heights recorded during the unloading of a railroad car onto a pushcart are shown in Fig. 5 (curve 1) and are based upon 310 observations. The packages ranged in weight from 10 to 100 lb, with the most common weight between 30 and 39 lb. The curve shows that 5 percent of the packages had drops over 8 in. and 1 percent over 16 in. The sorting (according to destination) of packages prior to

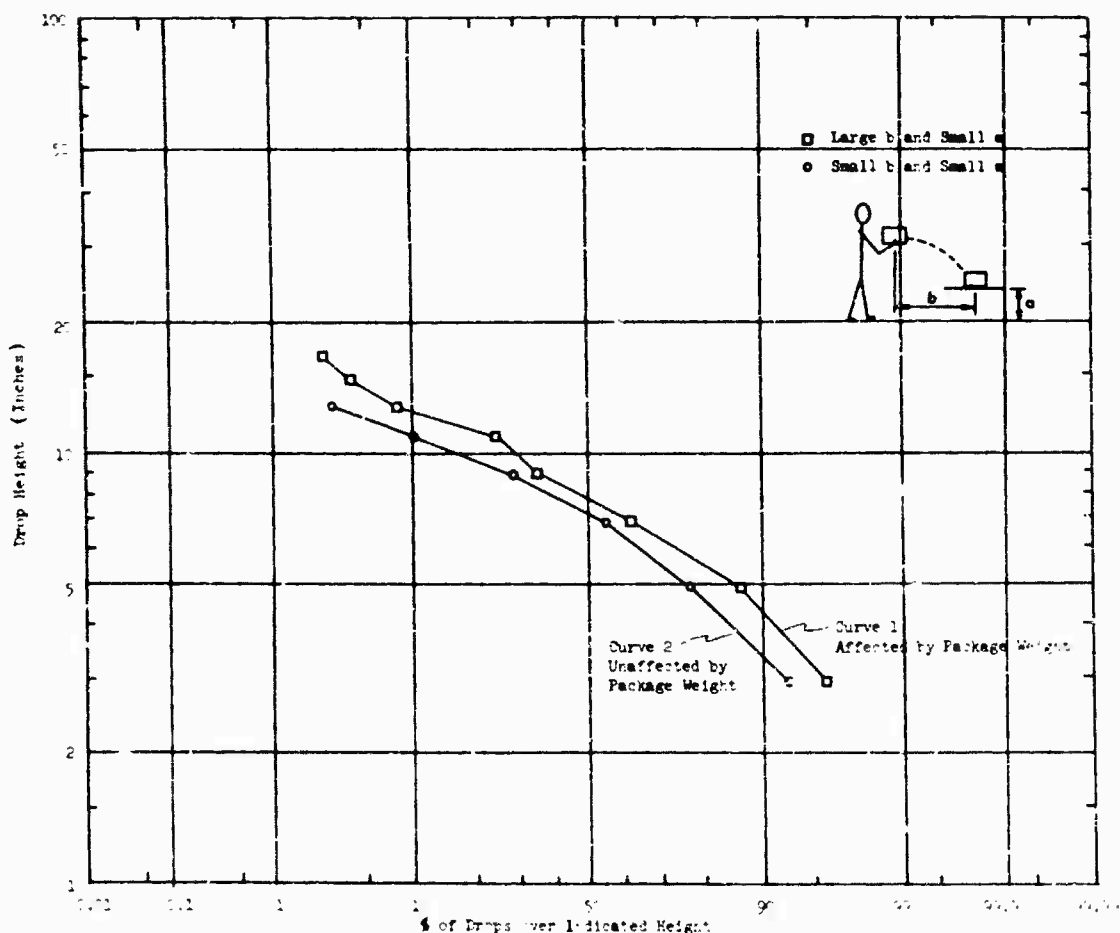


Fig. 4. Drop height: railroad depot loading operation -- severest handling operation

loading the pushcart is shown as curve 2. This curve is based upon 113 observations. Higher drops occurred during this operation, with 5 percent being dropped over 16 in. It was found that one in three packages were handled for sorting, while all packages were loaded on the cart.

Handling operations where packages are thrown result in higher drops. This is shown by curve 3 in which the unloading from trucks directly into railroad cars (walking to and fro) was observed. Here 5 percent of the drops were over 26 in.

Drops occurring during two different sorting operations are shown in Fig. 6. Curve 1 applies to sorting prior to unloading railroad cars, and curve 2 applies to sorting prior to loading a truck. It can be seen that the drop height distributions are similar for the two operations.

#### Number of Drops Received Per Package

Damage to packaged items from drops incident to the handling environment can be cumulative. For packages of this nature, the number of drops at different heights which the package receives, as well as the maximum drop height, must be known.

The number of drops recorded above given heights are presented in Fig. 7 for a 43-lb container shipped via Railway Express and in Fig. 8 for a 22-lb container shipped via rail (mixed-goods consignments).

Other studies yielding information on the number of drops have been conducted by the Packaging and Allied Trades Research Association employing the PATRA journey shock recorder. This instrument consists of a spring-mass system attached to a counter unit and

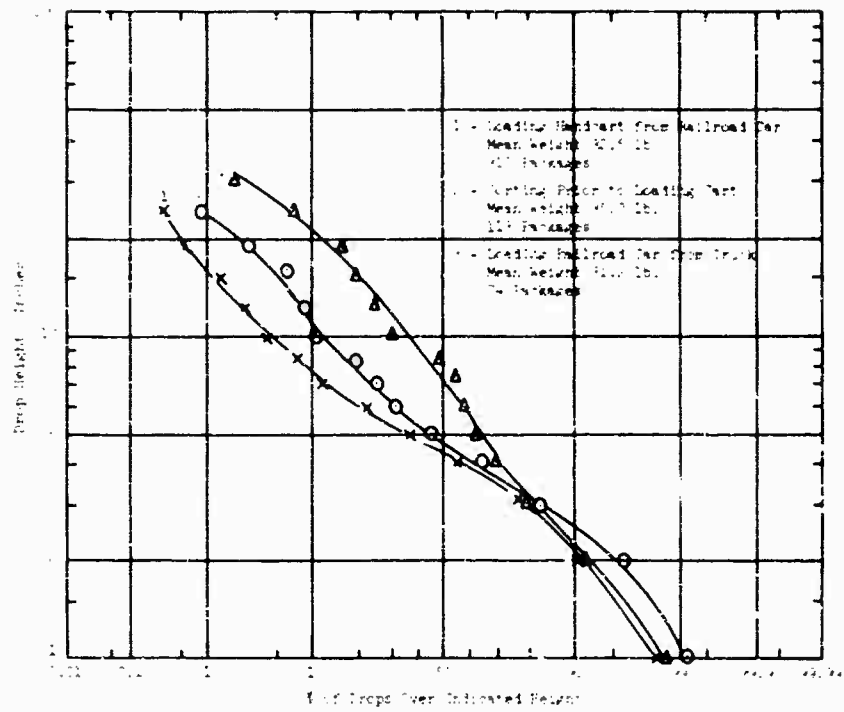


Fig. 5. Drop height, loading and sorting operation

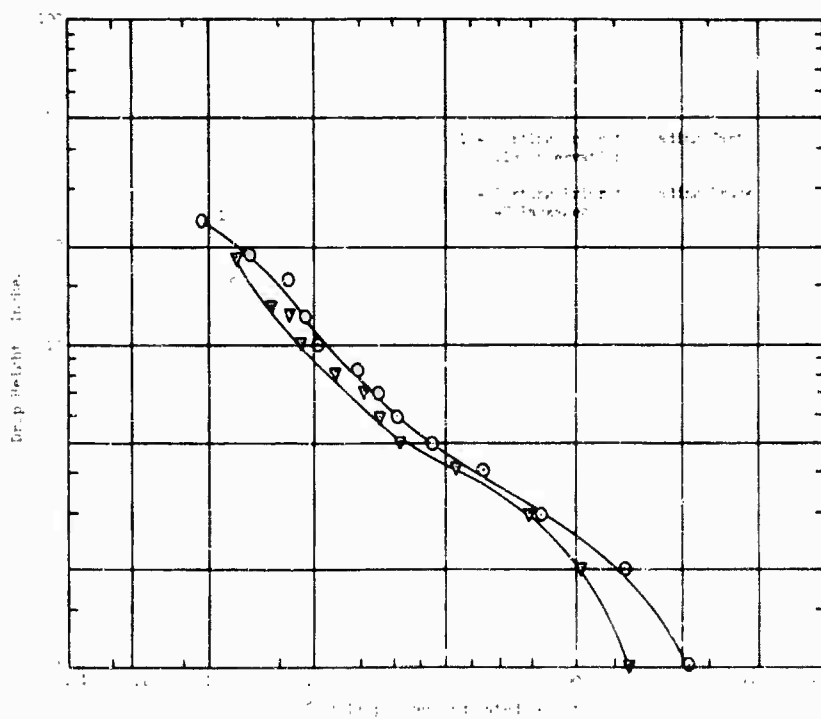


Fig. 6. Drop height, two sorting operations

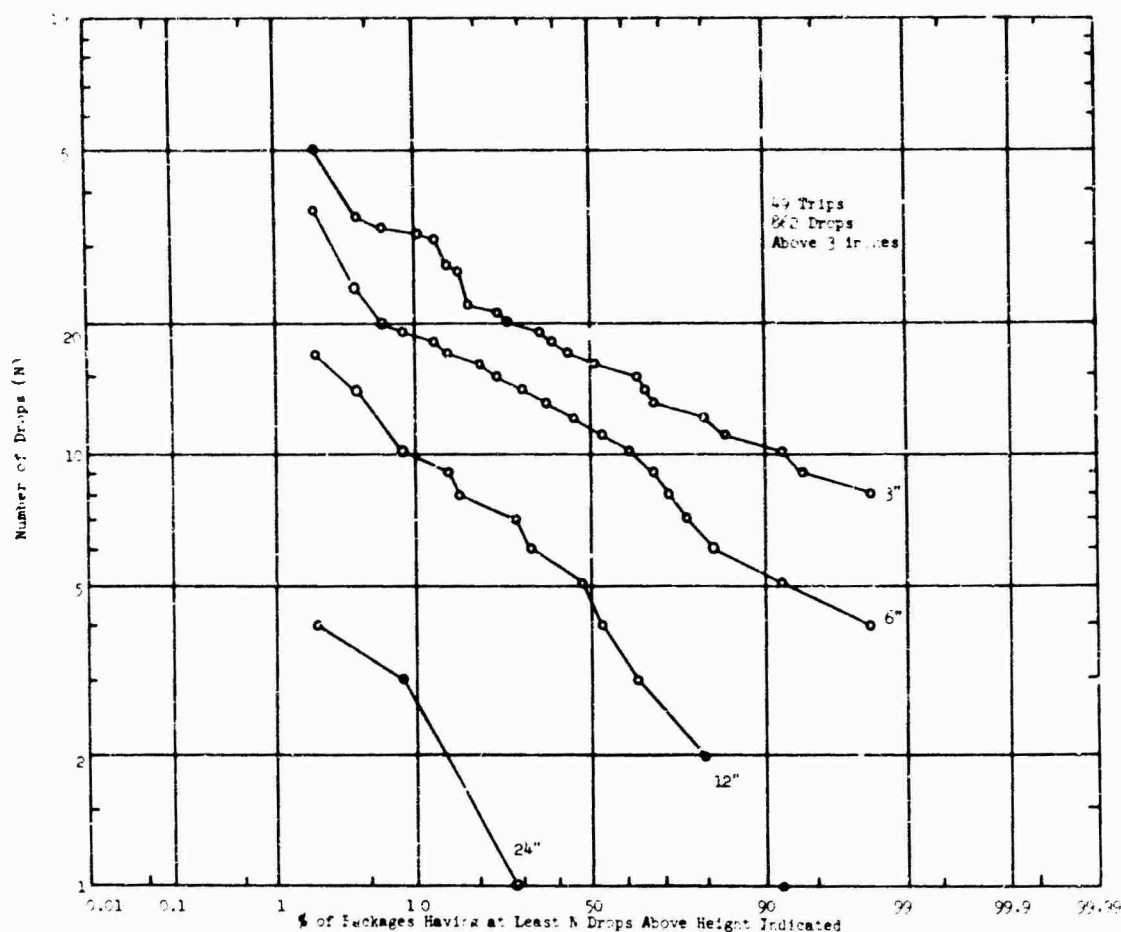


Fig. 7. Number of drops: 43-lb cleated plywood box (19 by 19 by 19 in.) sent by Railway Express

immersed in oil. Each unit has unidirectional sensitivity and counts the number of drops above a preset height on a given face of the package. By using a number of counters, which cover the different faces and are set to record at different heights, the drops can be estimated between the heights set for the different counters. This instrument is also packed with a 2-in. layer of cushioning around the recorders. The cushioning makes the acceleration pulse acting on the recorder independent of the compressibility of the surface on which the package is dropped. Thus the response of the recorder is primarily a function of drop height and secondarily of the angle of the package on impact.

Results of tests conducted with these instruments are shown in Fig. 9 for passenger train shipments and in Fig. 10 for mixed-goods railroad shipments. Twenty-four packages were shipped over six different routes (144 package-trips).

#### Effect of Distribution System

The distribution system influences the drops received by packages. Shown in Tables 2-4 are the mean numbers of drops received per package for rail, road, and overseas shipments. These data show that 52-lb packages shipped by passenger train are exposed to the severest handling, followed by truck and mixed-goods rail shipments.

The effect of mixed-goods consignments via railroad as opposed to full container loads is shown in Fig. 11 [7]. These data are based upon six shipments of four instrumented packages. The outgoing shipment was in packages in full-load consignments and the return shipment was as mixed goods. These results show that mixed-goods shipments received on the average more severe handling than full-load consignments. It further shows that the handling received by individual packages is variable and

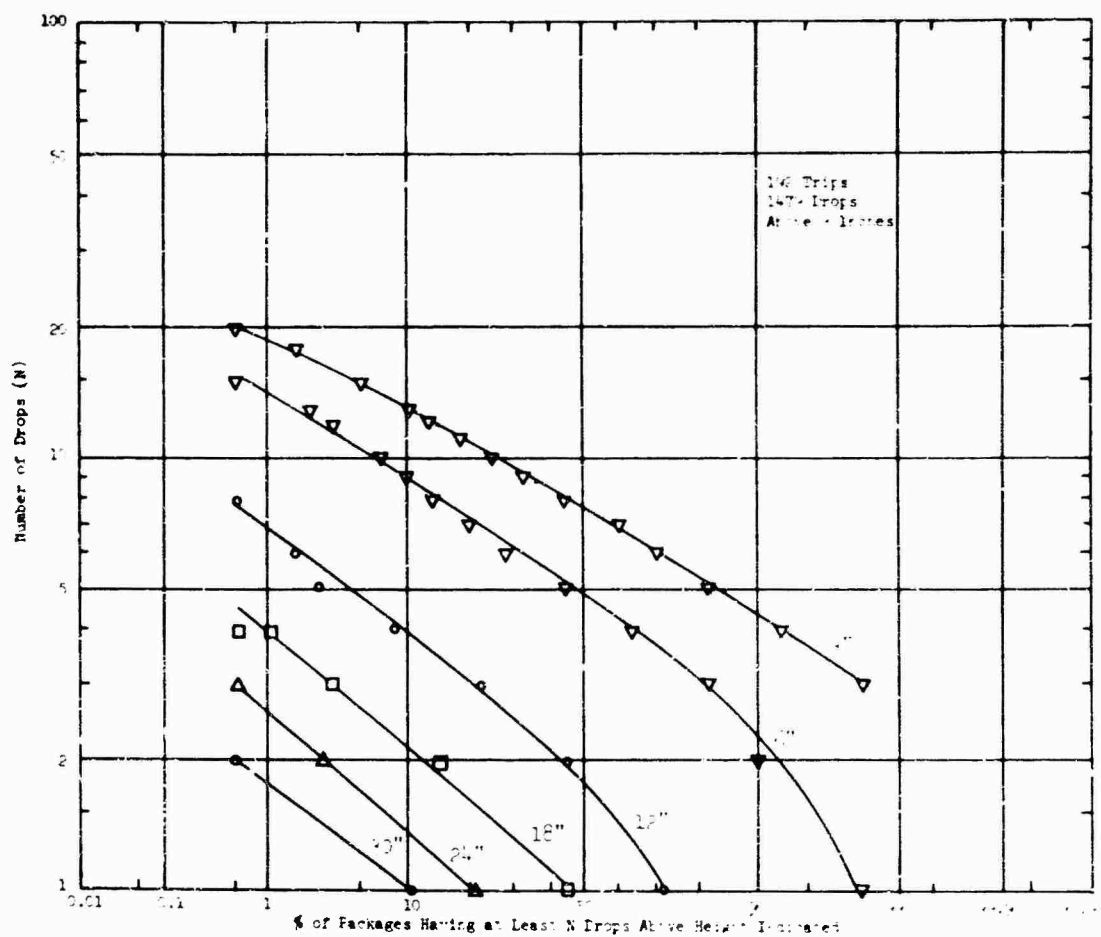


Fig. 8. Number of drops: 22-lb corrugated fiberboard box (17.5 by 12 by 11.5 in.) sent by rail (mixed goods)

TABLE 2  
Effect of Distribution System

Drop Height (in.)	Mean Number of Drops per Trip per Package <sup>a</sup>				
	Rail (Passenger)	Rail (Mixed Goods)	Rail (Mixed Goods)	Rail (Fuel Container Load)	Truck
Over 3			12.0	5.3	
6	8.3	3.4	3.2	1.6	4.1
12	2.5	1.1	1.0	0.71	1.4
18	0.8	NR <sup>b</sup>			NR <sup>b</sup>
24	0.3	0.12			0.2
36	NR <sup>b</sup>	0.0			0.0

<sup>a</sup>52-lb package; 17 by 13 by 12 in.

<sup>b</sup>Not recorded.

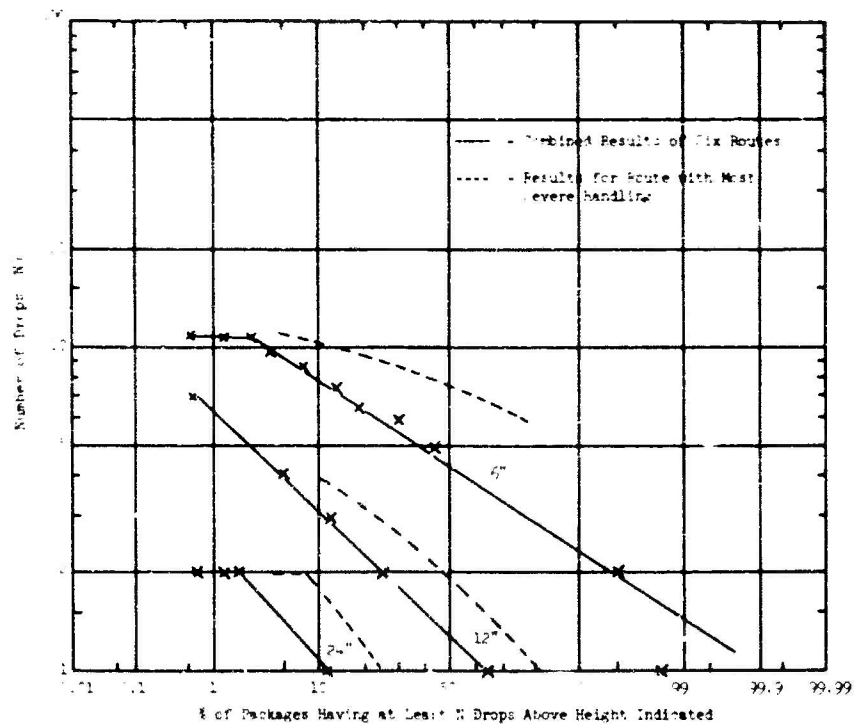


Fig. 9. Number of drops: 52-lb fiberboard box (17 by 12 by 13 in.) sent by rail (mixed goods)

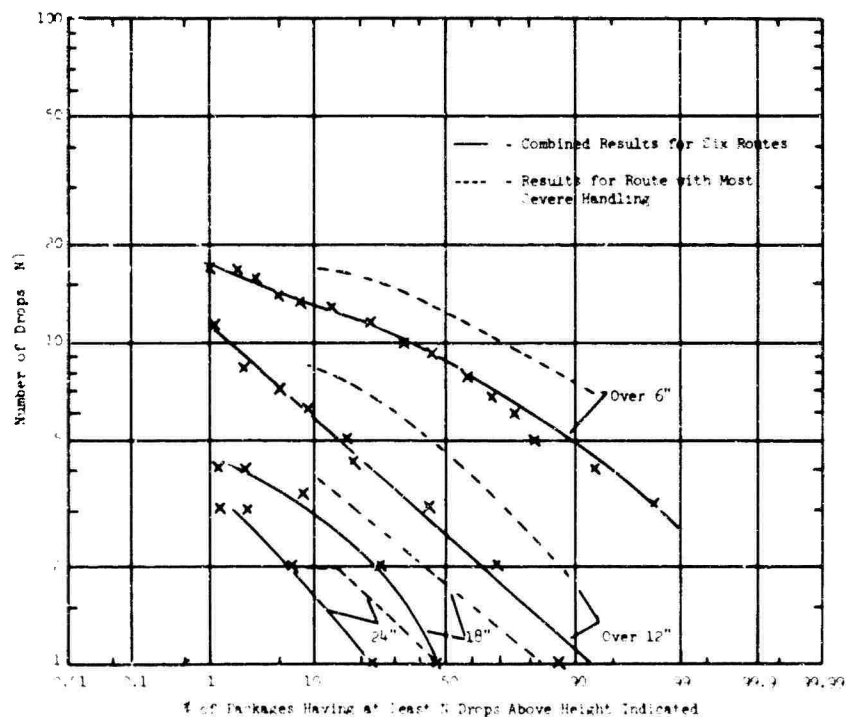


Fig. 10. Number of drops: 52-lb fiberboard box (17 by 12 by 13 in.) sent by passenger train



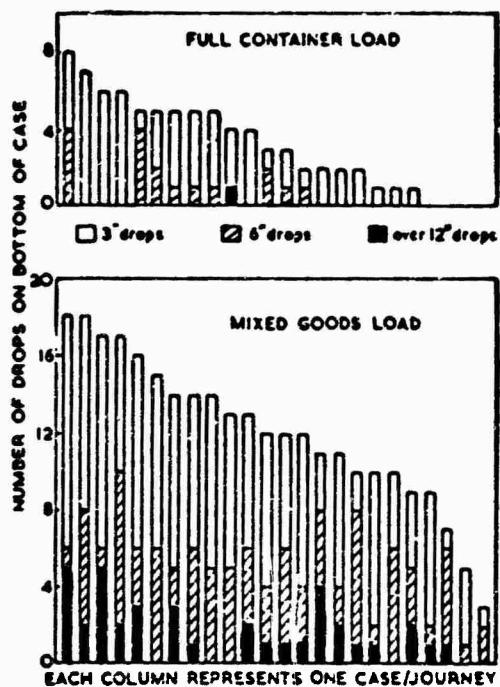


Fig. 11. Variability in handling of cases: railroad shipment

TABLE 3  
Effect of Distribution System

Drop Height (in.)	Mean Number of Drops per Trip per Package		
	Rail (Passenger) <sup>a</sup>	Rail (Mixed Goods) <sup>a</sup>	Railway Express <sup>b</sup>
Over 6	5.7	4.6	11.5
12	1.8	1.5	4.9
18	0.7	0.6	1.6
24	0.34	0.24	0.52
30	0.13	0.10	
36	0.06	0.03	0.01

<sup>a</sup> 22-lb package, 17.5 by 12 by 11.5 in.

<sup>b</sup> 43-lb package, 19 by 19 by 19 in.

that misleading information can result if only a few packages are monitored.

The mean number of drops received in overseas shipments [5] is much lower than the other distribution systems. This results in part from the weights of the packages shipped. Results of a series of overseas shipments are

TABLE 4  
Effect of Distribution System:  
Overseas Shipment

Drop Height (in.)	Mean Number of Drops per Trip per Package				
	80-lb Pkg	150-lb Pkg	250-lb Pkg	500-lb Pkg	800-lb Pkg
Over 6	1.4	2.3	0.45	0.23	1.9
9	NR	NR	0.22	0.25	0.083
12	0.43	0.47	NR	0.104	0
18	NR	NR	0.017	0	0
24	0.11	0.012	0	NR	NR
36	0.0	NR	NR	NR	NR

Note. -- NR = not recorded.

shown in Table 5. The shipments were from the United Kingdom to Cyprus to Aden to Bahrain to Aden to Cyprus to the United Kingdom. Crane operations and off loadings from ships to lighters were involved. It can be seen from these results that as the weight of the package increases, the maximum drop height decreases.

TABLE 5  
Mean Number of Drops Recorded in  
Overseas Shipments

Package Weight (lb)	Number of Package Trips	Drop Height (in.)					
		6	9	12	18	24	36
80	72	122	NR	31	NR	8	0
150	84	194	NR	40	NR	1	NR
250	60	27	13	NR	1	0	NR
500	48	11	12	5	0	NR	NR
800	24	46	2	0	0	NR	NR

Note. -- NR = not recorded.

#### Distribution of Drops Over Faces

The distribution of drops over the faces of packages has been determined in most studies [5]. Table 6 is a listing of the reported distributions. Although these results apply to a limited range of package sizes, weights, and distribution systems, the results indicate a general trend. That is, few drops are recorded on the top of a package (10 percent with the remaining drops divided approximately equally

TABLE 6  
Distribution of Handling Drops over Package Faces

Package Face	52-lb Package (17 by 13 by 12 in.)			22-lb Package (17.5 by 12 by 11.5 in.)	
	Rail (Mixed Goods)	Rail (Passenger)	Road	Rail (Mixed Goods)	Rail (Passenger)
Top	5%	3%	5%	9%	8%
Bottom	52%	77%	44%	45%	43%
Sides	43%	20%	51%	49%	49%

between the bottom and sides. These results would not apply to very large containers where drops would occur more frequently on the base.

#### Angle of Impact

The angle of the package at the instant it strikes the ground depends on the type of handling operation. Typical data are shown in Table 7. In loading and stacking it is reported that the lower drops are at a slight angle [5]. Usually one edge is lowered near the stack and then the case dropped. The higher drops are closer to being flat (to prevent toppling). More corner and edge drops are received by packages which are thrown. Edge and corner drops are defined as those with the impact face angled at more than 10 deg to the ground. The results indicate that no more than 25 percent of the total drops received by a package are angle drops.

TABLE 7  
Distribution of Impact Angles during Handling Operations

Angle of Impact	Sorting and Loading		Unloading and Stacking			
Top	5.1%	7%	75%	93%	89%	76%
Bottom	48.0%	60%				
Sides	40.6%	30%				
Edges	5.1%	1%	25%	7%	11%	22%
Corners	1.4%	2%	0%	0%	0%	0%

#### Effect of Handholds

The effect of handholds on packages sent by passenger train is shown in Table 8. In this program [5] a number of packages (52 lb,

17 by 12 by 13 in.) were fitted with handholds on the ends and shipped in pairs. The results showed a significant reduction in the number of drops, with greater difference in drops over 12 in.: the overall reduction was 17 percent, whereas drops over 12 in. were reduced by 33 percent. One reason stated for the reduction is that use of the handholds allows the case to be carried about 10 in. lower.

TABLE 8  
Effect of Handholds on Drop Height

Drop Height (in.)	Without Handholds	With Handholds
Percentage of Total Drops Recorded		
Over 6	100	100
12	30.5	24.4
18	9.4	7.2
24	3.7	1.8
Number of Drops Recorded		
6-11	555	501
12-17	168	114
18-23	45	36
24 and over	30	12
Total	709	773

#### Effect of Labels

Labels on packages influence the manner in which they are handled. Investigations conducted by PATRA [5] have shown that the position of the address labels affects the handling. For example, address labels affixed to the top of packages tend to be handled with the label on the top, i.e., face up. In the studies conducted,

50 to 60 percent of all drops occurred on the face opposite the label (designated the base).

The effect of warning labels such as Handle With Care and This Side Up was studied on packages shipped by railroad. The results indicated a greater portion of base drops and lower drops in general. The overall effect, however, was small. One reason for the small influence of warning labels is that they are currently misused. Warning labels can be applied by shippers to any package. Further, the carriers load their vehicles to their advantage to attain the maximum payload. This can result in almost any orientation of the package.

#### Effect of Package Weight

The effect of package weight on drop height is shown in Fig. 12. The data used in constructing this plot were obtained from observational studies at a large railroad goods depot [6]. The data represent the severest handling operation at the depot (loading a handcart from a conveyor). Only fiberboard boxes less than 80 lb were handled. The maximum drop height recorded was 24 in. The data show that heavier packages are dropped from lower heights.

For the packages studied, drop height was related to package weight by the following:

Drop Height =  $22 - 0.18W$ , where drop height is in inches and W is in pounds.

In another study [5] in which packages were unloaded from trucks, the mean drop height was related to package weight by the following:

Drop Height =  $17.1 - 0.26W$ .

This relationship is based upon measurements of 71 packages between 20 and 75 lb.

The effect of package weight on drop height for very large containers can be noted from the test results of overseas shipments (Table 5). Maximum drop height for 80-lb containers was 24 in., while the maximum drop height recorded for 800-lb containers was 9 in.

#### Effect of Package Size

The effect of package height on drop height is shown in Fig. 13. These results apply to the same loading operation described for determining

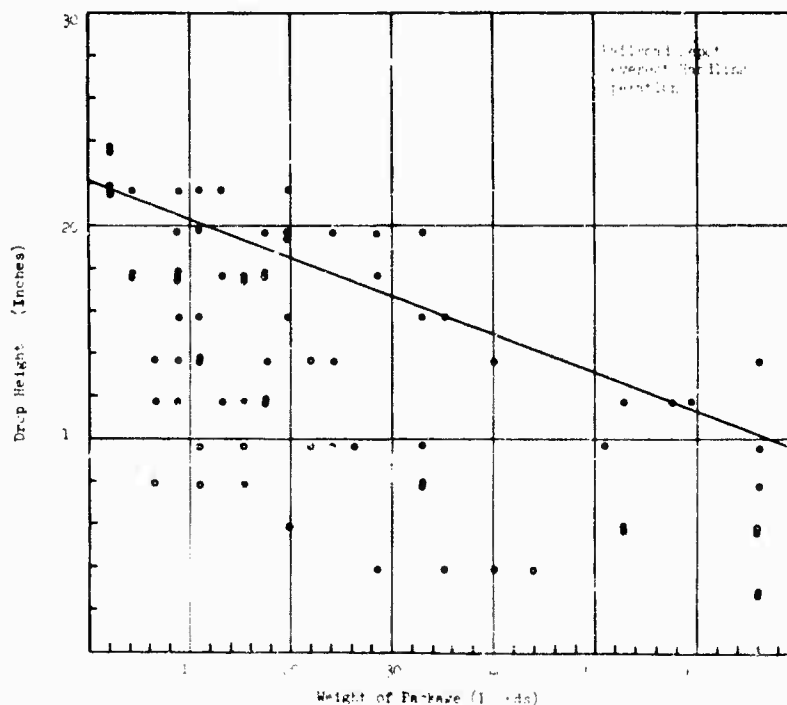


Fig. 12. Drop height vs package weight

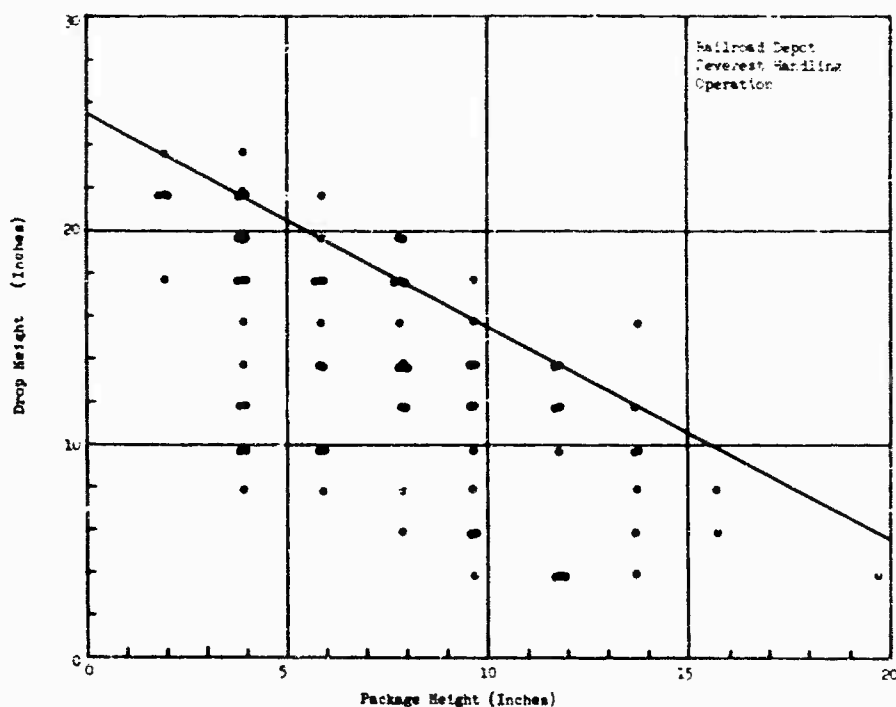


Fig. 13. Drop height vs package height

the effect of package weight, i.e., unloading packages from a conveyor onto a handcart. Again, the maximum recorded drop height was 24 in. For this loading operation, the drop height is related to package height by the following:

Drop Height = 25.5 - H, where drop height is in inches and H is package height in inches.

As expected, the drop height decreases with increasing package height.

#### Case History

A study of a product packed in paper sacks has been reported by PATRA. It illustrates a program to determine the drop height history over a complete trip from manufacturer to customer [5]. The data were obtained by systematic observation of all stages in the manufacturing plant and distribution system.

The particular product line investigated was the packing of chemicals in 112-lb sacks. The distribution system consisted of shipments sent to the customer by truck in either palletized or unpalletized loads.

The results showed that in most of the handling operations observed, there was an upper limit to the drop height as a result of the method of carrying the sack, the sack weight, and the height of the impact surface. This was reflected in a leveling off of the drop height curves at higher drop heights. This fact should be remembered when attempting to extrapolate any data to an upper limit. The drops received at the different operations are shown in Table 9. The number of observations recorded, the maximum drop height, and the height of drop exceeded by various percentages of the sacks from 5 to 90 percent are tabulated.

#### Shock Spectra

High-cost research items such as missiles and spacecraft are usually monitored through all phases of transportation. Once the normal environment has been determined, measurements continue only to monitor the loads during accidents. The shock and vibration environment on large equipment is generally monitored by accelerometers mounted at various equipment locations. Recordings are made either intermittently or continuously during the shipment (in-transit and transfer operations). The data

TABLE 9  
Summary of Drops Received in Different Operations. 112-lb Sacks

No.	Operation	Sack	Faced	Scale <sup>a</sup>	N <sup>b</sup>	Drop Heights <sup>c</sup> (in.)							Notes
						Max.	5%	10%	30%	50%	70%	90%	
1	On stitcher		B	A	281	8	6.5	6.6	4.9	4.2	3.4	2.4	1-man operation (tamping drop)
2	Palletizing		F	F	133	15	12.5	10.5	7.3	5.8	4.5	3.1	2-man operation
3	Palletizing		F	A	421	30	22	19.2	12.8	8.5	4.5	2.0	1-man operation
4	Loading trucks:												
5	Depalletizing on to truck		F	A	422	39	35.5	31.5	23	17	11.5	5.5	1-man operation
6	Depalletizing on to truck		B	L	83	30	30	26	15.5	11	7.6	4.7	1-man operation
7	Loading by conveyor, stacked vertically		B	A	99	39	37	34	28.5	24.5	20	14.5	{ Differences between crews. Sacks received at waist level and stacked 2 high
8	Loading by conveyor, stacked vertically		B	A	74	27	26	23.5	18	13.5	6.0	5.0	1-man operation
9	Loading by conveyor, flat onto layer of vertical sacks		F	A	78	30	28	25	14	9.0	7.0	4.0	1-man operation
10	Unloading trucks:												
11	by sling, 1 man		F	L	273	27	24	20	12.5	9.5	6.8	4.9	Sling on truck, 19 in. above ground. Handled by 2 men. No attempt to build at neat stack.
12	by sling, 1 man at docks		F	L	53	24	23	20	12.5	8.5	5.0	—	
13	by sling, 2 men at docks		F	L	39	15	14	12.5	8.5	6.0	4.2	2.4	
14	Stacking:												
15	From sling to stack		F	A	233	36	27	23	15	9.0	6.5	4.0	Sling on truck, 19 in. above ground. Handled by 2 men. No attempt to build at neat stack.
16	Stacking on floor, some sacks thrown		F	A	290	78	58	54	43	32	18	10.5	
17	Stack, all sacks carried, 1 or 2 men		F	A	144	30	24.5	24	14	11	7.5	4.5	
18	Operation performed by 1 man		F	A	921	39	31	27	17.5	12	6.2	2.5	
19	Operation performed by 2 men		F	A	445	27	20	17	11.6	9.0	7.0	5.0	

<sup>a</sup>A = arithmetic height scale; L = logarithmic height scale.

<sup>b</sup>N = number of observations.

<sup>c</sup>Max = maximum height observed; 5, 90% = percentage of sacks receiving drops at or above heights given in table.

<sup>d</sup>B = butt, F = face.

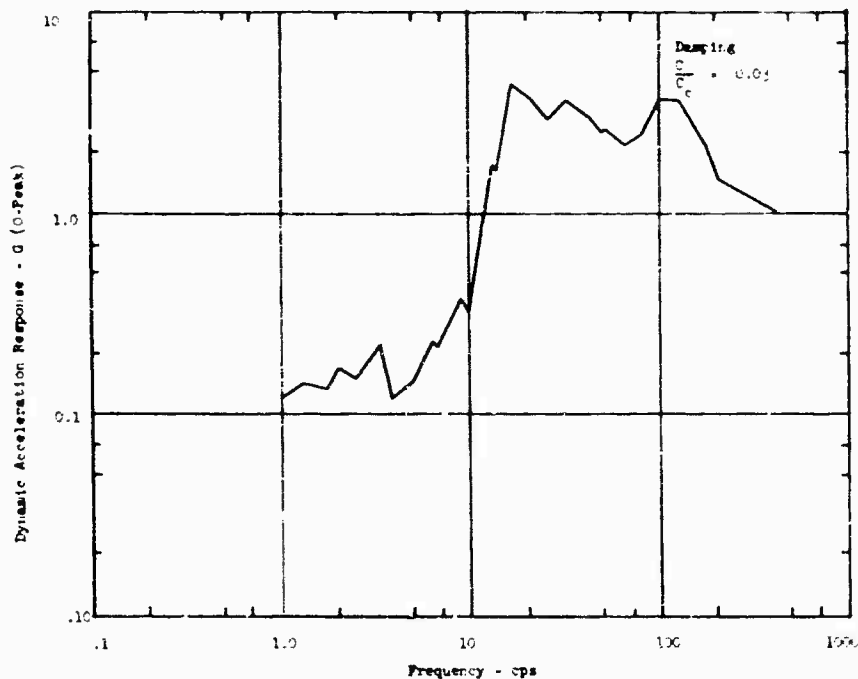


Fig. 14. Shock spectrum of handling shock:  
3-in. drop of Saturn rocket stage

are reviewed and, where significant levels are produced, shock spectra are computed. Typical of these is the shock spectrum shown in Fig. 14. It was computed from data recorded during a transfer operation of the Saturn rocket stage. The shock was produced when the forward end of the stage dropped from a height of 3 in. The plot envelops the shock spectrum at four locations on the rocket. This form of data gives the maximum dynamic acceleration response which can be expected by components mounted at the instrument locations.

#### CONCLUSIONS AND RECOMMENDATIONS

The severest shock environment encountered by cargo being shipped occurs during handling operations. Data are insufficient at present to describe accurately the handling shock environment for any given package and distribution system.

The number of drops received by a package is highly variable. Very misleading information can be obtained from measurements recorded on a few packages. The maximum shocks incident to the handling environment occur so infrequently that it is uneconomical to design a package to protect it against these accidents unless very costly items are involved.

The drops received by a package comprise a large number of small drops and relatively few higher drops. Most packages receive only one drop at the higher levels; very few have more than two. Therefore it would be very easy to overtest a package when applying the higher drop heights to the various corners, edges, and faces.

There is a great deal of interest in the cargo handling environment, and many organizations have reported measurement programs in progress or being planned. Instruments are currently being developed by a number of organizations and should provide excellent tools for future cargo-handling measurement programs.

## REFERENCES

1. F. E. Ostrem and M. L. Rurerman, "Transportation Shock and Vibration Design Criteria Manual," General American Research Division Final Rept. MR 1262, Sept. 1965
2. Anon, "What Happens to Your Product In Transit," *Finish-The Magazine of Appliance and Metals Products Manufacturing*, Nos. 8 and 9, Aug. 1954.
3. J. McAleese, "Study of Tests and Test Procedures for Packaged and Packed Electronic Equipment," Packaging Consultants, Inc., Washington, D. C., Apr. 1962
4. K. W. Bull and C. F. Kossack, "Measuring Field Handling and Transportation Conditions," WADD Tech. Rept. 60-4, Feb. 1960
5. V. G. W. Harrison, "Evaluation of Package Performance," Proc. PATRA Packaging Conference, Oxford, England, Sept. 1963, pp. 250-264
6. Y. Dagel, "Ermittlung der Fallhöhen von Packstücken beim Verladen auf einem Güterbahnhof mit Hilfe einer Filmmethode," *Verpackungs - Rundschau* No. 6, June 1961
7. F. A. Paine, "Some Aspects of Packaging," *Chem. and Indust.*, No. 52 pp. 1656-1633, Dec. 1957

## DISCUSSION

Mr. Gertel (Allied Research Assoc.): I just wanted to make an observation of some of the data presented. I was particularly interested in the statistics on flat drops vs edge or corner drops. One of the tables showed a relatively very small percentage was corner drops and edge drops. From a practical point of view, if anybody has ever tried to make any drop tests, you will find that only with extreme care can you even make a flat drop. I would be inclined to think that in service where the conditions are random, the majority of drops should have been edge or corner contacts.

Mr. Ostrem: These data were obtained by observational studies and there could be an

error. It shouldn't be more than 10 deg either way, I would assume.

Mr. Sandler (Control Data Corp.): Do you have any information on what the effect is of the FRAGILE or other stickers?

Mr. Ostrem: This was investigated by PATRA and they have found that in general a slightly lower drop height is encountered. However, a large sampling is needed to show any effect, and this is one of the reasons why they concluded that the labels are misused. Any shipper can put a label on anything, so it does not have much effect.

\* \* \*

## A NEW LOOK AT TRANSPORTATION VIBRATION STATISTICS\*

John W. Schlue and William D. Phelps  
Jet Propulsion Laboratory  
Pasadena, California

Amplitude statistics of vibration data measured on the floor of air-ride suspension vans and airplanes are presented in this report. Power spectral density plots of the vibration are also included. Evidence supporting the qualification of vans prior to their use is shown and discussed.

### INTRODUCTION

It has been a requirement at JPL that all vehicles transporting flight spacecraft be instrumented for shock and vibration measurements. Data from air-ride truck vans are presented elsewhere [1]. This paper presents additional information on the dynamic environment of spacecraft transportation in truck vans and aircraft.

Amplitude statistics relating peak g levels to trip duration are presented for air-ride suspension vans and two different airplanes. This information is intended for the engineer concerned with equipment fatigue resulting from exposure to transportation vibration.

A need for air-ride van qualification tests prior to their use in shipping electronic equipment is discussed. Data justifying qualification tests are presented. Knowledge of the dynamic characteristics of a van prior to its use may avoid an adverse dynamic environment.

### MODES OF TRANSPORTATION

Spacecraft systems under management or cognizance of JPL are transported by air-ride vans or aircraft. In most cases the transportation involves a cross-country trip from California to Florida. A typical trip duration via truck is 90 hr, whereas this time is commonly reduced to 8 hr by airplane. In every instance the truck van has been equipped with

a tandem axle system employing an air bag suspension.

Three different airplanes have transported the spacecraft. The data contained in this report cover two of these, the C-133 and C-130. The magnetic tapes from the third airplane, the Super Guppy, were not available for analysis. The C-130 and C-133 are propeller-driven commercial aircraft.

### INSTRUMENTATION

Piezoelectric accelerometers measured the shock and vibration levels at two specific points. The first point was the vehicle floor, and the second was the input to the spacecraft at the spacecraft-transport fixture attachments. The accelerometer signals were amplified by charge amplifiers and FM recorded with a magnetic tape recorder designed for this type of application. The record speed was generally 1-7/8 ips giving a flat frequency response to 525 Hz. The recorder was operated with dc or ac power, depending on the availability of ac power. Figure 1 shows a typical instrumentation setup.

The final section of this report indicates the desirability of real-time monitoring capabilities. Associated instrumentation is described in this discussion. Experience at JPL with real-time monitoring instrumentation is limited, although a few spacecraft shipments were equipped with an audio warning device.

\*This paper presents the results of one phase of research carried out under Contract NAS 7-100 from the National Aeronautics and Space Administration.





Fig. 1. Instrumentation for recording shock and vibration data

Oscilloscopes and rms voltmeters were used to check the accelerometer systems and to qualify the van prior to shipping.

#### DATA ANALYSIS TECHNIQUES

This section briefly describes the analysis procedures applied at JPL to produce the data plots and amplitude distribution information in this report. The power spectral density (PSD) program analyzes data samples selected from time-coded oscillograms of the vibration data. The amplitude distribution program analyzes all data. The computer analyses are required since the vibration environment of transportation vehicles is random.

##### Power Spectral Density Plots

The PSD program is digital and requires an analog to digital conversion of the recorded data. The program computes the PSD of the selected sample length, making use of the fast Fourier transform (Cooley-Tukey) computation technique. The plots in this report were produced with this program. The reference is  $0 \text{ db} = 1 \text{ g}^2/\text{Hz}$ .

The resolution of the plots is dictated by the user of the plotted data. A fine resolution

is required to plot sharp peaks in the low frequencies. A resolution of 0.244 is used here to present vibration spectral shapes below 30 Hz or so. Plots with resolutions of 2.44 and 4.88 are included to show higher frequency response.

The rms g level of each plot calculated by the computer is the square root of the area under the curve. The degrees of freedom (DOF) indicated on each plot is the sample period times twice the bandwidth.

##### Amplitude Distribution Data

This program does not correlate amplitudes with frequency but rather with time duration. Each analog tape is played back at a speed of 60 ips and digitized at 10,000 samples per second. This is an effective sample rate of over 310 samples per second. The digital tape is read by the computer which records a count each time a data point exceeds a preset acceleration level. Four levels are monitored concurrently. The total number of counts for each level and the total number of sampling counts for each tape are multiplied by the sample rate and typed out by the computer. The time required to digitize is  $1/32$  the data period, and the analysis time is three times the digitizing time. Since the analysis time is dependent on the computer capabilities, this time could be decreased with a larger computer.

## PRESENTATION OF DATA

Contained in this section are selected data from both air-ride vans and airplanes. Since Ref. 1 discusses in detail the normal characteristics of air-ride van vibration, the van data review here concentrates on vibration differences that are possible from one van to another.

### Truck Van

Two sets of data are presented from the air-ride vans. Each set is displayed in the form of PSD plots and amplitude statistics.

**Power Spectral Density Plots** — Figures 2 through 7 show PSD plots of data measured in three axes on a van floor. For identification this van is referred to as van A. The lateral axis is perpendicular to the van sides, the longitudinal is parallel with the van sides, and the vertical axis is normal to the van floor.

These plots have resolutions of 0.24 and 2.4 cycles to show clearly the low- and high-frequency vibration characteristics. The 0.24-cycle resolution plots indicate a common trait of air-ride suspension vans — the low-frequency peak response between 10 and 20 Hz.

These plots may be compared with data presented in Ref. 1. A trait less common with air-ride vans is demonstrated in the 2.4-cycle plots, however. These plots indicate significant amplitudes at frequencies out to 600 Hz. A comparison of the rms g levels for the narrow-band and wideband plots of Figs. 2 and 5 indicates the narrow-band rms value to be only 5.4 percent of the wideband rms level. (This percentage calculation assumes stationarity of data.)

The high-frequency content may present a fatigue problem to electronic or other equipment sensitive to vibration in the 40-600 Hz range. Evaluation tests to determine van characteristics are discussed later.

Figures 3 and 4 demonstrate significant excitation in the lateral and longitudinal axes also. All three axes contain high-frequency energy as well as peak responses below 20 Hz.

Figures 8 through 13 are PSD plots of data measured in another van, van B, in the same three axes as the previous set of plots. These plots also have resolutions of 0.24 and 2.4 cycles.

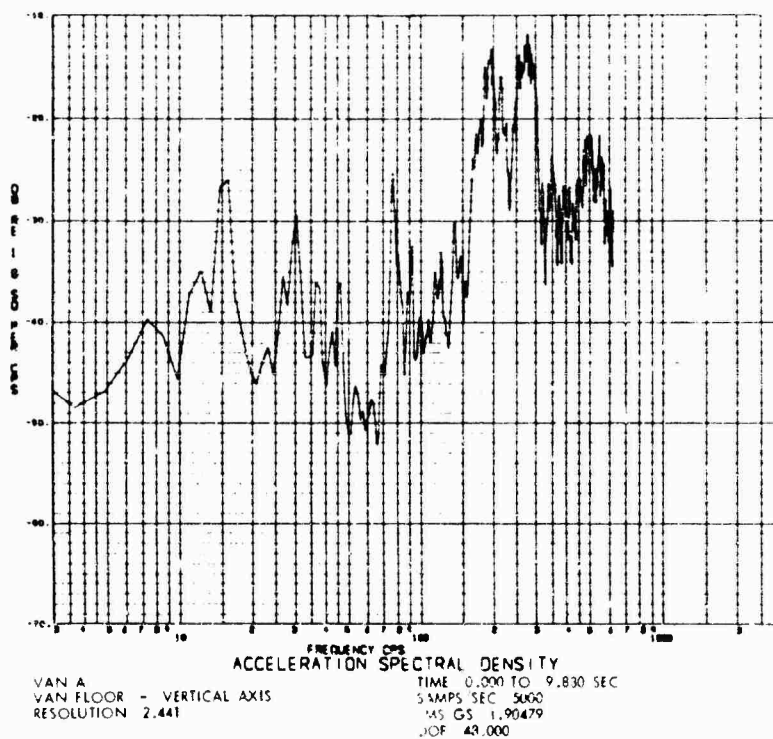


Fig. 2. PSD plot for vertical axis of van A floor: resolution, 2.441; time, 0.000-9.830 sec; samples per second, 5000; rms g, 1.90479; DOF, 48.000

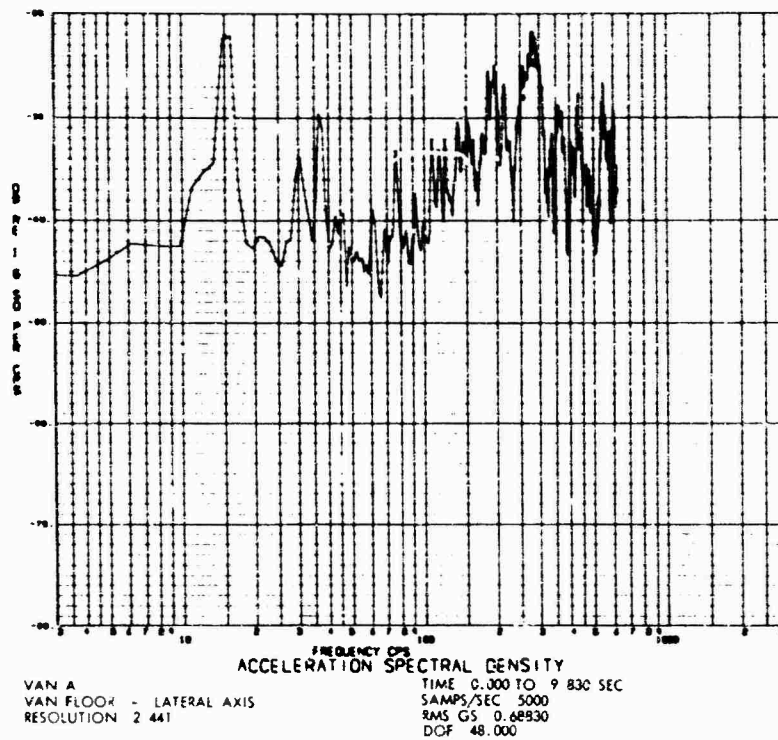


Fig. 3. PSD plot for lateral axis of van A floor: resolution, 2.441; time, 0.000-9.830 sec; samples per second, 5000; rms g, 0.68830; DOF, 48.000

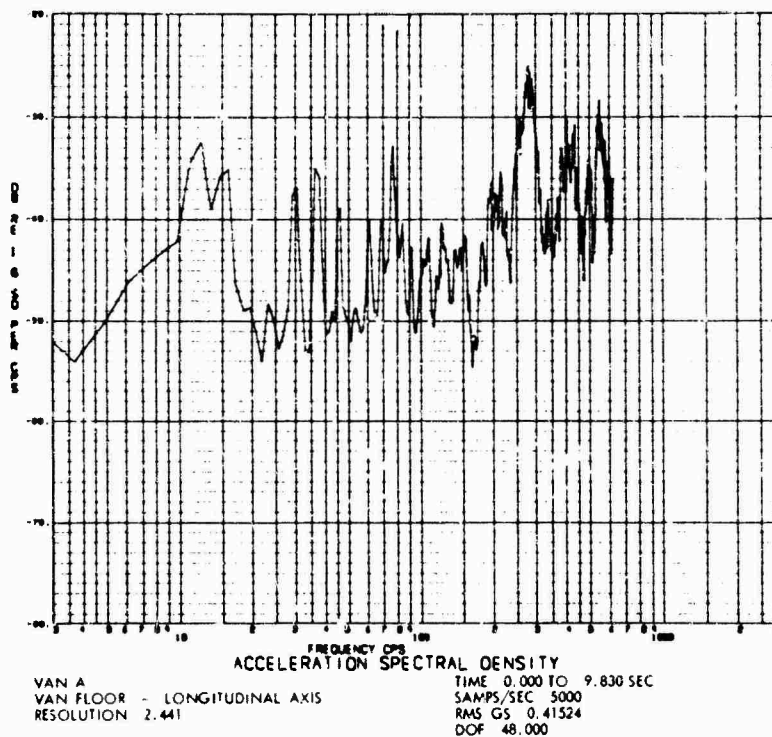


Fig. 4. PSD plot for longitudinal axis of van A floor: resolution, 2.441; time, 0.000-9.830 sec; samples per second, 5000; rms g, 0.41524; DOF, 48.000

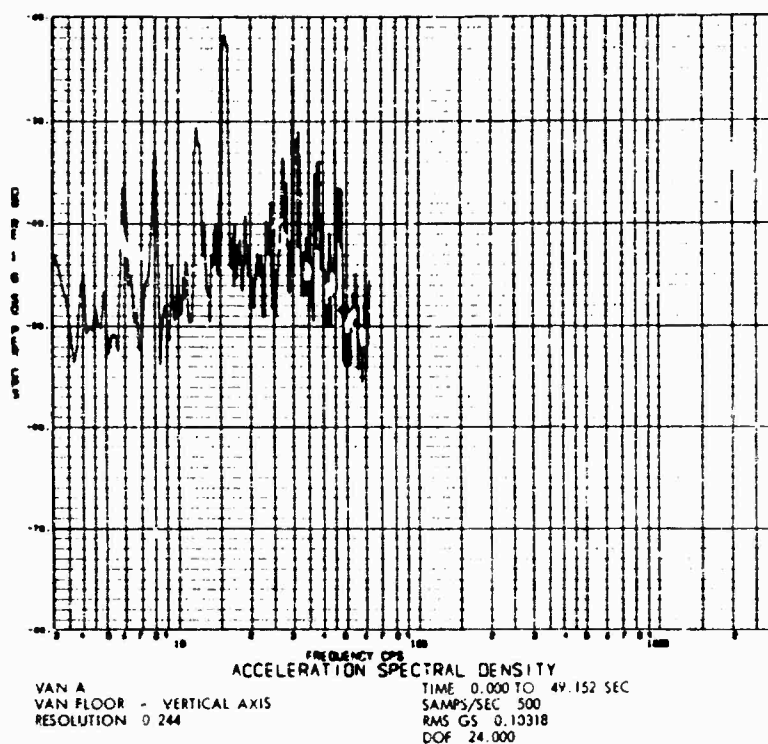


Fig. 5. PSD plot for vertical axis of van A floor: resolution, 0.244; time, 0.000-49.152 sec; samples per second, 500; rms g, 0.10318; DOF, 24.000

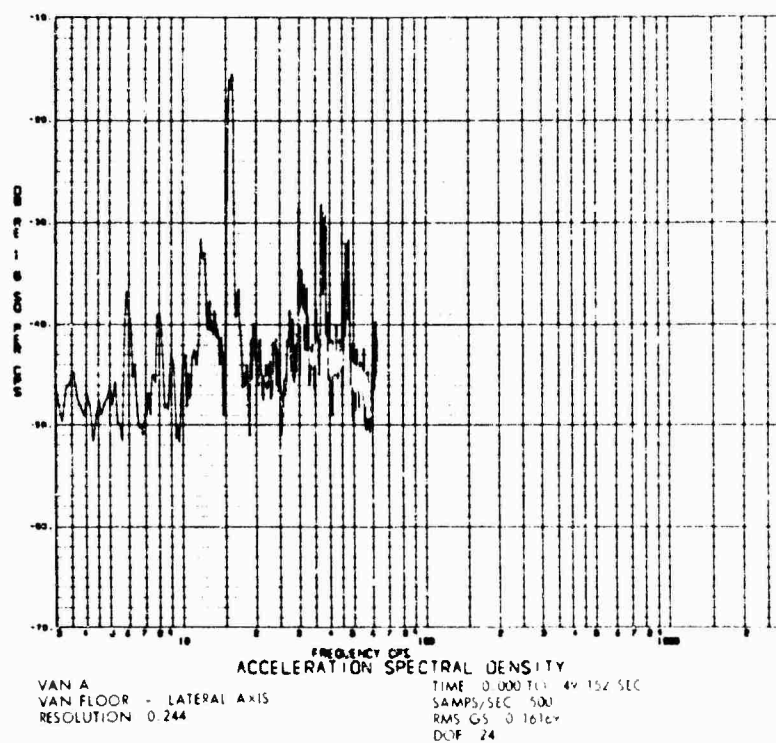


Fig. 6. PSD plot for lateral axis of van A floor: resolution, 0.244; time, 0.000-49.152 sec; samples per second, 500; rms g, 0.16169; DOF, 24.000

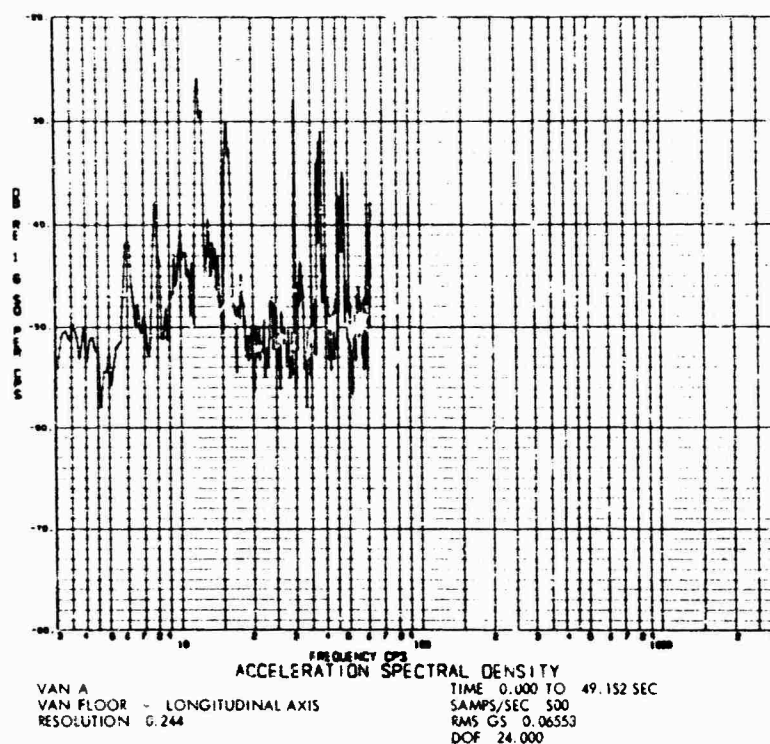


Fig. 7. PSD plot for longitudinal axis of van A floor: resolution, 0.244; time, 0.000-49.152 sec; samples per second, 500; rms g, 0.06553; DOF, 24.000

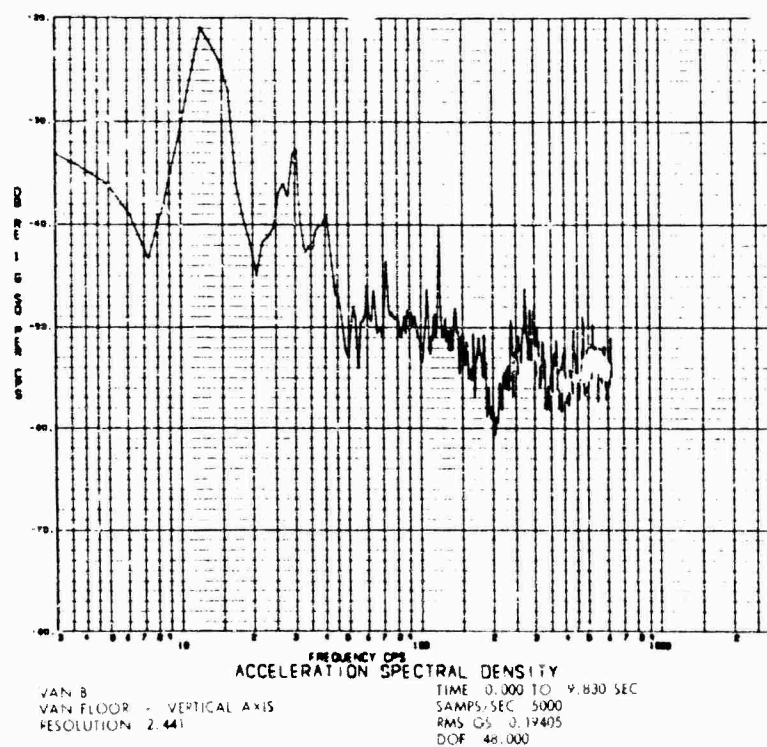


Fig. 8. PSD plot for vertical axis of van B floor: resolution, 2.441; time, 0.000-9.830 sec; samples per second, 5000; rms g, 0.19405; DOF, 48.000

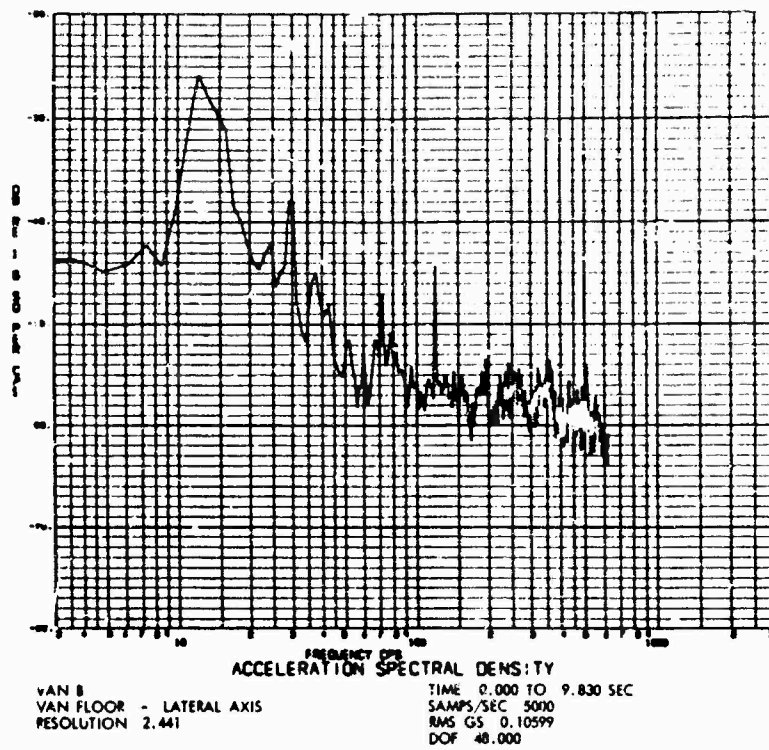


Fig. 9. PSD plot for lateral axis of van B floor: resolution, 2.441; time, 0.000-9.830 sec; samples per second, 5000; rms g, 0.10599; DOF, 48.000

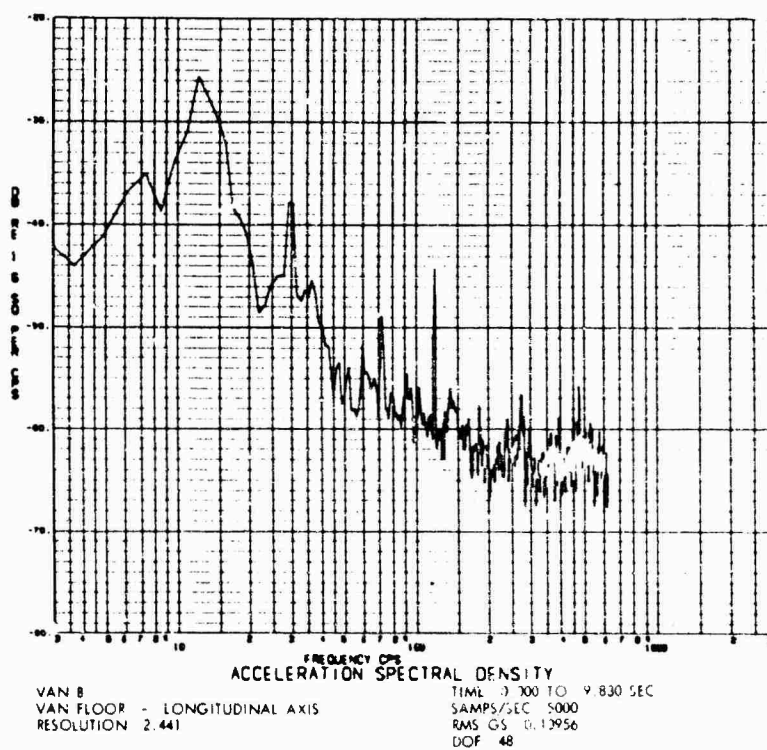


Fig. 10. PSD plot for longitudinal axis of van B floor: resolution, 2.441; time, 0.000-9.830 sec; samples per second, 5000; rms g, 0.10956; DOF, 48.000

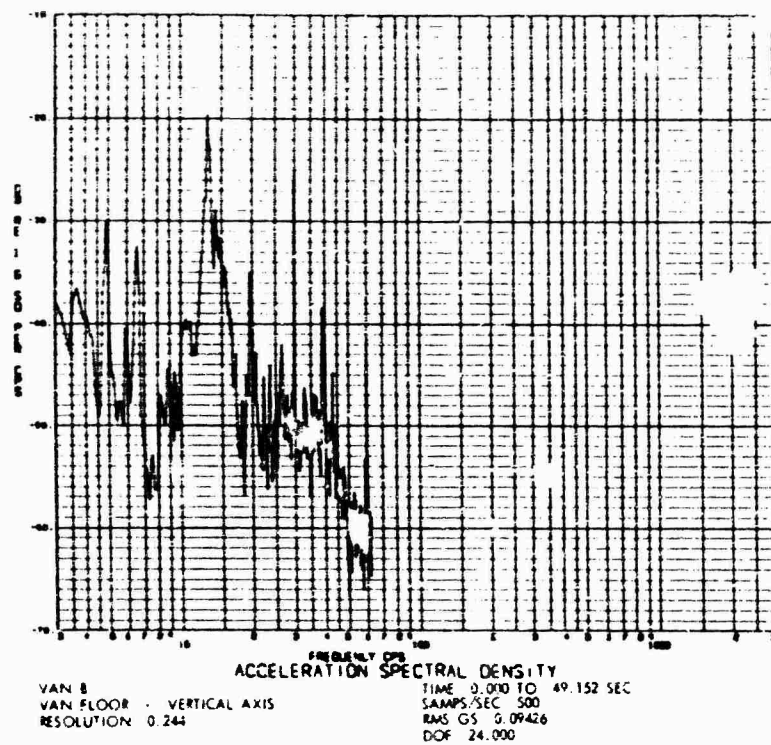


Fig. 11. PSD plot for vertical axis of van B floor: resolution, 0.244; time 0.000-49.152 sec; samples per second, 500; rms g, 0.09426; DOF, 24.000

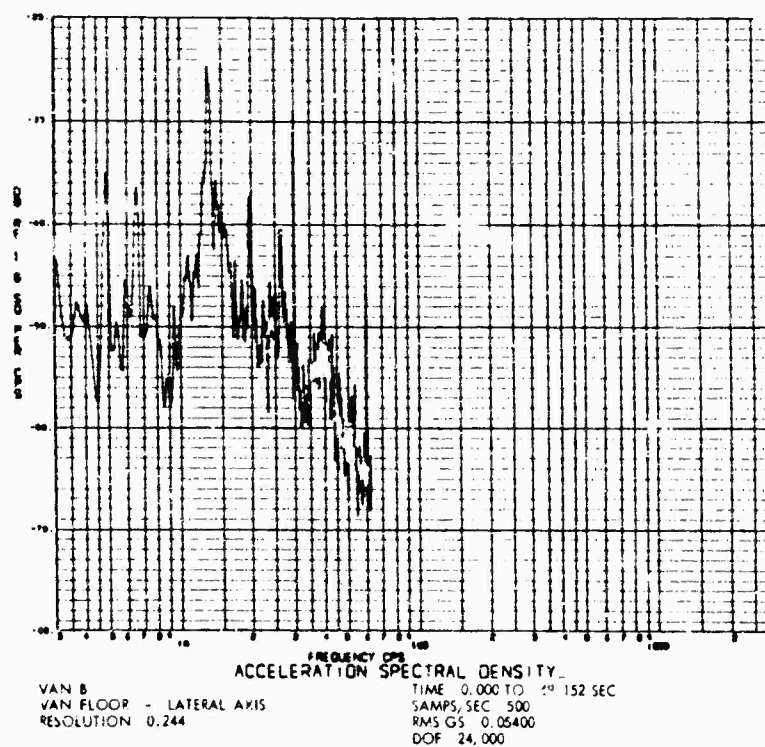


Fig. 12. PSD plot for lateral axis of van B floor: resolution, 0.244; time, 0.000-49.152 sec; samples per second, 500; rms g, 0.05400; DOF, 24.000



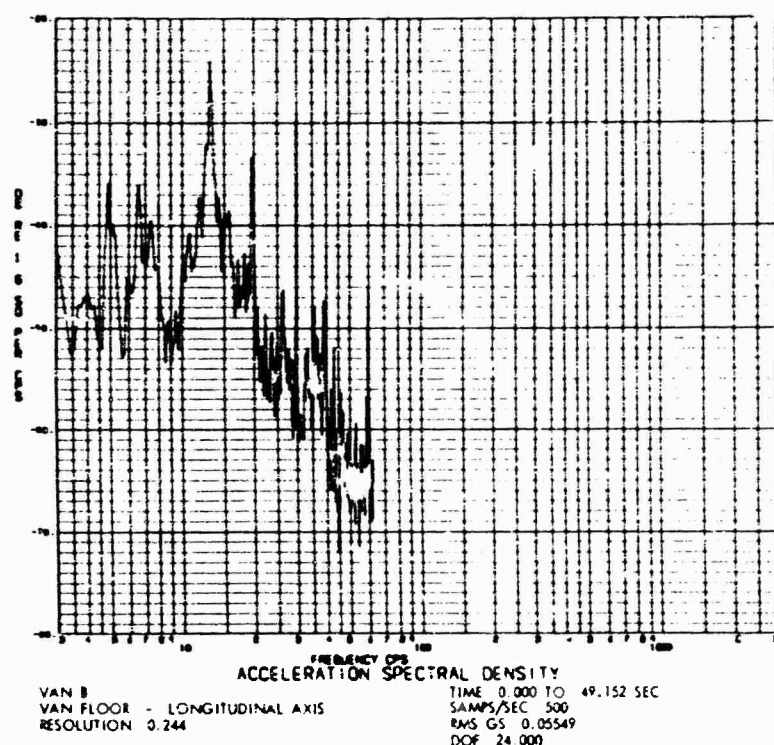


Fig. 13. PSD plot for longitudinal axis of van B floor: resolution, 0.244; time, 0.000-49.152 sec; samples per second, 500; rms g, 0.05549; DOF, 24.000

The wideband resolution plots (Figs. 8 through 10) indicate the vibration amplitudes to be negligible above 40 Hz in all three axes. The low-frequency peak response occurs at the same frequency in all three axes, although the peak amplitudes are lower in the lateral and longitudinal axes than in the vertical.

Two important differences in vibration excitation are apparent between these vans. First, the high-frequency energy existing in the van A set of data is nonexistent in the latter set. Second, the indication of significant excitation in the nonvertical axes is not evident in the van B data discussed. In spite of the fact that both vans had air-ride suspension systems, these differences did exist in their vibration

characteristics. Experience at JPL has shown that these differences are definitely not attributable to the inherent design features of various models or makes of air-ride suspension systems, but rather they are probably a function of the condition of the systems. A van with high-frequency excitation was modified, and it performed nominally with negligible vibration above 40 Hz. Table 1 compares the rms levels of the PSD plots from the two vans. These are maximum rms levels noted from the data samples studied.

Amplitude Statistics — Tables 2 and 3 contain the amplitude statistics for the two vans A and B. These tables indicate the percentage of time that specified peak g levels were exceeded

TABLE 1  
Comparison of rms Acceleration Levels For Two Air-Ride Suspension Vans

Van	Longitudinal Axis		Lateral Axis		Vertical Axis	
	3-600 Hz	3-60 Hz	3-600 Hz	3-60 Hz	3-600 Hz	3-60 Hz
A	0.42	0.10	0.69	0.09	1.91	0.12
B	0.110	0.06	0.106	0.054	0.194	0.094



**TABLE 2**  
**Van A Amplitude Statistics (High-Frequency Excitation)**

Amplitude (peak g)	Percentage of Time Exceeded							
	Reel 1 (3.2 hr) <sup>a</sup>		Reel 5 (4.1 hr) <sup>a</sup>		Reel 9 (3.6 hr) <sup>a</sup>		Reel 19 (3.9 hr) <sup>a</sup>	
	Vert	Lat	Vert	Lat	Vert	Lat	Vert	Lat
0.25	38	13	17	8	25	10	42	23
0.50	11	5	12	4	20	5	23	9
0.75	8	3	9	3	16	3	16	6
1.00	6	2	7	2	13	2	12	4
1.25							10	2
1.50							8	1.6
1.75							7	1
2.00							6	0.7

<sup>a</sup>Data time per reel.

on the van floor. Table 2 gives evidence that higher g levels were exceeded a much greater percentage of time in van A than in van B. The levels are extended to 2.0 g peak for reel 19 to give an indication of the maximum amplitudes produced. The data reels included in the tables are a typical representation of the amplitude statistics for a normal cross-country trip.

#### Airplane

Airplane data have been analyzed in the same formats as the van data. Data from C-130 and C-133 airplanes, presented in this section, were derived from two spacecraft shipments to Cape Kennedy from California. The instrumentation was the same for airplane transportation as it was for the truck vans.

**Power Spectral Density Plots** – Figures 14 through 16 contain the PSD plots of vibration data measured on the floor of a C-130 airplane. Three axes of measurements are represented in the plots: longitudinal, lateral, and vertical. The data were plotted with a resolution of 4.88 cycles. The data are from the same time sample and represent the maximum amplitude stationary vibration data noted on the oscillograph playback. The vibration was generated at takeoff.

The maximum wideband rms value is 0.65 g rms in the vertical axis data of Fig. 14. The predominant frequency in this axis is about 68 Hz. The peak rms value at 68 Hz is between 0.15 and 0.30 g rms and could be as high as 50 percent of the wideband value. It should be noted that the peak frequency of 68 Hz also

**TABLE 3**  
**Van B Amplitude Statistics (No High-Frequency Excitation)**

Amplitude (peak g)	Percentage of Time Exceeded					
	Reel 3 (4.1 hr) <sup>a</sup>		Reel 5 (4.1 hr) <sup>a</sup>		Reel 11 (3.9 hr) <sup>a</sup>	
	Vert	Lat	Vert	Lat	Vert	Lat
0.25	47	42	47	58	45	56
0.50	0.3	0	0.2	0	5	0
0.75	0	0	0	0	0	0
1.00	0	0	0	0	0	0

<sup>a</sup>Data time per reel.

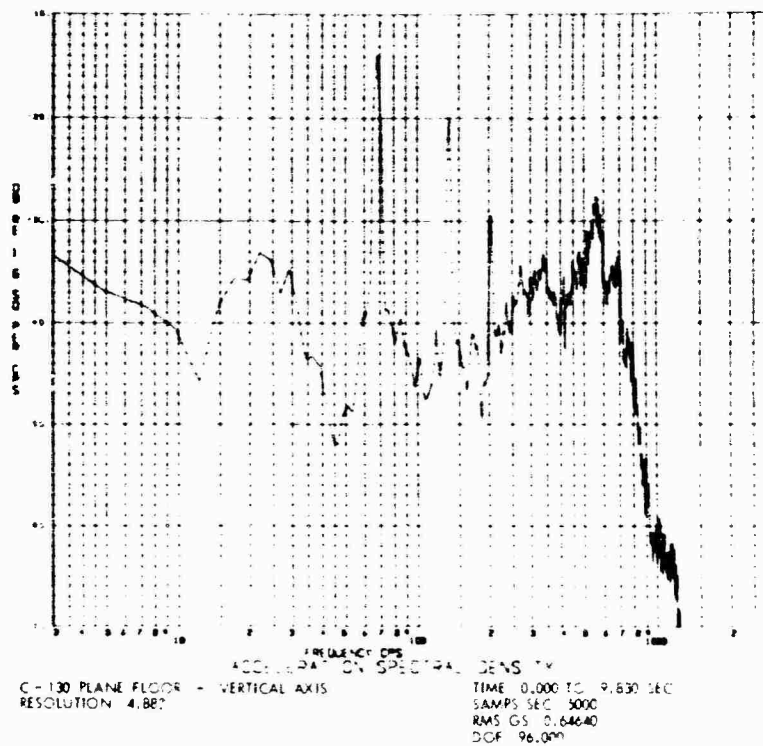


Fig. 14. PSD plot for vertical axis of C-130 plane floor: resolution, 4.883; time, 0.000-9.830 sec; samples per second, 5000; rms g, 0.64640; DOF, 96.000

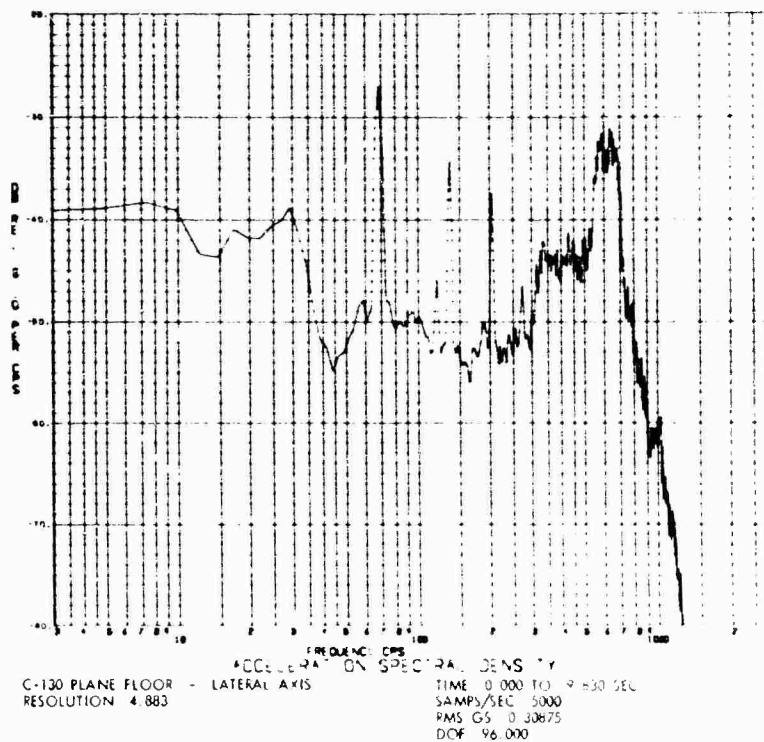


Fig. 15. PSD plot for lateral axis of C-130 plane floor: resolution, 4.883; time, 0.000-9.830 sec; samples per second, 5000; rms g, 0.30875; DOF 96.000

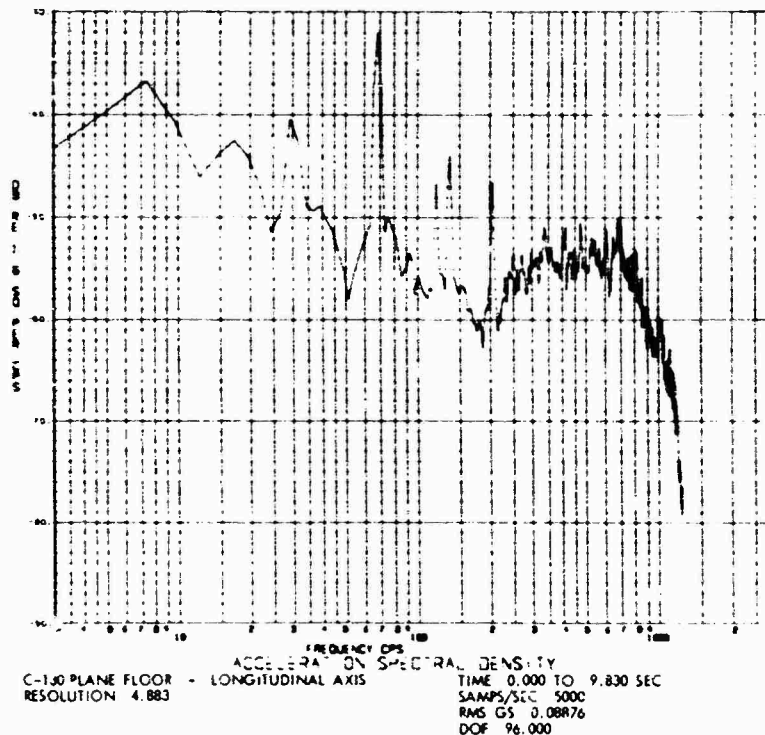


Fig. 16. PSD plot for longitudinal axis of C-130 plane floor: resolution, 4.883; time, 0.000-9.830 sec; samples per second, 5000; rms g, 0.08876; DOF, 96.000

exists in the lateral and longitudinal axes, but does not have the amplitude of the vertical axis component. The longitudinal axis wideband rms is 13 percent of the vertical axis, and the lateral is 47 percent of the vertical wideband level. These axes are plotted in Figs. 15 and 16.

Figures 17 through 19 contain PSD's of cruise-mode vibration for comparison with the takeoff data. These plots present the vibration characteristics that typify the greatest percentage of the trip duration.

Data from the C-133 airplane are contained in Figs. 20 through 23. The measurements were made on the airplane floor in the same three axes as the other data recordings. The longitudinal axis has been omitted, however, since it is lower in amplitude than the vertical or lateral axes and as shown for the C-130 airplane is essentially negligible.

The PSD plots for the C-133 indicate a peak frequency at 48 Hz in both the lateral and vertical axes. In the vertical axis, the wideband rms acceleration level is 0.6 g rms for takeoff. The peak is in the range of 0.3-0.5 g rms or possibly as great as 83 percent of the wideband level. The lateral wideband level is about 38 percent of the vertical. Figure 22 is the vertical axis data sampled during cruise mode, and Fig. 23 is the lateral axis during this period of flight. The resolution of all these plots is 4.88 Hz. Table 4 compares the C-130 and C-133 airplanes.

**Amplitude Statistics** — Tables 5 and 6 contain amplitude statistics from the two airplane flights. These tables indicate the percentage of time that various peak g levels were exceeded. Table 7, which contains additional information from a third flight to Cape Kennedy, shows the maximum levels occurring in a normal cross-country flight with the C-130 airplane.

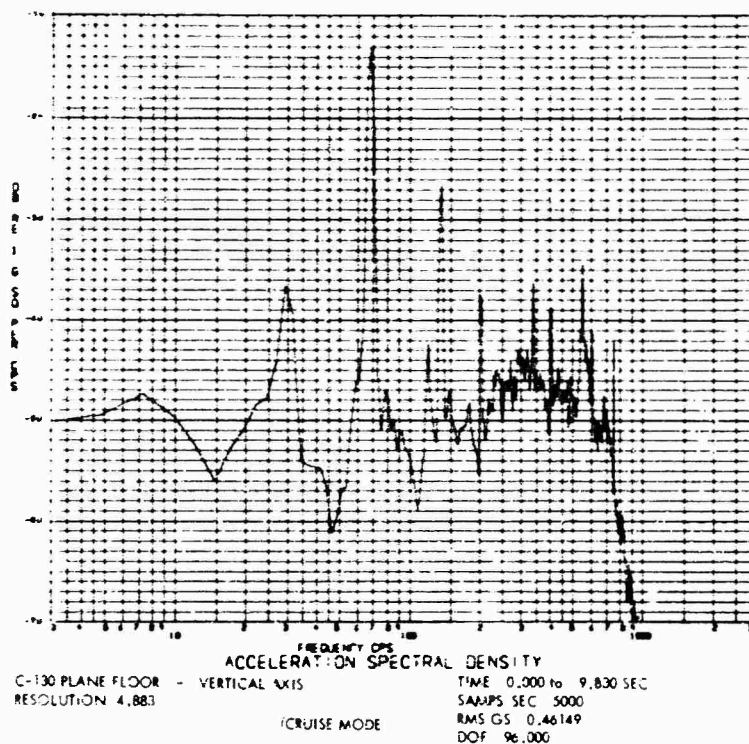


Fig. 17. PSD plot for vertical axis of C-130 plane floor (cruise mode): resolution, 4.883; time, 0.000-9.830 sec; samples per second, 5000; rms g, 0.46149; DOF, 96.000

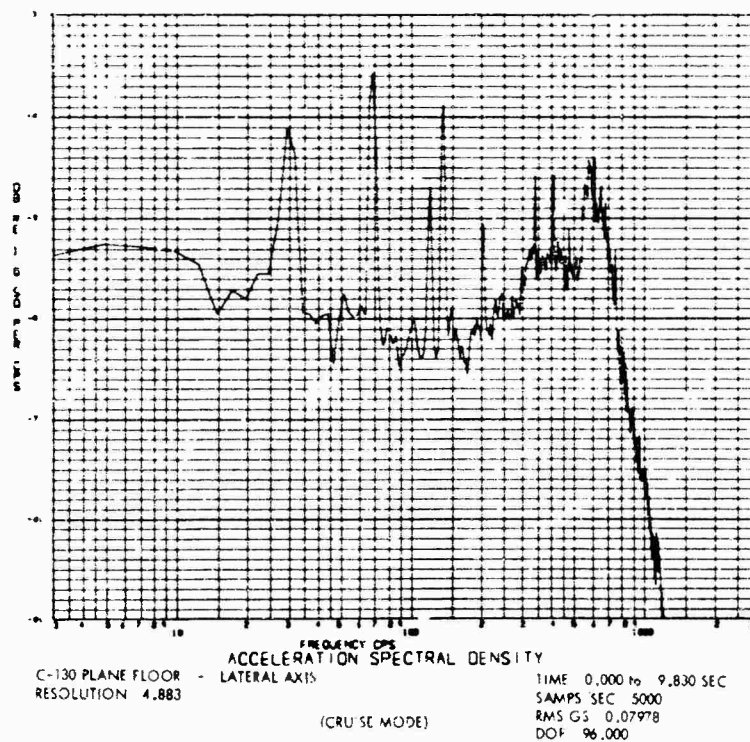


Fig. 18. PSD plot for lateral axis of C-130 plane floor (cruise mode): resolution, 4.883; time, 0.000-9.830 sec; samples per second, 5000; rms g, 0.07978; DOF, 96.000

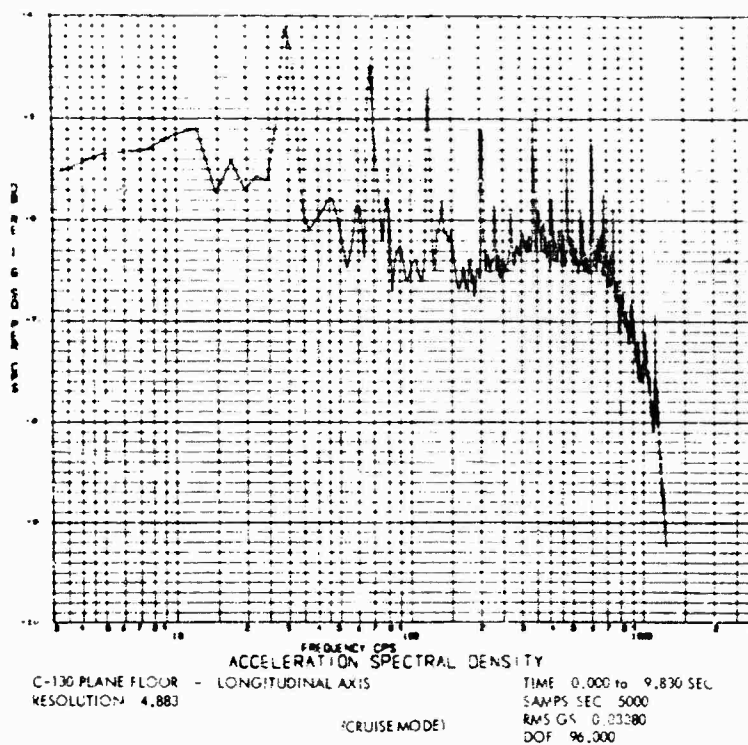


Fig. 19. PSD plot for longitudinal axis of C-130 plane floor (cruise mode): resolution, 4.883; time, 0.000-9.830 sec; samples per second, 5000; rms g, 0.03380; DOF, 96.000

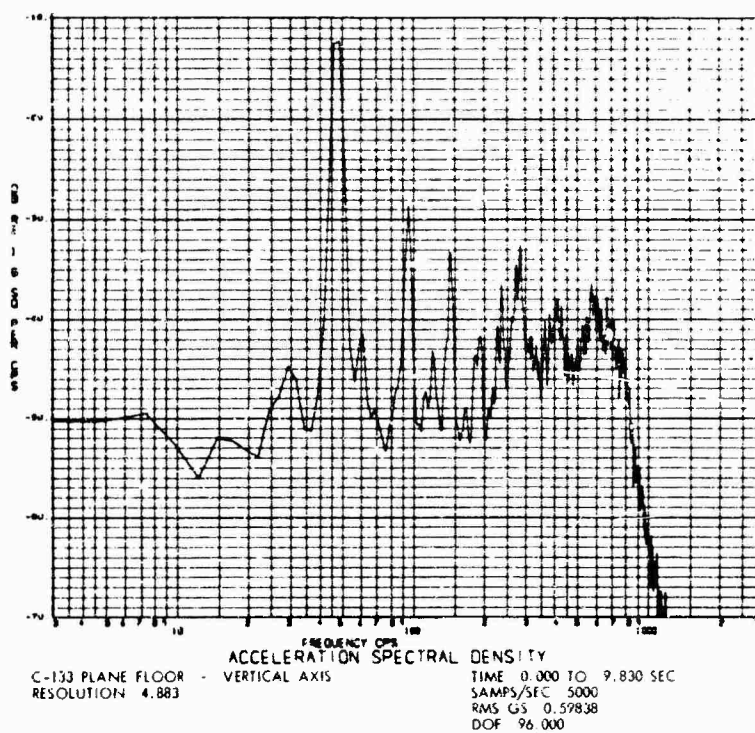


Fig. 20. PSD plot for vertical axis of C-133 plane floor: resolution, 4.883; time, 0.000-9.830 sec; samples per second, 5000; rms g, 0.59838; DOF, 96.000

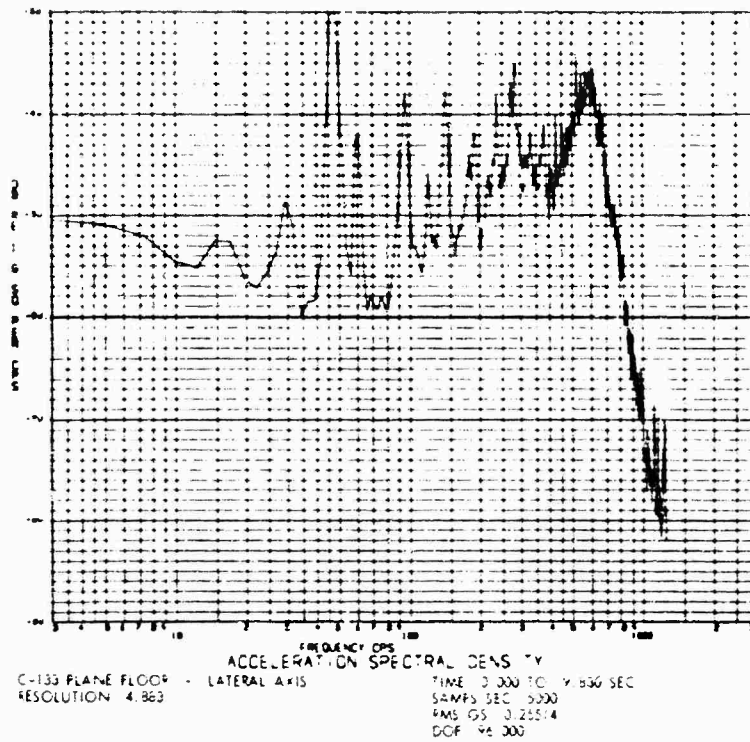


Fig. 21. PSD plot for lateral axis of C-133 plane floor; resolution, 4.883; time, 0.000-9.830 sec; samples per second, 5000; rms g, 0.25514; DOF, 96.000

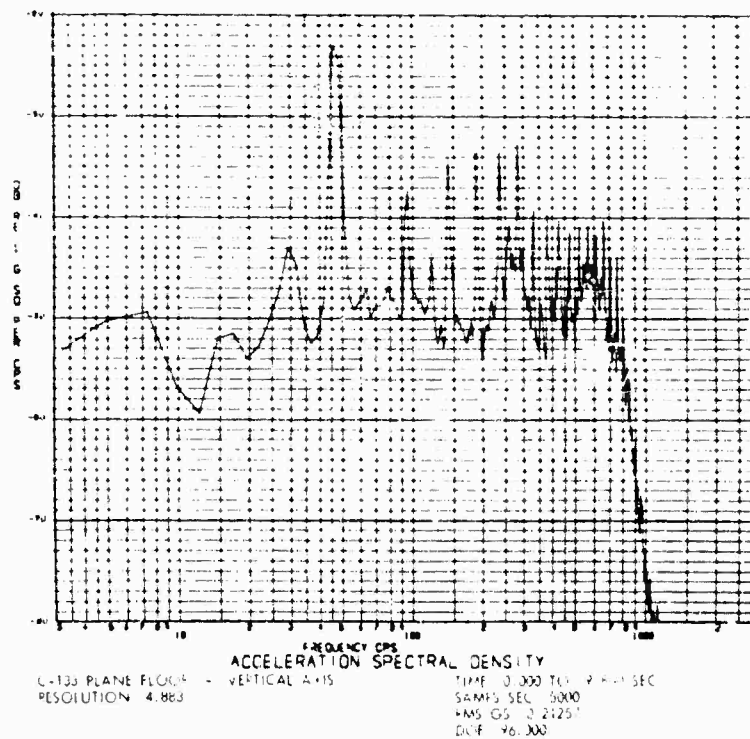


Fig. 22. PSD plot for vertical axis of C-133 plane floor; resolution, 4.883; time, 0.000-9.830 sec; samples per second, 5000; rms g, 0.21257; DOF, 96.000

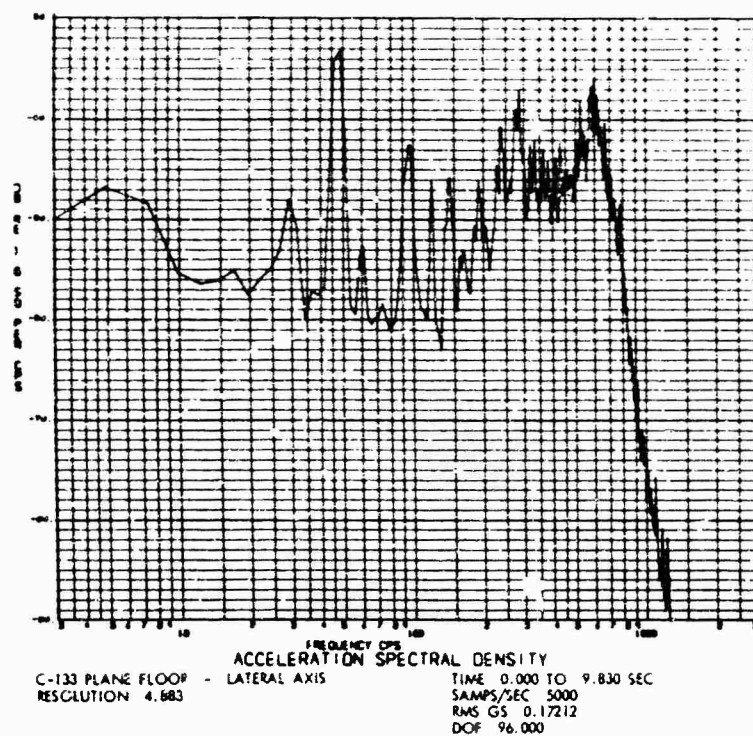


Fig. 23. PSD plot for lateral axis of C-133 plane floor: resolution, 4.883; time, 0.000-9.830 sec; samples per second, 5000; rms g, 0.17212; DOF, 96.000

TABLE 4  
Comparison of C-130 and C-133 Airplane Data

Axis	Peak Frequency (Hz)		Peak Amplitude (db)		RMS Level	
	C-130	C-133	C-130	C-133	C-130	C-133
Takeoff						
Vert	68	47	-14	-12	0.64	0.60
Lat	68	47	-27	-30	0.31	0.23
Cruise Mode						
Vert	68	47	-13	-23	0.46	0.21
Lat	68	47	-35	-33	0.08	0.17

TABLE 5  
C-130 Airplane Amplitude Statistics

Amplitude (peak g)	Percentage of Time Exceeded					
	Reel 1 (2.5 hr) <sup>a</sup>		Reel 2 (3.5 hr) <sup>a</sup>		Reel 3 (1.1 hr) <sup>a</sup>	
	Vert	Lat	Vert	Lat	Vert	Lat
0.25	40	35	38	38	35	32
0.50	22	12	18	16	12	10
0.75	9	3	7	5	3	2
1.00	3	0.4	2	0.9	0.5	0.4

<sup>a</sup>Data time per reel.

TABLE 6  
C-133 Airplane Amplitude Statistics

Amplitude (peak g)	Percentage of Time Exceeded					
	Reel 1 (3.6 hr) <sup>a</sup>		Reel 2 (3.8 hr) <sup>a</sup>		Reel 3 (1.5 hr) <sup>a</sup>	
	Vert	Lat	Vert	Lat	Vert	Lat
0.25	24	17	32	21	20	12
0.50	10	3	13	3	4	1
0.75	3	0.6	4	0.2	0.6	0
1.00	0.8	0.4	0.6	0	0	0

<sup>a</sup>Data time per reel.

TABLE 7  
C-130 Airplane Amplitude Statistics

Amplitude (peak g)	Percentage of Time Exceeded
0.25	38
0.50	25
0.75	14
1.00	5
1.25	0.9
1.50	0.1
2.00	0

## CONCLUSIONS AND RECOMMENDATIONS

It is concluded that:

1. The normal vibration characteristics of air-ride vans and the two aircraft discussed above should not be detrimental to the structural or functional integrity of electronic

equipment unless resonant frequencies of the equipment are the same as the peak frequencies of the transportation excitation.

2. Air-ride suspension systems with many miles of travel may have abnormal ride qualities with high-frequency excitation. The acceptance of a particular van should be based on preestablished criteria. Vans with high-frequency excitation can often be identified by simply riding in them. These vans have a characteristic banging sound.

3. Amplitudes exceeding 1 g peak rarely occur in an airplane or truck van cross-country trip. These amplitudes do occur with abnormally functioning suspension systems, however.

It is recommended that:

1. Individual truck vans should be qualified to an established criterion prior to their use as a means of transportation for flight spacecraft equipment. The qualification requirements should be dictated by the payload dynamic characteristics and fragility levels if they have been determined. The test procedure should specify the instrumentation to be employed, the van locations for this instrumentation, the road test route to be followed, and the speeds at which the route should be traversed. The acceptance criterion should specify the maximum acceptable g levels measured on the van floor. It should indicate the acceptable spectral shape if certain frequencies are critical. For instance, the high-frequency excitation noted on the van discussed here may be damaging to certain equipment being transported. These frequencies must then be avoided.

2. Real-time vibration monitoring instrumentation should be developed for long distance transportation. It is possible for the payload vibration environment to change during transit. This change could be the result of vehicle changes, such as a failure in the suspension system of a van or engine phenomenon on an airplane. Shock loads could be introduced to the payload if the tiedowns become unsecured. The real-time monitoring instrumentation would detect this abnormal excitation en route and perhaps indicate the need of repairs before fatigue damage to the payload has occurred. The instrumentation must of course be designed for the application. An oscilloscope may be sufficient if, for instance, a technician is accompanying the payload on an airplane flight. An audible signal generator such as a buzzer in the truck cab may be required for a van shipment where the personnel are not in the immediate vicinity of the payload and bulky monitoring



equipment is not practical in the cab with them. The device can be located in the accelerometer amplifier output circuit.

3. If an organization is faced with the review of a large number of transportation data tapes because of the lack of real-time monitoring or the requirement for permanent data records, it should consider two alternatives to make the review efficient and prompt. The first alternative is a system that records only data exceeding preselected parameters such as acceleration amplitude and frequency content. Systems such as this are being developed and equipment can be purchased that functions in

this manner. The second alternative is to develop a computer program, such as that available at JPL, to establish the time duration of input loadings exceeding selected amplitudes. As indicated previously, this information can be very useful to the design engineer or to the engineer with the responsibility of assuring a satisfactory ride for the payload.

#### REFERENCE

1. J. W. Schlue, "The Dynamic Environment of Spacecraft Surface Transportation," Jet Propulsion Laboratory, TR 32-876, Mar. 1966

#### DISCUSSION

Mr. Rice (Goodyear Aerospace Corp.): Did you have any instrumentation on the package being shipped? Did you try to correlate that with what you measured on the deck?

Mr. Schlue: Yes, we did have instrumentation on the packages themselves. I haven't presented any of that here because I wanted to keep this a general type presentation. We have noticed that for most frequencies we have attenuation, although in the higher frequencies we were concerned about some of the local resonances. That is why we did an exhaustive study on the spacecraft after this particular trip. What you see on the package is going to depend on the type of mounting, whether isolators are used, or whether the package is hard mounted to the floor.

Mr. Gertel (Allied Research Assoc.): If I understood some of the data you presented, I see PSD levels which are very very low compared to flight vibration observations, or the levels that have been used in environmental laboratories for qualifying flight hardware. It almost seemed to suggest that there is no transportation vibration problem.

Mr. Schlue: Your point is well taken, but remember that we are talking about cross-country trips which may last as long as 96 hours where fatigue enters in. Although the levels may be equal to or less than ground test data the time duration at some of these levels may far exceed the time on a vibration test. I think fatigue is very significant here.

Mr. Harvey (Goodyear Aerospace Corp.): I would like to comment on some of your data. I have done considerable work along this line

and have found that air-ride suspension systems have a natural frequency ordinarily no greater than 2 Hz. I was a little shocked to see some of the data that you had at the higher frequencies. I would strongly suspect that your instrumentation is not mounted properly. You should not be measuring responses above 50 Hz.

Mr. Schlue: I have to admit, when I first looked at these data on the trip from Florida to California, I thought they had forgotten to hook up the accelerometers. We made exhaustive tests to verify the data. We had the technicians examine the recorder very carefully. We went through the whole system and checked out the amplifiers. In fact, we wanted to make so sure that this was good data that we actually brought back the same van and reran tests on it. That picture of all the instrumentation was indeed this van that we were retesting. We were even using dual recorders to make sure it was not a function of the recorder. Now, I know everybody says that the natural frequency is 2 Hz. If you are talking about the bed itself, which would bounce up and down at 2 Hz this is probably true. But I think most of the excitation is due to wheel bounce or something of that sort. That seems to be somewhere between 10 and 20 Hz.

Mr. Biamonte (Army Electronics Command): Are the levels that you have reported in van A and van B considered destructive? They seem to be pretty low.

Mr. Schlue: This again I think would depend on the payload and on the response of the payload to this type of excitation. We are looking at data down on the floor and it could be that most of this excitation will be attenuated. We

had some equipment on the spacecraft that had resonances within the high frequency ranges about which we were concerned. This is one reason that we made an extensive study of the spacecraft after this trip.

Mr. Morrow (LTV Research Center): I don't think that the high frequency content should be very surprising if there is a little bit of looseness somewhere in the suspension. It should not be a real difficult problem to provide some isolation, at least if one doesn't work too hard at it and make a big problem out of it. However, my general reaction is very much like Maurice Gertel's. These levels are pretty

low, and after all, fatigue is very level sensitive, more level-sensitive than time-sensitive. It would seem to me the chance of getting fatigue damage is pretty small and maybe one should design the equipment so that it should survive this sort of environment as well as the flight environment. After all, the state of the art of simulation is not such that we can readily distinguish between something that has to survive for a long time and something that has to survive very briefly. So, maybe your equipment will survive.

Mr. Kirchman: I would like to comment in closing that the only two identifiable failures I have seen were in transportation.

\* \* \*

## RECENT SHOCK AND VIBRATION MEASUREMENTS ON THE M-151 (JEEP) VEHICLE

Ronald D. Brunner and George M. Pomonik  
Hughes Aircraft Company  
Canoga Park, California

A test program and data acquired during a field test conducted to measure shock and vibration environment for the TOW weapon system as mounted on the M-151 vehicle (jeep) are described. Test conditions included operation over various road surfaces from smooth to unimproved, over cross-country terrain, and over a Munson-type road course. Instrumentation consisted of piezoelectric accelerometers with charge amplifiers for signal conditioning and a portable (14-track) magnetic tape recorder. Examination of the data leads to the conclusion that the vibration environment is no more severe than that specified in MIL-STD-810A, Figure 514-5, "Vibration test curve for equipment installed in ground vehicles."

### INTRODUCTION

An environmental measurement program was conducted to determine the level of shock and vibration to which the TOW weapon is subjected when installed on the M-151 vehicle. The weapon system and vehicle were subjected to various operational field transportation tests. Data were obtained over a range of vehicle speeds and conditions. These test conditions consisted of five basic field environments:

1. Munson road course (spaced bumps on concrete surface)
2. Primary road (hard surface blacktop)
3. Secondary road (dirt and gravel combination)
4. Primitive road (dirt, dust, rock, and grass)
5. Cross-country terrain (open field — no road)

These environments are associated with the operational field conditions which the weapon system is subjected to during a portion of its life cycle. The TOW weapon system adapter kit for the M-151 vehicle consists basically of the launcher system, missile stowage rack, and missiles. A complete adapter kit was installed during the M-151 field test.

The M-151 jeep is a high-production multi-purpose vehicle with an individual wheel suspension system. Its proposed uses include transportation of personnel, communications for observation and fire control, and a special purpose weapons carrier for heavy assault weapons such as the TOW weapon system.

### TEST OBJECTIVES

The test objectives were:

1. To measure the vibration and shock environment which occurs during field operations of the M-151 (Jeep) vehicle. The data were compared with current TOW design criteria documents [1,2,3] and with the section of MIL-STD-810A [4] which pertains to ground vehicles.
2. To demonstrate the design adequacy of the TOW missile/launcher-system adapter kit hardware and installation on the vehicle during field use.
3. To obtain response data from the TOW missile in the stowed and deployed configurations during field testing.

### DETAILS OF TEST

The test was conducted in two phases, vibration and shock. The shock test was

conducted at the Hughes Aircraft Company, Fullerton Facility, Munson road course, Fullerton, California, and the field environments at Wyle Laboratories, Norco, California.

The M-151 vehicle used was a 1966 Ford S/N 2K5872 with less than 200 miles on the odometer. A complete TOW weapon system kit was installed on the vehicle as shown in Fig. 1.

#### INSTRUMENTATION

Figures 2 and 3 show the accelerometer locations for both the shock and vibration phases. Piezoelectric accelerometers were used for all tests, and the data were recorded on a 14-track magnetic tape recorder. The block diagram for the data acquisition system is shown in Fig. 4. All data acquisition equipment was carried in an M-416 1/4 ton trailer.

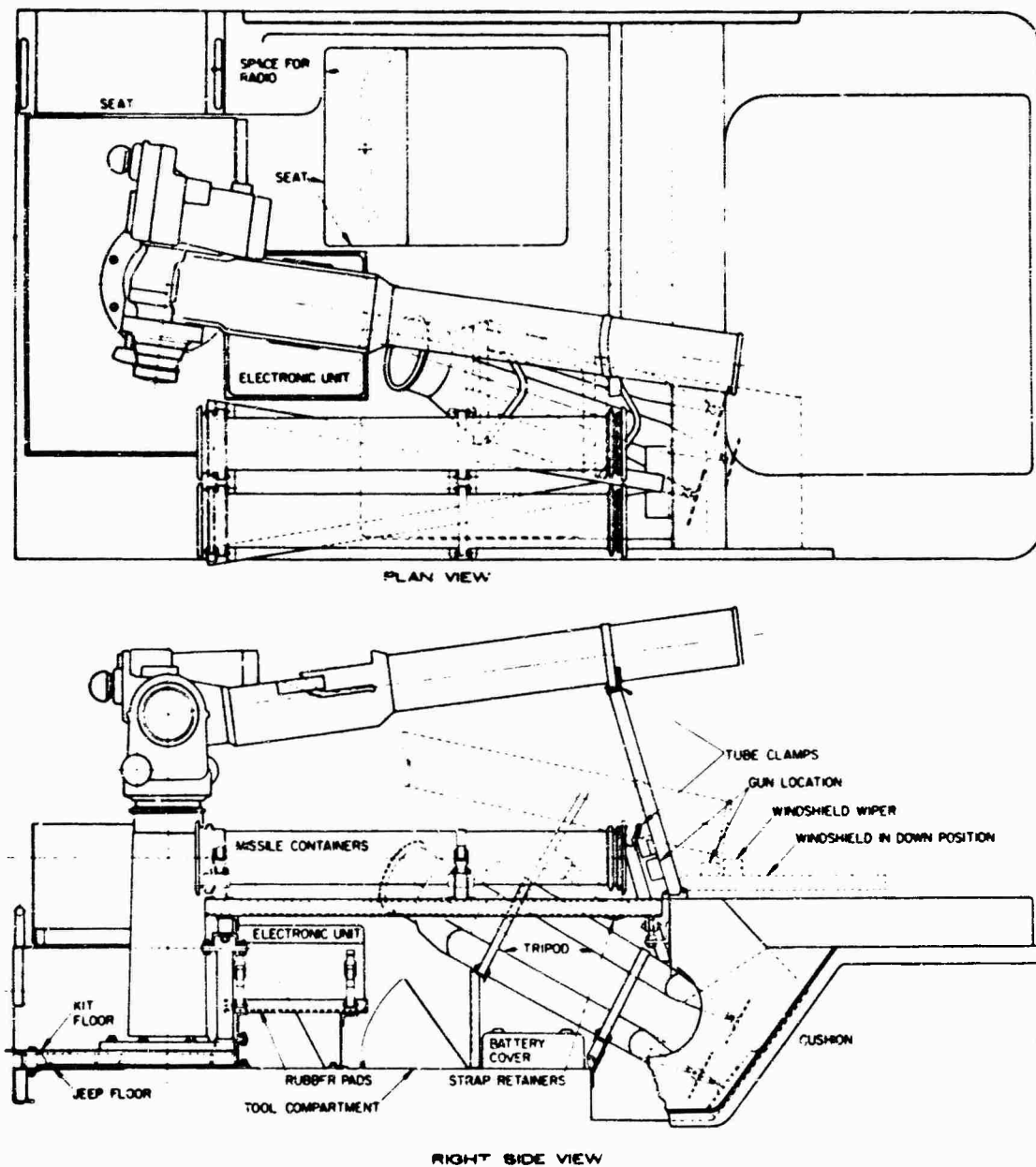


Fig. 1. TOW missile launcher system installation in M-151 jeep 1

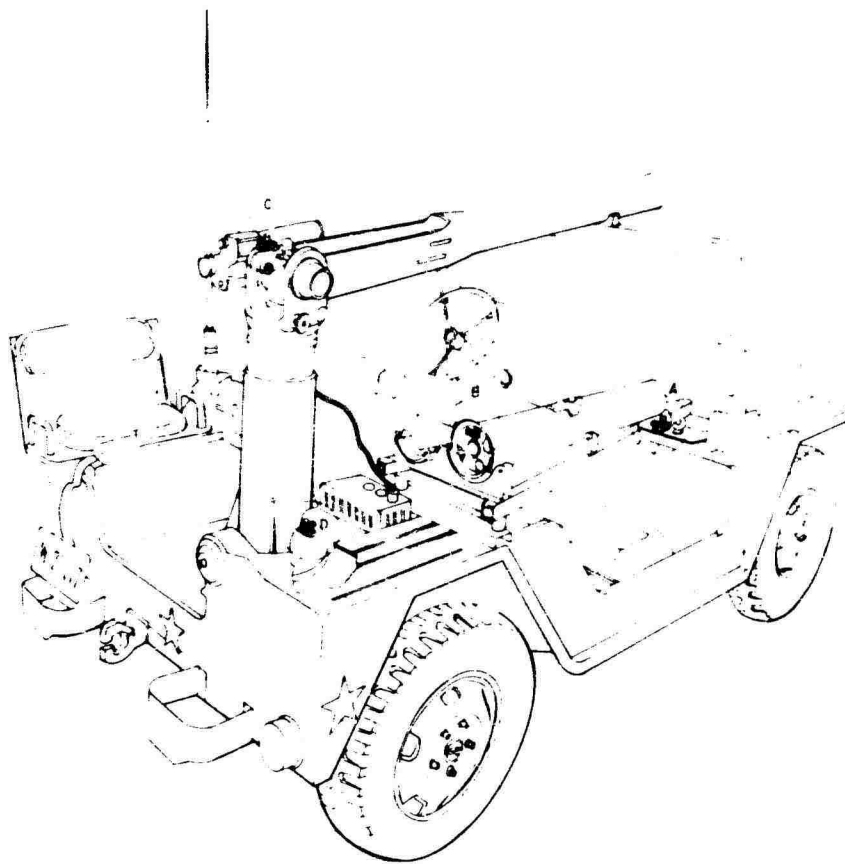


Fig. 2. M-151 jeep road test accelerometer orientation and location

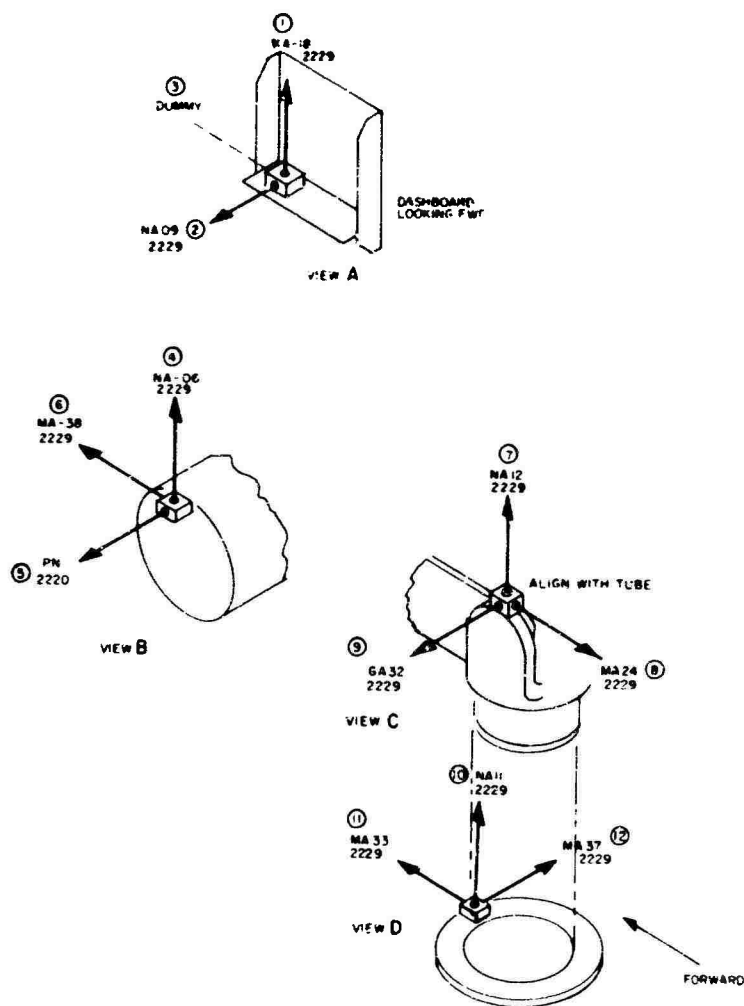


Fig. 3. Accelerometer locations

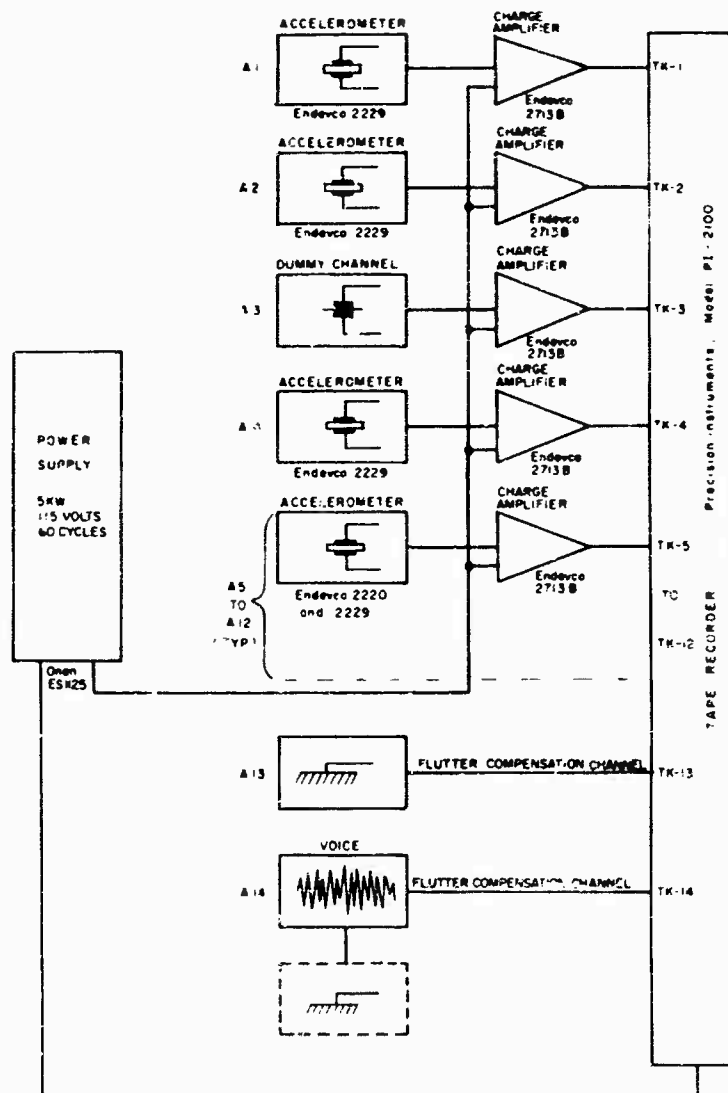


Fig. 4. Data acquisition system

During the Fullerton shock test, the recording and signal conditioning instruments were towed next to the test vehicle by another jeep. The trailer was towed behind the test vehicle during all other tests.

#### TEST AND MEASUREMENTS CONDITIONS

With the TOW system installed and instrumented, the M-151 vehicle was subjected to the following:

1. The vehicle was driven over the spaced bump course at speeds ranging from 5 to 35 mph in 5-mph increments.

2. The vehicle was driven over a primary road (hard surface blacktop) at speeds ranging from 5 to 45 mph in 5-mph increments.

3. The vehicle was driven over a secondary road (dirt and gravel combination) at speeds ranging from 5 to 35 mph at 5-mph increments.

4. The vehicle was driven over a primitive road (dirt, grass, and rocks) at speeds ranging from 5 to 25 mph at 5-mph increments.

5. After completing this test, the vehicle was subjected to the cross-country terrain. During this test, the vehicle was driven over the open field at three speeds, 5, 15, and 25 mph, and the data were recorded.

In the Munson road course, the test vehicle was subjected to 10 road bumps placed on an oval track. These bumps were oriented at 90, 113, 128, 67, and 52 deg to the direction of travel, as shown in Fig. 5.

#### TEST RESULTS AND ANALYSIS

A direct comparison of Munson road (shock) test data to the MIL-STD-810A was not possible; however, a comparison was made of the M-113 shock data (Fig. 6). This is an approximation based on shock spectral analysis from the M-113 vehicle [5], and a shock pulse recorded on channel 10 at 35 mph on the Munson course (see Figs. 7 and 8).

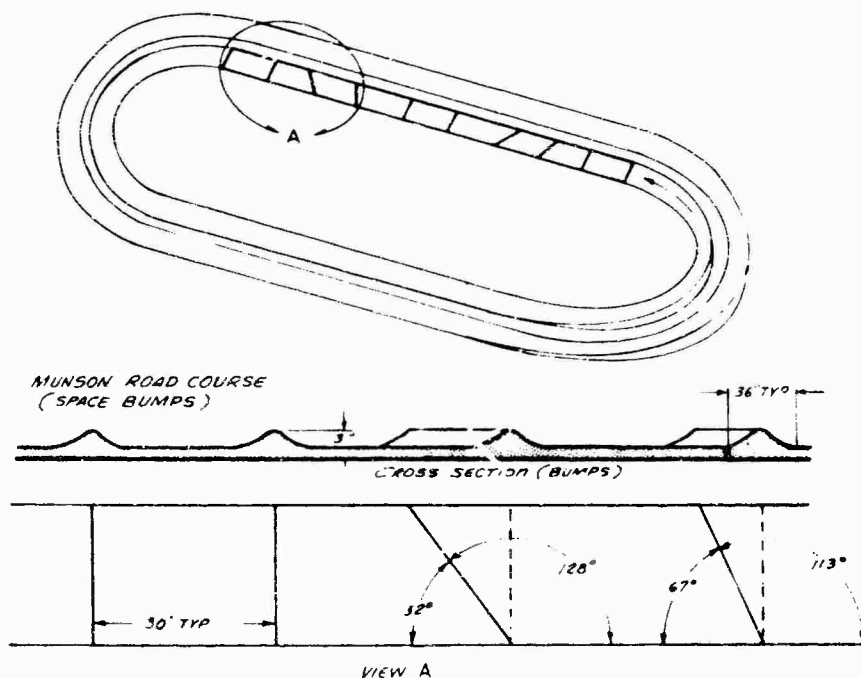


Fig. 5. Munson-type road course



Fig. 6. Shock spectral comparison of M-113 vehicle, and M-151 vehicle

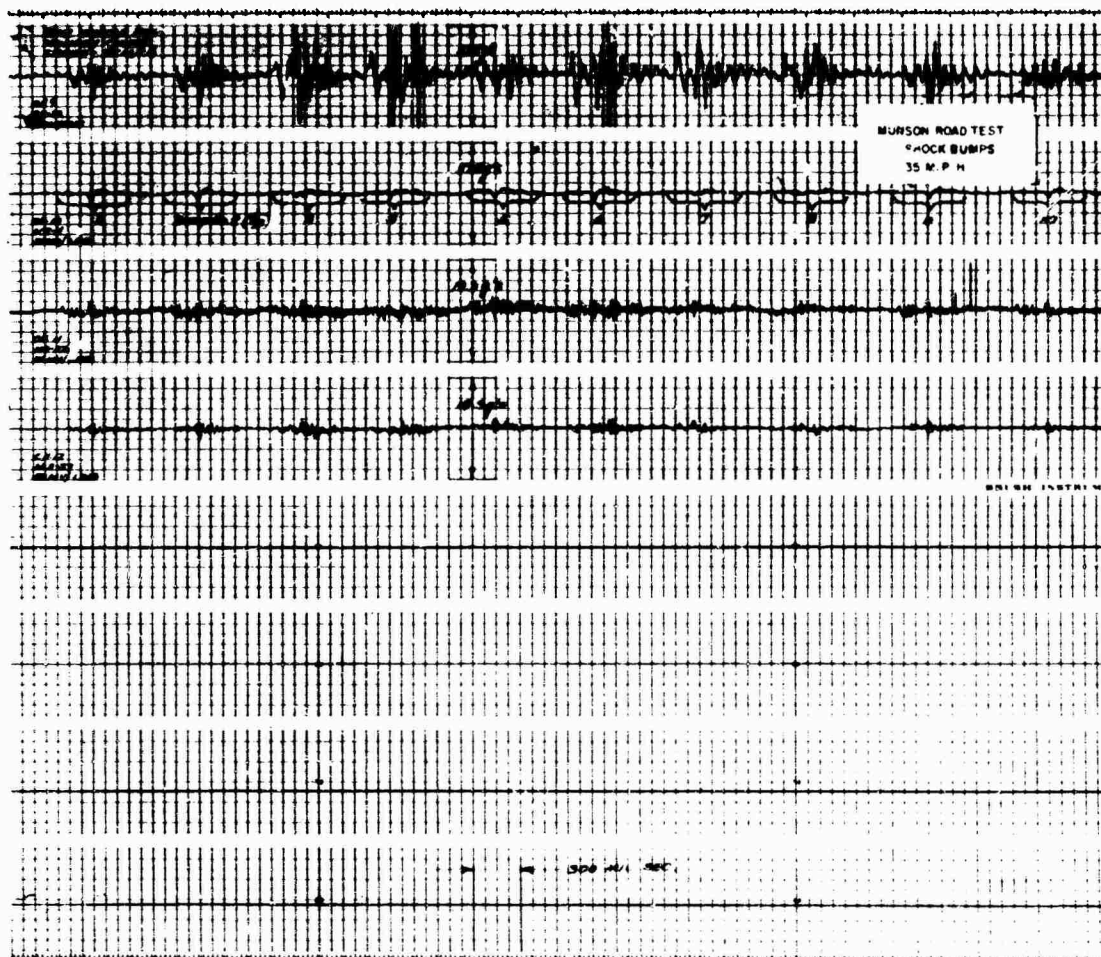
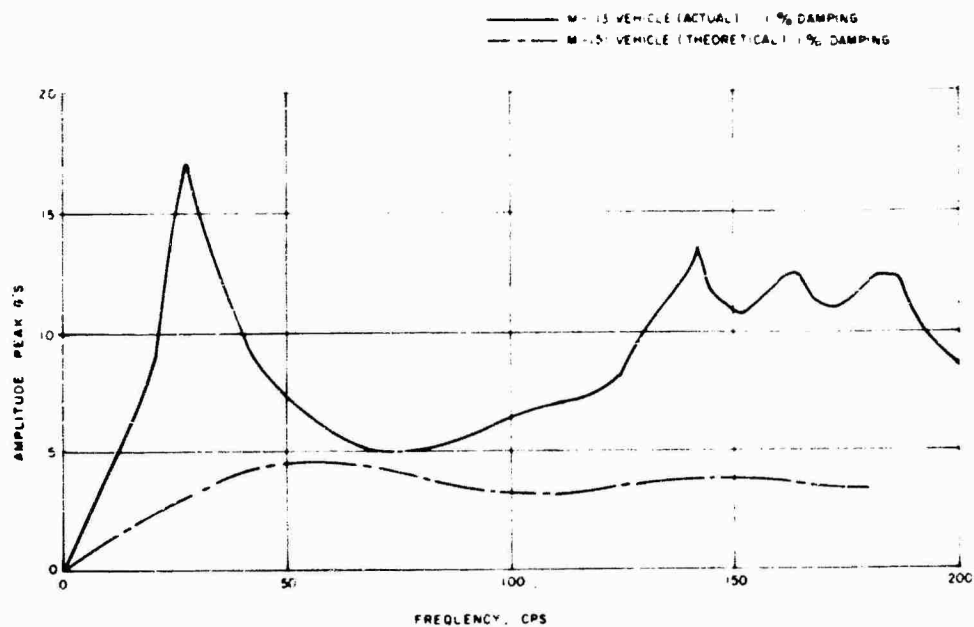


Fig. 7. Munson road test, time history of shock bumps at 35 mph



The pulse being used for comparison was an isosceles triangle with an amplitude of 3.7 g and a duration of 0.023 sec (see Figs. 7 and 8 for the time traces). The approximation shows that the levels of shock experienced are far greater on the M-113 vehicle than that recorded on the M-151 vehicle. Figures 9 and 10 show peak g as a function of vehicle speed on the Munson course.

Review of the peak responses from the Munson road course showed channel 1 as seeing

31.9 g at 35 mph over shock bump 7 (see Fig. 11). This shock response was of high frequency and low energy. Channel 1 monitors the input to the missile stowage rack at the dashboard attachment point. At the time 31.9 g on channel 1 was recorded, the instrumented missile was in the deployed position. The eccentric loading of the rack accounts for this high response acceleration occurring during this condition. As a comparison, the peak acceleration recorded at the same location with both missiles in the stowage rack was 17.1 g (see Fig. 12).

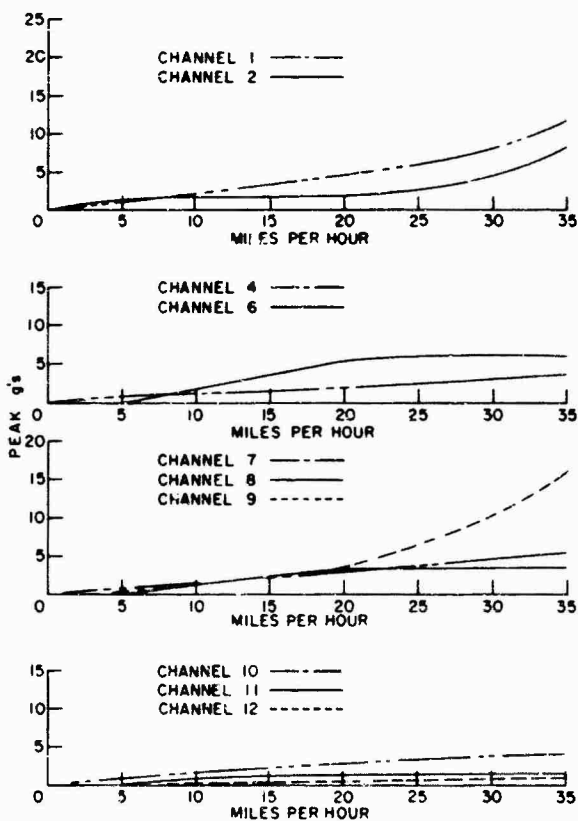


Fig. 9. Peak acceleration to shock bump 2, 90-deg, Munson road course

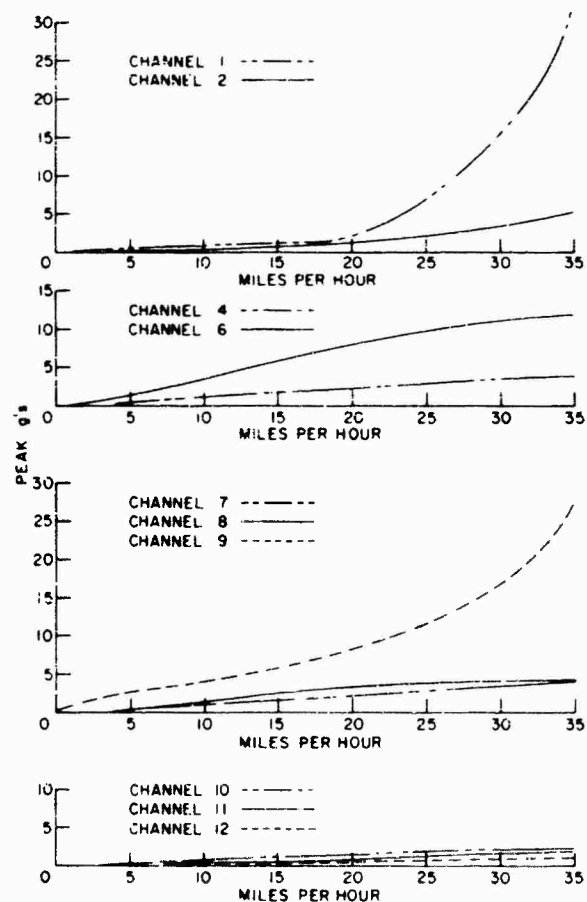


Fig. 10. Peak acceleration to shock bump 7, 62-deg, Munson road course

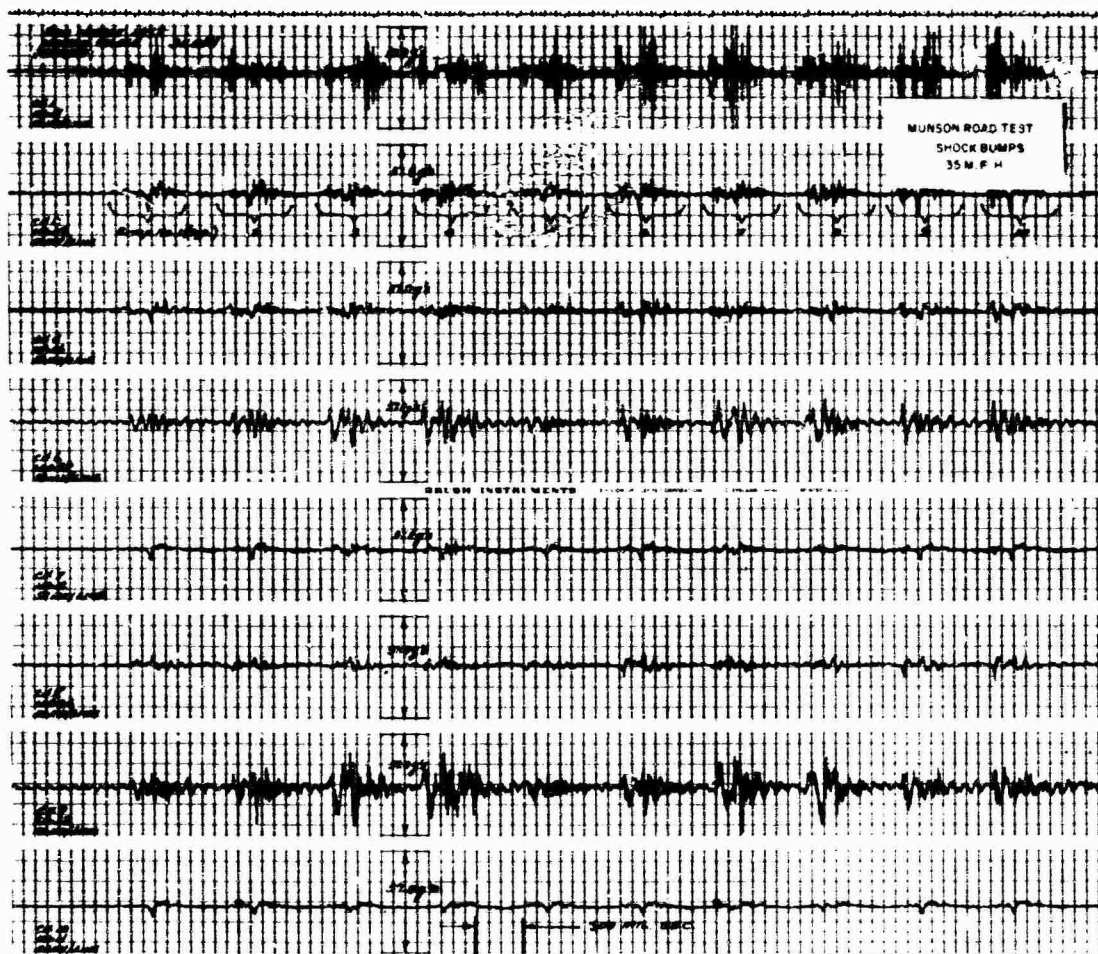


Fig. 11. Munson road test, time history of shock bumps at 35 mph (missile deployed)

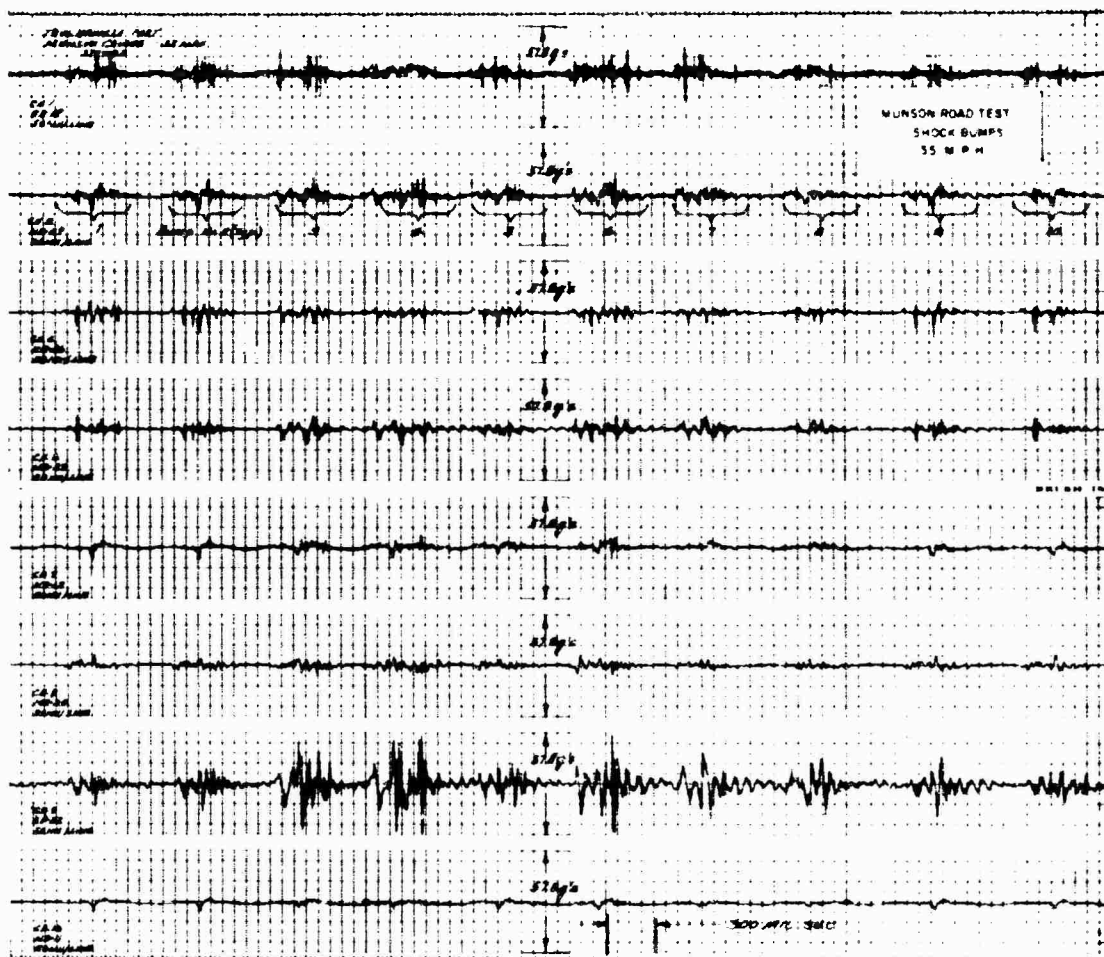


Fig. 12. Munson road test, time history of shock bumps at 35 mph (missile stowed)

### Primary Road

Three channels were picked for analysis and compared with MIL-STD-810A. Channels 10, 11, and 12 were chosen as the most representative input levels to the TOW system (see Figs. 2 and 3). These locations represent the vertical, lateral, and longitudinal axes on the vehicle floor. Of the three channels chosen,

### Secondary Road

During this test condition the test vehicle was driven over a dirt and gravel road at speeds up to 35 mph. The TOW weapon system, when subjected to this environment, showed no major signs of impairment. An analysis was made of channels 10, 11, and 12 at 35 mph over the secondary road. This condition was also

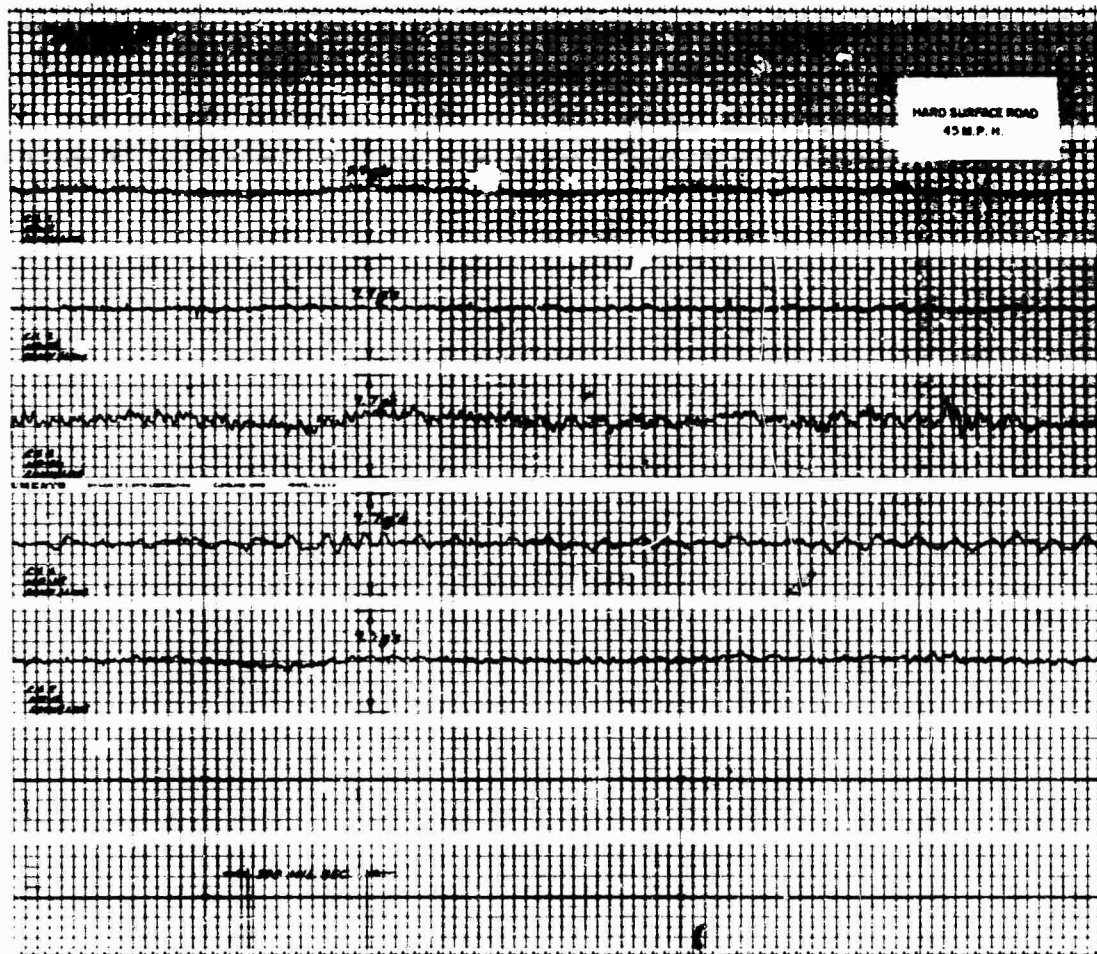


Fig. 13. Hard surface road (blacktop), time history at 45 mph, channels 1, 2, 4, 6, and 7

channel 10 vertical, input to base of launcher pedestal, gave the greatest responses in almost all cases. The sample of data reviewed on channel 10 showed three predominant frequencies: 209 cps, 39 cps at 0.5 g peak, and 1 cps at 1.7 g peak (see Figs. 13 and 14). The low frequency of 1 cps is considered to be the fundamental frequency of the vehicle suspension system.

found to have three predominant frequencies (of lesser amplitudes) somewhat similar in frequency. The frequencies observed were 169 cps, 13 cps at 1.0 g and 2 cps at 0.5 g. Figures 15 and 16 are a time history, and Figs. 17, 18, and 19 show the PSD at 35 mph.



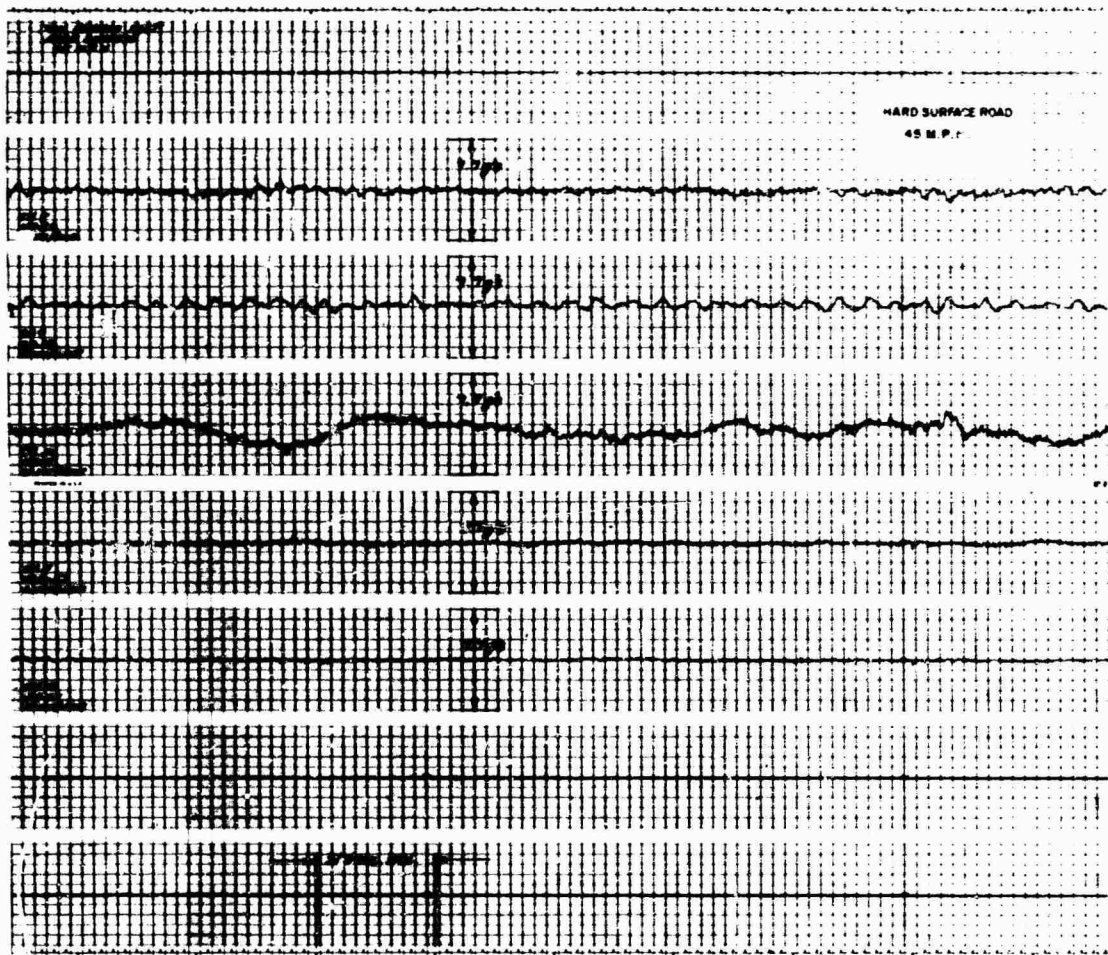


Fig. 14. Hard surface road (blacktop), time history at 45 mph, channels 8, 9, 10, 11, and 12

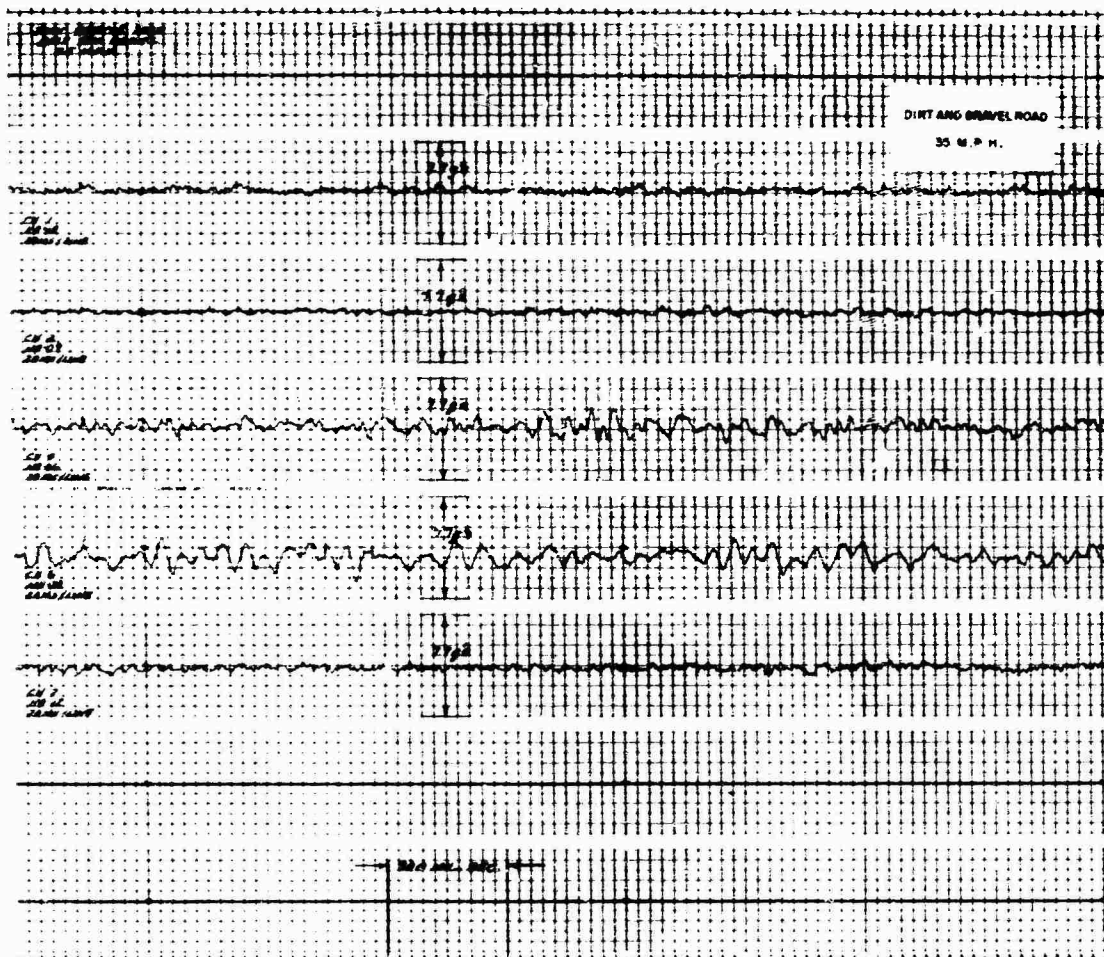


Fig. 15. Dirt and gravel road, time history at 35 mph, channels 1, 2, 4, 6, and 7



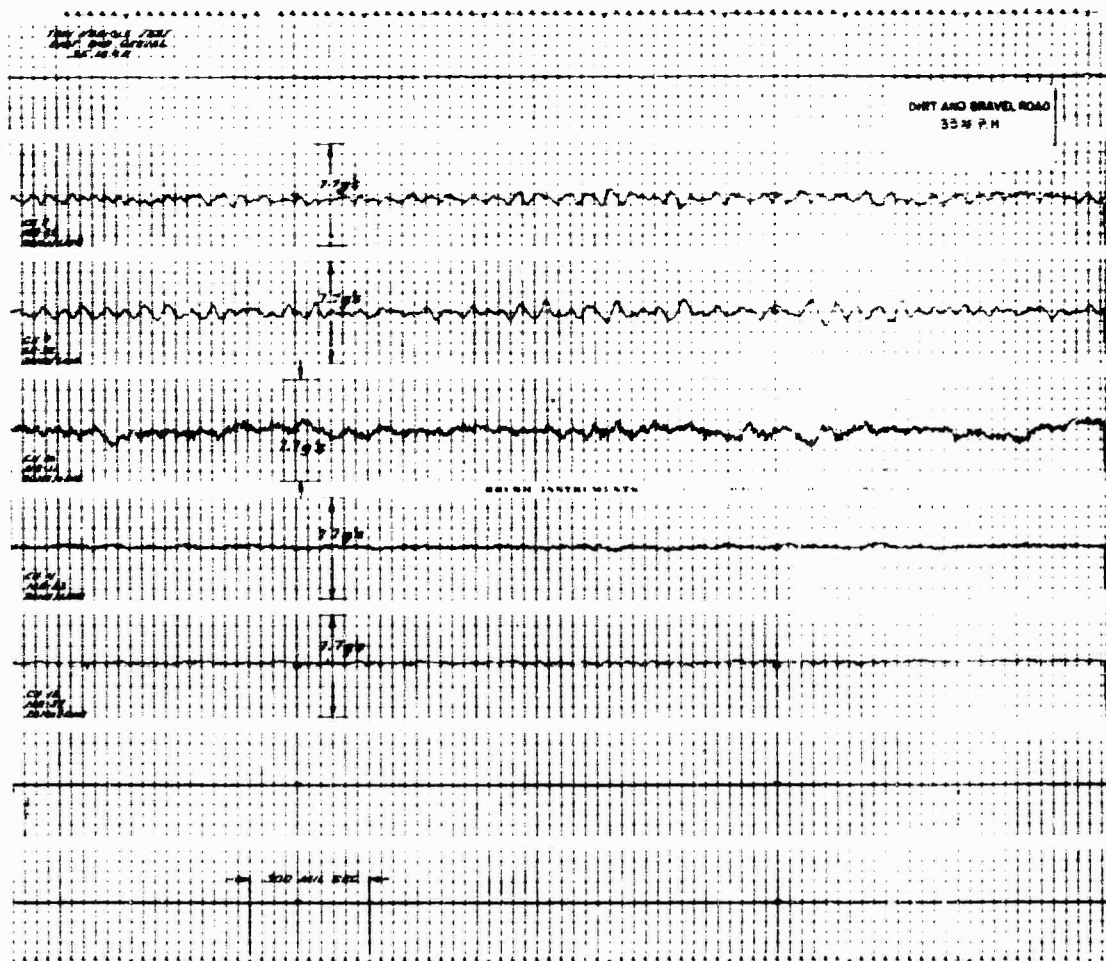


Fig. 16. Dirt and gravel road, time history at 35 mph, channels 8, 9, 10, 11, and 12

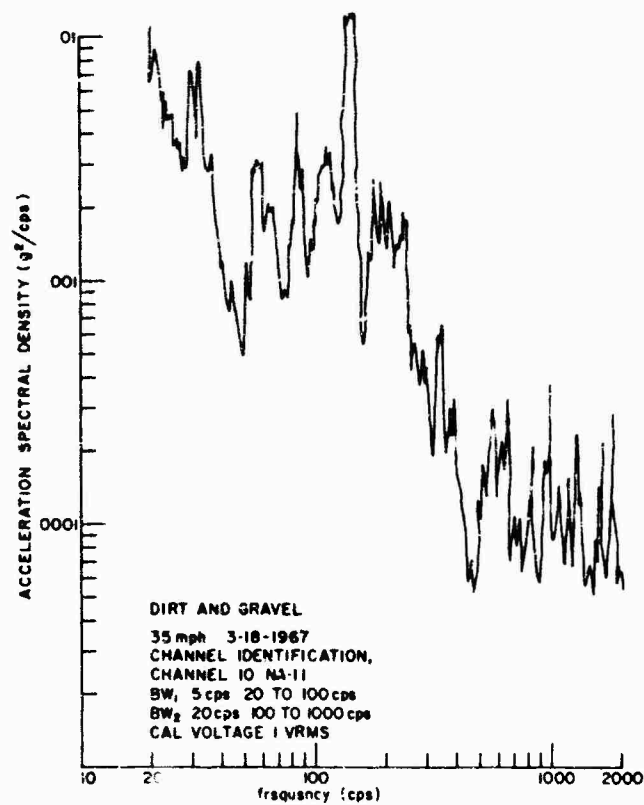


Fig. 17. Acceleration spectral density, dirt and gravel road at 35 mph, channel 10

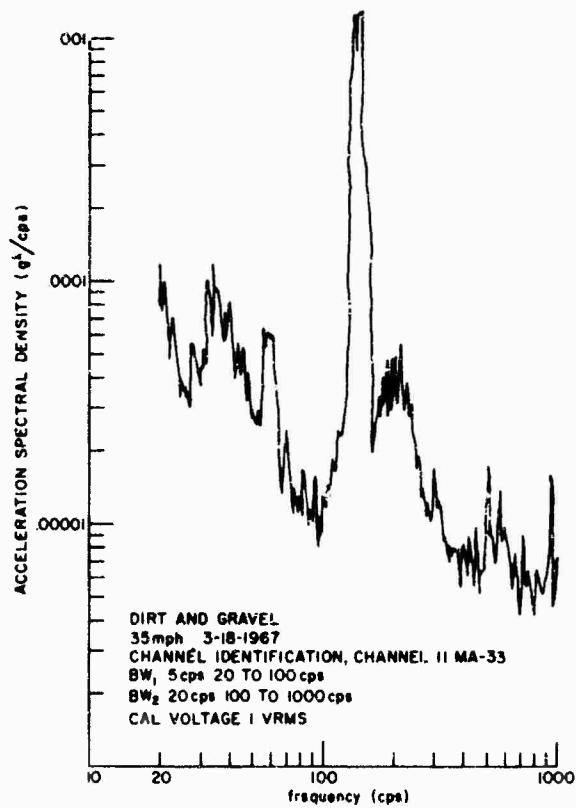


Fig. 18. Acceleration spectral density, dirt and gravel road at 35 mph, channel 11

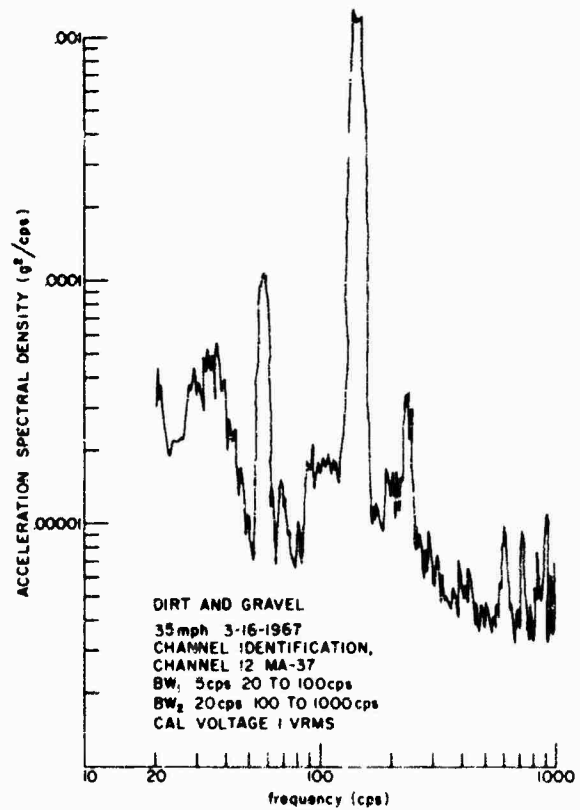


Fig. 19. Acceleration spectral density, dirt and gravel road at 35 mph, channel 12

### Primitive Road

The missile/launcher-system combination was mounted on the M-151 vehicle and subjected to the primitive road environment at speeds up to 25 mph (see Figs. 20 through 23). After review of the data acquired, it was determined that this condition represented the most severe environment and therefore would be used for comparison with MIL-STD-810A. The comparison (see Appendix A) showed MIL-STD-810A to be more severe.

### Cross-Country Terrain

The vehicle was subjected to the cross-country terrain as specified in the previous three tests: channels 10, 11, and 12 were analyzed (see Figs. 24 through 29).

### CONCLUSIONS

#### Spaced Bump Course

The test specimens successfully passed the shock bump environment without structural

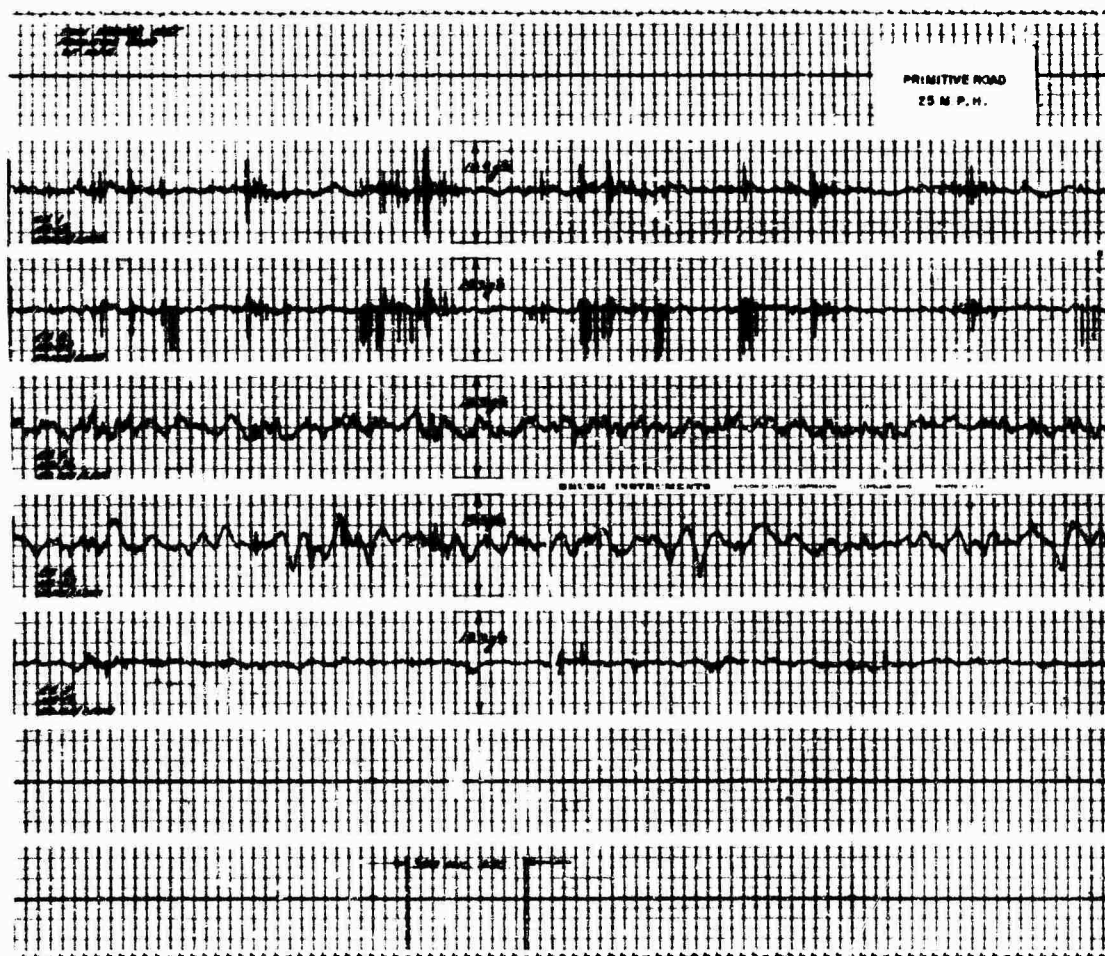


Fig. 20. Primitive road, time history at 25 mph, channels 1, 2, 4, 6, and 7

failures. After review of the test results and recorded data, it may be concluded that the shock environment observed on the M-151 vehicle and missile launcher system is not a design consideration and does not exceed shock levels of the M-113 vehicle.

#### Primary, Secondary, and Primitive Roads, and Cross-Country Terrain

The test specimens were subjected to these four field environments as described in this report. After reviewing these results, it becomes clear that the vehicle measured

environment is less severe than that specified by MIL-STD-810A for this type of terrain.

#### M-151 Vehicle Suspension System

A review of the test data, between the M-151 vehicle frame and snubbers under static load, indicates the left rear suspension system bottomed frequently during road testing. However, no instabilities or adverse vehicle handling characteristics were noted during test operations (see Appendix B).

Time plots and PSD's of other data points are available from the authors.

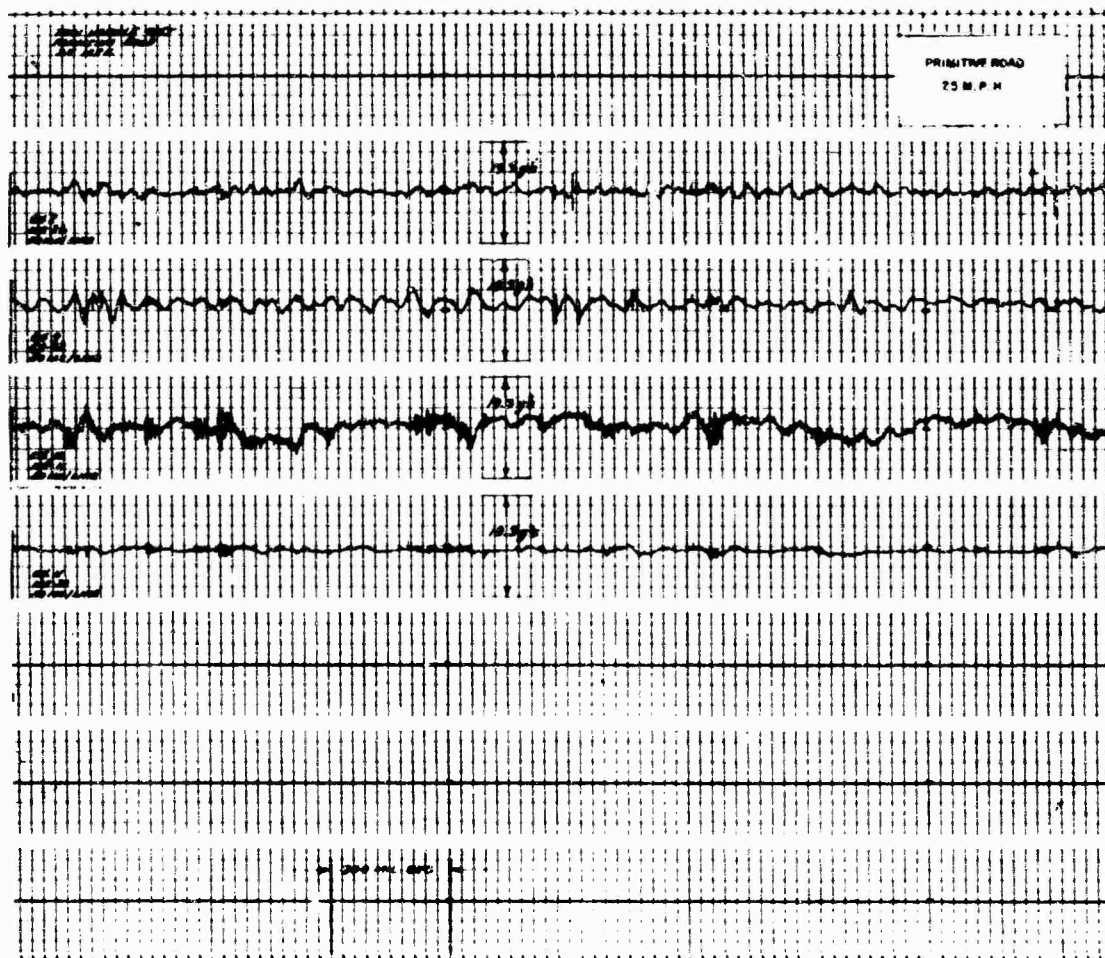


Fig. 21. Primitive road, time history at 25 mph, channels 8, 9, 10, and 11

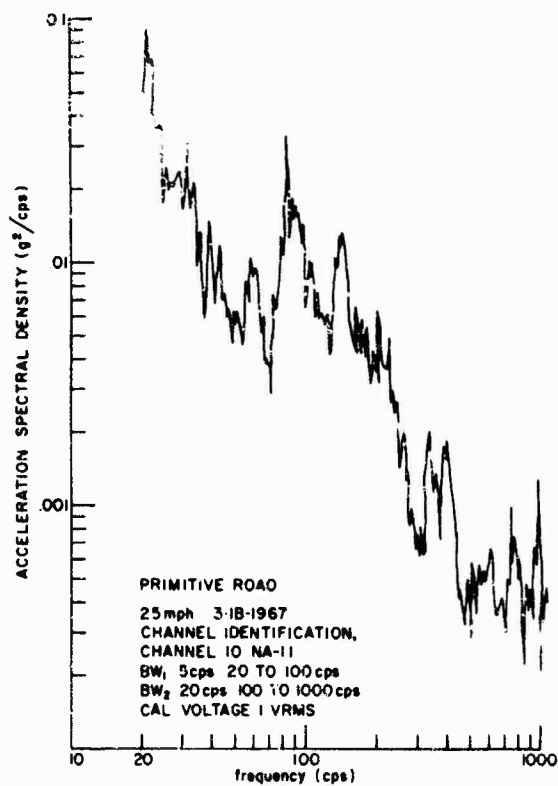


Fig. 22. Acceleration spectral density, primitive road at 25 mph, channel 10

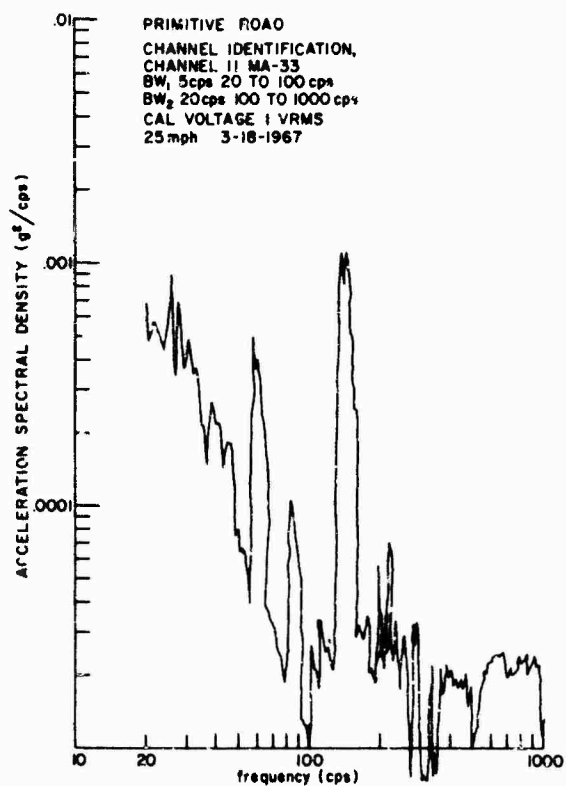


Fig. 23. Acceleration spectral density, primitive road at 25 mph, channel 11

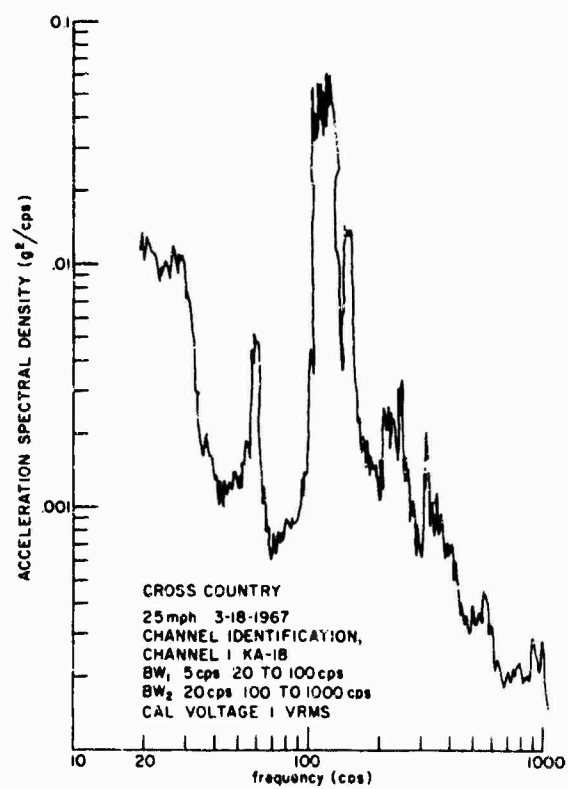


Fig. 24. Acceleration spectral density, cross-country terrain at 25 mph, channel 1

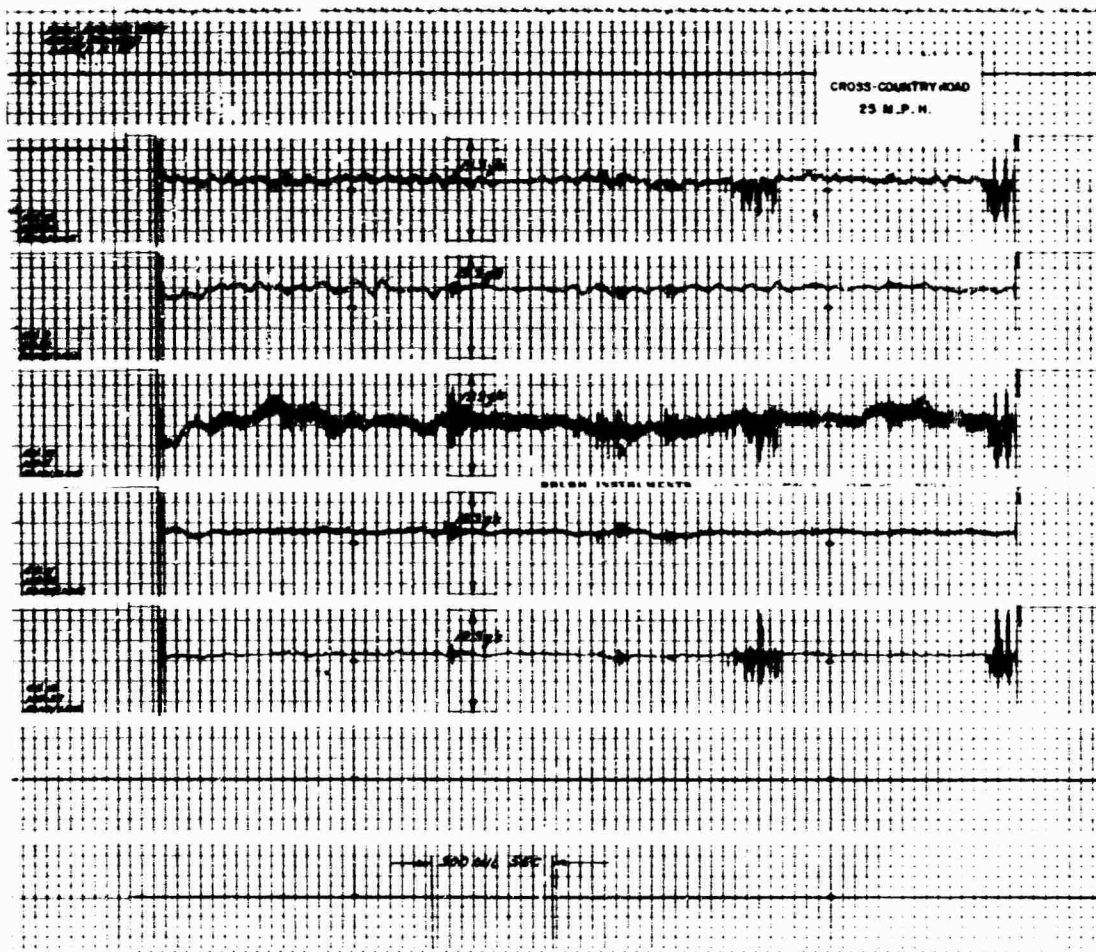


Fig. 25. Cross-country terrain, time history at 25 mph, channels 8, 9, 10, 11, and 12



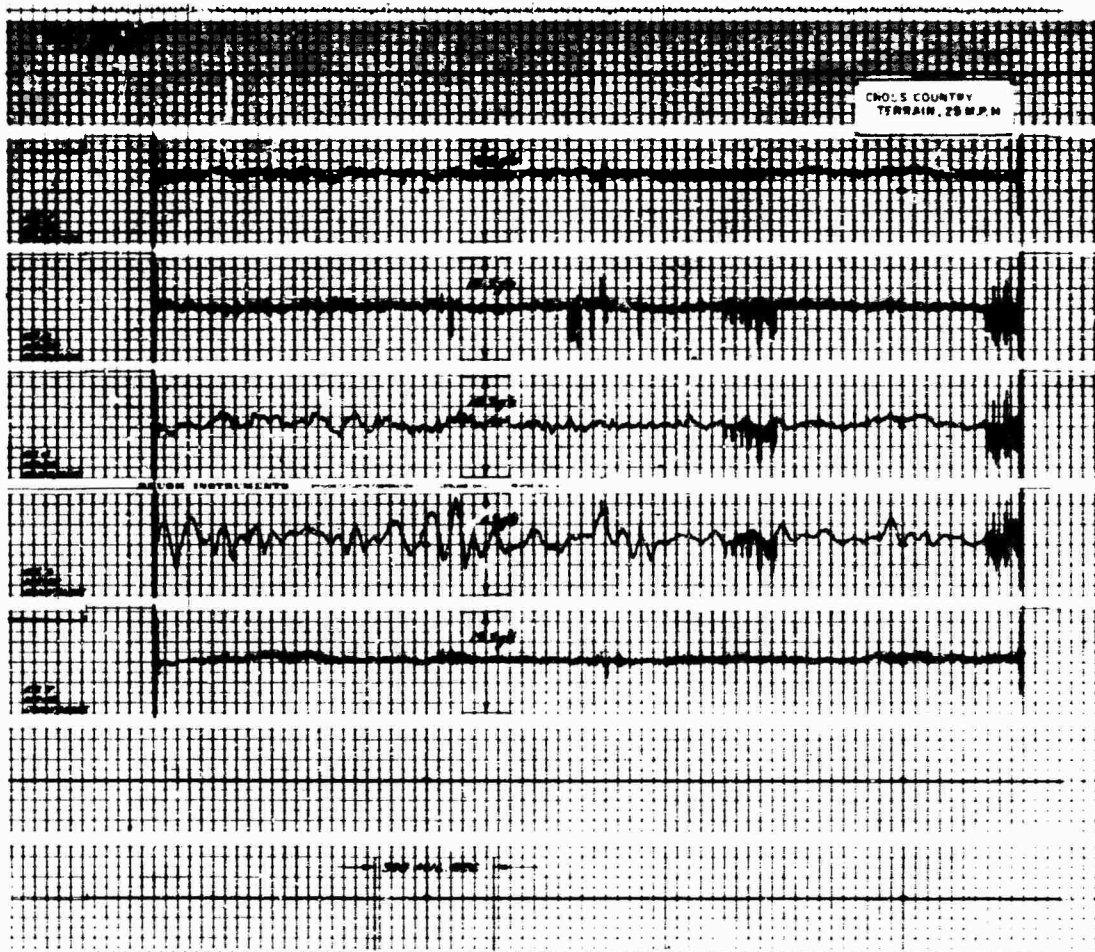


Fig. 26. Cross-country terrain, time history at 25 mph, channels 1, 2, 4, 6, and 7

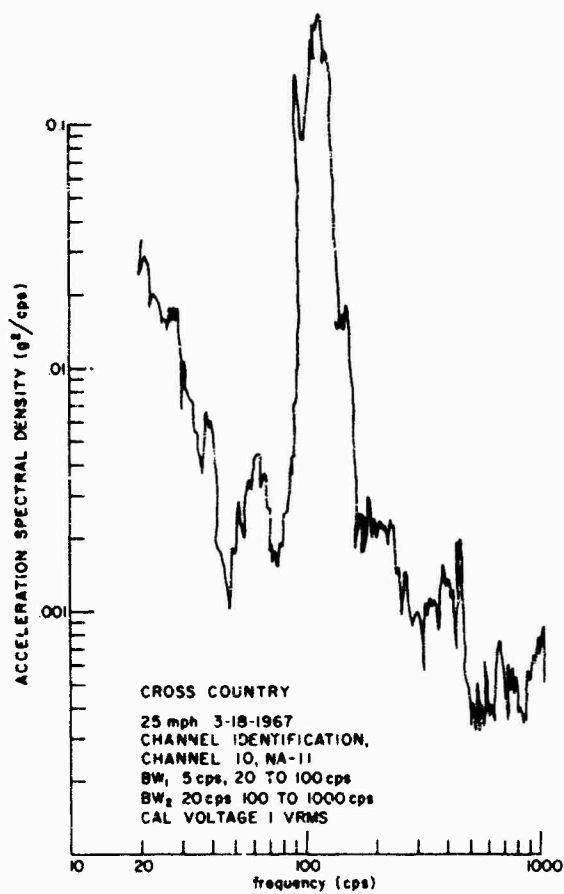


Fig. 27. Acceleration spectral density, cross-country terrain at 25 mph, channel 10

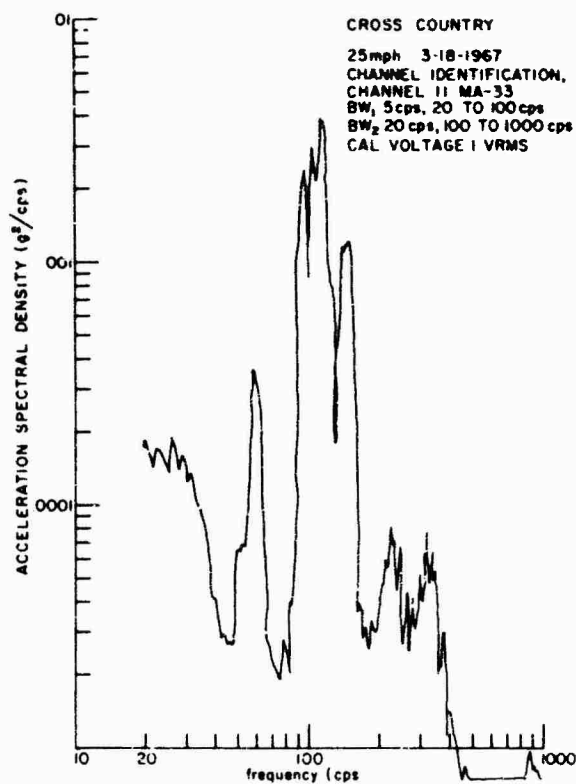


Fig. 28. Acceleration spectral density, cross-country terrain at 25 mph, channel 11

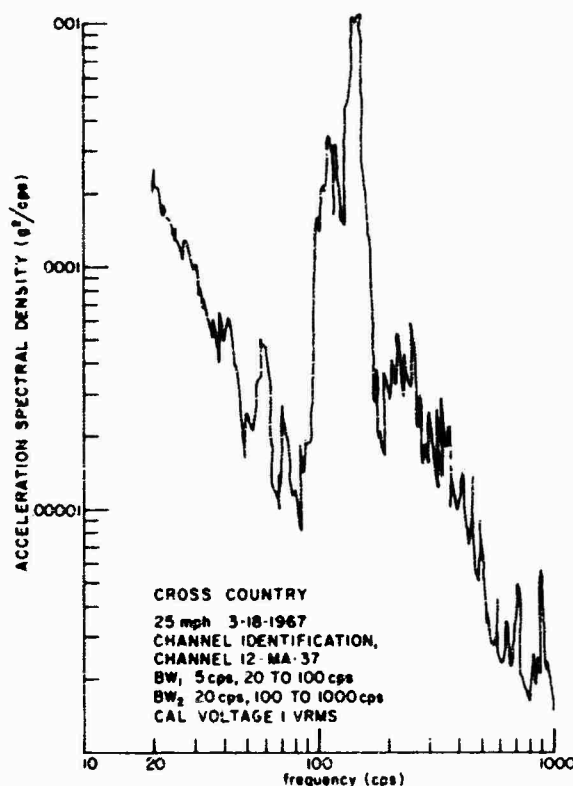


Fig. 29. Acceleration spectral density, cross-country terrain at 25 mph, channel 12

#### Appendix A

#### COMPARISON OF TWO SYSTEM RESPONSE TO ROAD CONDITIONS AND TO MIL-STD-810A

To make a comparison of sine vibration with random vibration, certain simplifying assumptions and calculations had to be made:

Select  $0.01 \text{ g}^2/\text{cps}$  from 0 to 1 kc as representing the worst random input measured in test. This will then be compared with a 2.5 g peak sine sweep from 5 to 500 to 5 cps, as designated in MIL-STD-810A (Fig. 1) for cross-country travel in a field vehicle.

In the past, major units (such as the missile, the sight sensor, etc.) of the TOW weapon system have been represented (for simple analytical purposes) as a single-degree-of-freedom system with a natural frequency ( $f_n$ ) of 35 Hz and a resonant amplification factor ( $Q$ ) equal to 5. The method used for comparing the environments (those measured, and those specified by MIL-STD-810A) is to determine the fatigue damage effect upon the analytical model.

#### Response of the Model to the Sine Vibration (Specification Limit):

$$g_{\text{out}} = Q g_{\text{in}} = (5)(2.5) = 12.5 \text{ g peak at 35 Hz}$$

#### Response of the Model to the Random Vibration (As Measured):

$$\text{Response } g_{\text{rms}} = \pi/2 (Q f_n F)^{1/2}$$

$$Q = 5$$

$$f_n = 35 \text{ cps}$$

$$F = 0.01 \text{ g}^2/\text{cps}$$

$$g(\text{rms}) = \pi/2 [(5)(35)(0.01)]^{1/2} \\ = 2.08 \text{ g rms}$$

For the same fatigue damage, the equivalent sine response is  $2.17 \times 2.08 \text{ g rms} = 4.52 \text{ g [6]}$ .

Again, referring to the Shock and Vibration Handbook, we find that 0.5 hr of a resonant dwell (MIL-STD-810A) for the above model is equivalent to approximately 5000 hr of the random level. This assumes that the S-N curve given in the reference applies to the model and

that the loads occur in the sloped portion of the S-N curve. Five thousand hours is far less than the service life of the TOW system on board the M-151 vehicle. Therefore, MIL-STD-810A is more severe and will be retained as design criteria.

## Appendix B

### M-151 VEHICLE WEIGHT AND C.G.

The vehicle weight, c.g., and deflection at the snubbers were studied for information purposes. At the start of testing there was some question as to the need for a special heavy-duty suspension system for the vehicle with the TOW system installed. No vehicle instabilities or handling problems were noted during these tests using the standard suspension system. Some bottoming of the suspension system did take place during testing.

The system-vehicle weight and c.g. are given in Fig. B-1. The vehicle suspension system when loaded with a complete TOW launcher system adapter kit, two simulated missiles, and

two men (200 lb each) gave the following static deflections:

	<u>Clearance of Snubber to Frame</u>	
	<u>Fwd Snubber</u>	<u>Aft Snubber</u>
Right rear	0.613 in.	0.826 in.
Left rear	0.030 in.	0.308 in.

The above test was conducted with a 100-lb hitch load, the gas tank half full, and no spare gas cans on board.

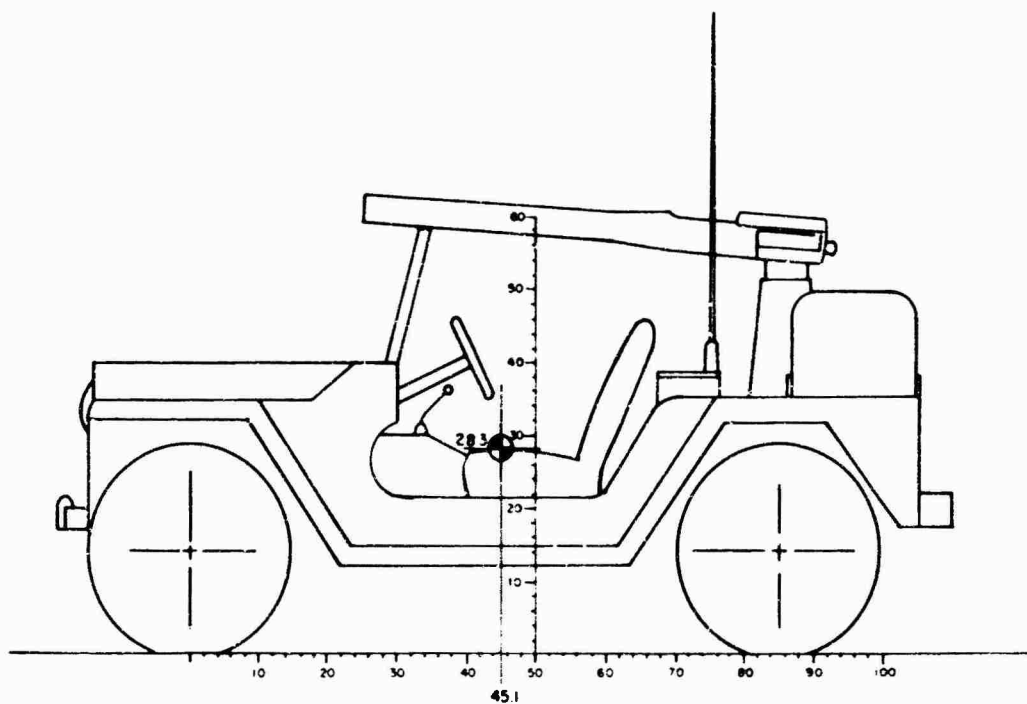
## REFERENCES

1. "TOW Environmental Criteria, Rev. B," HAC Rept. TOW T-3, Oct. 1966
2. "TOW Launcher Assembly and Missile Container Structural Design Criteria and Design Loads, Rev. B," HAC Rept. 2342.30/47, Aug. 1966
3. "TOW Missile Structural Design Criteria and Design Loads, Rev. A," HAC Rept. 2342.30/22, June 1966
4. "Military Standard Environmental Test Methods for Aerospace and Ground Equipment," MIL-STD-810A
5. G. M. Pomonik and N. G. Tinling, "Dynamic Environment of M-113 Armored Personnel Carrier," Shock and Vibration Bull. No. 35, Part 5, pp. 115-128, Feb. 1966
6. C. M. Harris and C. E. Crede, Eds., Shock and Vibration Handbook, Chap. 24, McGraw-Hill, New York, 1961

## DISCUSSION

Mr. Harvey (Goodyear Aerospace Corp.): Were your PSD data plots from a single accelerometer or a collection from all accelerometers?

Mr. Brunnemer: They were from one particular accelerometer. It was the vertical input at the base, which was determined to be the worst environment.



Item	W (lb)	X (in.)	W <sub>x</sub>	Z (in.)	W <sub>z</sub>
Jeep, curb weight	2400	37.5	90,000	23.9	57,360
Remove					
Spare tire	60	106.0	6,360	34.0	2,040
Seat, passenger	28	54.0	1,512	26.0	728
Gas can	30	106.0	3,180	28.0	840
Add					
Spare tire	60	22.0	1,320	32.0	1,920
Seat, jump	8	90.0	720	36.0	288
Gas can	30	19.0	570	34.0	1,020
Pedestal base	116	87.0	10,092	26.0	3,016
Pedestal	39	87.0	3,393	36.0	1,404
Support rad, ant.	24	70.0	1,680	30.0	720
A frame rack	65	48.0	3,120	38.0	2,470
Tripod rack	15	62.0	930	36.0	540
Elect. support	44	60.0	2,640	27.0	1,188
Tube support	3	30.0	90	42.0	126
Miscellaneous	20	66.0	1,320	30.0	600
Seat support	13	90.0	1,170	36.0	468
Radio and ant.	51	70.0	3,570	40.0	2,040
Traversing unit	50	88.0	4,400	58.0	2,900
Sight sensor	24	88.0	2,112	60.0	1,440
Launch tube	13	68.0	884	60.0	780
Tripod	21	56.0	1,176	26.0	546
Electronics and btry.	53	56.0	2,968	38.0	2,014
Missiles and contr (2)	95	54.0	5,130	40.0	3,800
Driver	200	51.0	10,200	32.0	6,400
Gunner	200	90.0	18,000	46.0	9,200
	3426	45.1	154,433	28.3	96,632

Fig. B-1. TOW/M-151 launcher system c.g. and weight distribution

\* \* \*

## LATERAL IMPACT SHOCK DURING SHIP LOADING OF THE A3 POLARIS MISSILE

E. G. Fischer, C. R. Brown, and A. J. Molnar  
Westinghouse Electric Corporation  
Pittsburgh, Pennsylvania

Lagrange's equations have been used to predict the large-angle, double-pendulum type of motion observed when the A3 Polaris missile-liner system is subjected to lateral impact shock during transfer from supply ship to submarine. Modal vibration effects for the flexible missile-liner combination are superimposed on the rigid body solution of the problem. In addition, lateral shock tests have been made on a full-scale A3 missile test vehicle, using a crane and barge simulation at the San Francisco Bay Naval Shipyard.

### INTRODUCTION

Polaris missiles are transferred from supply ships to tenders and submarines under protected harbor conditions. Occasionally, however, the relative motion between ships in at least two of these harbors causes low-level impacts in both the vertical and lateral directions. Analyses and tests of the vertical landing impact have been reported [1] for various (rigid) missile-liner combinations.

Subsequently, similar analyses have been made of the missile system subject to lateral landing shock. As shown by Fig. 1, the extended length of the supply ship cable becomes important in that lateral impact can produce large-angle, compound-pendulum motions of the (rigid) missile-liner combination. In addition, when structural flexibility is superimposed on the rigid body motions, the resulting lateral vibration between missile and liner could signify excessive bending stresses.

The lateral-shock analysis has been derived from Lagrange's equations of motion and is considered a unique contribution because it includes the nonlinear effects allowed by the large-angle coordinate systems and nomenclature given by Figs. 2 and 3. A total of 66 pages of equations [2] was required for this extensive treatment of the flexible missile-liner system. However, only the method of attack need be outlined here.

Concurrent lateral-shock tests have been made on a full-scale A3 missile test vehicle and

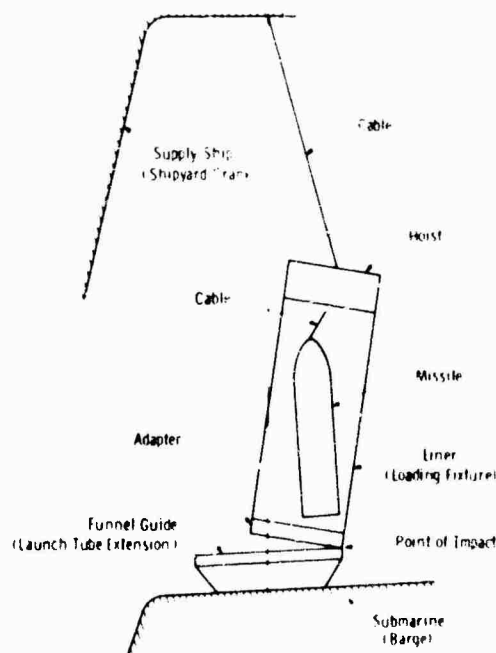


Fig. 1. Lateral impact shock of missile during ship loading (or shipyard simulation test)

liner assembly using a yard crane and floating barge simulation at the San Francisco Bay Naval Shipyard. Figure 4 shows the location of the test instrumentation consisting of accelerometers and strain gages. Measurements were

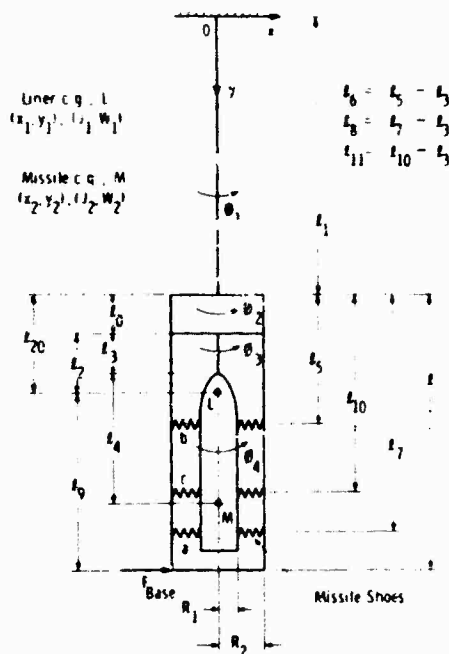


Fig. 2. Simplified location dimensions for missile-liner system

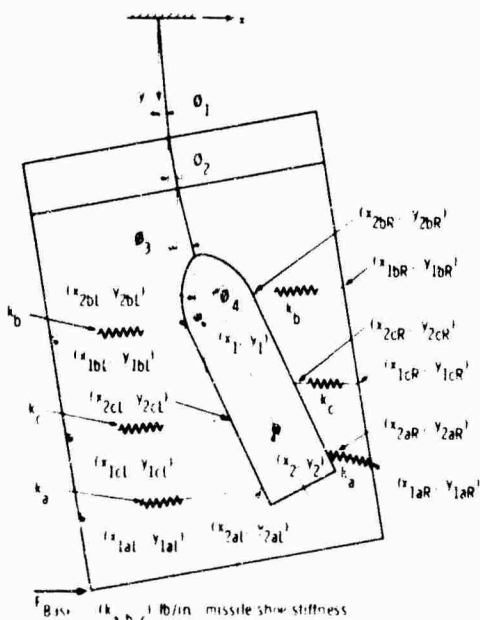


Fig. 3. Schematic diagram of nomenclature for calculating missile shoe forces

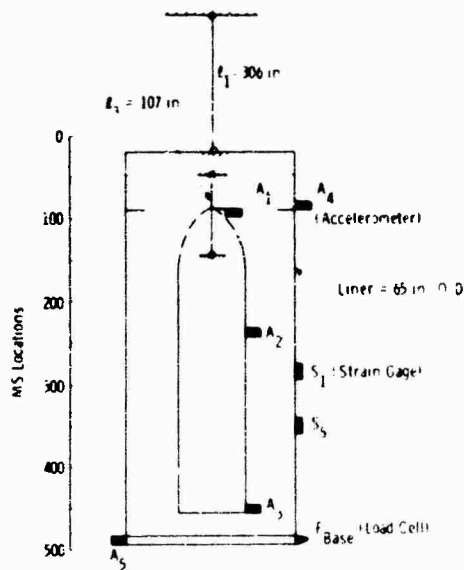


Fig. 4. Location of test instrumentation and corresponding computer program readout

made over a range of lateral impact velocities up to about 3 fps.

The tested and calculated values were considered to be in general agreement when allowance was made for the difficulty in getting field-test conditions to duplicate the idealizations needed to complete the analysis. Both procedures showed acceptable missile and liner loadings at the specified shock level of 1 fps. This information will be used in the design of the forthcoming Poseidon missile and handling equipment.

#### DERIVATION OF EQUATIONS OF MOTION

The expression for Lagrange's equation of motion is

$$\frac{d}{dt} \left( \frac{\partial L}{\partial \dot{q}} \right) - \frac{\partial L}{\partial q} + f\dot{q} = F \quad (1)$$

where  $L = T - V$  represents the difference between the kinetic and potential energy in the missile-liner system. The term  $f\dot{q}$  signifies velocity-type damping in the system. The right-hand term  $F$  represents externally applied

forces, which can act on either missile or liner.

The generalized coordinates for the rigid body motions are shown in Fig. 2 as  $\theta, \psi, \phi$ . Similarly, the generalized (modal) coordinates for the flexible body (missile-liner) motions are shown in Fig. 5 as  $r_1, \dots, r_5$  (five missile modes) and in Fig. 6 as  $p_1, \dots, p_5$  (five liner modes).

The kinetic energy  $T$  of the missile-liner system includes rigid body translation and rotation terms, as well as lateral flexibility terms. The latter consist of summations involving the generalized masses and modal coordinates.

The potential energy  $V$  of the missile-liner combination includes the effect of gravity, the stored (spring) energy in the missile shoes, and the stored (flexure) energy in the missile-liner structural mode shapes. Again, the latter terms consist of normal mode summations involving the generalized masses, a diagonal matrix of the modal frequencies squared, and the modal coordinates. (Note that Fig. 3 shows a distinction made between left-hand and right-hand missile shoes so that nonlinear effects in the large-angle theory can be taken into account.)

## GEOMETRIC RELATIONSHIPS

The rigid body geometry shown in Figs. 2 and 3 yields the following relationships between the Cartesian ( $x, y$ ) coordinates and the pendulum system angles ( $\theta, \psi, \phi$ ).

Liner c.g. coordinates (rigid)

$$x_1 = l_1 \sin \theta_1 + l_{20} \sin \theta_2$$

and (2)

$$y_1 = l_1 \cos \theta_1 + l_{20} \cos \theta_2$$

Missile c.g. coordinates (rigid)

$$x_2 = l_1 \sin \theta_1 + l_0 \sin \theta_2 + l_3 \sin \theta_3 + l_4 \sin \theta_4$$

and (3)

$$y_2 = l_1 \cos \theta_1 + l_0 \cos \theta_2 + l_3 \cos \theta_3 + l_4 \cos \theta_4$$

In a similar manner, the two rigid body coordinates at both ends of the six missile shoes lead to an additional 24 equations relating linear and angular coordinates.

The original length of the missile shoe spring is  $R_1 - R_2$ . The new length of the deflected spring is

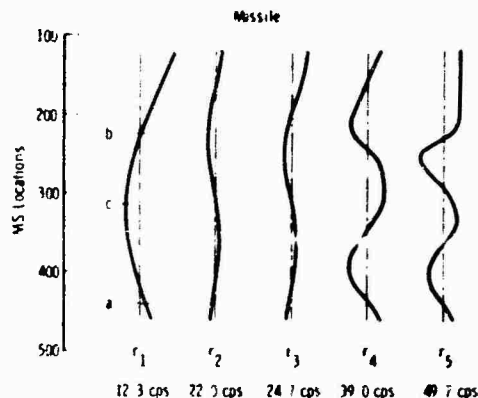


Fig. 5. Free-free lateral mode shapes for A3 missile

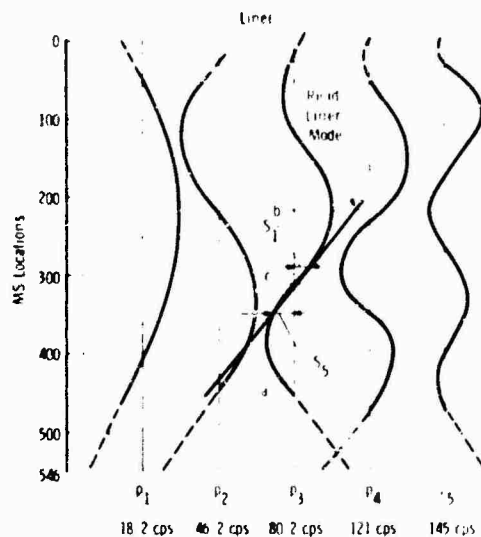


Fig. 6. Free-free lateral mode shapes for A3 liner

$$D_{1,R} = \sqrt{(x_{1b,R} - x_{2b,R})^2 + (y_{1b,R} - y_{2b,R})^2} \quad (4)$$

To this result must be added the change in length caused by the lateral flexibility of the missile-liner system. The latter consists of the difference in normal mode summations with appropriate factors to give actual missile and liner elastic deflections.

Since only lateral flexure of the structures is considered, then left-hand and right-hand modal deflections are equal but of opposite sign. Also, it is assumed that the flexibility effect occurs along the axis of the deflected spring in the direction corresponding to Eq. (4).



There is a total of six equations for relative displacements across the shoes on both sides of the missile.

### EVALUATION OF KINETIC ENERGY TERMS

The kinetic energy expression  $T$  requires that velocity-squared terms corresponding to the velocity of the missile-liner c.g.'s be substituted. Using the liner as an example, they can be derived from Eq. (2) as

$$\dot{x}_1 = l_1 \cos \varphi_1 \dot{\varphi}_1 + l_{20} \cos \varphi_2 \dot{\varphi}_2$$

(5)

and

$$\dot{y}_1 = -l_1 \sin \varphi_1 \dot{\varphi}_1 - l_{20} \sin \varphi_2 \dot{\varphi}_2$$

(liner c.g.). Thirteen terms are needed to express the kinetic energy of the rigid body translation in the large-angle coordinate systems. In addition, there are two terms expressing the rigid body rotational energy, and two series of terms expressing the lateral vibrational energy of the flexible missile-liner system. The latter consist of so-called normal mode summations.

### EVALUATION OF POTENTIAL ENERGY TERMS

The expression for stored (spring) energy in the missile shoes requires that displacement-squared terms corresponding to the net deflections in the six shoes be substituted. In turn, the latter deflections require the substitution of the  $x$ - $y$  diagonal length as given by Eq. (4), which can be evaluated in terms of angular coordinates as typified by Eqs. (2) and (3).

In addition to the shoes, the potential energy expression  $V$  contains two terms expressing the effect of gravity at the missile-liner c.g.'s, and two normal mode summations expressing the lateral stored (flexural) energy of the missile-liner combination.

### SUBSTITUTION IN LAGRANGE'S EQUATIONS

Since  $L = T - V$  in Eq. (1), then for  $q = x_1$

$$\frac{d}{dt} \left( \frac{\partial T}{\partial \dot{x}_1} - \frac{\partial V}{\partial \dot{x}_1} \right) - \left( \frac{\partial T}{\partial x_1} - \frac{\partial V}{\partial x_1} \right) = F_1 \quad (6)$$

Substitution of the various terms found for the kinetic and potential energy evaluations results in some lengthy expressions involving the

dimensions in Fig. 2 and the angular coordinates, both as time derivatives and sine-cosine functions. In similar fashion expressions are obtained for  $q = y_1, y_2, y_3, y_4$ .

The energy terms obtained by normal mode summations for the missile-liner system are not functions of the angular coordinates. Hence, they do not contribute terms to Lagrange's equations as typified by Eq. (6). However, the missile-liner deflections have been accounted for in the energy terms for the net (missile) shoe deflections, whereby the normal mode shapes given in Figs. 5 and 6 have been introduced.

### RIGID BODY MOTION EQUATIONS IN MATRIX FORM

Considering only the rigid body motions specified by the angles  $\varphi_1, \varphi_2, \varphi_3$ , and  $\varphi_4$ , there are four second-order (nonlinear) differential equations which can be written in matrix form as

$$M\{\ddot{\varphi}\} + D\{\dot{\varphi}^2\} + \{G\} + \{K\} = \{F\}, \quad (7)$$

where  $\{\ddot{\varphi}\}$  and  $\{\dot{\varphi}^2\}$  are column matrices involving the angular coordinates  $\varphi_1 \dots \varphi_4$ .

The coefficient of the angular acceleration vector is the  $4 \times 4$  symmetrical inertia matrix  $M$ . The coefficient of the angular velocity-squared vector (nonlinear) is the  $4 \times 4$   $D$  matrix with diagonal terms equal to zero. The remaining terms in Eq. (7) are column matrices for the gravity vector  $G$ , the (missile shoe) potential energy vector  $K$ , and the (lateral impact) forcing function vector  $F$ , with only one term  $F_{Base}$ .

### LATERAL FORCES ON FLEXIBLE MISSILE-LINER COMBINATION

To write the standard modal differential equations for the flexible system, it is necessary to define all the lateral forces acting on the missile-liner combination.

Figure 3 indicates that the forces acting on the missile are the shoe forces (a, b, c) and the tension in the hoist cable. The lateral component of the tension acting at the nose tip of the missile was calculated by assuming that the vertical component supports the weight of the missile (lateral direction means normal to the axis of the flexible structure). The effect of lateral vibration of the missile on the hoist cable force has been included.

The lateral component of the tension in the main cable acting at the top of the liner was calculated by assuming that the vertical component supports the weight of both the liner and missile. In addition, the lateral component of the tension in the hoist cable was for simplicity assumed to act at the top of the liner. The effect of lateral vibration of the liner on the main cable force has also been included.

Finally, the impact force was calculated in terms of the base spring stiffness and the liner rigid body motion, as modified by the lateral vibration of the liner.

#### FLEXIBLE MISSILE-LINER MOTION IN MATRIX FORM

In addition to the rigid body motion, the lateral vibration for the missile-liner structure can also be derived from Lagrange's equation. In fact, investigation of the kinetic and potential energy expressions shows that the standard modal differential equations are satisfactory.

Considering the missile modes gives

$$M_M\{\ddot{r}\} + A_M\{\dot{r}\} = S_{i,j}\{F_M\} \quad (8)$$

(five missile modes), where  $M_M$  is the diagonal matrix of the generalized modal masses,  $A_M$  is the diagonal matrix of the modal frequencies squared, and  $S_{i,j}$  is the transpose of the matrix taken from the missile modes at the points where the four lateral forces act.

The flexible liner structure is analyzed in the same manner in terms of the five liner modes of vibration shown in Fig. 6.

#### BENDING MOMENT CALCULATIONS

Bending moments in both the missile and liner are calculated by the so-called acceleration method used in previous shock studies [3,4]. This method has the advantage of producing a satisfactory solution with fewer modes than those required by the displacement method. This advantage is especially important in the case of the liner, since the higher modes contain inaccuracies because of the small number of degrees of freedom included in the lumped-parameter model.

The equation for bending moment becomes

$$M_k = M_{zk}\ddot{Z} + M_{\theta k}\ddot{\theta} - \sum_j \frac{M_{kj}\ddot{q}_j}{\omega_j^2} + \sum_i (F_i \cdot L_i - L_k) \quad (9)$$

where

$\ddot{Z}$  is rigid body translational acceleration,

$\ddot{\theta}$  is rigid body rotational acceleration,

$M_{kj}$  is the moment coefficient taken directly from the modal data,

$\ddot{q}_j$  is the acceleration of the  $j$ th modal coordinate, and

$\omega_j$  is the natural frequency of the  $j$ th mode.

The  $F_i$ 's are the forces acting on the body;

$\epsilon = 0$ , when  $F_i$  acts below point  $k$ ,

$\epsilon = 1$ , when  $F_i$  acts above point  $k$ , and

$M_{zk}$  and  $M_{\theta k}$  are the T and P moments for location  $k$ .

These numbers were available for the A3 missile, but it was necessary to calculate them for the liner.

#### COMPUTER RUNS VERSUS TEST RESULTS

As mentioned previously, the actual test results were found to be in general agreement with the calculated values obtained by the computer runs. This statement makes allowance for the fact that field-test conditions did not duplicate all the idealizations needed to keep the computer evaluation within reasonable limits. Nevertheless, important test results verified the main features of the analysis. Since the computer runs were more extensive and more consistent than the actual impact tests, they will be used in this discussion as the basis for comparison.

Figure 7 shows the multiple bounces of the double-pendulum system when the base spring is relatively rigid ( $k_{base} \approx 1 \times 10^6$  lb/in.). Introducing the flexibility of the missile-liner structure into the rigid body calculation evidently reduces the severity of the peak impact force, but increases the number of bounces as

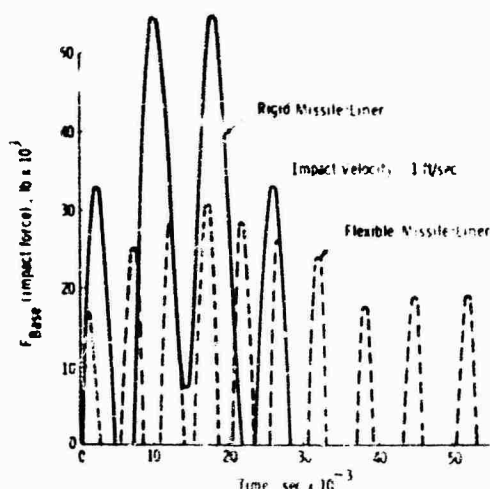


Fig. 7. Typical time variation of impact force at base of liner showing multiple bounces

well as the overall time of contact. In the actual test, the liner was permitted to bounce only once, and it was found to have a measured pulse duration of about 110 msec.

Figure 8 shows how the severity of the impact force can also be reduced by assuming smaller values for the stiffness of the impact spring. In the actual test for the A3 missile, the calculated stiffness for the combined liner adapter and funnel guide (see Fig. 1) with contact at the top inside edge of the funnel was equivalent to  $k_{Base} = 0.1 \times 10^6$  lb/in. Also, in the actual test with an impact velocity of 1 fps, the load cell at the point of impact gave a measured peak force of  $F_{Base} = 10,000$  lb.

The top portion of Table 1 lists the values just mentioned under the heading of the flexible bird test. These results are compared with similar values obtained in the computer runs for both rigid and flexible missile-liner systems. Based on this evidence, it is concluded that the flexible missile-liner calculations are in general agreement with the flexible bird test results. In other words, for an assumed base spring stiffness and impact velocity as shown, the analysis predicts a satisfactory time of contact and peak contact force.

On the other hand, the rigid missile-liner calculations with the same assumptions of 1 fps and  $0.1 \times 10^6$  lb/in. predict much too large a force with a relatively short time of contact. Figure 8 indicates that to obtain a contact force of 10,000 lb the base spring would have to be reduced to  $0.04 \times 10^6$  lb/in., which does not

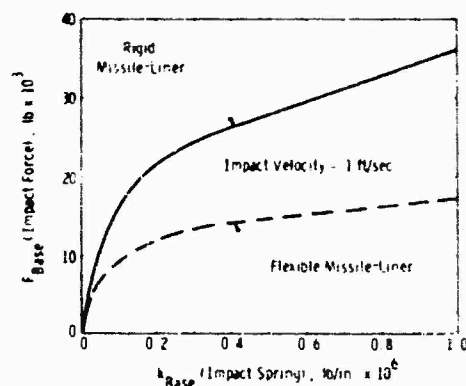


Fig. 8. Effect of base spring stiffness on impact force

appear to agree with the stiffness calculation. Also, all the other quantities listed in Table 1 under rigid missile-liner calculated values would probably be reduced by a factor of 1.58 ( $= 15,800/10,000$ ).

The values of stress and acceleration shown in the bottom portion of Table 1 are discussed in terms of curve plotting (Figs. 9, 10, 11) for the flexible missile-liner system. The abscissa for all curves is the time elapsed since impact, measured in milliseconds.

## CURVE PLOTTING

Both computer curve plotting and actual test oscillograms show that two important "wobble" modes of vibration are simultaneously present in the flexible missile-liner system. The low-frequency motion at about 12 cps is associated with the first mode flexural vibration

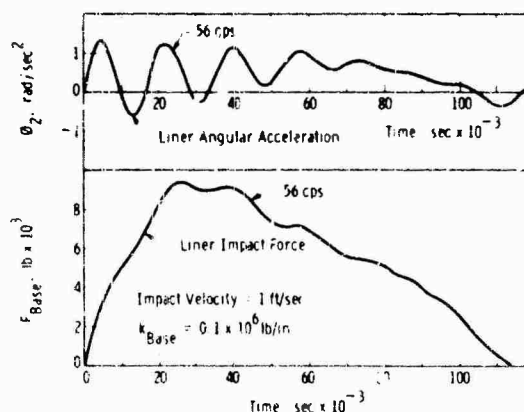


Fig. 9. Base impact force showing liner angular acceleration on base spring

**TABLE 1**  
Calculated and Test Values for Lateral Impact Shock

Missile Stations	Parameter	Rigid		Flexible	
		Missile-Liner (Calculated)	Bird (Actual)	Missile-Liner (Calculated)	Bird (Actual)
493	Contact force, $F_{B_{AV}}$ (lb)	15,800		9,400	10,000
493	Base spring stiffness (lb/in.)	$0.1 \times 10^6$		$0.1 \times 10^6$	$0.1 \times 10^6$ (calc)
	Time of contact (msec)	74		114	110
Acceleration <sup>a</sup> (g)					
94	$A_1$	0.50	0.48	1.57	0.78
234	$A_2$	0.06		0.55	0.28
460	$A_3$	0.85	0.65	0.83	0.65
89	$A_4$	0.41	0.48	0.64	0.40
489	$A_5$	0.40	2.50	1.05	2.15
Stress <sup>b</sup> (psi)					
288	$S_1$	1320	1550	1370	1500
353	$S_5$	3150	3000 (max)	4340	1000 (max)
160	$\bar{x}_1$ (liner c.g.)	0.41		$0.41 + 0.35$	
368	$\bar{x}_2$ (missile c.g.)	0.54		$0.31 + 0.12$	

Note.—Impact at top of funnel guide; impact velocity = 1 fps; 10 percent damping.

<sup>a</sup>A = accelerometer location.

<sup>b</sup>S = strain gage location.

of the missile as shown in Fig. 5. The high-frequency motion at about 56 cps is associated with a rigid body rotation of the liner about the middle shoe as shown in Fig. 6. The latter mode is governed by the flexibility of the top and bottom shoes, b and a, respectively. Both the base spring and the cable attachments disorient these two modes to produce the complicated wobble motions. The following discussion of the flexible vs rigid missile-liner calculations supports the aforesaid conclusions.

Figure 9 shows that the impact force on the liner is not a simple half-sine pulse variation with elapsed time. The distortion corresponds to flexure of the missile mode at about 12 cps. By comparison, the same curve for the rigid missile-liner system (although not plotted

in this report) is essentially symmetrical and of only 74-msec duration. Also shown in Fig. 9 is the liner angular acceleration at about 56 cps. The same curve for the rigid system shows a slightly higher frequency, but the vibration is no longer damped out. Hence, the liner mode must involve a rigid body rotation since the only damping effect in the system (10 percent of critical) is associated with either missile or liner flexural vibration. In this instance the missile mode at 12 cps must have provided the damping.

Figure 10 shows the liner stress variation with time, as based on bending moment calculations. It is significant that in the first half-cycle, the stresses at  $S_1$  and  $S_5$  are of opposite sign. As shown in Fig. 6, this result confirms

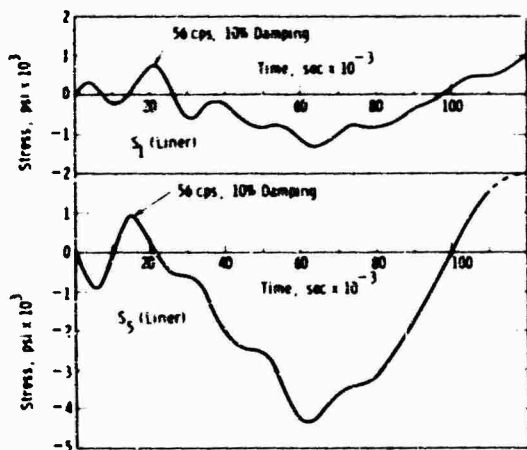


Fig. 10. Stress in liner at  $S_1$  and  $S_5$  based on bending moment calculations

the presence of a rigid body rotation of the liner. Although a flexural mode in the liner is not apparent, Eq. (9) shows that bending moments can still materialize in terms of rigid body oscillations. Figure 10 also shows that the rigid liner vibration at 56 cps is heavily damped by the effect of the missile mode flexure at 12 cps. Again, when the same curves are plotted for the rigid system, the low-frequency missile mode effect disappears and the rigid liner oscillation is no longer damped out.

Figure 11 shows that the acceleration builds up at the top of the missile in the low-frequency flexural mode. On the other hand, the initial acceleration is a maximum at the base of the liner in the high-frequency rigid liner mode, which is shock excited by the base spring impact. Once again, when the same curves are plotted for the rigid system, the missile flexure mode disappears and the rigid liner mode is no longer damped out.

All of the results under discussion correspond to an impact velocity of 1 fps. Up to about 10 fps, the motion responses appear to increase proportionately. However, for a velocity of 100 fps (required because of the relatively soft base spring), the angles involved reach 20 to 30 deg and the system response is distinctly nonlinear.

#### TEST RESULT DISCREPANCIES

In general, the actual oscillograms for the flexible bird test duplicated the various motion

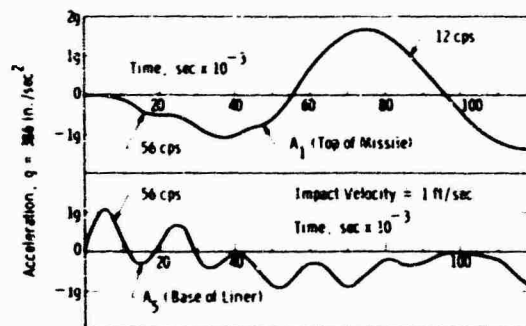


Fig. 11. Top and bottom (linear) accelerations of flexible missile-liner system

characteristics previously plotted for the flexible missile-liner calculations. In particular, the strain gage readings (maximums) and the calculated stresses were in good agreement as shown in Table 1. (Some results for the rigid bird test are also compared with the rigid missile-liner calculations. The contact force was not measured in the test, but the impact velocity was 1 fps.) It should be pointed out that, in both the rigid and flexible bird tests, the liner was flexible. However, the computer analysis has shown that only the rigid-body oscillation of the liner was significant.

The most noticeable discrepancy in the test results showed up as a high-frequency component of acceleration in the base of the liner ( $A_5$ ) at about 100 cps. As a result, the test values are much larger than the accelerations calculated for both the rigid and flexible systems. It is believed that the 100-cps vibration is associated with radial (elliptic) distortion of the liner adapter ring, which is shock excited by the base spring impact. This effect was not included in the flexural modes of the liner.

In addition, the rigid liner oscillation at 56 cps showed up as a high-frequency component of acceleration in the nose of the missile ( $A_1$ ). It is possible that the accelerometer attachment was in resonance with the trace of vibration excitation at 56 cps noticed in the curve for  $A_1$  in Fig. 11. Otherwise, the calculated values of acceleration as shown by Table 1 were invariably larger than the test measurements.

#### CONCLUSIONS

In general, it is not an easy matter to conduct a full-scale shock test and obtain reproducible shock measurements [5]. Usually the

strain gage measurements are easier to correlate than the accelerometer readings, which tend to overemphasize the spurious high-frequency effects. This was the case in the A3 lateral impact tests.

On the other hand, the computer analysis requires that all of the energy involved in the impact must materialize in certain specified, restricted modes of vibration. In a practical

test, such idealizations are usually not duplicated. Hence, the calculated results for the flexible missile-liner system are quite conservative except where noted in the previous discussion.

Finally, both test and analysis showed acceptable missile and liner loadings at the specified impact shock level of 1 fps. These results are available for the design of the forthcoming Poseidon missile and handling equipment.

#### REFERENCES

1. C. R. Brown and A. J. Avis, "Missile Handling Analysis," Shock and Vibration Bull. No. 36, Part 7, pp. 141-151, Feb. 1967
2. E. G. Fischer and A. J. Molnar, "Lateral Impact Shock of the A3 Polaris Missile-Liner System During Ship-Loading," Westinghouse Res. Lab. Tech. Rept., Jan. 1967
3. R. L. Bisplinghoff, G. Isakson, and T. H. H. Pian, "Methods in Transient Stress Analysis," J. Aeronaut. Sci. 17, 1950
4. E. G. Fischer, C. R. Brown, and R. W. Miller, "Design Computations and Shock Tests of the Flexible Polaris Missile on a Liquid Spring Mounting," Shock and Vibration Bull. No. 30, pp. 108-118. Mar. 1962
5. D. C. Kennard and Irwin Vigness, "Shock Testing Machines and Procedures," Shock and Vibration Instrumentation, an ASME publication, June 1956

#### DISCUSSION

Mr. Fritz (General Electric Co.): Would it be possible for the 56 cps liner frequency to excite the next modal frequency of the missile? The missile apparently had frequencies up to 49 cps. The next flexural mode appeared to be around 55 cps.

Mr. Fischer: It is perfectly possible but it didn't seem to show up in the calculated results. The opposite statement applies. The first mode in the missile obviously showed up in the liner. That definitely occurred and apparently it was because of the fact that the first mode in the missile was just big enough in amplitude.

Mr. Fritz: Is my impression correct that on the missile, only the modes below 49 cps were put in?

Mr. Fischer: That is correct, we didn't go beyond 49 cps.

Voice: How many tests were run?

Mr. Fischer: Impact velocities of 1, 2, and 3 fps were used. They tried various ways of entering the funnel guide and hitting on the outer edge. There were about a dozen tests run. For purposes of comparison we only

looked at several of the test records. The computer solutions are available for future use, and I think we might be inclined not to do much testing. It is time consuming and very expensive. On a computer you can go to 10 fps but not in the test. It would wreck things. At 10 fps the results indicate that we could have used small angle approximations. This sounds a little ridiculous but we had to go to 100 fps impact before we got to large enough angles so that the nonlinear theory took over. You can do that on a computer.

Voice: Did you have other criteria on the Polaris or was this just a feasibility study?

Mr. Fischer: They had a nominal value of something like 1 g allowable on the reentry body. That was not exceeded in the tests. These missiles are loaded very carefully. I did not witness the actual submarine loading tests. It was all we could do to get those crane operators to bump the thing. As soon as it got close they would get cautious and we wouldn't get the bump we wanted. Some of the test information we have resulted from accidents. We tested the shock mounting on a missile one time simply because the cable broke and the missile dropped down into the launch tube. The shock mounting worked well.

\* \* \*

## EMPIRICAL CORRELATION OF FLIGHT VEHICLE VIBRATION RESPONSE\*

W. H. Roberts  
Martin-Marietta Corporation  
Orlando, Florida

Objective of the study was correlating flight vehicle vibration response with the excitation and flight operating conditions. Emphasis was on study of local dynamic properties, as previous studies showed local response to be a dominant variable. The sources of importance were identified, and the response was related to a group of fundamentally independent variables chosen within the study period. The target was to reduce the prediction error by half.

The technique of empirical correlation is a powerful analytical technique of special value for complex systems where no adequate theory is developed but much input-output data has been measured. The value of the method was demonstrated in this study, where the errors between measured and predicted values averaged a factor of 1.5, or  $\pm 3.5$  db, a considerable advance over previous correlations. Accuracy targets were met rather easily. Subdivision of data accomplished this with little new material, except that which was automatic in the power of the method of regression analysis.

Influence of the variations in configuration is apparent in the data. The major flight environment and source of vehicle structural vibration is jet turbulence on jet aircraft at subsonic speeds. A major change takes place in the flight regime for vehicle velocities greater than sonic. The principal exciters are lost and lesser ones remain. The only exceptions to expectations of lower environments and responses occur with (a) vehicles whose aerodynamic contours are poor, and (b) vehicles whose propulsion systems generate high oscillatory thrust components.

With few exceptions the flight vibration levels encountered were low. The maximum response appearing in the study may have been in the area of 3 g, a local response deviating from the regression line which called for less than 0.5 g.

A study of the local responses in a compartment of the SM62 (Snark) leads to a basic correlation where the important parameters are circumferential attenuation and local mass. Excitation was provided by an acoustic horn outside the compartment. Local stiffness appeared to be an insignificant variable. The standard deviation for this study was small,  $\pm 2.65$  db, or a factor of 1.36.

### INTRODUCTION

The dynamic environments pose a more severe problem each time increased performance or more power is added to a vehicle. These dynamic environments are the source of vehicle vibration in flight. Vibration reaches levels sufficient to destroy structure and equipment in many cases. Therefore, to describe the sources and to predict the responses is an important first step in design. Typical vibration sources include jet turbulence, separated flow,

wakes, base pressure fluctuations, boundary-layer turbulence, and direct engine excitation.

Excitation includes an aerodynamic path such as that followed by jet turbulence which originates with the exhaust gases. Downstream turbulence follows; the excitation is returned upstream to the vehicle and flows over the vehicle as an acoustic field. Excitation also can follow a mechanical path such as the oscillatory thrust of the propulsion system which flows directly through structures. The resulting

\*Work was performed under contract AF33(657)-8218 with the Aeronautical Systems Division, Wright-Patterson Air Force Base, Ohio.

structural responses vary from pure random motion for structures and equipment located close to a random excitation to the filtered output of highly resonant structures which emerge as the sum of several sinusoids, each varying in amplitude and phase.

The study reported here was conducted with the objective of correlating structural response with the excitation and flight operating conditions. Emphasis was to be placed on the study of local dynamic properties, as previous studies showed local response to be a dominant variable. The sources of importance were to be identified and the response related to a group of fundamentally independent variables to be chosen within the study period. The accuracy target was to reduce the prediction error by half: from a standard deviation of 6 db to a factor of 2 to 3 db, or a factor of 1.4. All aspects of developing a method, preparing a computer program, and locating data to correlate were part of the program.

#### BACKGROUND AND HISTORY OF THE PROBLEM

For the last 10 years, very sophisticated studies of this problem have been undertaken. These involved study of the acoustic environment,

use of structural models to provide a preliminary design tool, empirical correlation of structural response with the sources of vibration, and direct analytical attack, with perhaps an undue amount of work on the turbulent boundary layer (Table 1).

As a result, the qualification of structures and equipment can proceed in an orderly manner on the basis of numbers which contain only moderate uncertainty. Further, the customer can receive a product close to the intended item regarding schedule, cost, performance, and service life.

The following were accomplished during the last decade:

1. Understanding of the physical phenomena (jet exhausts, aerodynamics excitation, structural responses, and the various modes of failure);
2. Development of adequate acoustic facilities;
3. Understanding of random vibration;
4. Experimental solution of the fatigue problem;
5. Qualification programs on all major systems;

TABLE 1  
Relative Order of Magnitude of External Pressure Fluctuations

Source	$P/q^a$	Approximate Magnitude of SPL or Equivalent SPL for $q = 8000$ psf (db—re. $0.0002$ dyne/cm <sup>2</sup> )	Approximate Order of Relative Scale Magnitude
Rocket noise	—	160-166 <sup>b</sup>	Large $\lambda = c/w$
Cavity resonance <sup>c</sup>	1.0	to 206	Smallest cavity dimension
Oscillating shock	0.20	192	Variable
Separated flow	0.1	179	Depends on dimensions of flow separation
Wakes from drag devices or projections	0.037	169	Given by dimensions of wake
Base pressure fluctuations	0.015	163	Large
Normal turbulent boundary layer	0.003-0.006	155	Very small

<sup>a</sup> $P/q$  is the ratio of rms pressure fluctuation to dynamic pressure.

<sup>b</sup>Maximum recorded, 172.

<sup>c</sup>Cavity resonance occurs at a series of harmonically related discrete frequencies; all other sources have broad frequency spectra.



6. Variation in response in different parts of the vehicle was incorporated in the predictions and qualifications.

Direct analytical attack is not possible in most areas, but preparation for the work is complete.

The first correlation development in this field was finding that the cockpit acoustic level is proportional to the dynamic pressure. The second was that the vibration response in the vehicle is related to the external acoustic field strength. This was extended to cover a number of vehicles (Fig. 1).

The proportionality between force and response varied at different frequencies, however, and pursuit of the point is instructive. At high frequency, a 2:1 increase in acoustic pressure results in a 2:1 increase in response for all vehicles. Steep gradients in pressure exist at both low and high frequencies over all the vehicles, and the proportionality between force and response occurs everywhere on the vehicle at high frequency.

At low frequency, however, a different phenomenon is present: the response of the vehicle tends to be a constant, because the vehicle is transparent to low-frequency passage of the excitation. In a sense, this is an attenuation phenomenon that required careful work to develop (Fig. 2). A vibration transmitted through structure from a point of strong excitation is greater than that generated by the local excitation. The low-frequency vibration level is sympathetic, therefore, to the highest pressures on the surface, no matter where they occur. The attenuation is given as a ratio of the amplitude of successive peaks (0.72 for the SM62

missile). The wave motion through structure occurs at a velocity of the surface waves in the manner of dispersive waves, with typical velocities varying from 2400 fps at 1200 cps to 600 fps at 100 cps. In the case studied, the transmission did not occur at the velocity of sound in the material (17,000 fps). The wavelengths associated with the motions are instructive and assist in visualizing the attenuation effects. The wavelength is 2 ft at 1200 cps and 6 ft at 100 cps.

The response of a point in the vehicle requires analytical integration of the excitation over the surface of the vehicle. The significant input becomes the transfer functions from various points on the surface to the receiver point. At low frequency, integration is only required in the region of maximum excitation, and at high frequency only in the region of the receiver. As frequency increases, integration over successively smaller surface areas is required. The problem is significant over approximately 8 octaves from 20 to 10,000 cps.

Model studies have developed other aspects of the phenomena shown in Figs. 3, 4, and 5. Figure 3 shows that all stiff structures such as panels, bulkheads, decks, and floors act as rigid links in transmitting motion. The motion is described in the most general way by an instantaneous center, and all parts of these relatively rigid items conform in one motion. Figure 4 shows that the responses of four different longeron sections have a general consistency, even though these items differ in cross-sectional area. Figure 5 shows how local response dominates the transmission process. Measurements within a few inches of a fuselage bulkhead forward, on, and aft of the bulkhead show wide

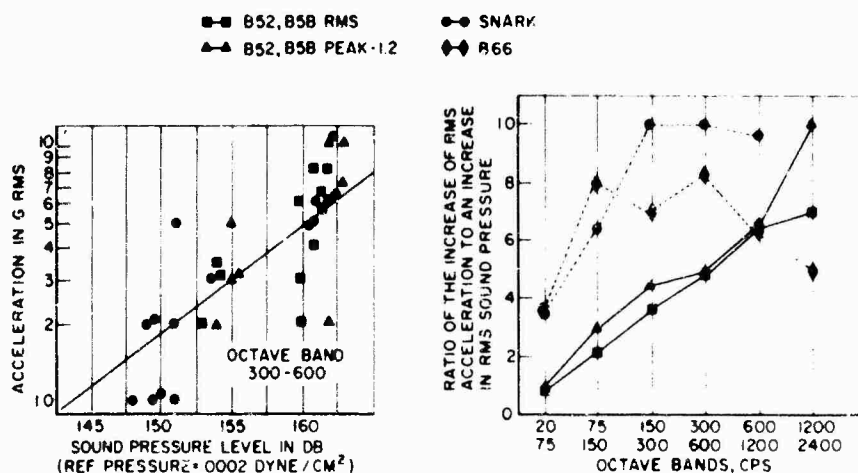


Fig. 1. Acceleration slope comparison for several vehicles

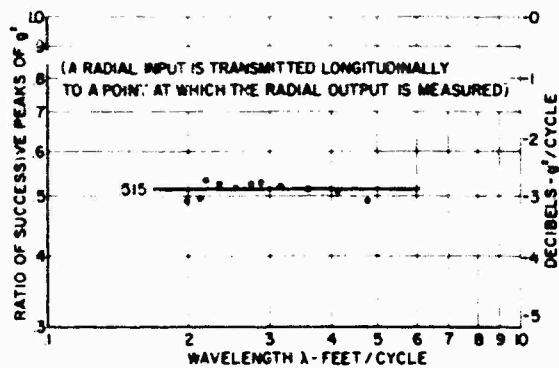


Fig. 2. Vibration attenuation, SM62 fuselage

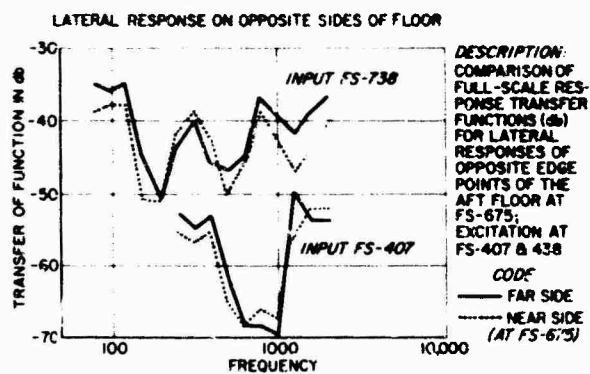


Fig. 3. Response of relatively rigid structure

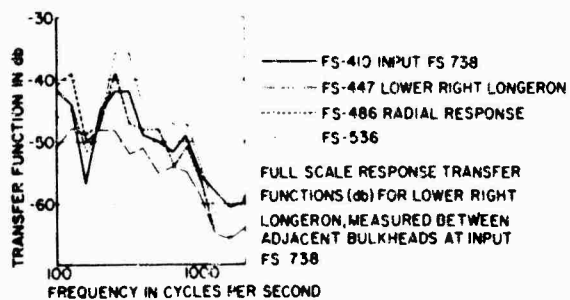


Fig. 4. Consistency in the response of longeron structure

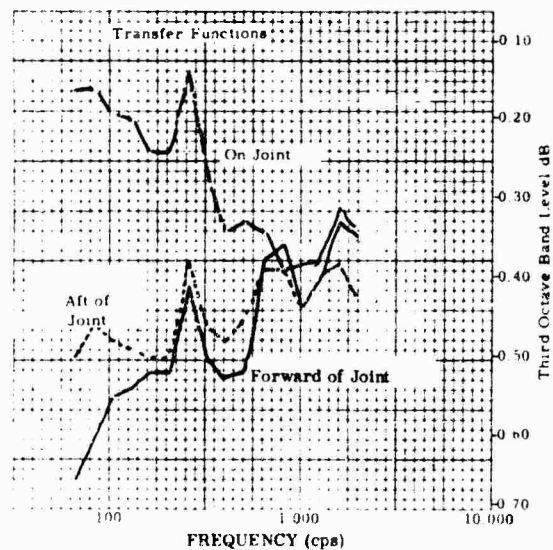


Fig. 5. Accelerometer comparison of local response

variations in response. A considerable body of material beyond Fig. 5 shows the importance of local response as compared to the transmission process.

## METHOD

Statistical inference includes regression and correlation analyses. A regression analysis provides a relationship between one dependent variable and several independent variables. The relationship is estimated by the least-squares methods for a given type of function such as linear, polynomial, trigonometric, or exponential, arbitrarily chosen in advance. Linear regression admits logarithmic functions. Where more than one independent variable exists, the regression proceeds in steps. The variables are tested to determine which variable will collapse the scatter to the greatest extent. Successive regressions are developed until all the independent variables are incorporated, which permits knowing the reduction in scatter accomplished at each step.

The criterion for selecting the most useful relationship at each step may be described also as:

1. The variable is chosen with the highest partial correlation with the dependent variable.
2. The variable chosen would have the highest F value.

Variables can be forced into the regression and later removed. Regression equations with or without the regression intercept may be selected.

The output of the regression analysis is an equation relating the independent variables to the dependent variables. A correlation analysis measures the error of the developed equation. It also measures the degree to which the equation represents the sampled population and the contribution of the independent variables in reducing the variance of the dependent variable.

From basic principles the acceleration response may be expected to follow a power law variation. A choice was possible which describes (a) the flight, (b) the possible source strengths, and (c) variables peculiar to a particular source only, to acceptance of the energy, or to the structural response. An end-to-end correlation, if successful, would provide the greatest information, so variables describing the flight were the principal ones tested. Specifically, dynamic pressures, Mach number,

engine speed, and vibration frequency were chosen as independent variables. A possible relationship between the variables was reasoned to be

$$Y = KX_1^{A_1} X_2^{A_2} X_3^{A_3} X_4^{A_4} \quad (1)$$

where

- Y = Acceleration (g)
- K = Constant
- X<sub>1</sub> = Frequency (cps)
- X<sub>2</sub> = Engine speed (rps)
- X<sub>3</sub> = Mach number
- X<sub>4</sub> = Dynamic pressure (psf)
- A<sub>i</sub> = Exponents to be determined.

Taking logarithms,

$$\text{Ln } Y = A_0 + \sum_{i=1}^4 A_i \text{Ln } X_i \quad (2)$$

This log linear form is suitable for regression and multiple variable correlation analyses. The regression analysis determines the constant and exponents of Eq. (1).

## CORRELATION ANALYSIS

The following linear function estimates the relationship between the dependent variable Y and the independent variables X<sub>i</sub>

$$Y_i - \bar{Y} = \sum_{j=1}^m B_j (X_{ij} - \bar{X}_j) \quad j = 1, 2, \dots, m \quad (3)$$

- Dependent variable Y
- Independent variables X<sub>1</sub>, X<sub>2</sub>, ..., X<sub>m-1</sub>
- Number of sets of observations m
- Weighted mean of i-th variable  $\bar{X}_i$

The error of the estimate of the i-th observed value of Y

$$E_i = (Y_i - \bar{Y}) - \sum_{j=1}^{m-1} B_j (X_{ij} - \bar{X}_j) \quad i = 1, 2, \dots, m \quad (4)$$

The correlation analysis minimizes the length of the vector

$$e^2 = (e, e) = \sum_{j=1}^m \left[ (Y_j - \bar{Y}) - \sum_{i=1}^{n-1} B_i (X_{ij} - \bar{X}_i) \right]^2 \quad (5)$$

Taking partial derivatives with respect to  $B_i$  and equating the result to zero results in the normal equations:

$$\sum_{i=1}^{n-1} \left[ \sum_{j=1}^m (X_{ij} - \bar{X}_i)(X_{tj} - \bar{X}_t) \right] B_t = \sum_{j=1}^m (X_{ij} - \bar{X}_i)(Y_j - \bar{Y}). \quad (6)$$

This is a set of  $n-1$  simultaneous equations in  $B_t$ ; the method of solution used is the Gaussian elimination method. At each stage of the elimination, a partial regression equation is obtained. At each step one equation is added.

## RESULTS

The raw data for the F-101 are presented in part in Figs. 6 through 9. The effect of flight

conditions on the variation of amplitude with frequency is presented for the B-52 (Fig. 10). The mean accelerations for all aircraft, all zones, and cruise at normal power are presented in Fig. 11

The principal results of the study are shown in Figs. 12, 13, and 14. Amplitude is presented as a function of frequency, Mach number, and dynamic pressure. The data contain a completely unexpected result in that the responses for all vehicles are essentially flat for variations in either  $q$ ,  $M_n$ , or engine speed. On the surface, this is an unreasonable result. Accepting the data for the moment and pursuing their possible meaning leads to the following reasoning:

1. If the response does not vary with  $q$  and  $M$ , then the aerodynamic excitation is not the predominant excitation.
2. The primary excitation must be generated by the propulsion system.
3. It cannot be mechanically transmitted propulsion system excitation, because this would increase as propulsion power increases.

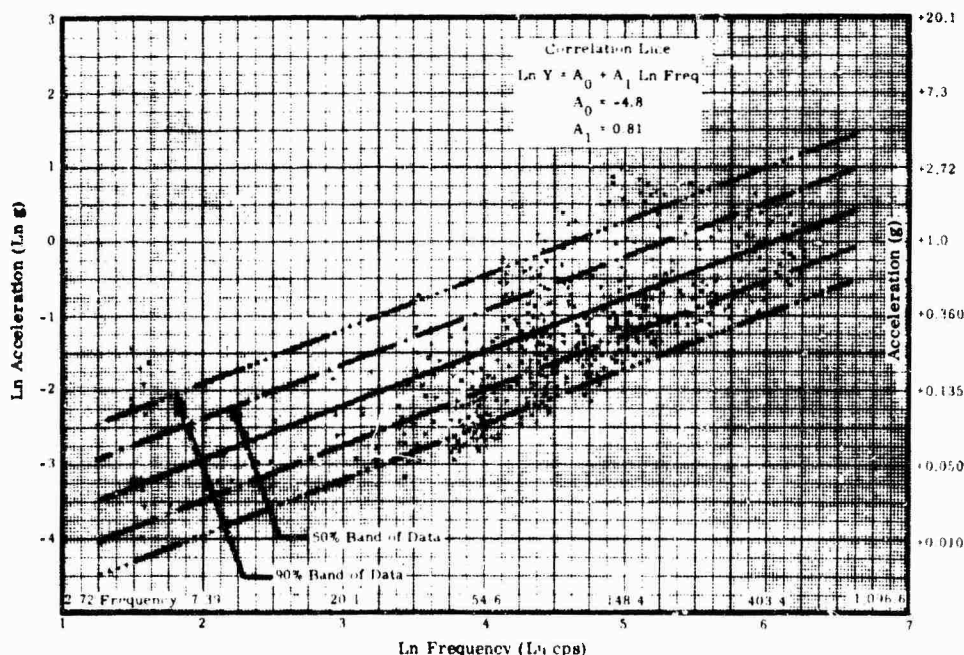


Fig. 6. Ground runup, all zones, F-101A

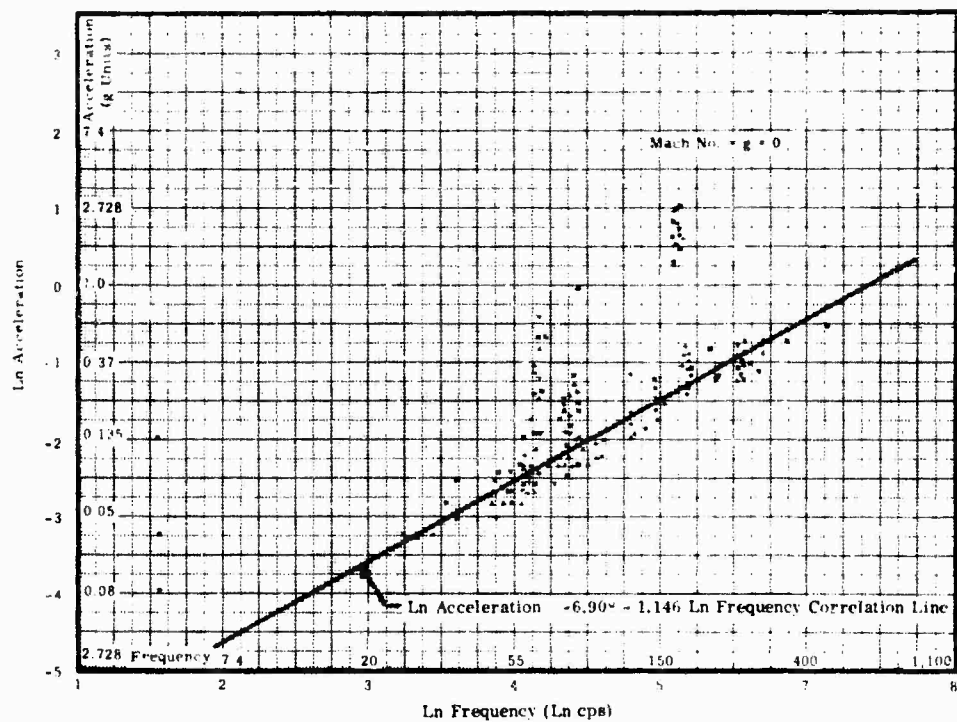


Fig. 7. Ground runup, mid fuselage, F-101A

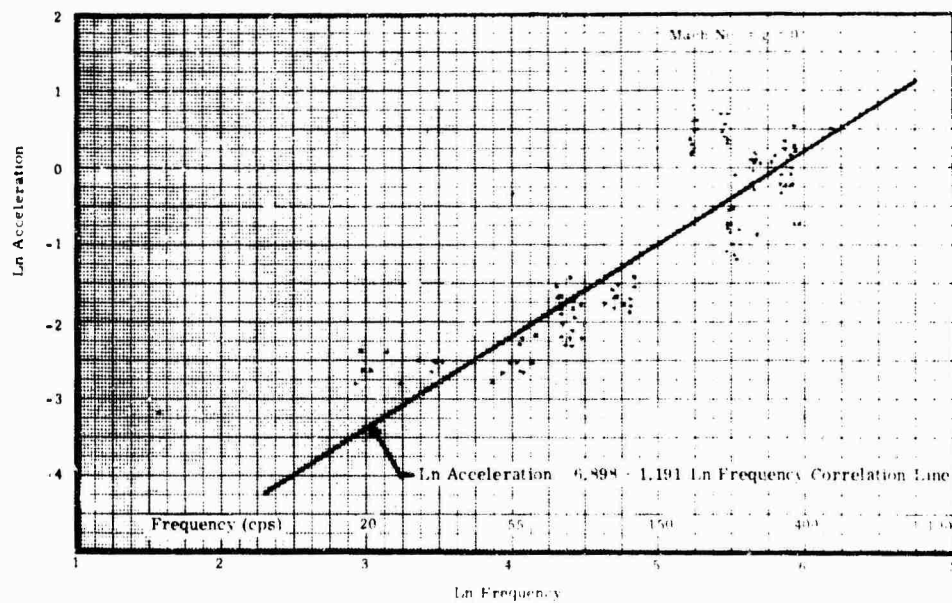


Fig. 8. Ground runup, aft fuselage, F-101A

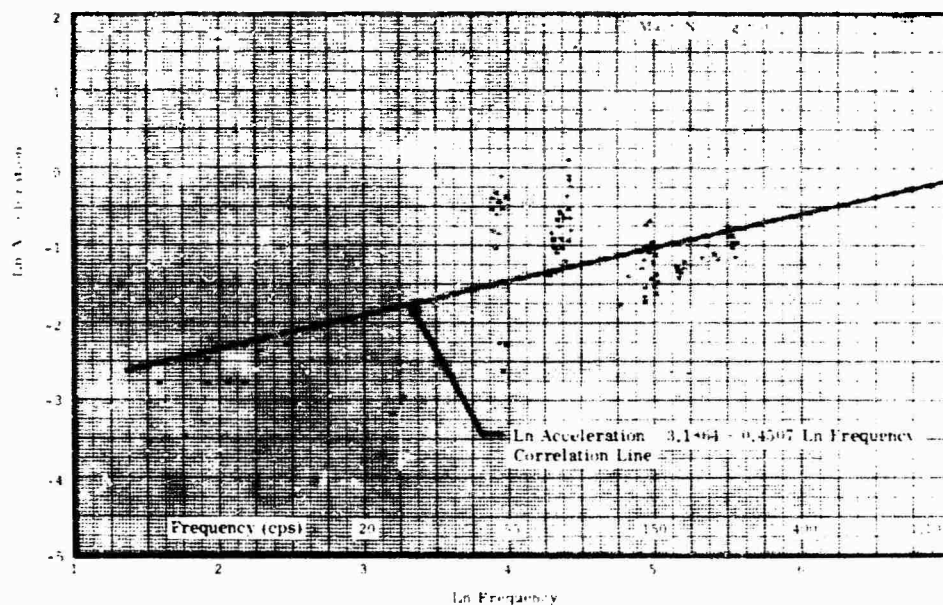


Fig. 9. Ground runup, wing tip, F-101A

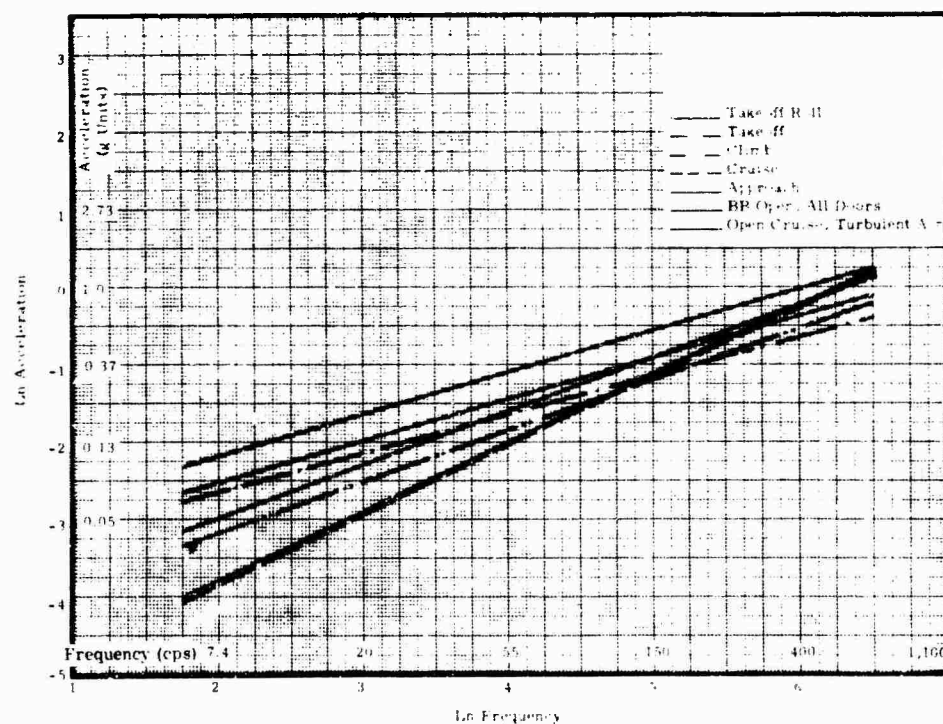
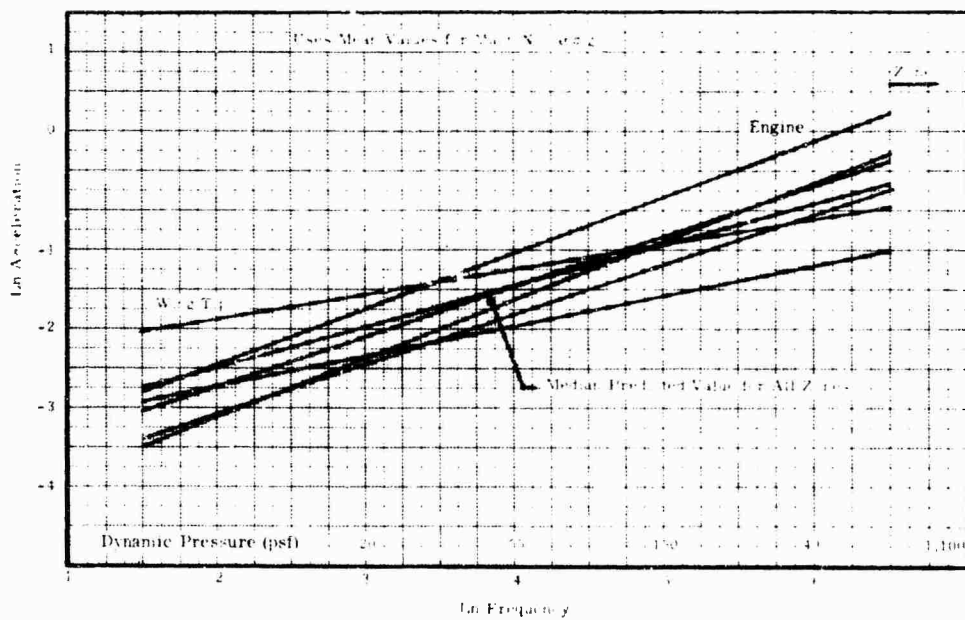
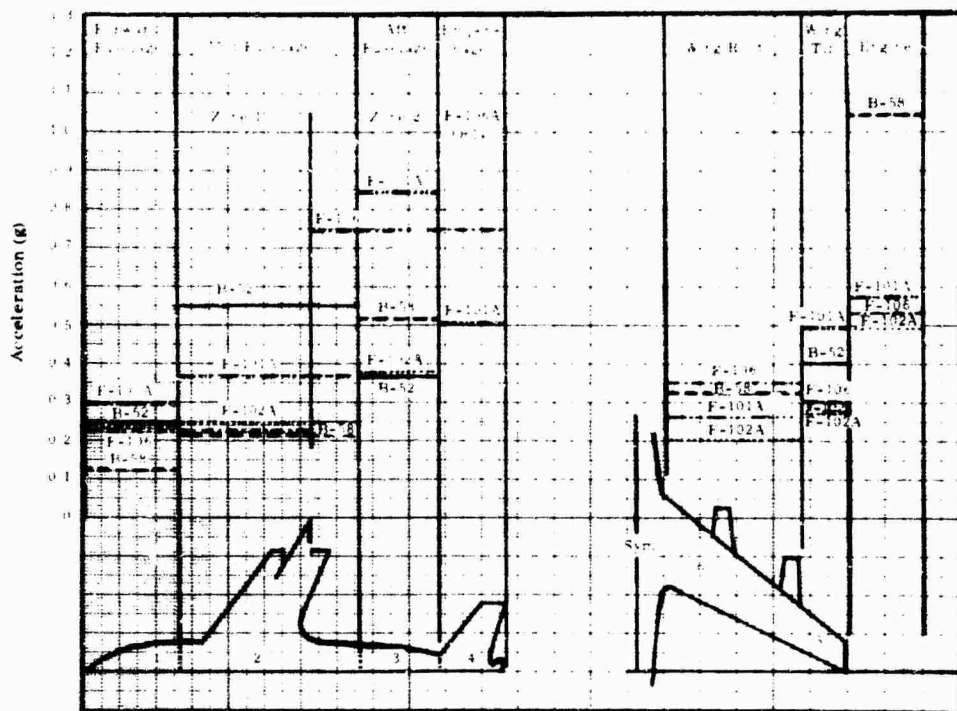


Fig. 10. Effect of flight condition, B-52





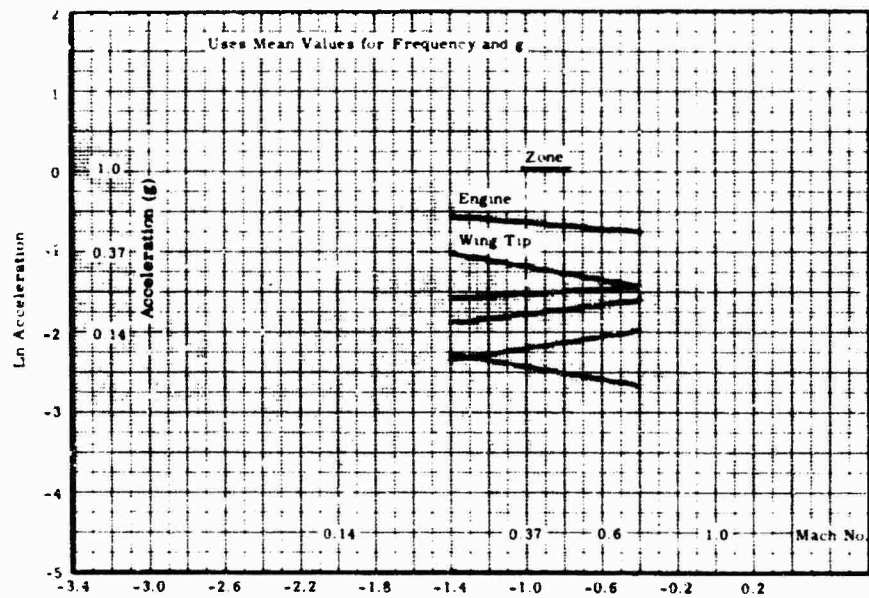


Fig. 13. Amplitude vs Mach number, B-58, cruise at normal power

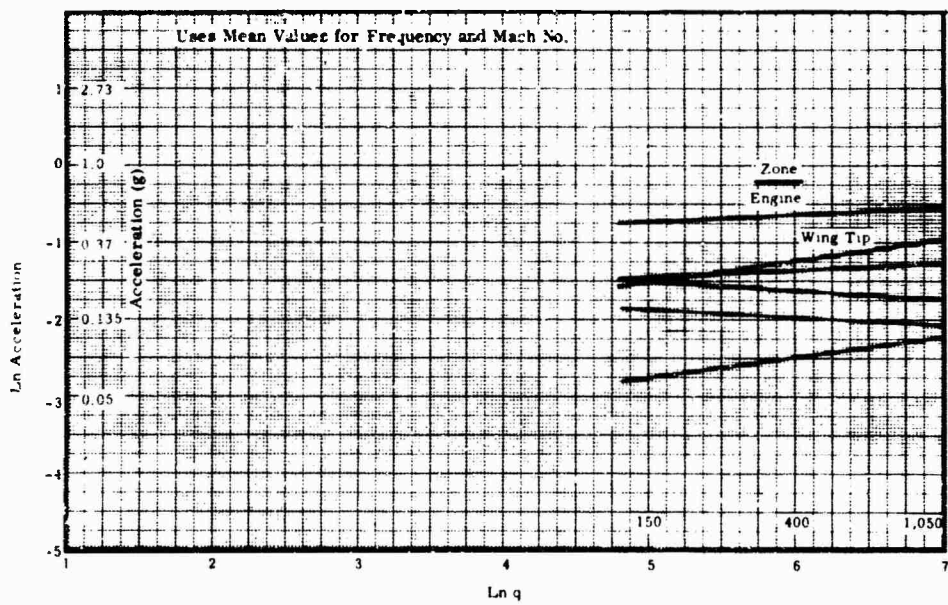


Fig. 14. Amplitude vs dynamic pressure, B-58, cruise at normal power



4. By elimination, therefore, the excitation is jet turbulence. By reference to the ground case, jet turbulence would increase both the excitation and response as engine power is increased, and the problem resolves itself into comparing the flight environment to the ground environment. Are there alterations in the flight environment which would be consistent with constant response? (The data contain a constraint concerning engine power. The only power changes occurring in the data which are subject to analysis are those associated with stabilized flight. Rapid power changes, while  $q$  and  $M_n$  remain essentially constant, were not recorded.)

5. The location of the mixing zone moves further downstream as the vehicle speed increases. Also, as the  $M_n$  is increased, the ability of the pressure pulsations in the mixing zone to be transmitted forward to the vehicle decreases for two reasons: the increased distance downstream, and the lesser ability to broadcast power upstream against the higher  $M_n$  stream.

The conclusion is that though the acoustic power has increased as a result of the increased engine power required at higher  $q$  and  $M_n$ , the excitation reaching the vehicle has not increased correspondingly. It is reasonable to accept the output of the study, therefore, and to conclude that the principal excitation in jet aircraft at subsonic speed is jet turbulence — the same principal excitation that occurs on the ground.

The possible sources of vibration are known, and were eliminated except for jet turbulence. The remaining source was examined to determine whether its known characteristics would

support the finding. The gross characteristics of the remaining source were shown to be consistent with the measurements and correlations.

Other significant outputs of this study were contained in two reports [1,2] which give the complete data and resultant predictions and a well-rounded discussion of empirical correlation.

Local dynamic response was studied in several ways. Impedance measurements were taken at 12 points on the SM62 vehicle. More acoustic and vibration work has been accomplished on this missile than any other flight structure because of the 40-g vibration levels imposed on the electronics of the guidance system; this work can be tied into many previous studies.

In addition, a compartment of the same vehicle was chosen for intensive study and measurements of its local parameters were made to determine whether obvious changes in stiffness and mass were affecting local response. The excitation for these studies was an acoustic horn broadcasting random power to the external surface of the compartment. The results (Figs. 15 through 19) show raw data, successive separate correlations against circumferential distance, stiffness and mass, and a final correlation against mass and distance. Responses were insensitive to structural stiffness. The circumferential attenuation occurs at the same rate as the longitudinal attenuation. The standard deviation between measured and predicted values would be less than 35 percent of  $\pm 2.7$  db. This same low error would not apply necessarily to the use of these data on another structure. Also, the prediction is after the fact.

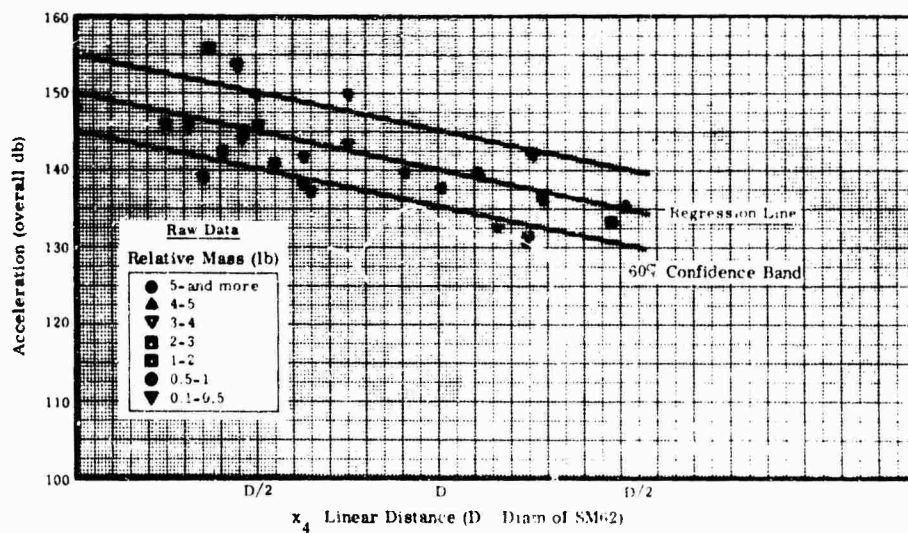


Fig. 15. Circumferential vibration attenuation, SM62

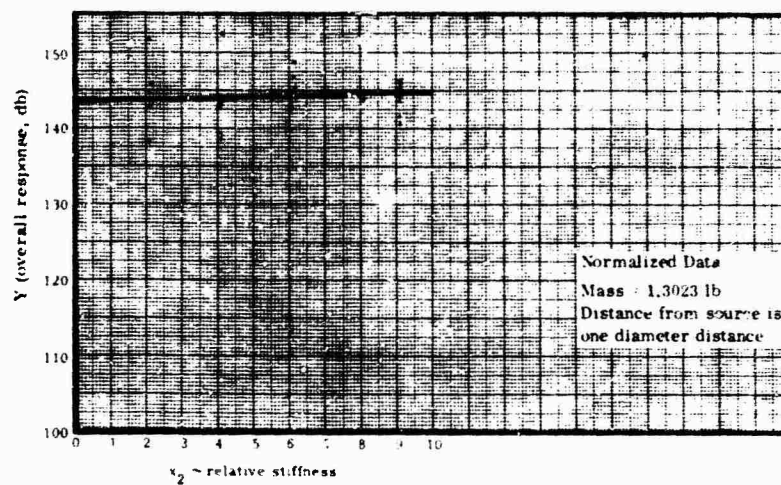


Fig. 16. Amplitude vs relative stiffness, normalized data, SM62

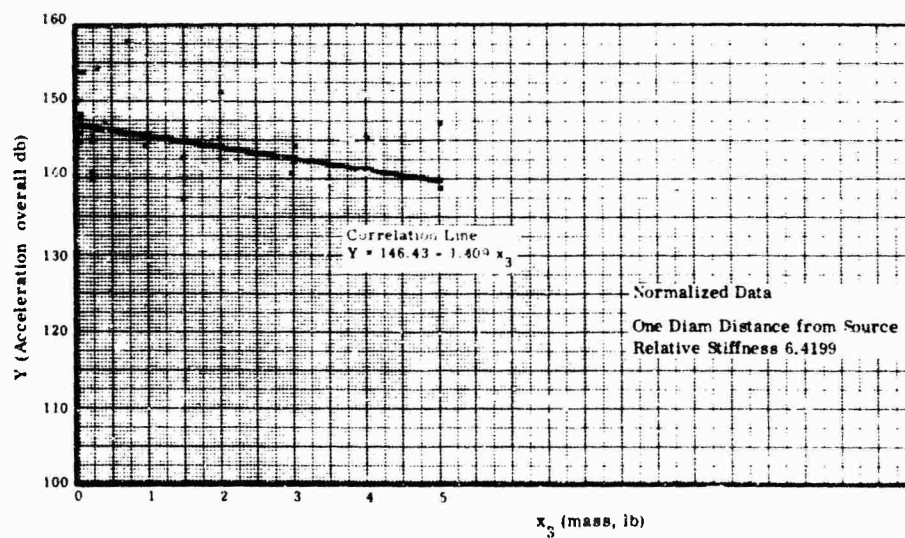


Fig. 17. Amplitude vs local mass, normalized data, SM62

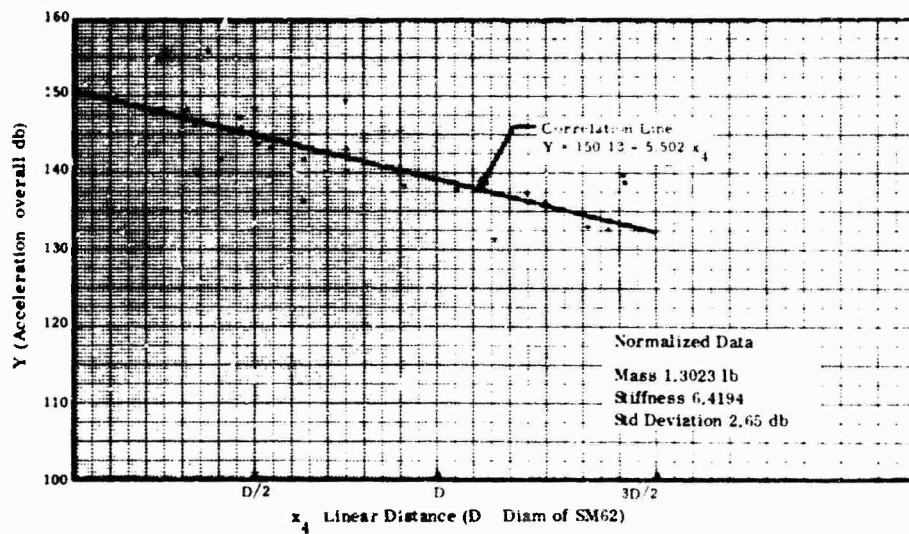


Fig. 18. Circumferential vibration attenuation, normalized data, SM62

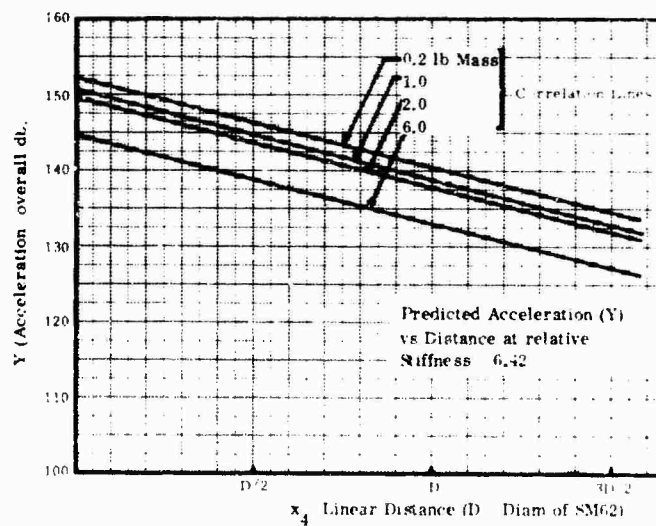


Fig. 19. Circumferential vibration attenuation, including variation and mass, SM62

The influence of the widely differing configurations is traceable in the results for the various vehicles. Four main features appear in the different configurations:

1. Underwing locations of the engines on the delta-winged B-58
2. Wing location of the B-52 engines
3. Direct exposure of the fuselage structure on the F-101
4. Conventional configuration on the F-102 and F-106

## CONCLUSIONS

This paper demonstrates the usefulness of the method of empirical correlation and the proper physical interpretation of the statistical results. System complexity is ignored; the system may be treated as an unknown black box. At face value the statistical results would be quite paradoxical, but examination showed that the story given was reasonable. Significant amounts of data were extracted short of developing an adequate theory. Sources, sensitivities, mechanisms, and physical understanding were typical of information extracted.

Comparisons with theoretical approaches to the problem may be made by the use of Refs. 3 through 6.

The technique of empirical correlation is a powerful analytical technique of special value for complex systems where no adequate theory is developed but much input-output data has been measured. The value of the method was demonstrated in this study, where the ratios of measured and predicted values averaged 1.5, or  $\pm 3.5$  db, a considerable advance over previous correlations.

The development of an adequate theory is the ultimate objective. This and similar studies

have progressed to the point where a direct approach is possible and desirable.

The data over widely differing configurations are amazingly consistent in terms of amplitude and variation with the key parameters. The accuracy targets of the study were met rather easily. Subdivision of data accomplished this with little new material, except that which was automatic in the power of the method of regression analysis.

Influence of the variations in configuration is apparent in the data. The major flight environment and source of vehicle structural vibration is jet turbulence on jet aircraft at subsonic speeds. A major change takes place in the flight regime for vehicle velocities greater than sonic. The principal excitors are lost and lesser ones remain. The only exceptions to expectations of lower environments and responses occur with:

1. Vehicles whose aerodynamic contours are poor;
2. Vehicles whose propulsion systems generate high oscillatory thrust components.

Boundary-layer turbulence is significant only when neither of the above conditions applies.

With few exceptions the flight vibration levels encountered were low. The maximum response appearing in the study may have been in the area of 3 g, a local response deviating from the regression line which called for less than 0.5 g.

A study of the local responses in a compartment of the SM62 leads to a basic correlation where the important parameters are circumferential attenuation and local mass. Excitation was provided by an acoustical horn outside the compartment. Local stiffness appeared to be an insignificant variable. The standard deviation for this study was small,  $\pm 2.65$  db, or a factor of 1.36.

## REFERENCES

1. Wang, et al., "Empirical Correlation of Vibration Response of Flight Vehicles," Northrop Corp. NORAIR Report
2. R. W. White, D. J. Bozich, and K. McK. Eldred, "Empirical Correlation of Excitation Environment and Structural Parameters With Flight Vehicle Vibration Response," TR-AFFDL-TR-64-160, Dec. 1964
3. E. J. Skudrzyk, "Vibrations of a System With a Finite or an Infinite Number of Resonances," JASA, Dec. 1958

4. E. J. Skudrzyk, "Sound Radiation of a System With a Finite or an Infinite Number of Resonances," JASA, Dec. 1958
5. E. J. Skudrzyk, "Theory of Noise and Vibration Insulation of a System With Many Resonances," JASA, Jan. 1959
6. Lyon and Maidanik, "Power Flow Between Linearly Coupled Oscillators," JASA, May 1962

#### BIBLIOGRAPHY

- |  |   |
|--|---|
| <p>K. McK. Eldred, W. Roberts, and R. W. White, "Structural Vibration in Space Vehicles," WADD TR 61-62, Mar. 1961</p> <p>P. T. Mahaffey, "Correlation of Flight Vehicle Response," Noise Control, 1959</p> <p>Mood, <u>Introduction to Statistics</u> (McGraw-Hill, New York)</p> | <p>W. H. Roberts and Finwall, "Vibration Responses on Dynamic Models of Complex Structures," ASD-TDR-63, Aug. 1963</p> <p>Rogers and Cook, "ASD Report on Cockpit Noise," ASD, Wright-Patterson AFB, Ohio</p> |
|--|---|

#### DISCUSSION

Mr. Glaubitz (Naval Research Laboratory): You spoke of high frequency vibrations, but I believe your charts showed only 500 cps.

Mr. Roberts: These data were recorded with a velocity pickup and, although the data are probably good to 1 kc, the study was limited to 500 cps.

Mr. Glaubitz: Do you have any idea whether the levels rise above that?

Mr. Roberts: Many studies have shown that the acceleration level does continue to rise, but this generally affects only smaller components. For the large structures, the important frequency band is below 500 cps.

\* \* \*

# VIBRATION DATA SUMMARY OF MINUTEMAN WING VI FLIGHT TEST MISSILES

Robert R. Burnett and Robert E. Morse  
TRW Systems  
Redondo Beach, California

Vibration data reduced by TRW Systems from 15 Minuteman Wing VI flight test missiles and 3 test missiles from a special flight test program are summarized. Included are data from measurement locations throughout the missile. Vibration instrumentation, equipment configuration and data analysis techniques are outlined. Profiles of the rms vibration as a function of flight time, as well as PSD analyses, are included when applicable.

These data are used to (a) verify the estimated environment used to derive dynamic test specifications; (b) measure the vibration along a transmission path for use in determining modes and transfer functions; (c) measure the response of equipment on structures to the vibration environment; (d) aid in guidance error analysis; (e) extrapolate to later Minuteman Wing environments; (f) establish structure load criteria; and (g) aid in flight failure analyses.

## INTRODUCTION

This report presents a comprehensive summary of the vibration data analyzed by TRW Systems from measurements flown on the Minuteman Wing VI flight test missiles (FTM's) and from three flight test missiles from a special program. These FTM's include 18 flights, 446 through 463; 446, 447, and 448 flew in the special program called the Fly-3 Program. This special program evaluated the Wing VI Stage II liquid injection thrust vector control (LITVC) system under flight conditions. Data are included from transducers at 41 locations or orientations. Most of the measurements were flown more than once. The total number of individual vibration measurements flown was 114. The data are presented by missile section starting from the forward end (reentry vehicle section) and moving down the missile toward the first stage.

Included here is a discussion of the instrumentation calibration and data analysis techniques. The vibration data are presented in various forms: rms acceleration (rms g) level vs flight time plots; broad-band PSD analyses, and narrow-band PSD analyses when applicable; and vibration oscillograph traces. The locations of the transducers are illustrated in Appendix A by photographs and sketches of the equipment.

A summary of vibration data taken from Minuteman Wing I flight test missiles appears in Ref. [1]. The report here complements those data and presents further information on the Minuteman dynamic environment. Two significant configuration changes in the Minuteman Wing VI necessitate a complete redefinition of the equipment environment in the Stage II motor area and in the guidance and control area. Attention was focused upon these two areas in this program.

## MEASUREMENT

A total of 114 measurements sampling the vibration environment at 41 locations or orientations, or both, were flown on 15 Wing VI FTM's and three FTM's from the Fly-3 Program. Each location and orientation has been assigned a separate number. Each measurement is identified by missile section in the number assignment. Figure 1 is an exploded view of a Wing VI FTM showing the missile sections with numbers of the sections. Table 1 lists the measurement numbers by missile section and gives the location as closely as possible. In addition, the significance of the measurement location (e.g., the missile guidance and control computer, D37, measurements describe the vibration input to the computer unit) is shown by listing each measurement's objective. Table 2

**TABLE 1**  
**Vibration Measurement Information**

Missile Section	Measurement Number	Location <sup>a</sup>	Figure Number (App. A)	Measurement Axis	Responsible Contractor	Objective of Measurements <sup>b</sup>
41	V1W01	Lockout switch mounting bracket at 130-deg azimuth, R = 4 in.	None	Longitudinal	R & Contractor	C
42	V2H01	Base of D37 computer, outboard mounting foot at memory end	A-1	0- to 180-deg lateral	Autonetics	A
42	V2H02	Base of D37 computer, outboard mounting foot at memory end	A-1	90- to 270-deg lateral	Autonetics	A
42	V2H03	Base of D37 computer, outboard mounting foot at memory end	A-1	Longitudinal	Autonetics	A
42	V2M01	G and C section, SS 80-8 deg	A-1	Longitudinal	Autonetics	B
42	V2P01	G and C IMU platform, parallel to platform x'' z'' plane	A-4	30 deg from x'' platform axis	Autonetics	D
42	V2P02	G and C IMU platform	A-4	Parallel to y'' platform axis	Autonetics	D
42	V2P03	G and C IMU platform, parallel to platform x'' z'' plane	A-4	30 deg from z'' platform axis	Autonetics	D
42	V2P04	G and C IMU support bracket cap at 130-deg azimuth	A-6	Longitudinal	Autonetics	A
42	V2P05	G and C IMU base, external surface, R = 4 in. at 90-deg azimuth	A-1	90- to 270-deg lateral	Autonetics	C
42	V2P06	G and C IMU support bracket cap at 130-deg azimuth	A-6	90- to 270-deg lateral	Autonetics	A
42	V2P07	G and C IMU support bracket cap at 130-deg azimuth	A-6	0- to 180-deg lateral	Autonetics	A
42	V2P08	G and C IMU base, external surface, R = 4 in. at 90-deg azimuth	A-1	0- to 180-deg lateral	Autonetics	C
42	V2U01	Base of P92, inboard mounting foot	A-1	0- to 180-deg lateral	Autonetics	A
42	V2U02	Base of P92, inboard mounting foot	A-1	Longitudinal	Autonetics	A
42	V2U03	Base of P92, inboard mounting foot	A-1	90- to 270-deg lateral	Autonetics	A
44	V4U01	Stage III actuator arm 4 near actuator, R = 12 in.	A-7	135- to 315-deg lateral	Autonetics	C
44	V4U02	Stage III actuator arm 4 near actuator, R = 12 in.	A-7	Longitudinal	Autonetics	C
44	V4U03	Stage III NCU base on side near junction of APS cover and base at 315-deg azimuth	A-7	45- to 225-deg lateral	Autonetics	A
44	V4U04	Stage III NCU actuator arm 4 near junction of arm and base at R = 8 in.	A-7	Longitudinal	Autonetics	C
44	V4U05	Stage III NCU base, on side near junction of APS cover and base at 315-deg azimuth	A-7	135- to 315-deg lateral	Autonetics	A
44	V4U06	Stage III NCU base, on side near junction of APS cover and base at 315-deg azimuth	A-7	Longitudinal	Autonetics	A
45	V5A02	II-III interstage aft on G and C angular accelerometer rack	None	Longitudinal	Boeing	C
46	A901V	Roll control gas generator	A-8	Radial	Aerojet	C
46	A902V	Thrust vector nozzle	A-8	Radial	Aerojet	C
46	A903V	Thrust vector nozzle	A-8	Longitudinal	Aerojet	C
46	A904V	Support structure for LITVC gas generator	A-9	Radial	Aerojet	A
46	A905V	Support structure for LITVC gas generator	A-9	Longitudinal	Aerojet	A
46	V6G01	LITVC gas generator	A-10	135- to 315-deg lateral	Aerojet	C
46	V6G02	LITVC gas generator	A-10	Longitudinal	Aerojet	C
46	V6T01	LITVC injector mounting pad on thrust nozzle at 0-deg azimuth	A-11	Longitudinal	Aerojet	A
46	V6T02	LITVC injector mounting pad on thrust nozzle at 0-deg azimuth	A-11	0- to 180-deg lateral	Aerojet	A
46	V6T03	Roll control valve at 107-deg azimuth	A-12	17- to 197-deg lateral	Aerojet	C
46	V6T04	Roll control valve at 107-deg azimuth	A-12	107- to 287-deg lateral	Aerojet	C
46	V6T05	LITVC system pressure relief valve parallel to pintle	A-10	Tangent	Aerojet	C
46	V6U01	ACI electronics base at 45-deg azimuth	A-13	Longitudinal	Autonetics	C
46	V6U02	ACI electronics base at 45-deg azimuth	A-13	45- to 225-deg lateral	Autonetics	C
46	V6U03	ACI electronics base at 45-deg azimuth	A-13	135- to 315-deg lateral	Autonetics	C
46	V8U01	Stage I actuator arm 1 near actuator	A-14	135- to 315-deg lateral	Autonetics	C
46	V8U02	Stage I actuator arm 1 near actuator	A-14	Longitudinal	Autonetics	C
46	V8U03	Stage I actuator arm 1 near NCU base	A-14	Longitudinal	Autonetics	C

Note: Both crystal and strain-gage accelerometers were flown, but data from the latter are not given here.

<sup>a</sup>G and C: guidance and control; IMU: inertial measurement unit; NCU: nozzle control unit; ACI: attitude control injector; APS: auxiliary power supply.  
<sup>b</sup>A: verify estimated environment; attachment point of a piece of equipment; B: measure vibration at a point along the transmission path for use in determining modes and transfer functions; C: measure response of equipment to vibration environment; D: guidance error analysis.

**TABLE 2**  
**Vibration Measurement Index**

Measure- ment Number	Operational on FTM's	Figure Number			
		Rms g vs Time	Broad-band PSD Analyses	Narrow-band PSD Analysis	Decaying Sinusoidal Shock Response
V1W01	462	4	—	—	5
V2H01	453, 454, 461	6	9	13	16
V2H02	453, 459, 460, 462	7	10, 11	14	17
V2H03	451, 457, 463	8	12	15	18
V2M01	455, 458	19	20	21	22
V2P01	499, 450, 453, 455, 458, 461, 463	23	26	—	30
V2P02	449, 452, 454, 456, 459, 462, 463	24	27	29	31
V2P03	449, 451, 452, 457, 458, 459, 463	25	28	—	32
V2P04	450, 454, 457, 461	33	36, 37, 38, 39, 40	43	46
V2P05	452	49	51	53	55
V2P06	452, 456, 460, 462	34	41	44	47
V2P07	453, 459	35	42	45	48
V2P08	451	50	52	54	56
V2V01	450, 455	57	60	64	67
V2V02	451, 457, 460, 461, 462	58	61, 62	65	68
V2U03	456	59	63	66	69
V4U01	449	—	—	—	70
V4U02	450, 460	—	—	—	71
V2U03	454	—	—	—	72
V2U04	455	—	—	—	73
V2U05	456	—	—	—	74
V4U06	458	—	—	—	75
V5A02	455, 456	—	—	—	76
V6G01	450, 453, 456, 458, 459	—	—	—	77
V6G02	452, 454, 457	—	—	—	78
V6T01	449, 450, 454, 460, 461, 462, 463	79	80	—	82
V6T02	449, 452, 457, 459, 461	—	81	—	83
V6T03	449, 451, 455, 458, 462	84	85	86	87
V6T04	451, 455	—	—	—	88
V6T05	453, 456, 457, 463	89	—	90	91
V6U01	450, 454, 459	—	—	—	94
V6U02	451, 453, 459	—	92	93	95
V6U03	458, 460	—	—	—	96
V8U01	449	—	—	—	97
V8U02	450	—	—	—	98
V8U03	460	—	—	—	99
A901V	446, 447, 448	—	—	—	—
A902V	446, 448	—	—	—	—
A903V	447	—	—	—	—
A904V	446, 447	—	—	—	—
A905V	443	—	—	—	—

Note.--Dash indicates no data reduced.



lists the measurements in numerical order, and enumerates the FTM's on which the measurement was flown. Data plots and oscillograph traces of the transducer locations are listed.

#### FLIGHT INSTRUMENTATION

Wing VI vibration measurements were taken using piezoelectric, and in some cases, strain-gage accelerometers. The various models used by the associate contractors are outlined in Table 3. (Data from the piezoelectric accelerometers only are reported here.)

The data were transmitted on channels 12, 13, C, and E of standard IRIG FM/FM telemetry systems. The channels used had standard IRIG frequency responses of 160, 220, 1200, and 2100 cps, respectively. It should be pointed out that there was no intentional frequency limiting at the input of the voltage-controller oscillator (VCO). It was thus possible to analyze high vibration frequency components. However, frequencies above the IRIG standards have a lower VCO modulation index. The entire data acquisition system from accelerometer to ground receiving station is shown in Fig. 2.

#### CALIBRATION PROCEDURE

Calibration of the acceleration ( $\pm g$ ) peak corresponding to plus and minus percentage deviation of the telemetry subcarrier frequency was supplied to TRW by Boeing Atlantic Test Center (BATC). The calibration procedure was as follows:

1. The contractor responsible for the measurement performed a calibration on the

combination of accelerometer, flight cable, and amplifier while vibrating the accelerometer at 20 percent increments of the specified amplitude, and at frequencies of 20, 100, 400, 1000, and 2000 Hz. Then, simulation currents were applied through the transducer calibration resistor simulating the stimulated values above. To be accepted, stimulation and simulation at all five levels must agree. The combination of accelerometer, flight cable, and amplifier was then installed for a particular vibration measurement.

2. At the Atlantic Missile Range (AMR), BATC performed an end-to-end simulation calibration on each vehicle measurement, using the same simulation levels and frequencies as previously conducted in the laboratory. The simulation provided a peak g vs VCO frequency calibration and a frequency response calibration for the telemetry system.

The percentage of telemetry channel bandwidth of each calibration step and its corresponding value in peak g's were supplied to TRW. These data were extrapolated by TRW to give the peak g value of the full channel bandwidth.

#### DATA ANALYSIS

##### General

The vibration data included here were analyzed using four processes: oscillograph traces, rms g vs flight time analyses, narrow-band PSD analyses, and broad-band PSD analyses. The instruments used to perform these analyses were, respectively, a Visicorder model 1012, the Mosely logarithmic converter model 1560A

TABLE 3  
Accelerometer and Amplifier Models

Contractor	Responsibility	Accelerometer	Amplifier
Aerojet	Stage II motor	Endevco 2242M5A	Endevco 2633M5B1
Autonetics	G and C, Stage I, II, and III NCU's	Endevco 2242M5A	EDC 2-210-2
Avco	Reentry vehicle	Endevco 2213M5	Wurlitzer 1204
Boeing	Overall airframe	Endevco 2242M5A	Endevco 2633M5B1 EDC 2-210-2
Hercules	Stage III motor	Endevco 2242M5A	Endevco 2633M5B1 EDC 2-210-2
Thiokol	Stage I motor	Endevco 2242M5A	Endevco 2620

coupled to an Electronics Associates Incorporated (EAI) x-y plotter model 110, a Davies 0-2000 Hz automatic wave analyzer, and a Visicorder recorder (model 1012). A second system of instrumentation to obtain the rms plots, consisting of an rms meter rectifier circuit of the Bruel and Kjaer (B & K) spectrum analyzer coupled to a Sanborn recorder, was used on some of the flights. A schematic outlining the data reduction processes is shown in Fig. 3.

#### Discriminator Output Filter

As the data were played back, they were filtered through a low-pass output filter. The upper limit of the filter was a function of the FM/FM telemetry channel on which the data were transmitted, or the destination of the signal in the data reduction process, or both. Generally, the following criteria were used in choosing the filter:

1. The IRIG recommended filter for FM/FM channel E (0 to 2100 Hz) was used if the data were transmitted on channels C (0 to 1200 Hz) or E.
2. The IRIG recommended filters were used when analyzing data transmitted on channels 12 and 13 (160- and 220-Hz cutoff filters, respectively).
3. On oscillograph runs where definition of low frequencies was desired, an appropriate filter having a lower cutoff was employed.

#### Oscillograph Recordings

Measured vibrations of the entire flight were initially reproduced in Greenwich mean time (GMT) flight time on oscillograph traces for quick-look examination. Additional traces of the data were requested, if needed, to define the frequencies better by varying the paper speed or discriminator output filter, or both. The following "numbers" were acquired from these traces:

1. The peak g amplitudes of all excitation of a transient nature (i.e., 100-msec duration);
2. The dominant frequencies, if any, of said vibrations;
3. The rms g level at liftoff for all of the rms g analyses. This was necessary since the averaging time of the rms system was too long to respond accurately to the short duration ( $\approx 100$  msec) vibration experienced at liftoff.

The rms g level was determined by assuming the data to have a Gaussian distribution limited to  $3\sigma$  peaks. This being the case, the rms g level was taken as one third of the peak g amplitude.

In addition to the above information, the traces were used to identify areas of questionable data and periods of sustained vibration. If periods of sustained random vibration existed, the times for performing narrow-band PSD analyses were chosen during these periods, and an rms g analysis of the data was performed to determine the time history of the rms g level during the flight.

#### Rms g Analyses

The rms g time history analyses were performed only on measurements experiencing periods of sustained vibrations; e.g., Mach 1 and max q periods. The analyses were produced by using the signal from the discriminator as an input to the rms meter of the B & K spectrum analyzer. The dc output of the meter was amplified and reproduced as a heated stylus strip chart by the Sanborn recorder. The rms g as a function of flight time was read directly from these charts and replotted. The overall averaging time constant of the system was 0.2 sec. For some flights (FTM's 446, 447, 449, 450, 451, 454, 455, and 459) the discriminator signal was fed to the Mosely logarithmic converter coupled to the EAI x-y plotter.

#### Narrow-Band PSD Analyses

Narrow-band PSD analyses were performed for periods when a relatively high sustained random vibration remained quasi-stationary for 2 sec or longer. Only two periods during the flight fit this description: reaching the speed of sound (Mach 1) and reaching maximum dynamic pressure (max q).

Only a small minority of the instrumented measurement locations experienced significant vibration during these periods and was also transmitted on telemetry channels of sufficient frequency response (i.e., channels C and E) to permit the performance of meaningful analyses; hence, narrow-band analyses were limited to measurements at these locations.

As mentioned above, the time periods for the analyses were chosen from the oscillograph traces. The data were played back during the period of interest through a standard channel E discriminator output filter (0 to 2100 Hz) and a

tape loop dubbed. Loop lengths of either 2 or 3 sec were used consistently, depending on the stationary quality of the data. The data on the loop were then analyzed by the Davies wave analyzer from 0 to 2000 Hz. However, because of inherent characteristics of the Davies instrument, the data under 30 Hz are not considered reliable. A filter bandwidth of 6 Hz was used with sweep rates of 3 and 2 Hz/sec for 2- and 3-sec loops, respectively. The resulting charts were read directly in  $g^2/Hz$  with the use of a multiplicative calibration constant and were re-plotted on a more desirable log-log scale. For some flights the Davies wave analyzer was coupled directly to the EAI x-y plotter to eliminate the need for replotting.

#### Broad-Band PSD Analyses

Broad-band PSD analyses were performed only on measurements recording severe vibration at liftoff. This type of analysis was used since the short duration of the liftoff vibration ( $\approx 100$  msec) made it impossible to perform narrowband analyses on available data reduction equipment. It should be stressed that since such analyses are only qualitative, they are useful only in determining the relative energy concentrations within the frequency bands indicated.

The broad-band PSD analyses were produced in the following manner. The output of the discriminator was played into a bank of bandpass filters consisting of 10 contiguous 100-Hz filters, covering the range from 0 to 1000 Hz, and a pair extending from 1056 to 1522 Hz and from 1522 to 2153 Hz, respectively. The outputs of these filters were recorded along with a composite trace and flight time by the Visicorder recorder, producing a time history of the vibration signal in each frequency band during the liftoff transient. The time of the most severe vibration was identified from the composite trace, and the peak  $g$  amplitude in each frequency band at this time was determined. Again employing the assumption that the data have a Gaussian distribution, dividing the peak levels by 3 produced an rms  $g$  level for each frequency band. The  $g^2/Hz$  energy level within the band was calculated by squaring the rms  $g$  level and dividing the result by the filter bandwidth. The levels were then plotted vs frequency on a log-log scale as a histogram.

#### VIBRATION ENVIRONMENT

The Wing VI vibration environment was generally transient in nature; i.e., usually lasting less than 500 msec. The three exceptions

were sustained vibrations occurring during the transonic (Mach 1) period, during the maximum aerodynamic pressure (max  $q$ ) period, and during the chamber pressure oscillations of the Stage III motor. The following is a brief explanation of the various events which affect the vibration environment during the course of a normal flight. The times at which the events occur are nominal ( $\pm 5$  sec) and are referenced to liftoff.

1. Battery Squib (minus 35 sec). — Explosive squibs release the acid into the guidance and control unit (G and C) battery. This event, as would be expected, is especially severe on measurements in the G and C section. The location of the battery is illustrated in Figs. A-1 and A-2 in Appendix A.

2. Umbilical Disconnect (minus 17 sec). — The G and C umbilical is separated from the G and C section by using an explosive charge. Again this affects mainly the measurements located forward. Figure A-3 illustrates the location of the umbilical connector in the G and C section.

3. Liftoff (0 sec). — Here the excitation has two sources. At ignition the initial thrust excites a low-frequency ( $\approx 60$  Hz) longitudinal missile mode; this is immediately followed by a high-level pressure pulse lasting approximately 100 msec, induced by the intense acoustic field within the silo. This event is most severe on measurements in close proximity to the missile skin and on those on the Stage I NCU.

4. Mach 1 (18 sec). — The increase in vibration is caused by an increase in intensity of the aerodynamic turbulence on the skin of the missile. The intensity varies from place to place, and depends on the local details of the missile profile.

5. Max  $q$  (37 sec). — An increase in vibration level results from the increase in aerodynamic turbulence as the missile reaches the region of maximum aerodynamic pressure.

6. Gas Generator Activation (59 sec). — An explosive squib opens a valve allowing the Freon propellant to be pressurized by helium. This precedes staging by 1 sec.

7. I-II Staging (60 sec). — This includes two occurrences approximately 500 msec apart: (a) separation. — Stages I and II are separated by a circular explosive charge ripping the inter-stage skin; (b) stage II ignition. — a burst of vibration lasting about 100 msec is caused by the ignition transient of the motor and the

vibration resulting from the interaction of the flame and the forward end of Stage I.

8. Stage II Skirt Removal (76 sec). — The removal of the aft skirt of Stage II by a circular explosive charge (applicable only to FTM 410 and subsequent FTM's).

9. II-III Staging (120 sec). — II-III staging is carried out in the same manner as I-II staging, with entirely similar results in the vibration environment.

10. Stage III Skirt Removal (121 sec). — The Stage III aft skirt is discarded by an explosive charge (applicable only to FTM 410 and subsequent FTM's).

11. Stage III Chamber Pressure Oscillations. — Depending on the flight, sinusoidal oscillations of the Stage III chamber pressure ranged in frequency from about 450 to 600 Hz and occurred at various times after Stage III ignition, with the time of maximum amplitude ranging from immediately after ignition to approximately 140 sec, referenced to liftoff. This phenomenon was not evident on every flight or every measurement.

12. Reentry Vehicle (R/V) Unlatch (170 sec). — The R/V is detached from the G and C section and Stage III motor by a circular explosive charge around the skin at the separation plane.

13. Port Blow (172 sec). The thrust of the Stage III motor is reversed by removing the covers of four holes or ports in the side of the motor casing with simultaneous explosive charges.

It should be pointed out that, because of their locations, very few of the measurements recorded measurable vibrations during all of the above events. For instance, measurements located on or near the missile skin or on beams attached to the skin emphasize Mach 1 or max  $q$ , or both, whereas measurements mounted toward the center, e.g., the NCU measurements, do not.

#### DATA PRESENTATION

The vibration data from each measurement are presented, when applicable, in one or more of the following forms: decaying sinusoidal shock response (DSSR) data; oscillograph traces; and plots of rms  $g$  and narrow-band and broad-band PSD analyses.

The DSSR data represent the decaying sinusoidal shock responses caused by shock-like events such as the squibbing of the G and C battery. These data are presented by plotting the recorded peak amplitude of each shock response vs its frequency. Separate symbols are used for each shock-producing event, and the time for the response to decay to one tenth of its maximum amplitude is included next to each point.

Oscillograph traces for these measurements are not included. See Appendix B.

Generally, all the rms  $g$  and PSD analyses for each measurement are included, with a brief discussion of the measurement, below. However, the volume of these data from several measurements (e.g., measurements in the G and C area) required summarization of the plots. The methods used to summarize these data are as follows:

1. To summarize the rms  $g$  analyses, a typical rms  $g$  vs flight time profile is included without a numerical rms  $g$  scale. The ranges of the rms  $g$  levels during the most severe events, i.e., Mach 1, etc., are tabulated.

2. The broad-band PSD analyses are summarized by plotting the maximum, minimum, and calculated mean  $g^2/\text{Hz}$  level vs frequency.

3. The narrow-band PSD analyses are summarized by plotting all the maxima appearing on each of the individual PSD plots on one graph.

To facilitate data presentation, the measurements are separated and discussed with respect to six major missile sections: the reentry vehicle, guidance and control section, II-III interstage, and Stage I, II, and III engines.

#### Reentry Vehicle

Only one vibration measurement was located in the R/V during the Wing VI Program, V1W01. This measurement was mounted longitudinally on the lockout switch mounting bracket at 130-deg azimuth, 4 in. from the missile centerline. It experienced its most severe vibration at port blow, a 19.7-g 0-peak high-frequency shock response with a duration of 80-msec. Measurement V1W01 was staged at I-II staging with V2P06; hence there were no data received by this measurement (V1W01) prior to I-II staging.

Figure 4 contains the rms g vs flight time in seconds from liftoff after I-II staging when this measurement was sequenced for operations. Figure 5 contains the summary of DSSR data. No PSD analyses were performed for this measurement.

#### Guidance and Control Section

Vibration measurements were located in five areas in the G and C section: the base of the D37 computer (V2H01, V2H02, V2H03), the G and C section skin (V2M01), the inertial measurement unit (IMU) stable platform (V2P01, V2P02, V2P03), input to and response of the IMU (V2P04 through V2P08), and the base of the P92 (V2U01, V2U02, V2U03). The location of each measurement is illustrated in Figs. A-1 through A-6.

**Base of the D37 Computer.** — Vibration data from measurements V2H01, V2H02, and V2H03 are summarized in Figs. 6 through 18. Typical rms g vs flight time analyses for these measurements are shown in Figs. 6, 7, and 8. Table 4 presents rms g ranges and averages at pertinent events for V2H01 and V2H02 (more than one flight record was analyzed).

Figures 9 and 10 summarize the broad-band PSD analyses performed on liftoff data and umbilical disconnect from measurement V2H01; Figs. 11 and 12 are the broad-band analyses performed for measurements V2H02 and V2H03, respectively, at liftoff. The narrow-band PSD analyses performed on the Mach 1 data of measurements V2H01, V2H02, and V2H03 are shown in Figs. 13, 14, and 15, respectively. The DSSR data for these measurements are contained in Figs. 16, 17, and 18.

**Guidance and Control.** — Vibration data from measurement V2M01 are shown in Figs. 19 through 22. This measurement was flown on two flight test missiles: FTM 455 and 458. The rms g vs flight time analyses summary is given in Fig. 19, the broad-band PSD analyses at liftoff are given in Fig. 20, the narrow-band PSD analyses at Mach 1 are given in Fig. 21, and the DSSR data are summarized in Fig. 22. Ranges and averages (rms g) at pertinent events appear in Table 5. The location of this measurement is shown in Fig. A-1 of Appendix A.

**IMU Stable Platform.** — Measurements V2P01, V2P02, and V2P03 were located inside the IMU on the stable platform, with measurement axes oriented in the axes of the sensing

TABLE 4  
Ranges and Averages (rms g) for V2H01 and V2H02

Event	Range		Average	
	V2H01	V2H02	V2H01	V2H02
Battery squib	1.0-1.4	0.7-1.6	1.2	1.0
Umbilical disconnect	2.3-2.6	3.5-4.0	2.4	3.8
Liftoff	2.0-9.6	3.8-9.7	5.8	9.2
Mach 1	1.7-3.9	2.0-3.9	2.3	2.7
Max Q		1.0-1.8	1.1	1.4
I-II Staging	5.5-6.8	1.5-6.8	6.0	3.8
Stage II skirt removal	8.1-9.4	7.1-8.2	8.9	7.8
II-III staging	0.7-4.2	0.9-1.0	3.0	1.0
Stage III skirt removal	0.7-7.0	0.9-1.3	3.6	1.0
R/V unlatch	0-1.2	0.3-3.3	0.4	1.6
Port blow	0-2.3	1.1-6.0	1.3	3.5

Note. — Three samples for each event.

TABLE 5  
Ranges and Averages (rms g) for V2M01

Event	Range	Average
Battery squib	0.7-0.9	0.8
Umbilical disconnect	3.0-3.6	3.3
Liftoff	11.0-13.0	12.0
Mach 1	3.8-4.3	4.1
Max Q	2.0-2.2	2.1
I-II staging	0.9-1.1	1.0
Stage II skirt removal	2.1-2.2	2.2
II-III staging	2.2-3.0	2.6
Stage III skirt removal	1.0-2.2	1.6
R/V unlatch	0-0.7	0.4
Port blow	2.4-3.0	2.7

Note.-- Two samples for each event.

instruments. Vibration measured on this unit, which is isolated, is relatively low in amplitude, as would be expected. These vibration data are used in the guidance system performance analysis. The location of these measurements is shown in Fig. A-6.

Figures 23, 24, and 25 contain the rms g vs flight time for V2P01, V2P02, and V2P03, respectively. Figures 26, 27, and 28 contain the broad-band PSD analyses of V2P01, V2P02, and V2P03 from FTM 463 at liftoff. A narrow-band analysis of V2P02 at Mach 1 on FTM 452 is presented in Fig. 29. Figures 30, 31, and 32 contain the DSSR data for these three measurements. Table 6 presents ranges and averages (g rms) at pertinent events for V2P02 and V2P03.

Input to the IMU. -- The vibration measurements located on the IMU support bracket cap are V2P04, V2P06, and V2P07 sensing the longitudinal, yaw, and pitch axes, respectively. Measurement V2P04 was transmitted on a 0- to 2100-Hz (channel E) telemetry channel on FTM's 450 and 457, and on a 0- to 1200-Hz telemetry channel (channel C) on FTM's 454 and 461. Measurements V2P06 and V2P07 were

TABLE 6  
Ranges and Averages (rms g) for V2P02 and V2P03

Event	Range		Average	
	V2P02	V2P03	V2P02	V2P03
Battery squib	0-0.9	0.0-0.6	0.45	0.3
Umbilical disconnect	0-0.6	0.0-0.8	0.3	0.4
Liftoff	0.7-1.5	0.9-0.96	1.1	0.93
Mach 1	0-1.0	0.0-0.46	0.5	0.23
Gas generator activation	0.2	0.9-0.3	0.2	0.15
I-II staging	0.4-1.0	-- 1.1	0.7	1.1
Stage II skirt removal	0.25-1.0	-- 0.35	0.7	0.35
II-III staging	0.2-2.4	1.0-1.6	1.3	1.3
Stage III skirt removal	0.1-0.2	0.0-0.2	0.15	0.1
R/V unlatch	0-0.4	0.0-0.5	0.2	0.25
Port blow	0.2-0.7	0.8-3.0	0.45	1.9

Note. -- Two samples for each event.

transmitted on channel E on each flight on which they were flown with one exception: measurement V2P07 was transmitted on a 220-Hz (channel 13) telemetry channel on FTM 453.

The rms g vs time data for V2P04, V2P06, and V2P07 are contained in Figs. 33, 34, and 35. The broad-band PSD analyses are contained in Figs. 36 through 42. Broad-band analysis was performed on data from V2P04 at liftoff, I-II staging, Stage II skirt removal, II-III staging, and Stage III skirt removal. These data are contained in Figs. 36 through 40. Figures 41 and 42 contain the broad-band PSD analyses for V2P06 and V2P07 at liftoff. Narrow-band analyses performed on V2P04, V2P06, and V2P07 at Mach 1 appear in Figs. 43, 44, and 45, respectively. The DSSR data for these same three measurements are contained in Figs. 46, 47, and 48. Ranges and averages (rms g) for pertinent events for V2P04 appear in Table 7.

TABLE 7  
Ranges and Averages (rms g) for V2P04

Event	Range	Average
Battery squib	1.0-1.3	1.1
Umbilical disconnect	2.6-5.0	3.7
Liftoff	8.7-15.0	11.7
Mach 1	3.2-4.6	3.8
Max Q	1.2-2.0	1.6
I-II staging	3.9-9.8	7.3
Stage II skirt removal	3.0-12.0	9.0
II-III staging	1.5-4.0	2.6
Stage III skirt removal	0.8-7.1	3.0
Port blow	1.7-3.4	2.5

Note. -- Four samples for each event.

The IMU external housing measurements V2P05 and V2P08 represent equipment response rather than input to a unit and have therefore been separated from the support bracket cap measurements. The location of these two measurements is shown in Figs. A-1 and A-2. They are located on the lower external body of the IMU housing, oriented in the 90- to 270-deg lateral axis (V2P05) and the 0- to 180-deg lateral axis (V2P08).

Figures 49 and 50 contain the rms g vs time data for V2P05 and V2P08; Figs. 51 and 52 contain the broad-band PSD analyses, Figs. 53 and 54 contain the narrow-band PSD analyses, and Figs. 55 and 56 contain the DSSR data for these two measurements.

Input to P92. -- Measurements V2U01, V2U02, and V2U03 are mounted at the base of the P92 amplifier assembly to determine the input to equipment mounted on the G and C structural mounting shelf. These measurements were oriented in the 0- to 180-deg lateral and longitudinal, and 90- to 270-deg lateral axes, respectively. Figures 57 through 69 contain the data from these measurements. Figures 57, 58, and 59 contain the rms g vs time history of this environment; Figs. 60, 61, and 63 contain broad-band PSD analysis at liftoff, with Fig. 62 defining the environmental PSD at umbilical disconnect for V2U02. Figures 64, 65, and 66 contain the narrow-band PSD analysis; and Figs. 67, 68, and 69 contain the DSSR data for V2U01, V2U02, and V2U03, respectively. Ranges and averages (rms g) for V2U01 and V2U02 appear in Table 8.

#### Stage III Engine

All vibration measurements taken in the Stage III engine area were on the NCU: V4U01, V4U02, V4U03, V4U04, V4U05, V4U06. Measurements V4U01 and V4U02 were on actuator arm 4 near the actuator. V4U03, V4U05, and V4U06 were on the NCU base on the side near the junction of the auxiliary power supply (APS) cover and the base at 315-deg azimuth measuring in the 45- to 225-deg lateral, the 135- to 315-deg lateral, and the longitudinal axes, respectively. Measurement V4U04 was mounted on NCU actuator arm 4 near the junction of the arm and base at R = 8 in.

Each of these measurements was flown on one flight and V4U02 was flown on two flights. The DSSR data for these measurements listed in alpha-numerical order are contained in Figs. 70 through 75.

#### II-III Interstage Area

A vibration measurement was made at a single location in the II-III interstage area on two flights. This measurement was V5A02, located aft of the angular accelerometer rack in the interstage area. Because of the extensive changes in the Stage II engine control system, the environment for the angular accelerometer had to be redefined.

**TABLE 8**  
Ranges and Averages (rms g) for V2U01 and V2U02

Event	Range		Average	
	V2U01	V2U02	V2U01	V2U02
Battery squib	2.6-3.5	0.5-1.7	2.9	1.2
Umbilical disconnect	5.0-5.4	3.0-3.7	5.2	3.3
Liftoff	8.6-14.4	5.0-10.6	11.0	6.9
Mach 1	3.5-5.0	1.2-1.4	4.2	1.3
Max Q	1.0-3.0	0.6-0.7	1.8	0.6
I-II staging	3.5-6.3	0.7-5.7	4.6	3.3
Stage II skirt removal	0-9.3	1.8-10.2	3.1	7.1
II-III staging	1.0-3.0	1.8-7.1	1.3	3.6
Stage III skirt removal	0-0.8	1.0-3.5	0.3	1.9
Port blow	2.5-3.0	1.1-12.0	1.8	5.5

Note. -- Three samples for each event.

The DSSR data from these two flights (FTM's 455 and 456) are contained in Fig. 76. The vibration data from measurement V5A02 were transmitted on telemetry channel 12 (0-160 Hz) so that only low-frequency data were recorded; all high-frequency data were attenuated.

#### Stage II Engine

During the Wing VI flight test program, vibration measurements were flown in eight locations in the Stage II engine area. These measurements can be separated with respect to the seven main equipments:

- Roll control gas generator (A901V)
- Thrust vector nozzle (A902V, A903V)
- LITVC gas generator (A904V, A905V, V6G01, V6G02)
- LITVC injector (V6T01, V6T02)
- Roll control valve (V6T03, V6T04)
- LITVC system pressure relief valve (V6T05)
- Attitude control injector (ACI) electronics package (V6U01, V6U02, V6U03)

The location of these measurements is shown in Figs. A-8 through A-13. The data for this missile section are arranged in the order listed above, except that the Fly-3 program data are not included. Since these measurements were for research and development verification purposes, complete data reduction was not accomplished on the telemetered data. The measurements, all made on the Wing VI flight configuration of the LITVC, are included in this section.

Measurements V6G01 and V6G02, located on the LITVC gas generator, were flown on five and three flights, respectively. On all of these flights, however, the data from these measurements were assigned to a low-frequency channel, channel 12 (160 Hz) or channel 13 (220 Hz). Therefore, all the high-frequency data are attenuated and no PSD analyses were performed. The DSSR data from these two measurements are contained in Figs. 77 and 78.

Measurements V6T01 and V6T02, located on the LITVC injector mounting pad, were flown on seven and five flights, respectively. The rms g vs time plot for V6T01 is presented in Fig. 79. None was made for V6T02. Broad-band PSD analyses for V6T01 and V6T02 were performed at I-II staging and are contained in Figs. 80 and 81. No narrow-band analyses were



performed on these measurements. The DSSR data for V6T01 and V6T02 are contained in Figs. 82 and 83.

Measurements V6T03 and V6T04 were located on the roll control valve. Figure 84 contains the rms g vs time plot for V6T03. Figure 85 contains the broad-band PSD analysis at I-II staging for V6T03, and Fig. 86 contains the narrow-band PSD analysis at Mach 1 for the same measurement. Figures 87 and 88 contain the DSSR data for V6T03 and V6T04, respectively.

Measurement V6T05 is located on the LITVC pressure relief valve. Figure 89 contains the rms g vs time plot, Fig. 90 contains the narrow-band PSD analysis at Mach 1, and Fig. 91 contains the DSSR data for V6T05.

Measurements V6U01, V6U02, and V6U03 were located on the attitude control injector electronics package. Broad-band PSD analysis was performed on V6U02 at I-II staging during FTM 45. These data are contained in Fig. 92. Narrow-band PSD analysis performed at liftoff for V6U02 is contained in Fig. 93. The DSSR data from V6U01, V6U02, and V6U03 are contained in Figs. 94, 95, and 96, respectively.

#### Stage I Engine

Only one vibration measurement location was used in the Stage I engine area: the Stage I

NCU (V8U01, V8U02, V8U03). Each of these measurements was flown on only one flight early in the program to verify that the vibration levels were similar to levels from the previous Wing I program. Since this system remained unchanged in configuration, very little change in vibration level was anticipated. Measurement V8U01 located on actuator arm 1 and measuring in the 135- to 315-deg lateral axis was flown on FTM 449. Measurement V8U02, also on actuator arm 1, measuring in the longitudinal axis, was flown on FTM 450. Measurement V8U03, located at the same place on actuator arm 1 and measuring in the lateral axis, was flown later on FTM 460 to establish environmental conformity. Figures 97, 98, and 99 contain the summaries of the DSSR data for measurements V8U01, V8U02, and V8U03.

Since no unexpected vibration occurred on these flights at this location, no PSD analyses were performed. Reference [1] contains a definition of the Stage I dynamic environment in terms of the frequency content of the power spectral density.

#### REFERENCE

1. J. H. McGehee, Jr., and R. E. Morse, "Vibration Data Summary of Minuteman Wing I Flight Test Missiles," TRW Space Technology Laboratories Rept. 6121-8722-RU-000, June 1964

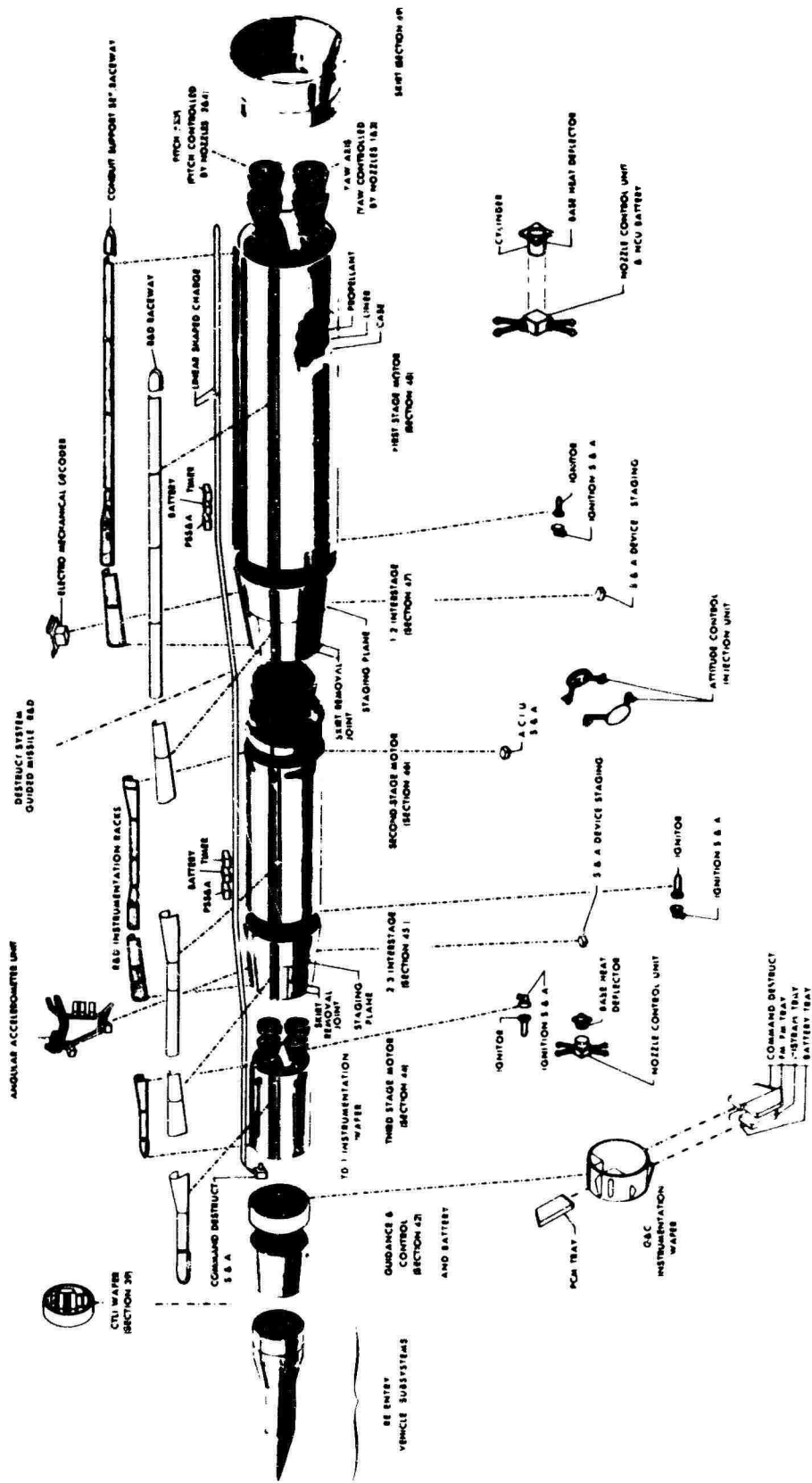


Fig. 1. Minuteman missile, exploded view

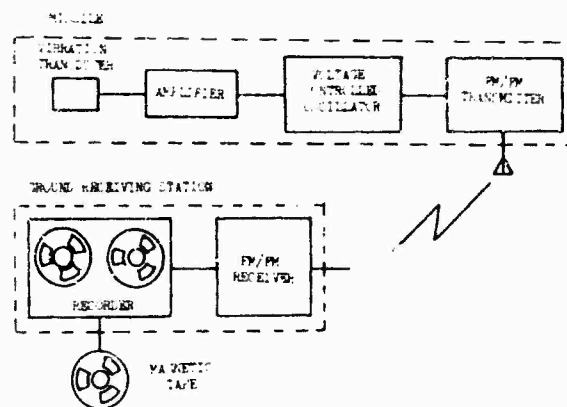


Fig. 2. Outline of the Minuteman Wing VI data acquisition system

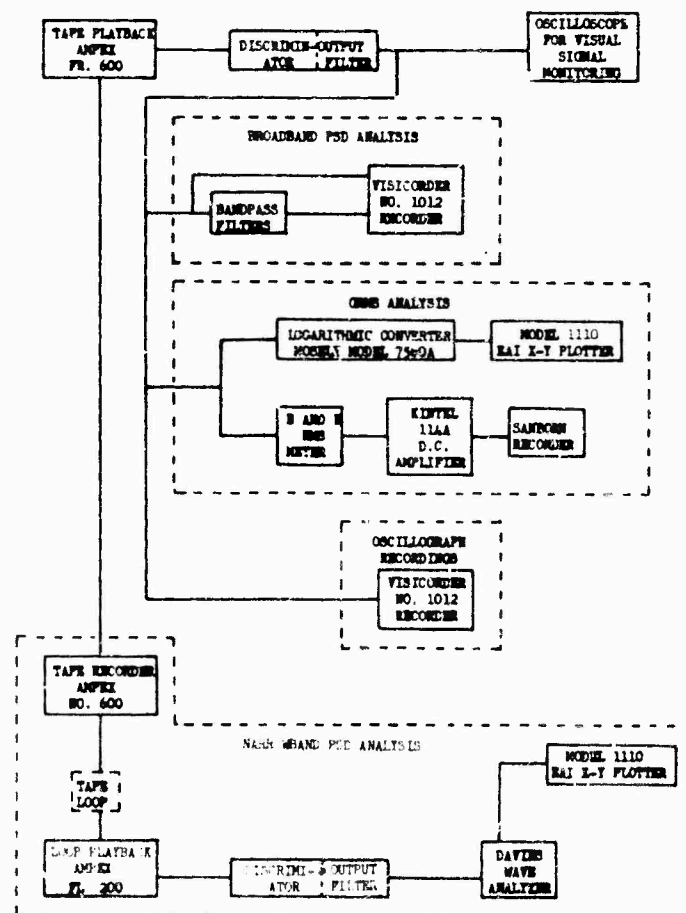


Fig. 3. Schematic of the Wing VI vibration data reduction system

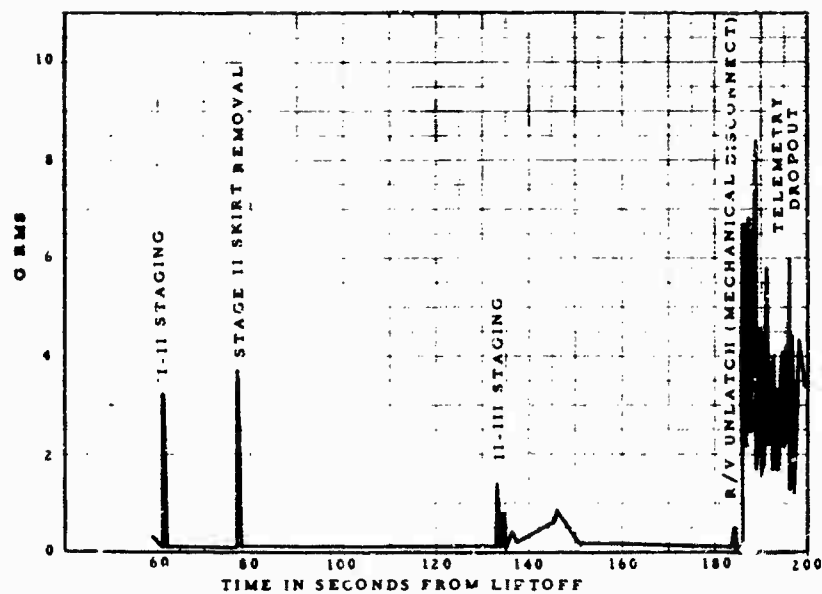


Fig. 4. Rms g vs flight time for measurement VIW01, R/V lockout switch mounting bracket

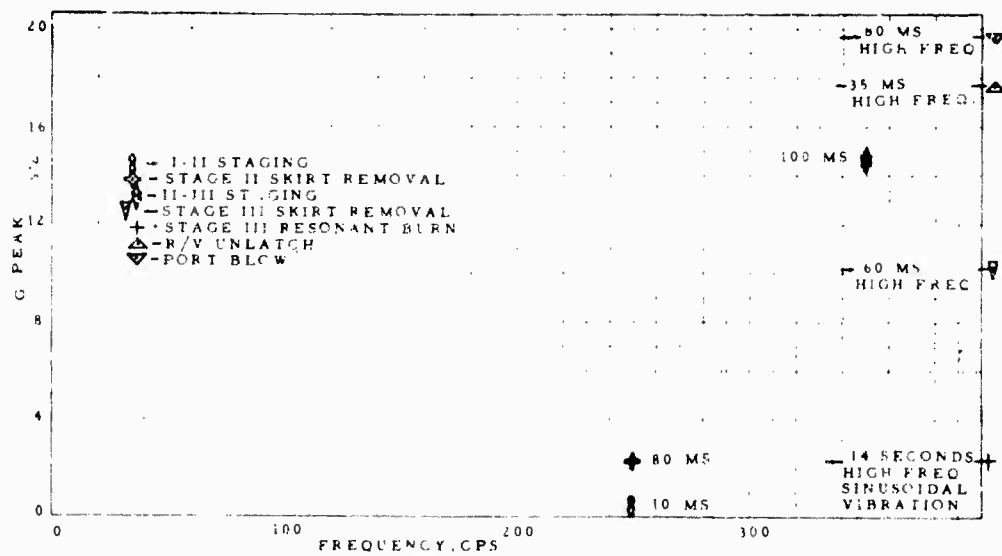


Fig. 5. Summary of decaying sinusoidal shock response data for measurement VIW01, R/V section



Fig. 6. Summary of rms g vs flight time data for measurement V2H01, base of D37 computer, 0- to 180-deg lateral axis

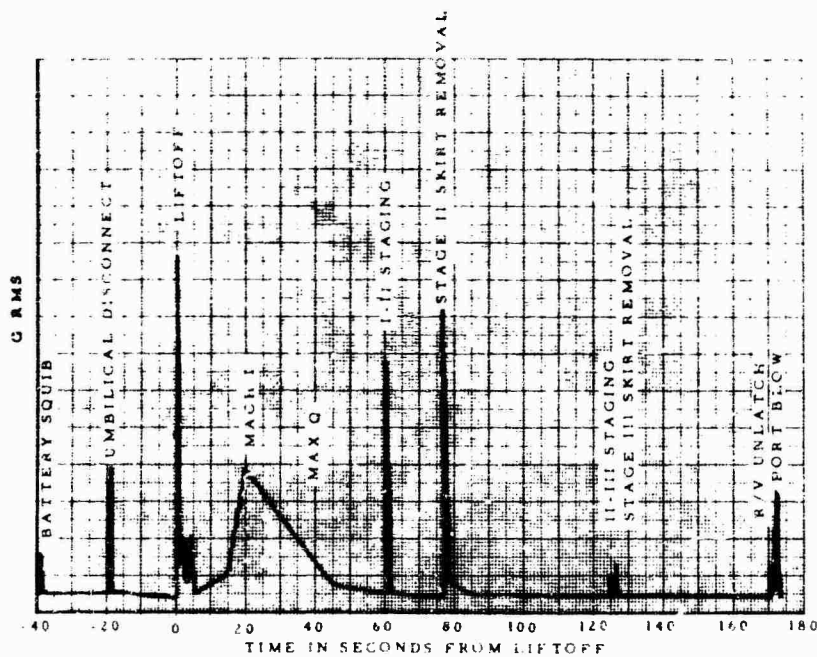


Fig. 7. Summary of rms g vs flight time data for measurement V2H02, base of D37 computer, 90- to 270-deg lateral axis

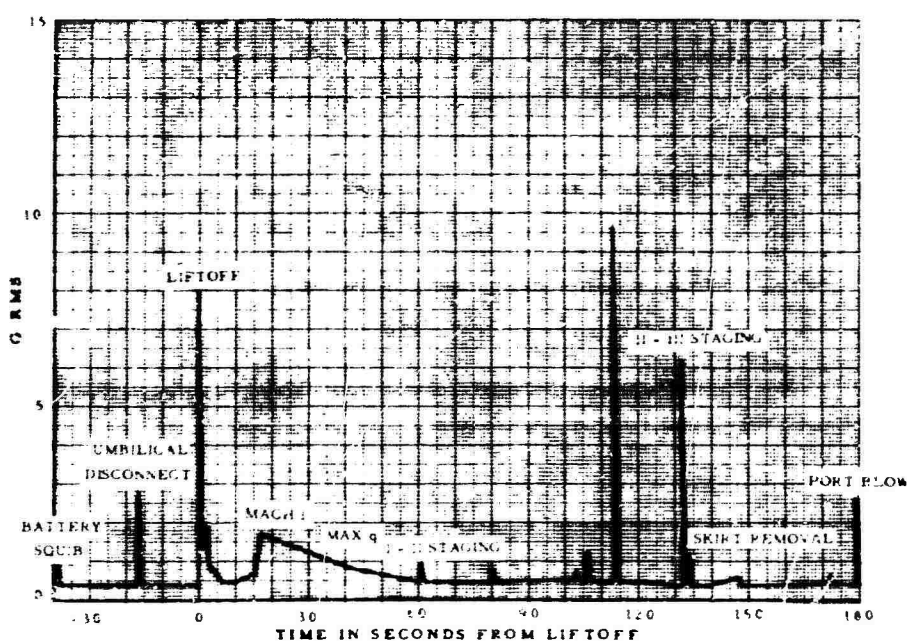


Fig. 8. Summary of rms g vs flight time for measurement V2H03, base of D37 computer, longitudinal missile axis

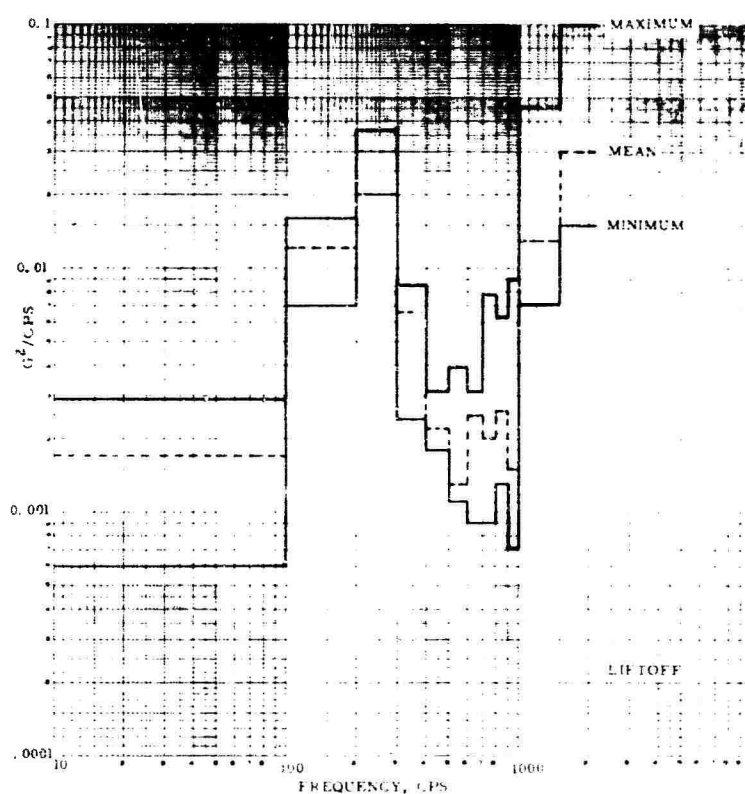


Fig. 9. Broad-band PSD analysis for measurement V2H01, base of D37 computer, 0- to 180-deg lateral axis

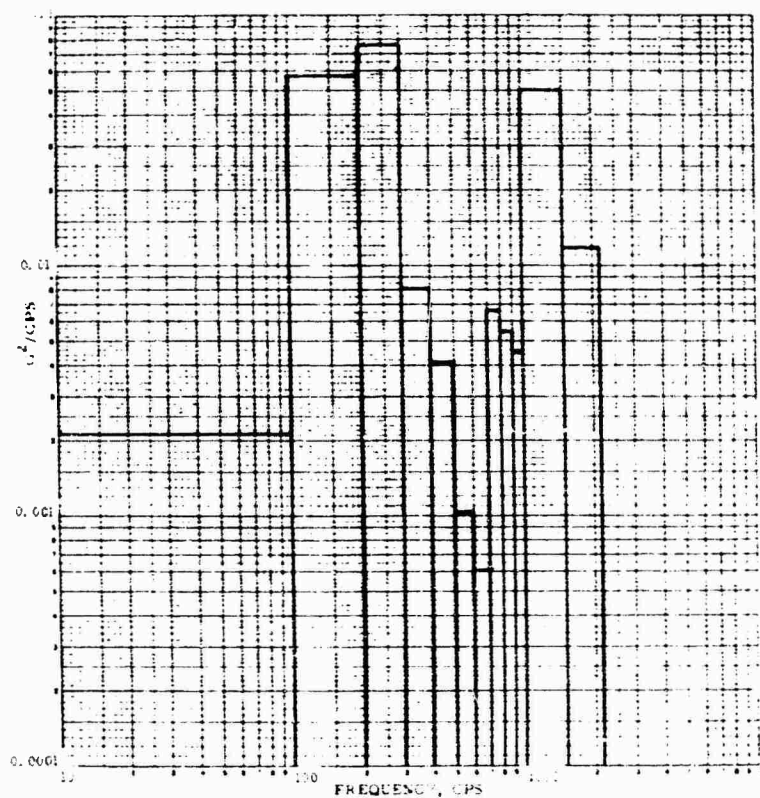


Fig. 10. Broad-band PSD analysis at umbilical disconnect for FTM 462, measurement V2H02

Fig. 11. Broad-band PSD analysis for measurement V2H02, base of D37 computer, 90- to 270-deg lateral axis

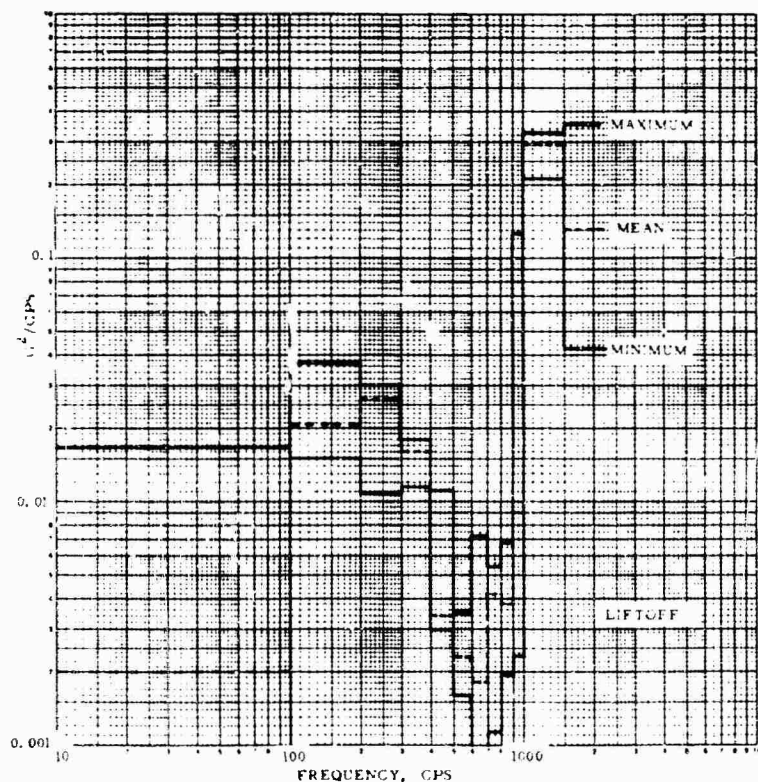


Fig. 12. Broad-band PSD analysis for measurement V2H03, base of D37 computer, longitudinal axis

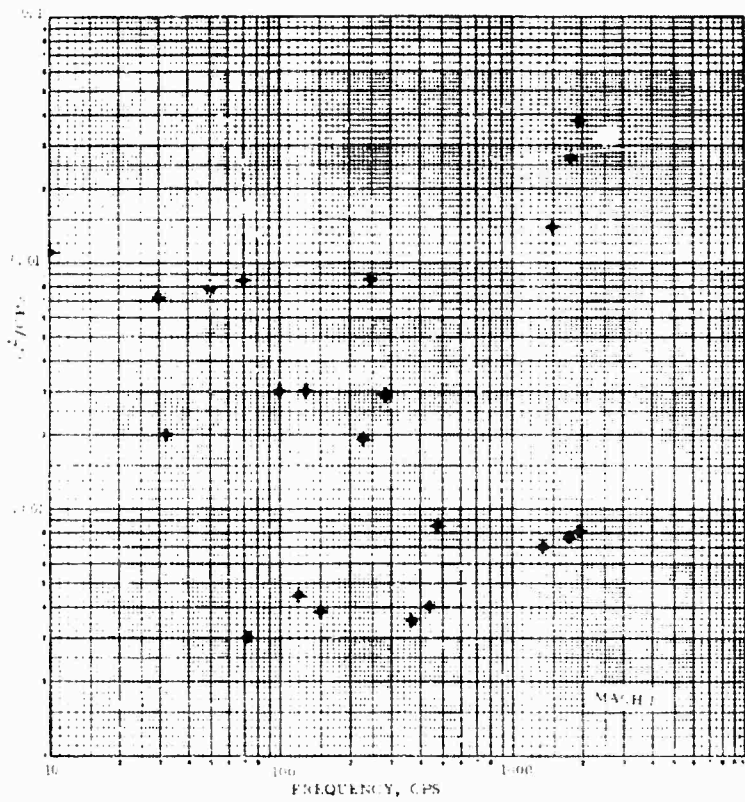
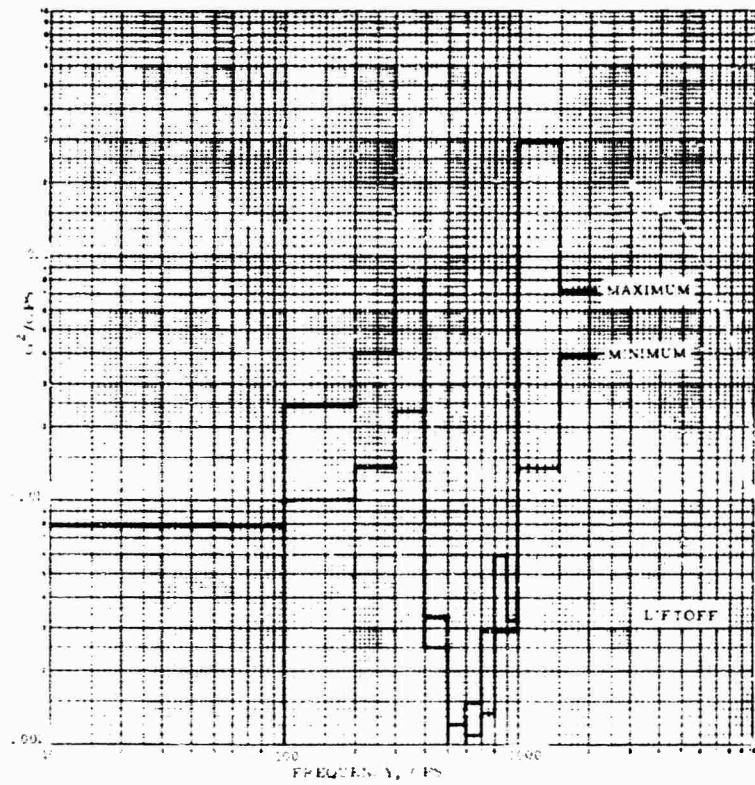


Fig. 13. Narrow-band (5 cps) PSD analysis for measurement V2H01, base of D37 computer, 0- to 180-deg lateral axis



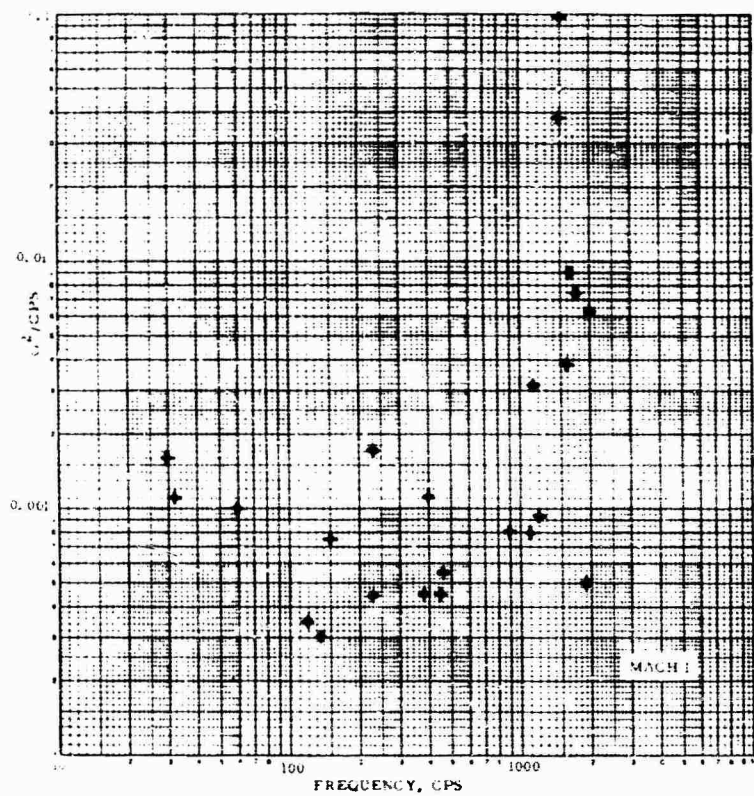
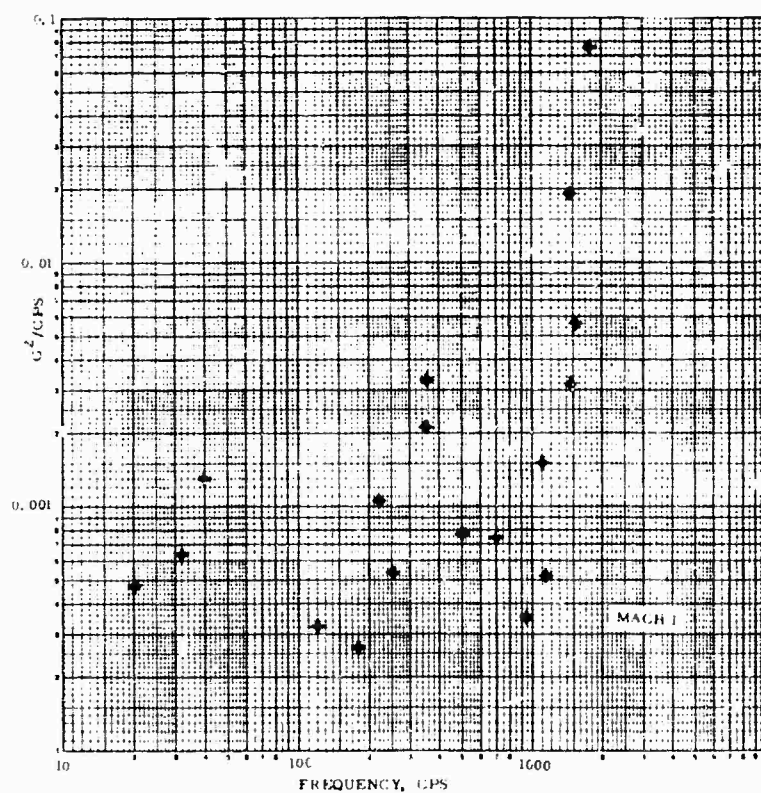


Fig. 14. Narrow-band (6 cps) PSD analysis for measurement V2H02, base of D37 computer, 90- to 270-deg lateral axis

Fig. 15. Narrow-band (6 cps) PSD analysis for measurement V2H03, base of D37 computer, longitudinal axis



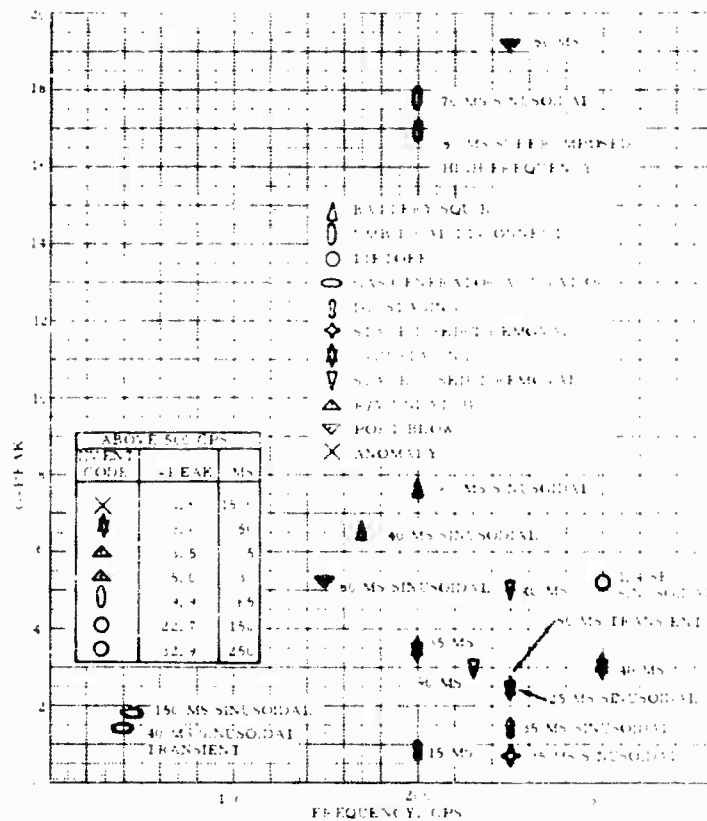


Fig. 1b. Summary of decaying sinusoidal shock response data for measurement V2H01, base of D37 computer

ABOVE 400 CPS		
EVENT CODE	G-PEAK	MS
8	1.3	100
X	1.4	10
V	1.4	50
+	1.4	20
+	1.9	100
+	1.9	110
8	1.9	15
△	4.1	20
△	4.6	45
△	5.2	25
△	5.5	30
+	5.8	25
△	6.1	40
△	6.3	30
+	7.1	40

ABOVE 400 CPS		
Event	G-Peak	MS
X	8.0	1000
△	8.3	60
△	9.1	30
+	9.5	30
+	10.0	70
0	20.4	65
0	27.5	80
0	35.2	190
0	35.4	200
0	39.9	105

△ BATTERY SQUIB

0 UMBILICAL DISCONNECT

0 LIFTOFF

0 GAS GENERATOR ACTIVATION

8 IN STAGING

+

+

△ STAGE III SKIRT REMOVAL

△ R/V UNLOCK

△ PORT BLOW

X ANOMALY

The graph displays the relationship between G-Peak and Frequency for various shock durations. The data points are as follows:

Duration (MS)	Frequency (CPS)	G-Peak
25	~100	~2.5
25	~120	~1.5
90	~100	~1.0
50	~180	~6.0
20	~200	~1.0
35	~280	~5.5
65	~280	~10.0
70	~300	~1.5
70 with superimposed high frequency	~300	~11.0

Fig. 17. Summary of decaying sinusoidal shock response data for measurement V2H02, base of D37 computer

114

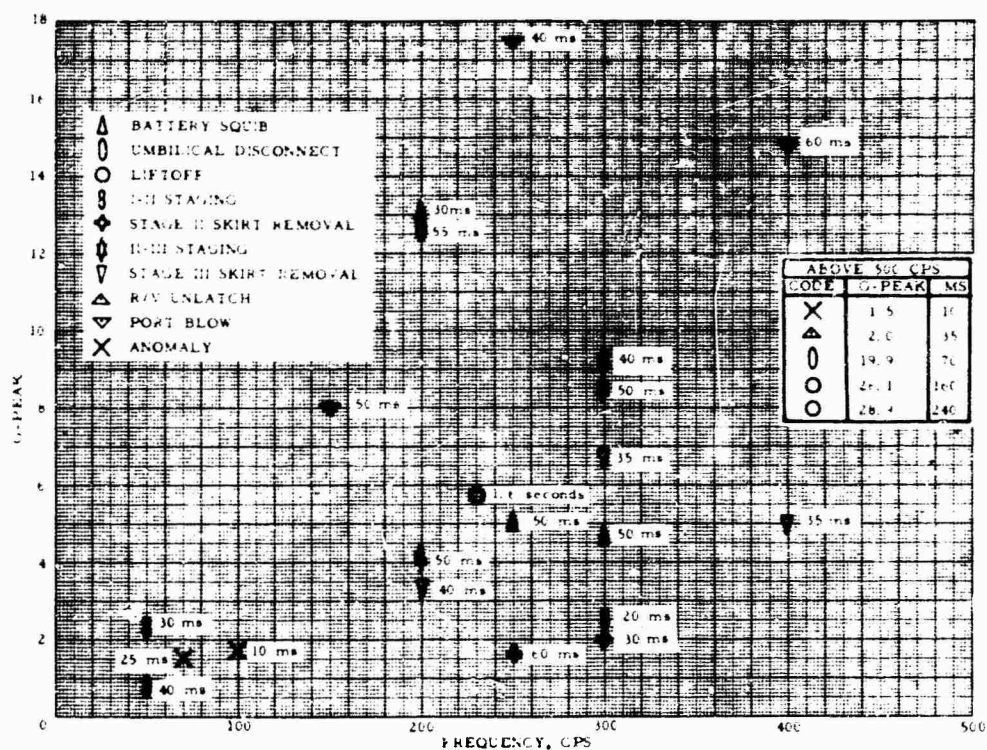


Fig. 18. Summary of decaying sinusoidal shock response data for measurement V2H03, base of D37 computer

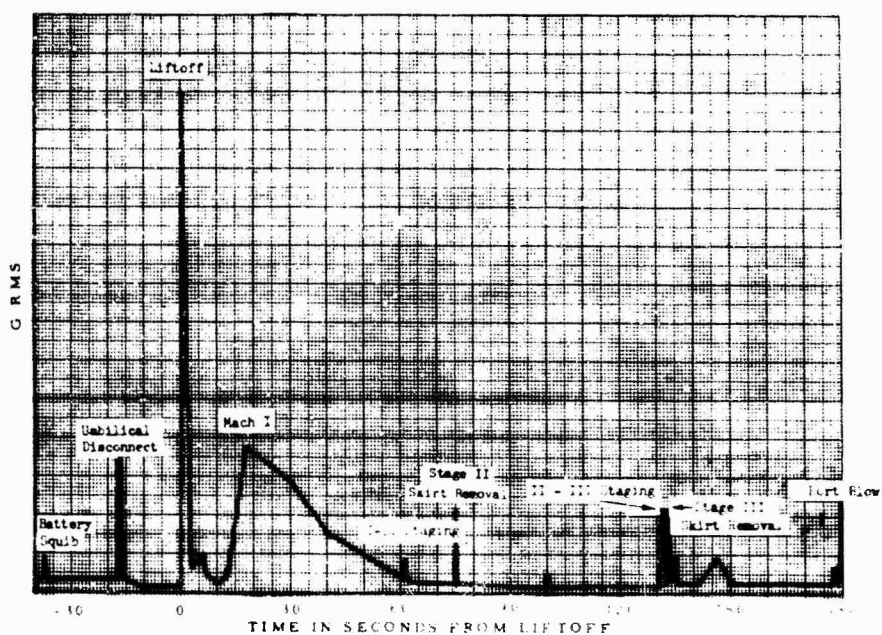


Fig. 19. Summary of rms g vs flight time data for measurement V2M01, G and C section structure

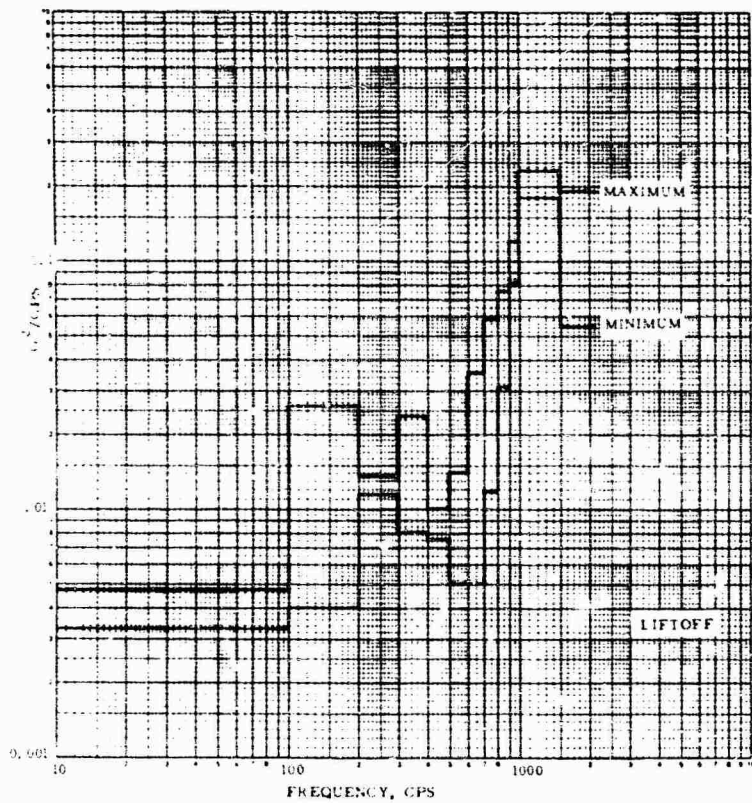


Fig. 20. Broad-band PSD analysis for measurement V2M01, G and C section structure, longitudinal axis

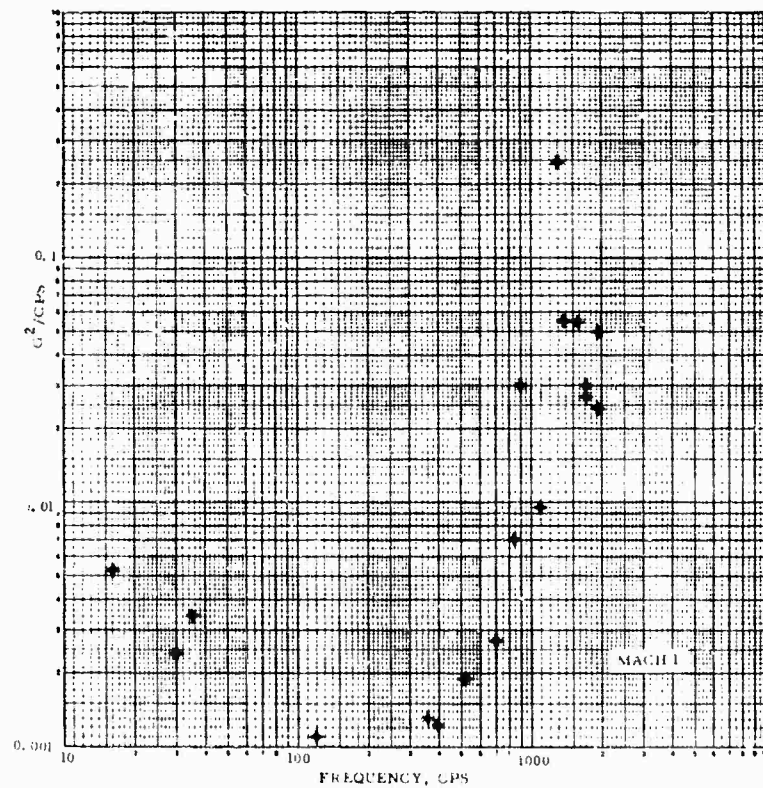


Fig. 21. Narrow-band (6 cps) PSD analysis for measurement V2M01, G and C section structure, longitudinal axis

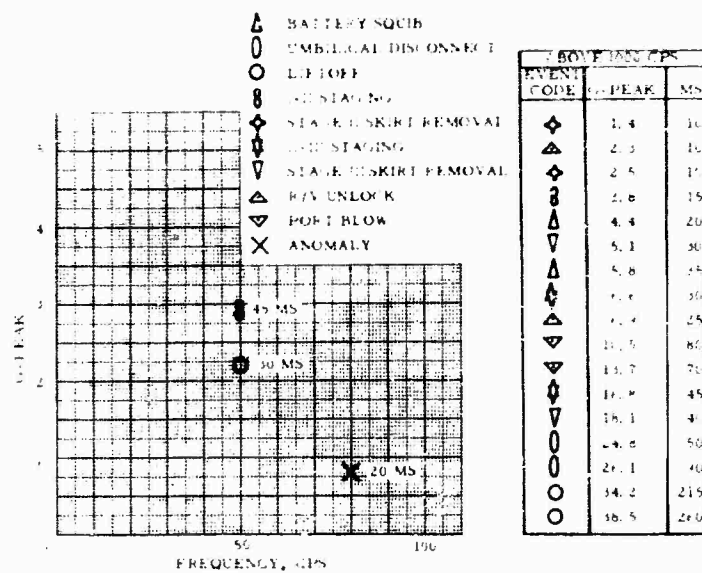


Fig. 22. Summary of decaying sinusoidal shock response data for measurement V2M01, G and C section structure

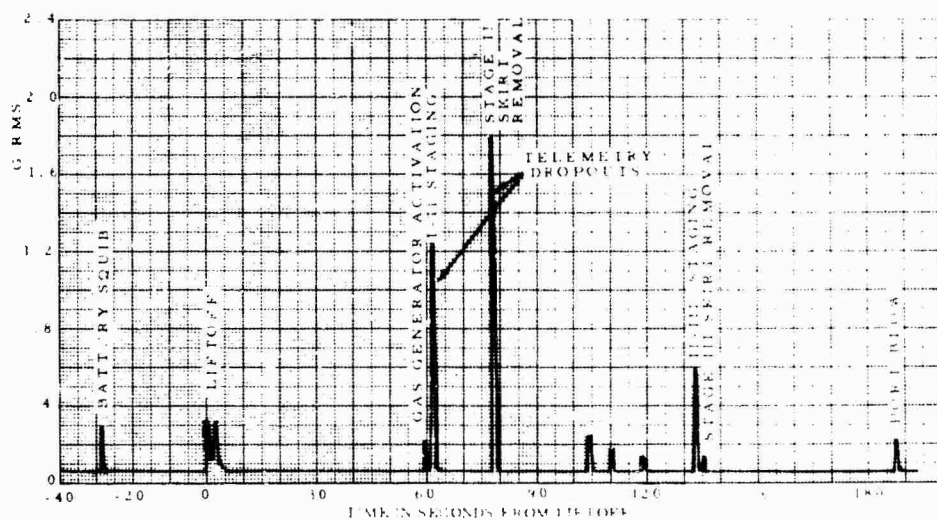


Fig. 23. Rms g vs flight time data for measurement V2P01, IMU stable platform



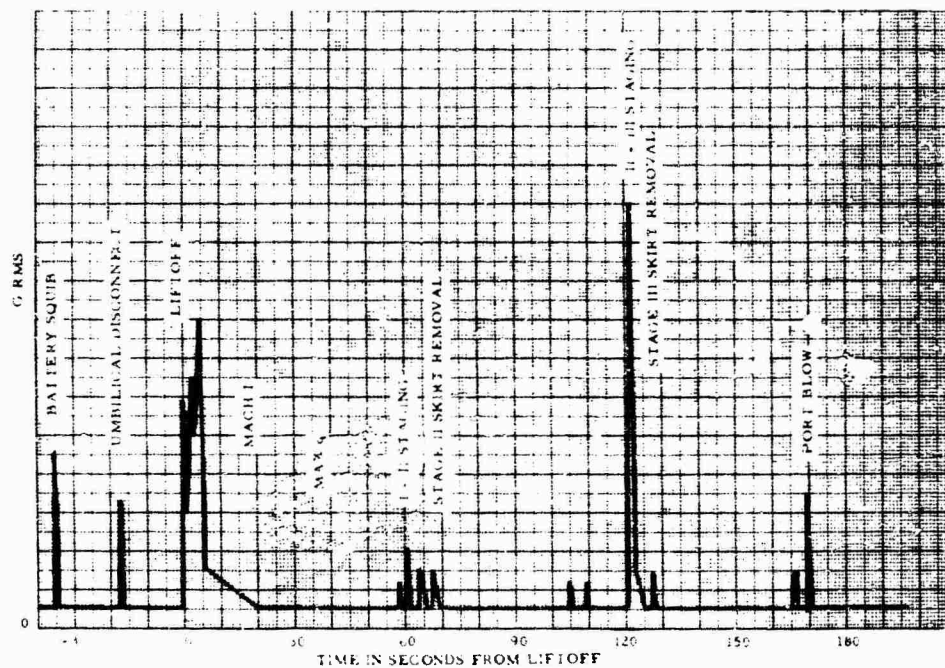


Fig. 24. Rms g vs flight time data for measurement V2P02, IMU stable platform

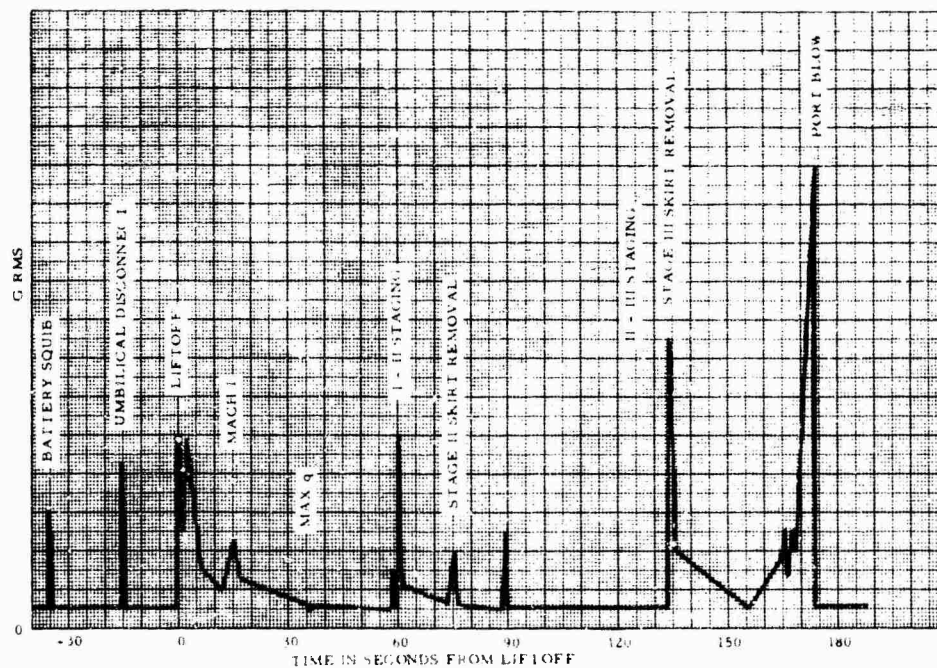


Fig. 25. Rms g vs flight time data for measurement V2P03, IMU stable platform

Fig. 26. Broad-band PSD analysis for measurement V2P01 at liftoff

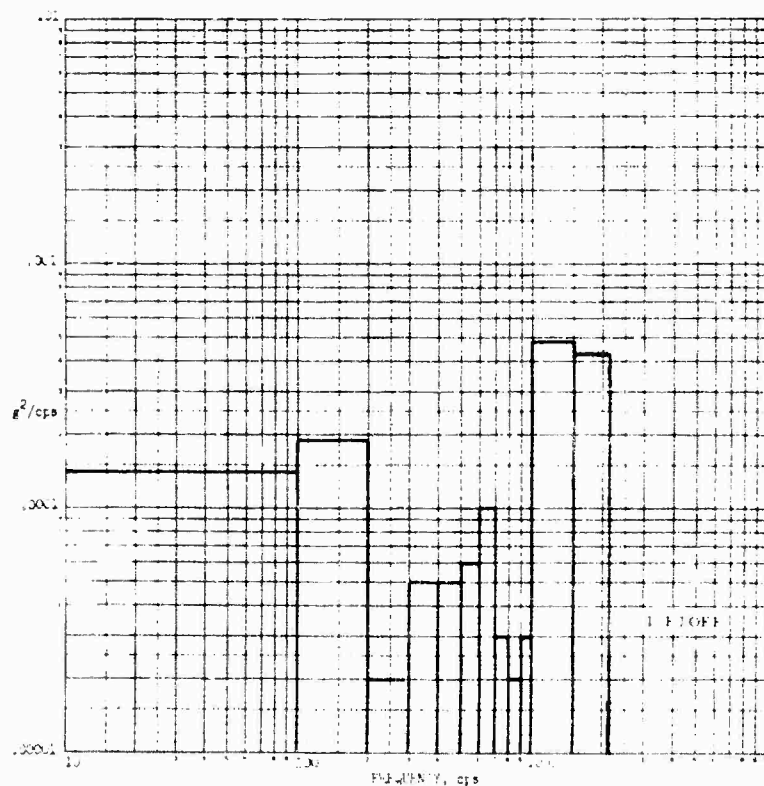
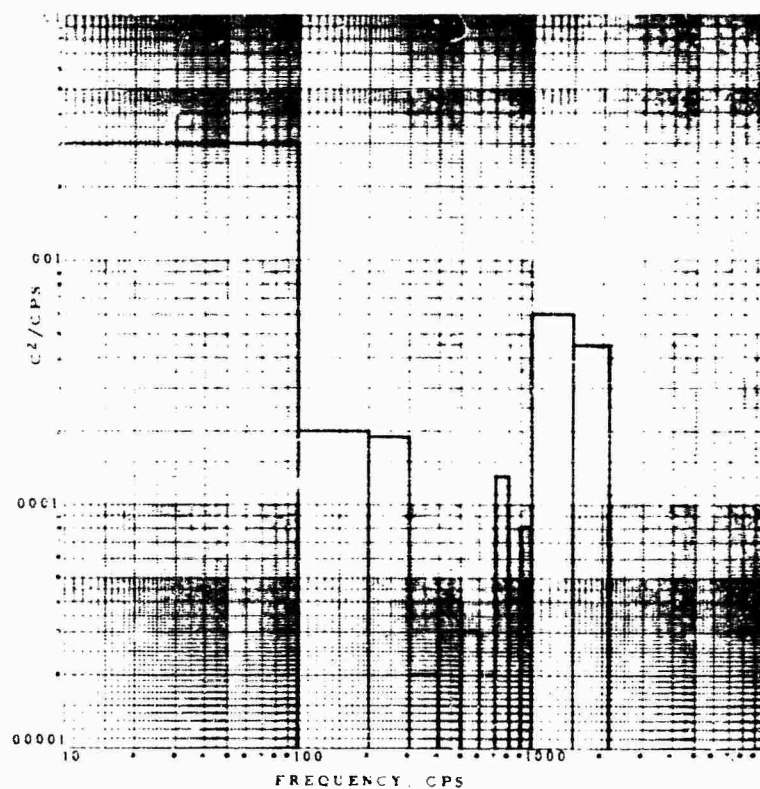


Fig. 27. Broad-band PSD analysis for measurement V2P02, IMU stable platform



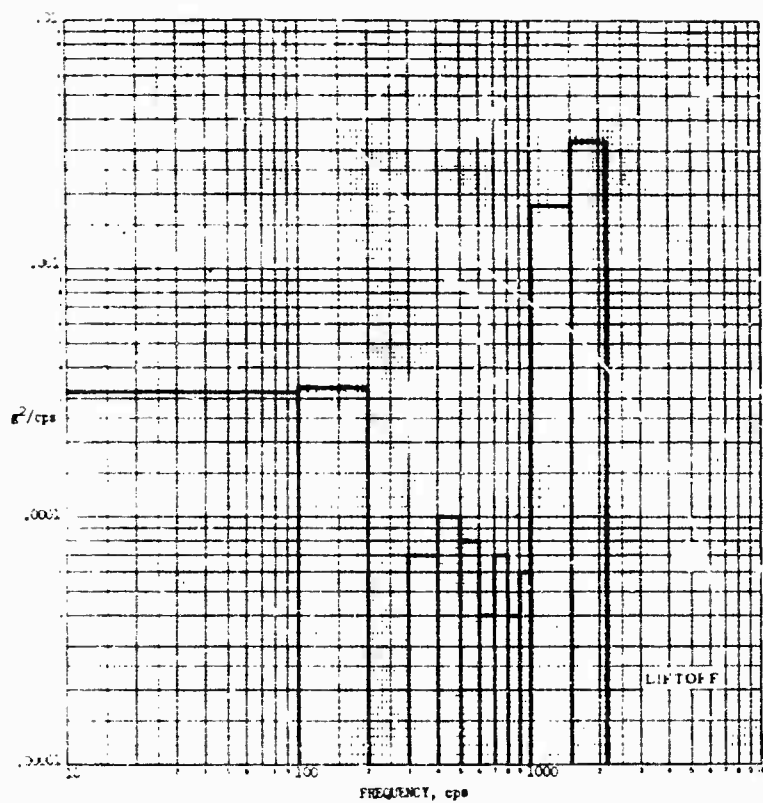
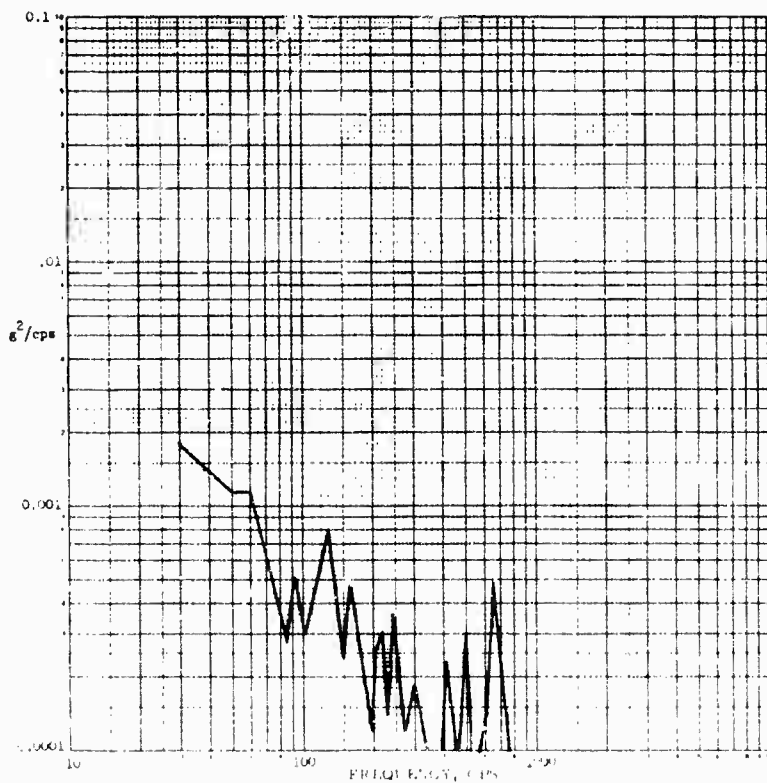


Fig. 28. Broad-band PSD analysis for measurement V2P03, IMU stable platform

Fig. 29. Narrow-band (5 cps) PSD analysis at Mach 1 for FTM 452, measurement V2P02, parallel to the "Y" platform axis mounted on the IMU platform



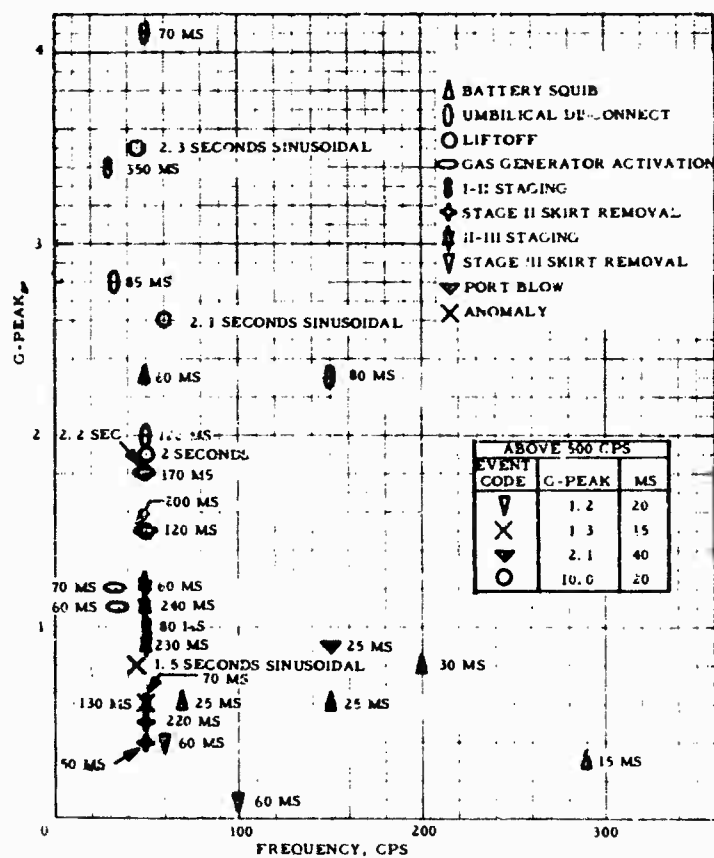


Fig. 30. Summary of decaying sinusoidal shock response data for measurement V2P01, IMU stable platform

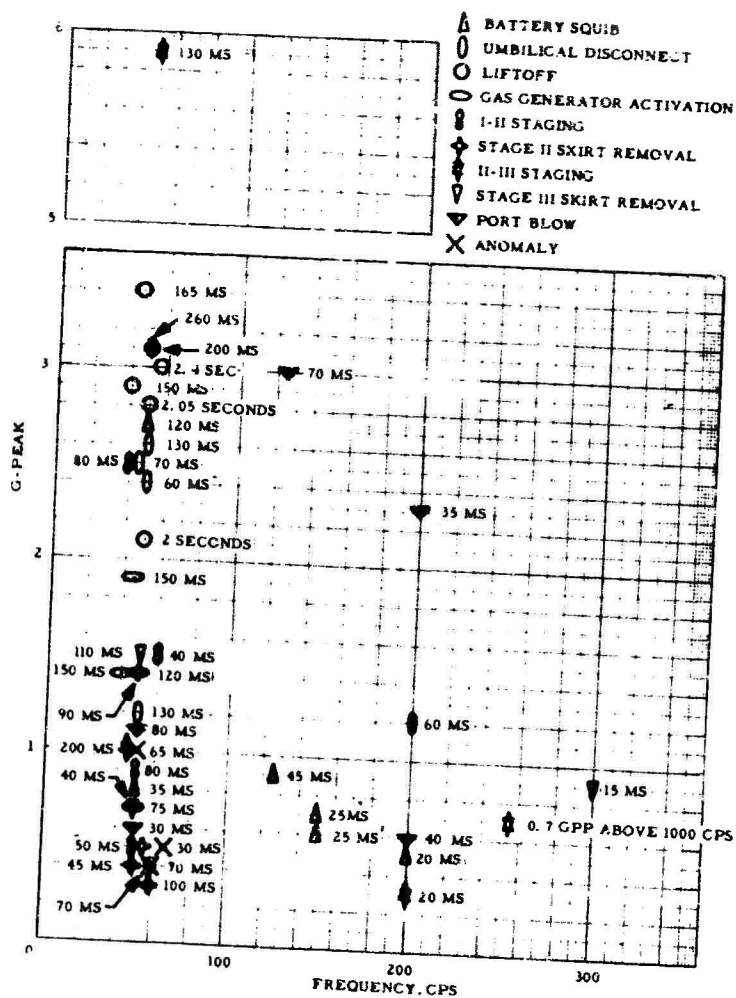


Fig. 31. Summary of decaying sinusoidal shock response data for measurement V2P02, IMU stable platform

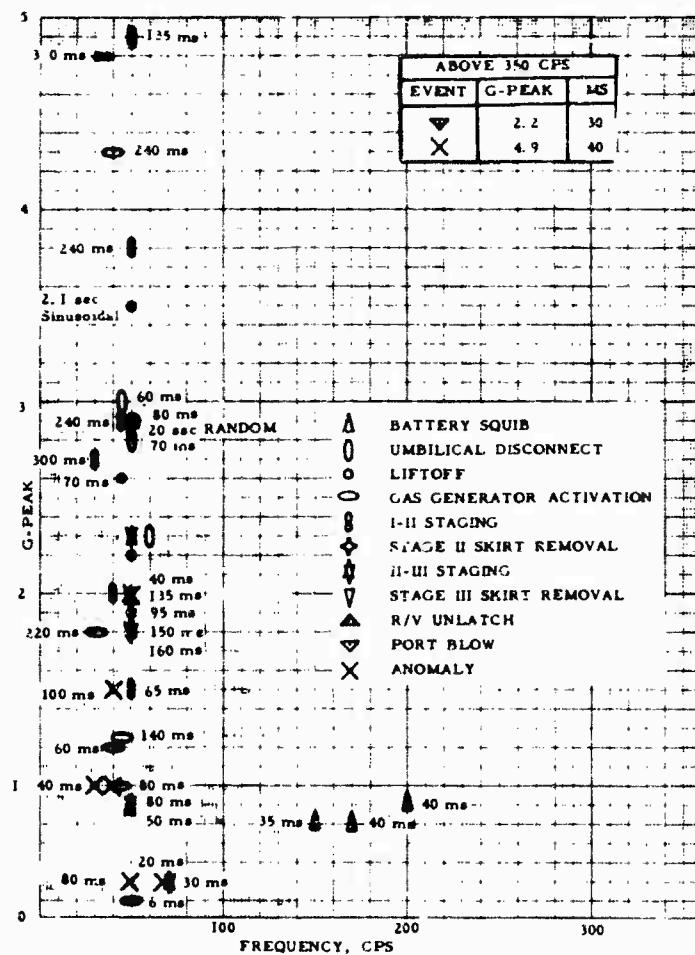


Fig. 32. Summary of decaying sinusoidal shock response data for measurement V2P03, IMU stable platform

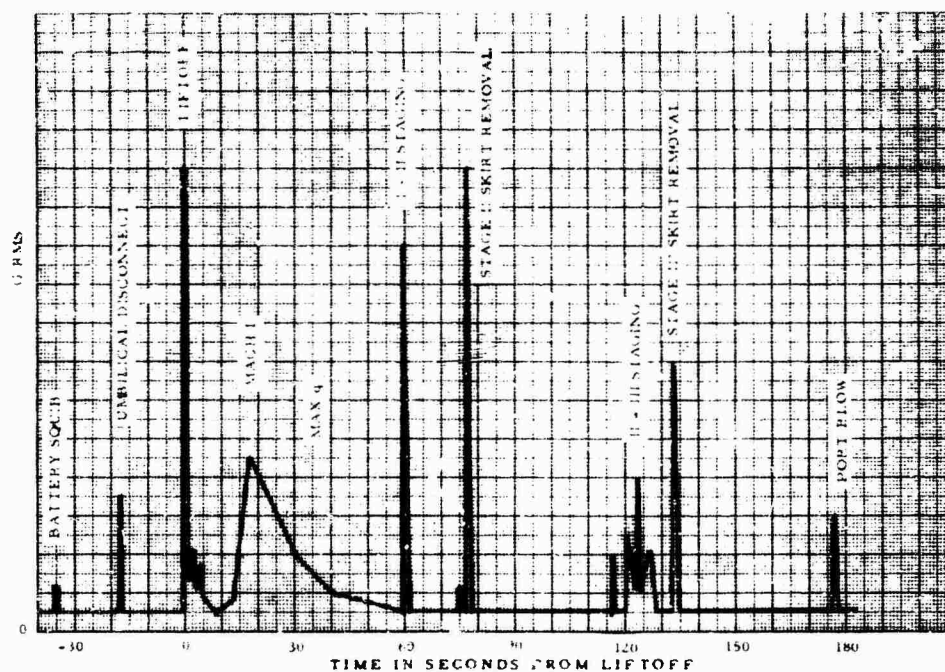


Fig. 33. Rms g vs flight time data for measurement V2P04, IMU support bracket, longitudinal axis

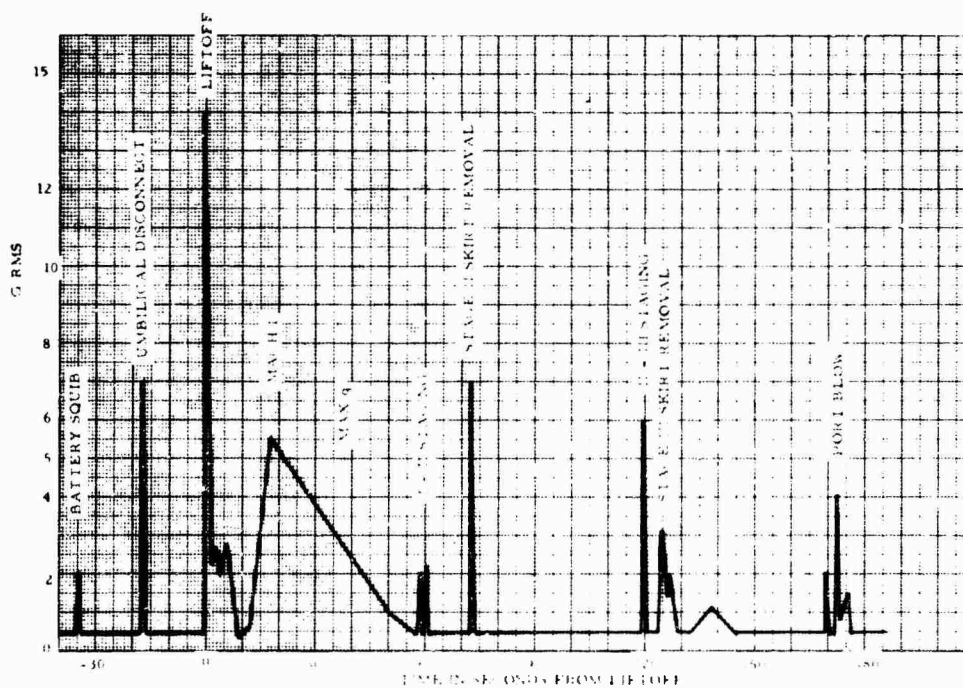


Fig. 34. Rms g vs flight time data for measurement V2P06, IMU support bracket, 90- to 270-deg lateral axis

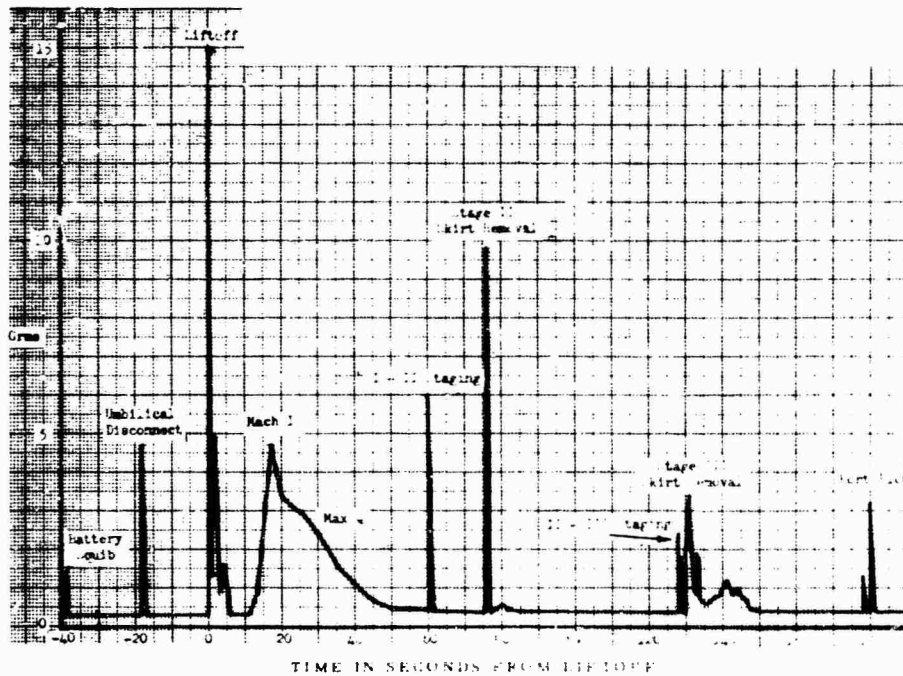


Fig. 35. Rms g vs flight time data for measurement V2P07, IMU support bracket, 0- to 180-deg lateral axis

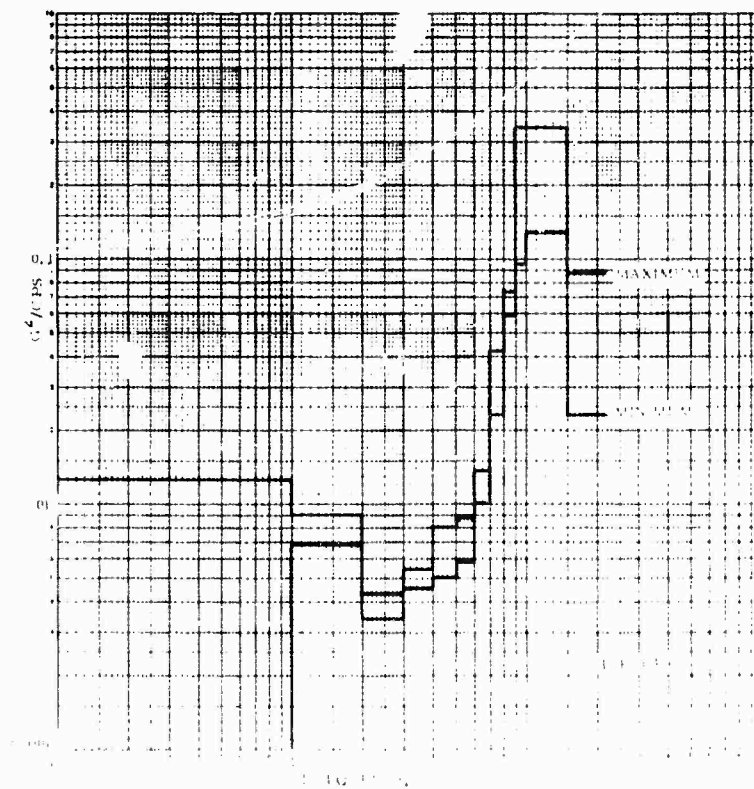


Fig. 36. Broad-band PSD analysis for measurement V2P04, IMU support bracket, longitudinal axis

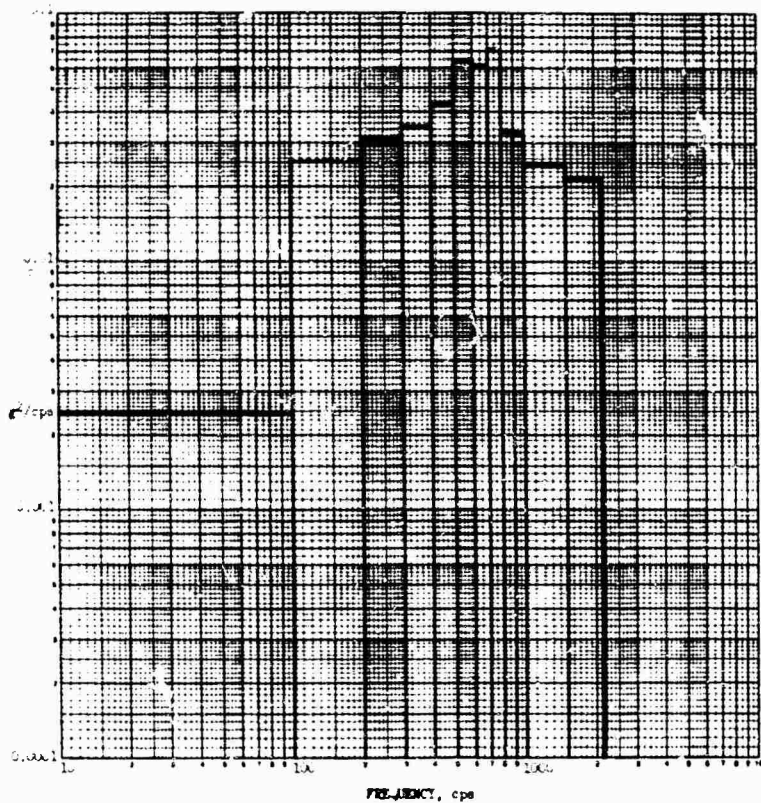


Fig. 37. Broad-band PSD analysis at I-II staging for FTM 461, measurement V2P04

Fig. 38. Broad-band PSD analysis at Stage II skirt removal for FTM 461, measurement V2P04

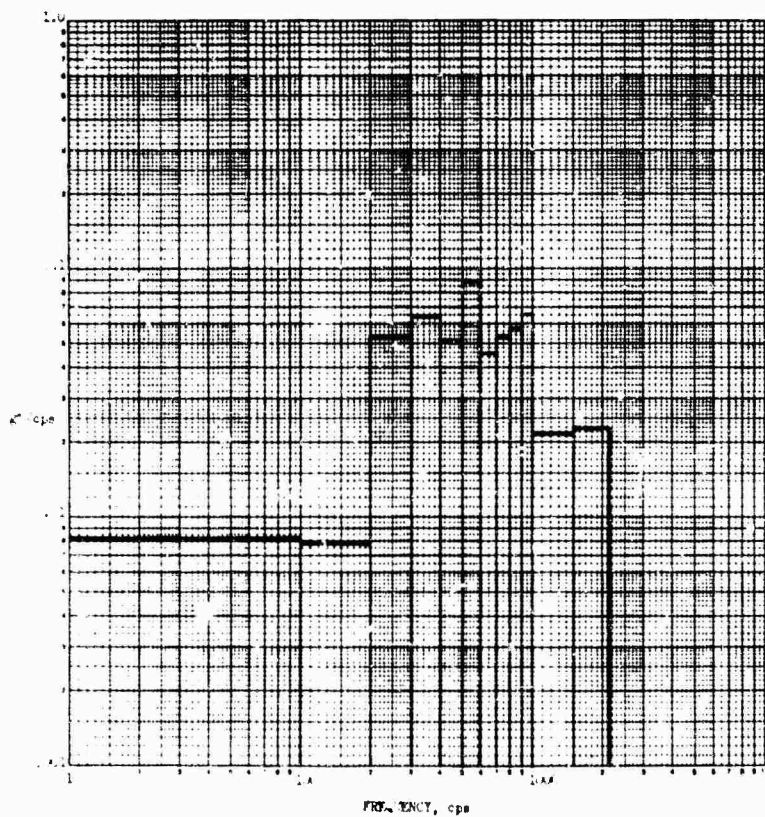




Fig. 39. Broad-band PSD analysis  
at II-III staging for FTM 461,  
measurement V2P04

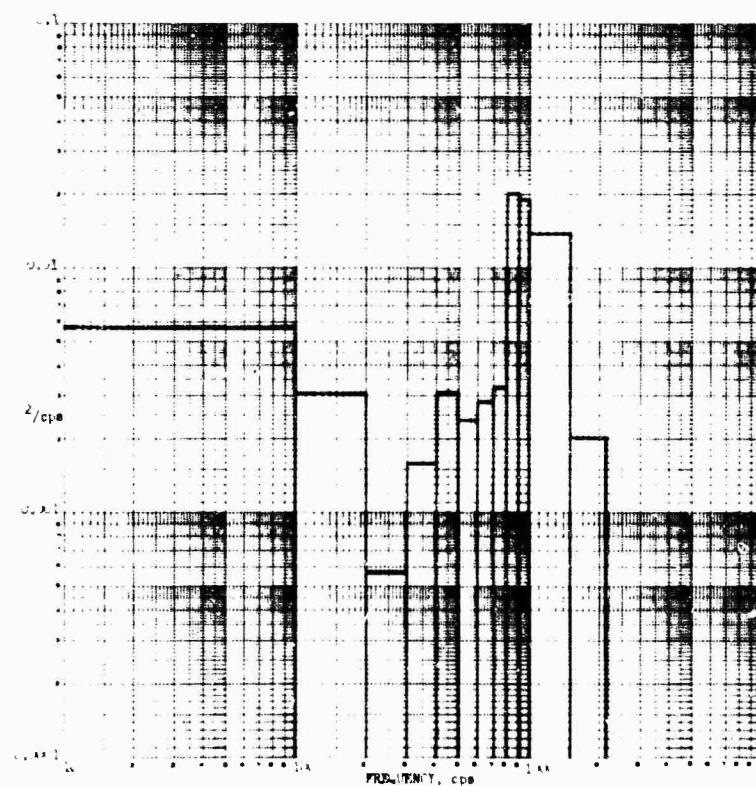
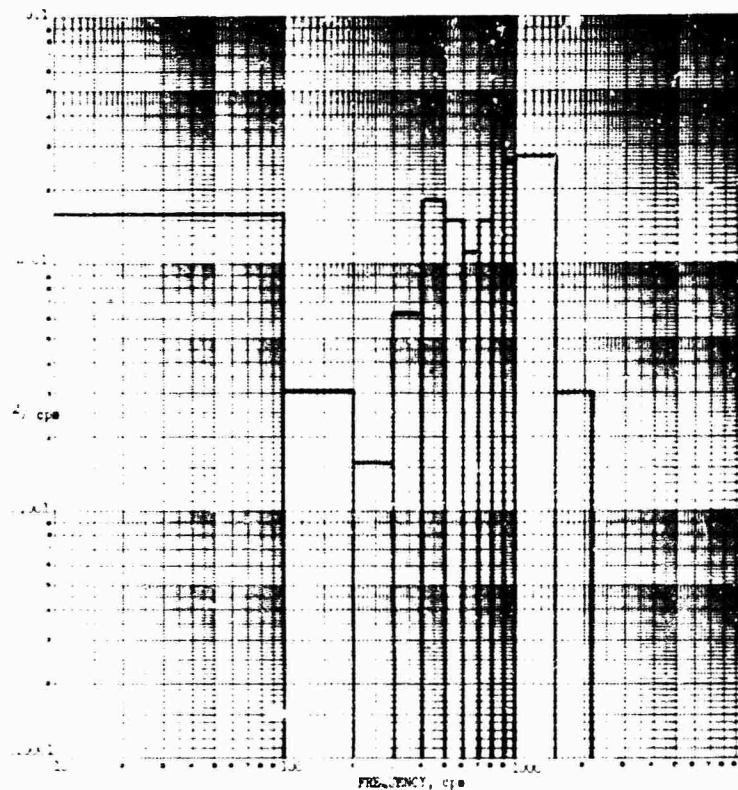


Fig. 40. Broad-band PSD analysis  
at Stage III skirt removal for FTM  
461, measurement V2P04



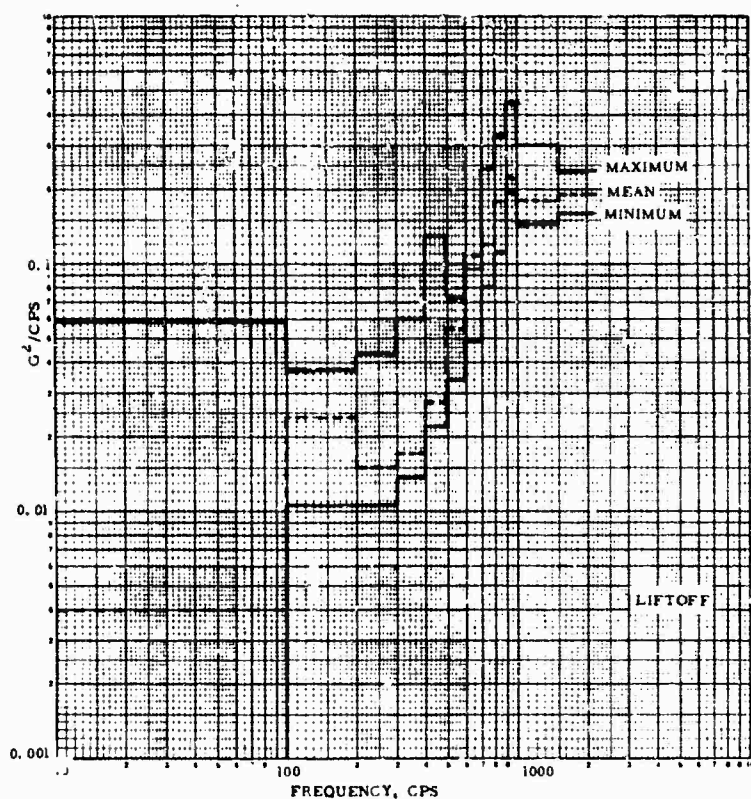


Fig. 41. Broad-band PSD analysis for measurement V2P06, IMU support bracket, 90- to 270-deg lateral axis

Fig. 42. Broad-band PSD analysis for measurement V2P07, IMU support bracket, 0- to 180-deg lateral axis

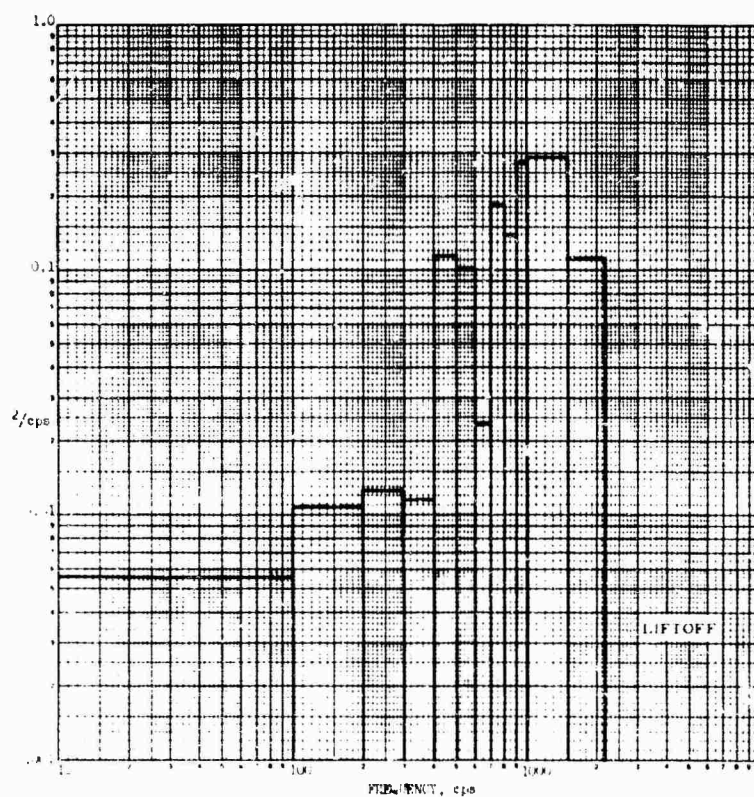


Fig. 43. Narrow-band (6 cps)  
PSD analysis for measurement  
V2P04, IMU support bracket,  
longitudinal axis

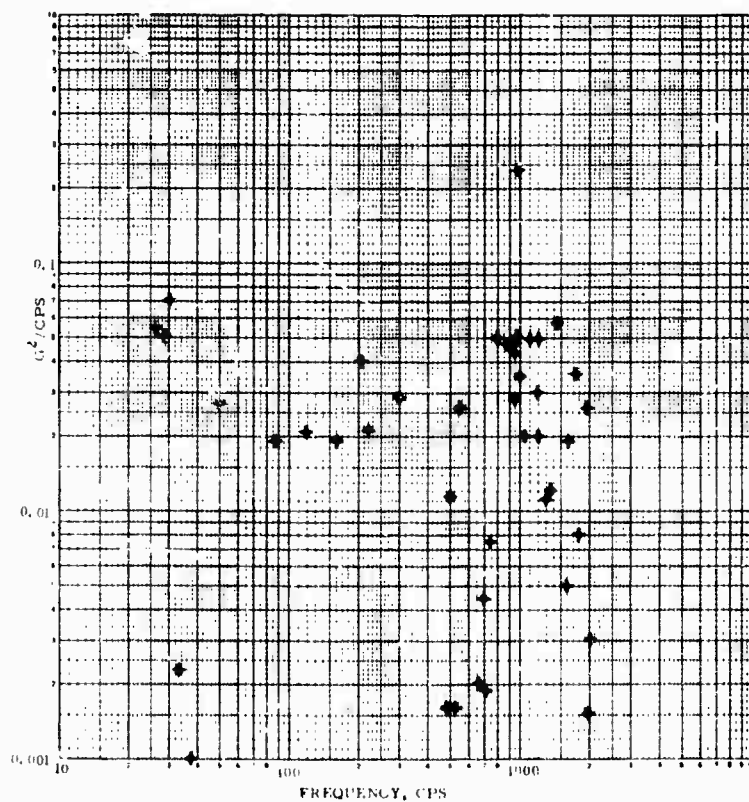
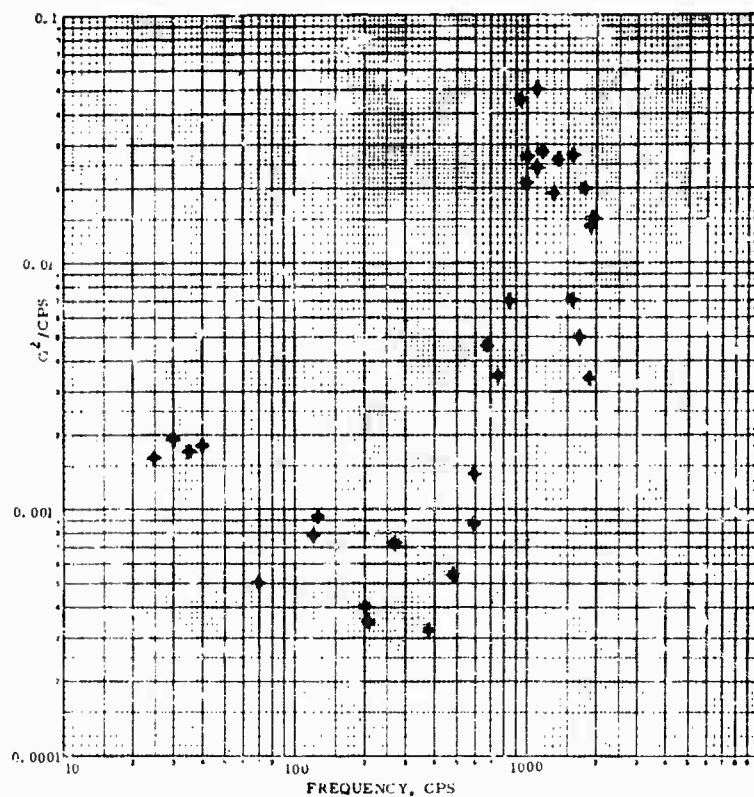


Fig. 44. Narrow-band (6 cps)  
PSD analysis for measurement  
V2P06, IMU support bracket,  
90- to 270-deg lateral axis

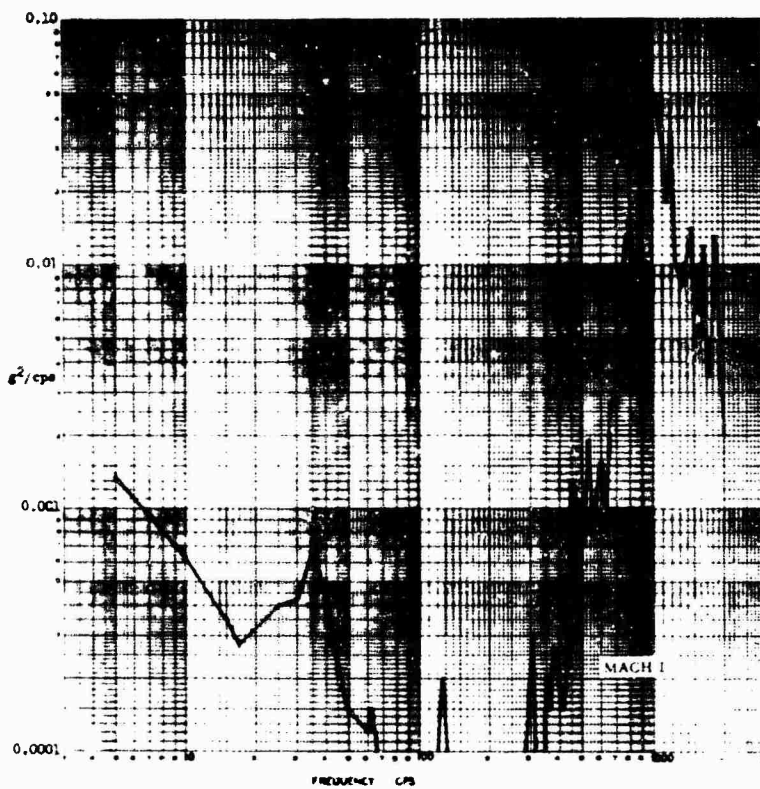
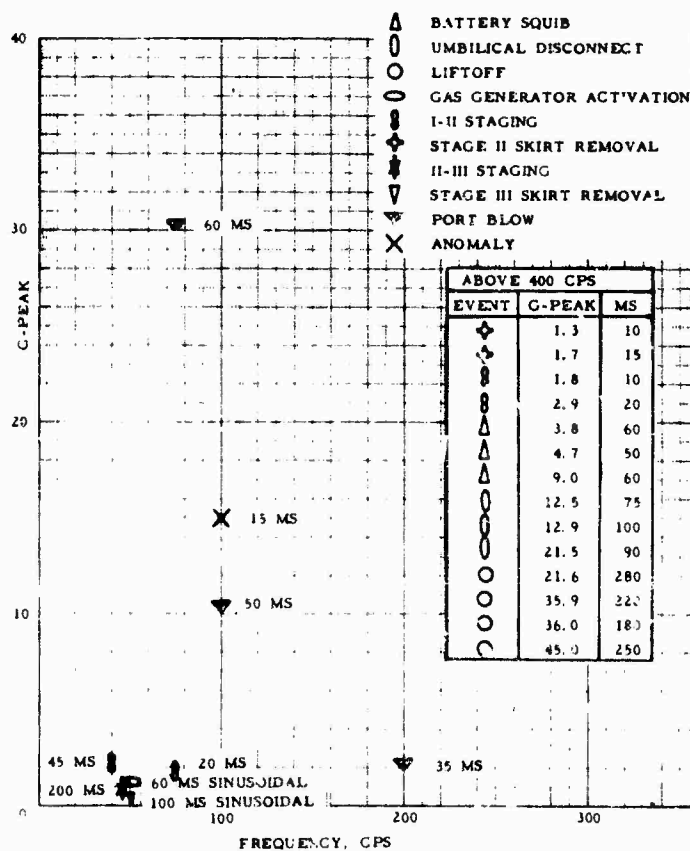


Fig. 45. Narrow-band (6 cps) PSD analysis for measurement V2P07, IMU support bracket, 0- to 180-deg lateral axis

Fig. 46. Summary of decaying sinusoidal shock response data for measurement V2P04, G and C IMU support bracket cap, longitudinal axis



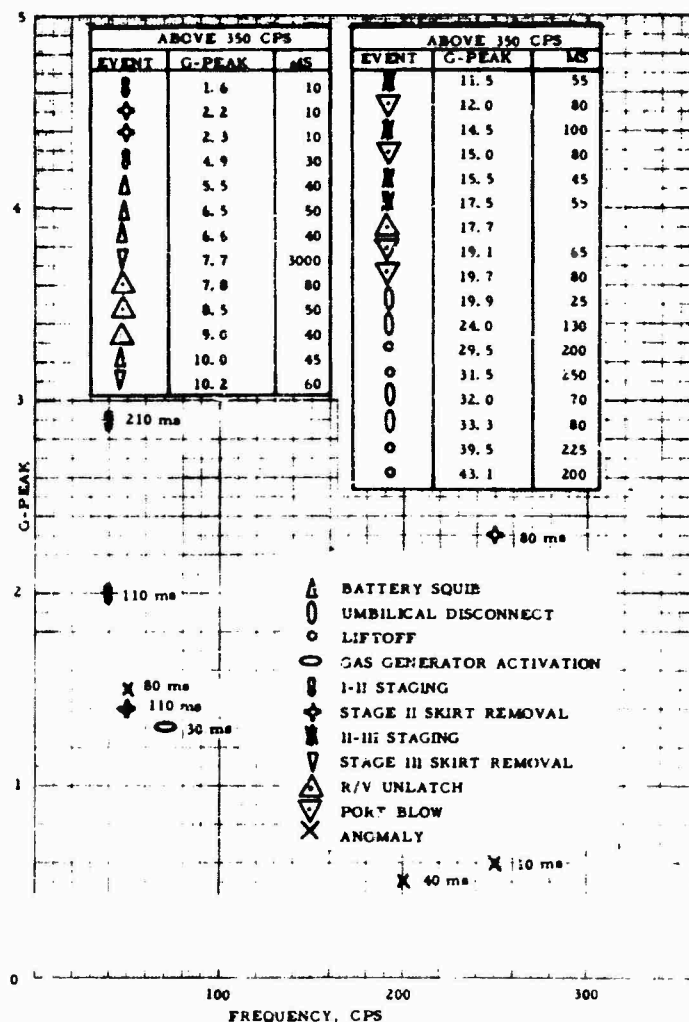


Fig. 47. Summary of decaying sinusoidal shock response, data for measurement V2P06, G and C IMU support bracket cap, 90- to 270-deg lateral axis

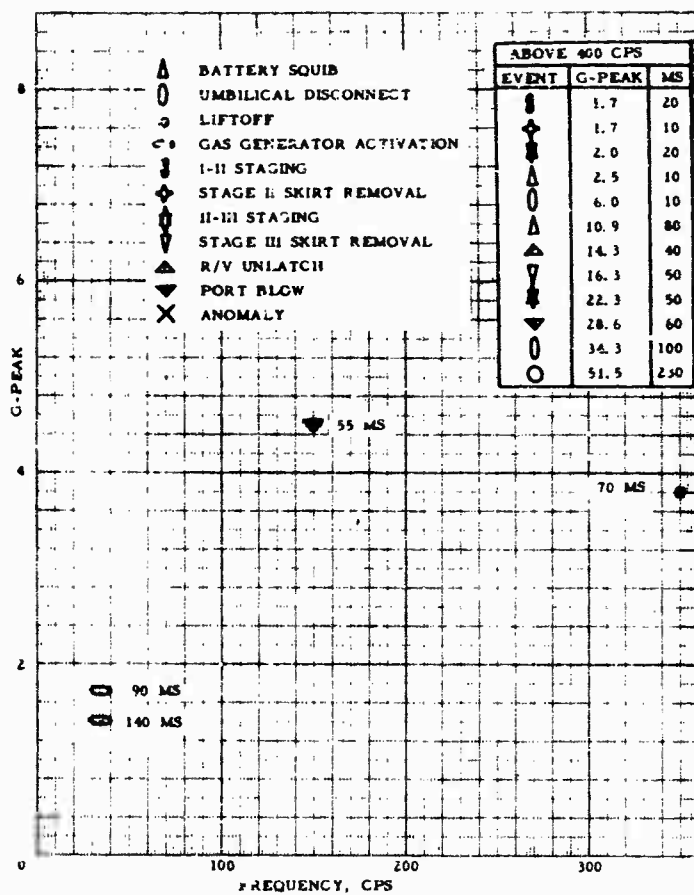


Fig. 48. Summary of decaying sinusoidal shock response data for measurement V2P07, G and C IMU support bracket cap, 0- to 180-deg lateral axis

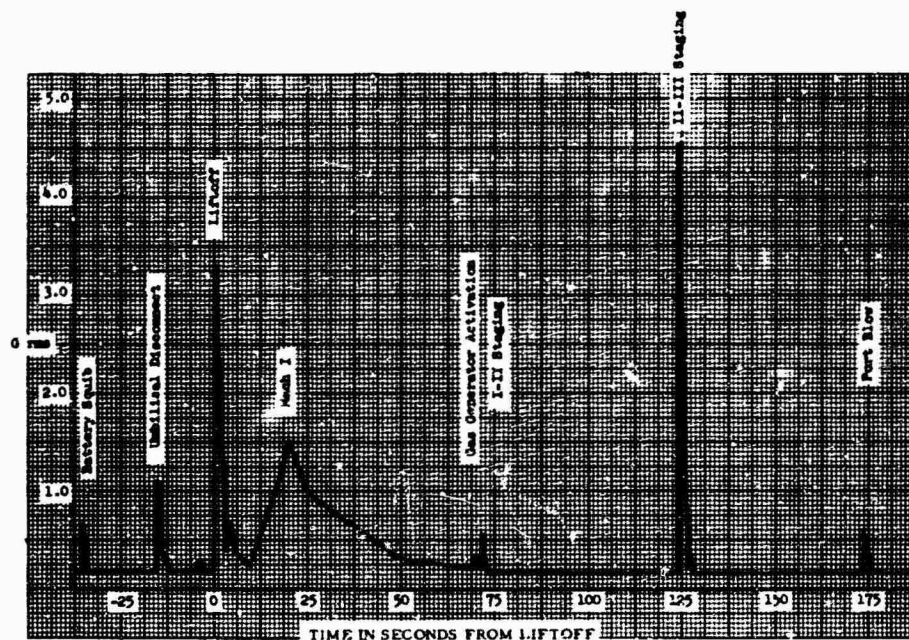


Fig. 49. Rms g vs flight time data for measurement V2P05, IMU base, 90- to 270-deg lateral axis

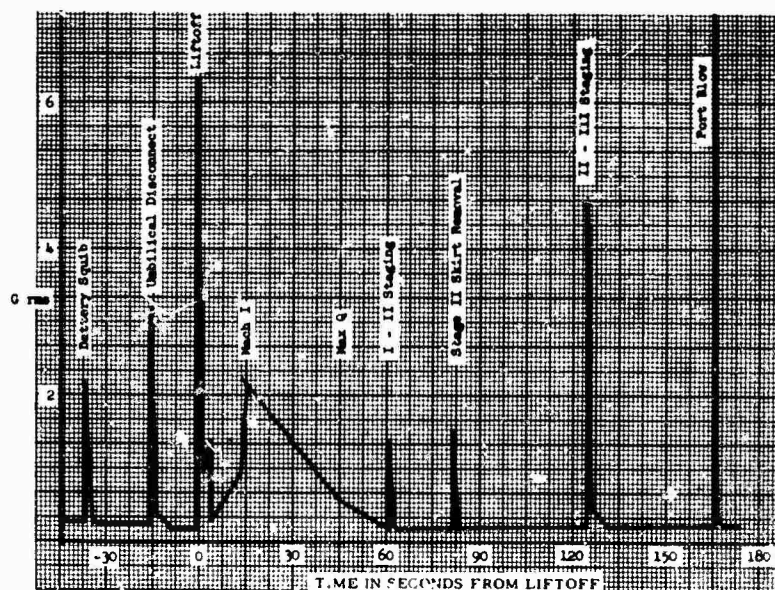


Fig. 50. Rms g vs flight time data for measurement V2P08, IMU base, 0- to 180-deg lateral axis

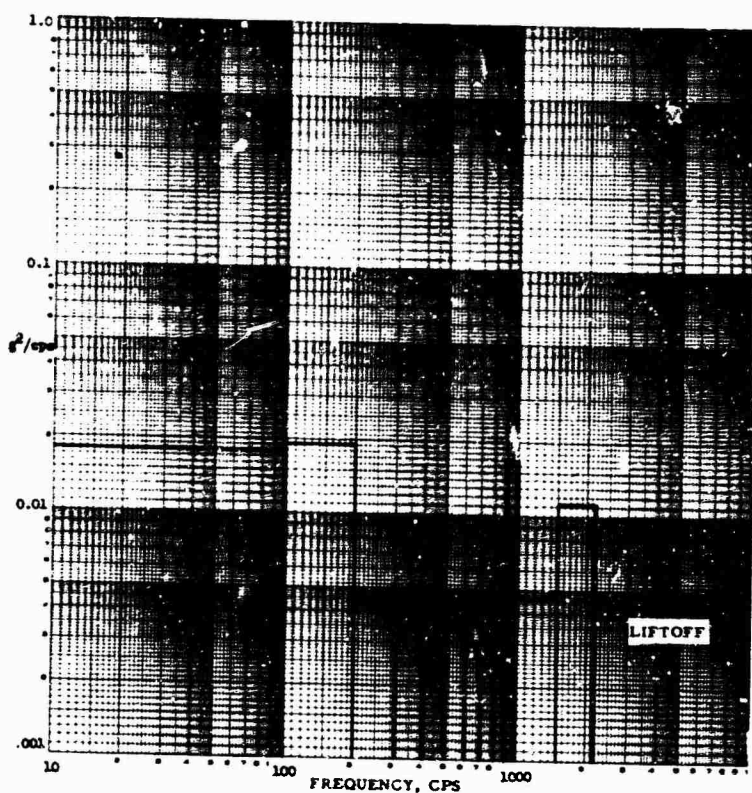


Fig. 51. Broad-band PSD analysis for measurement V2P05, IMU base, 90- to 270-deg lateral axis

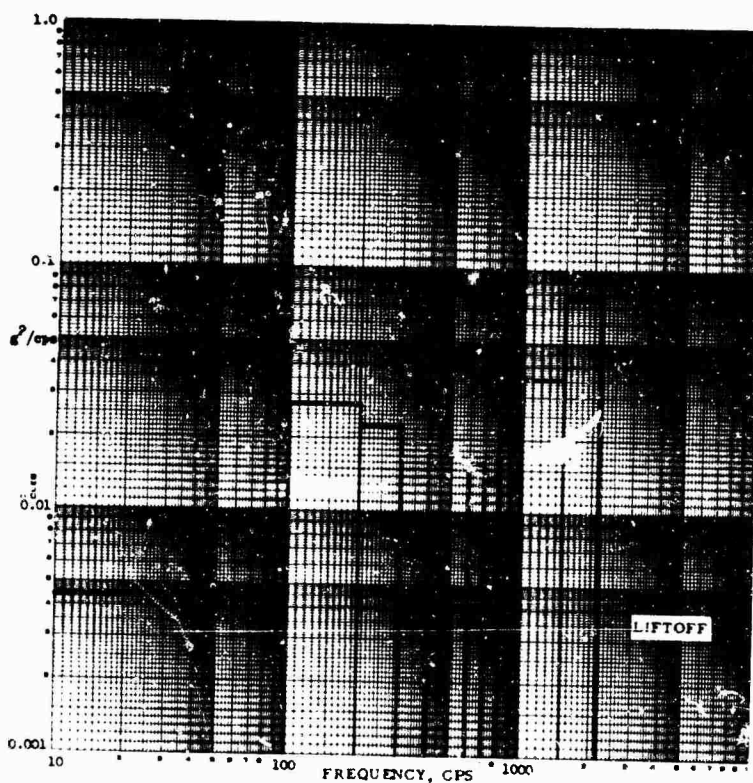


Fig. 52. Broad-band PSD analysis for measurement V2P08, IMU base, 0- to 180-deg lateral axis



Fig. 53. Narrow-band (6 cps) PSD analysis for measurement V2P05, IMU base, 90- to 270-deg lateral axis

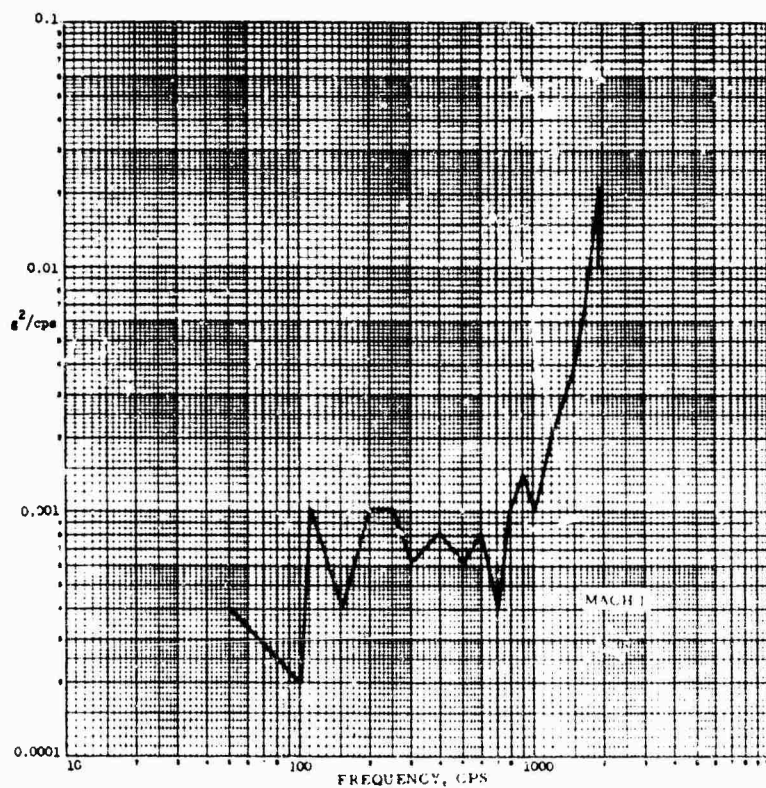
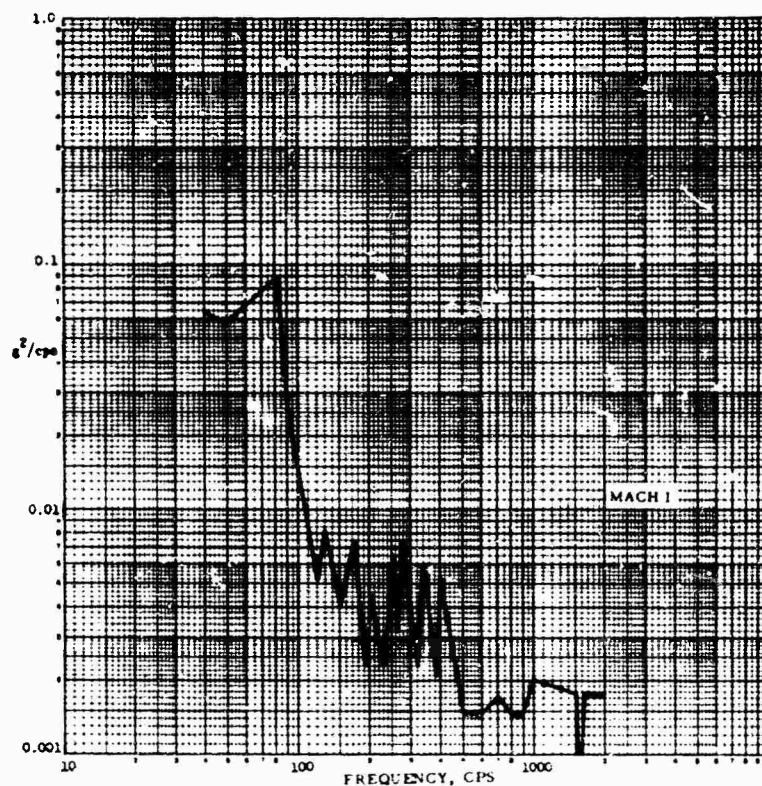


Fig. 54. Narrow-band (6 cps) PSD analysis for measurement V2P08, IMU base, 0- to 180-deg lateral axis



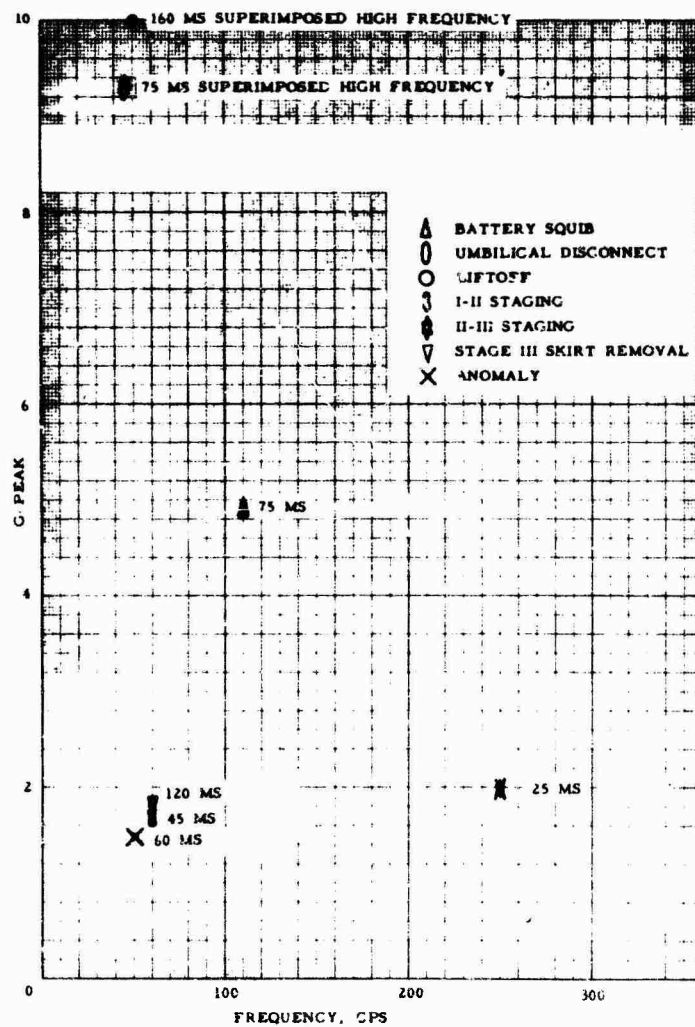


Fig. 55. Summary of decaying sinusoidal shock response data for measurement V2P05, IMU base, external surface, 90- to 270-deg lateral axis

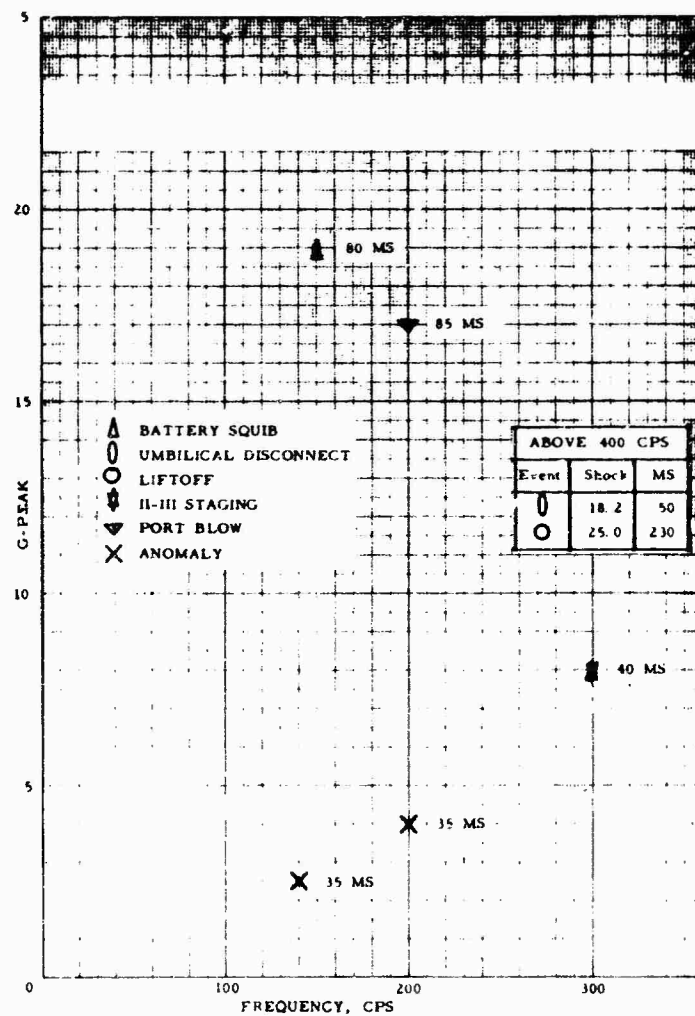


Fig. 56. Summary of decaying sinusoidal shock response data for measurement V2P08, IMU base, external surface, 0- to 180-deg lateral axis

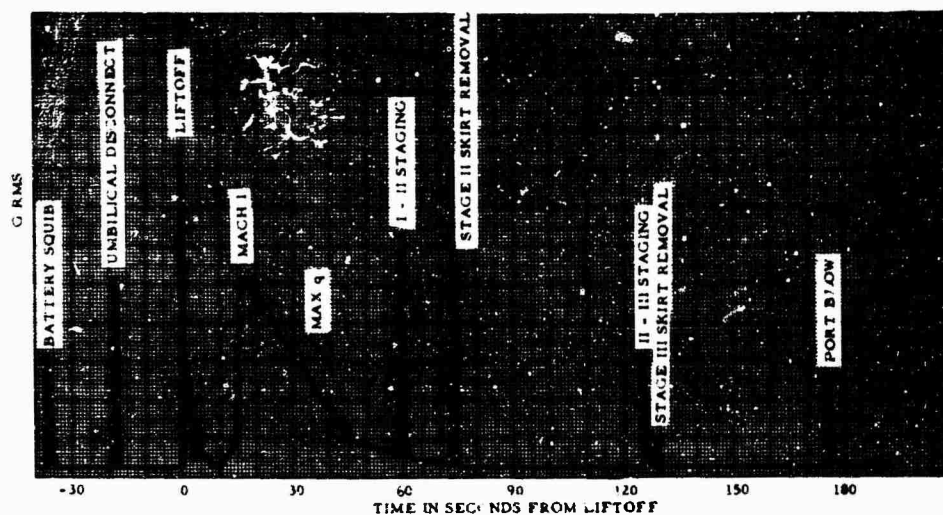


Fig. 57. Rms g vs flight time data for measurement V2U01, base of P92, 0- to 180-deg lateral axis

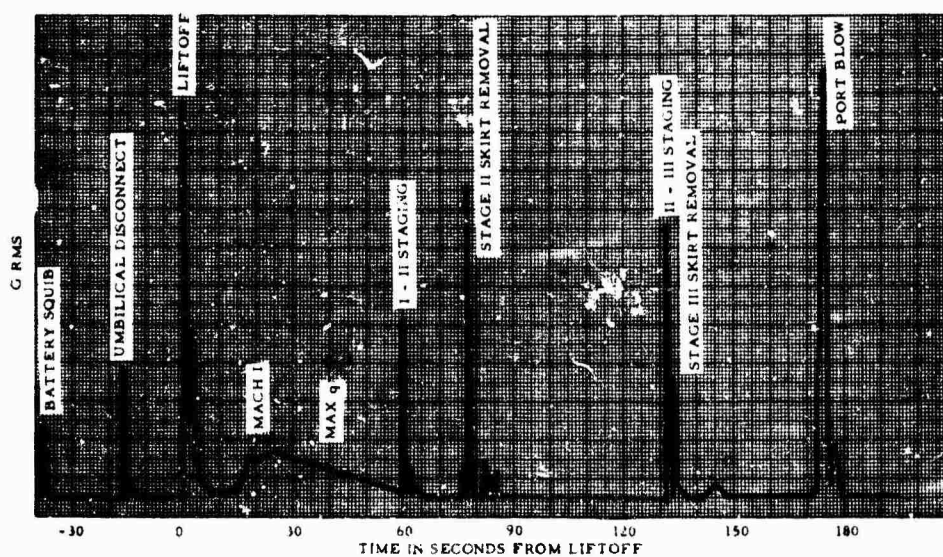


Fig. 58. Rms g vs flight time data for measurement V2U02, base of P92, longitudinal axis

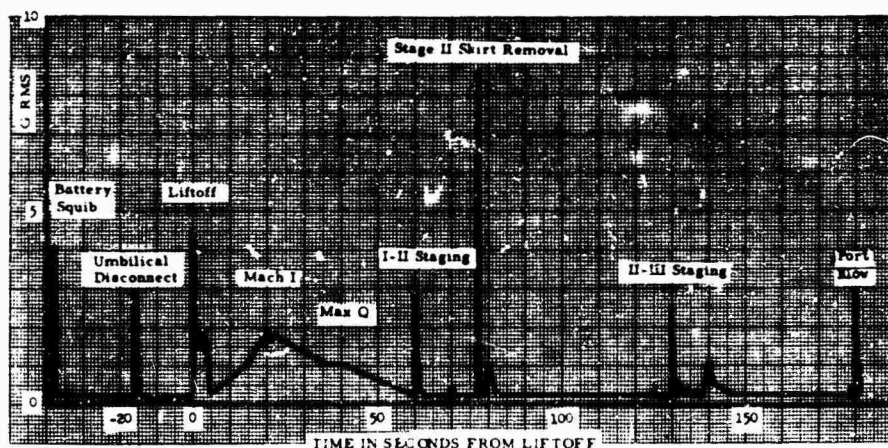


Fig. 59. Rms g vs flight time data for measurement V2U03, base of P92, 90- to 270-deg lateral axis

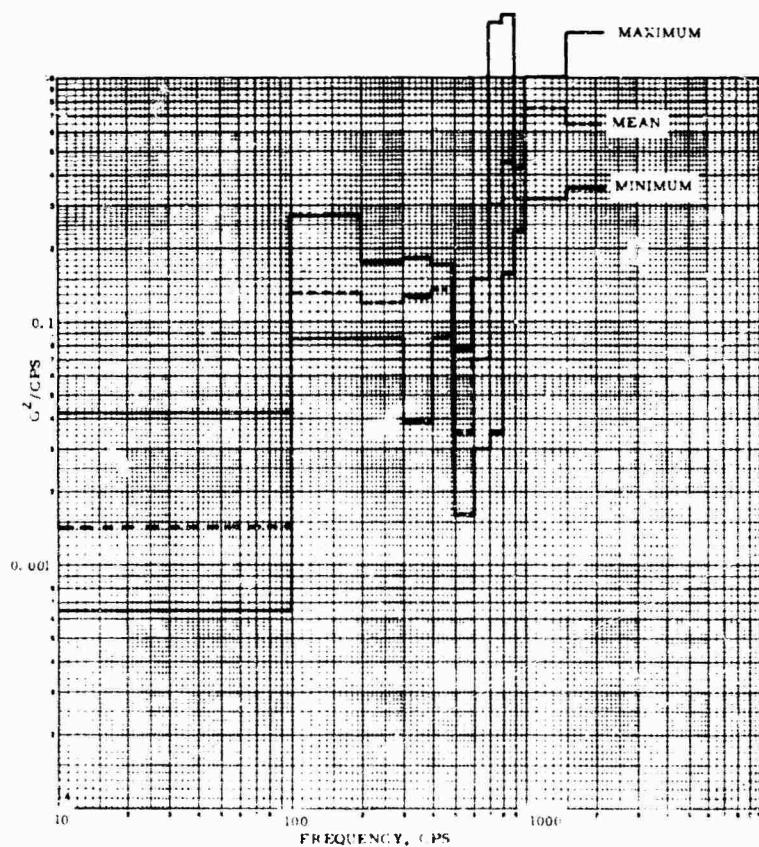


Fig. 60. Broad-band PSD analysis for measurement V2U01, base of P92, 0- to 180-deg lateral axis

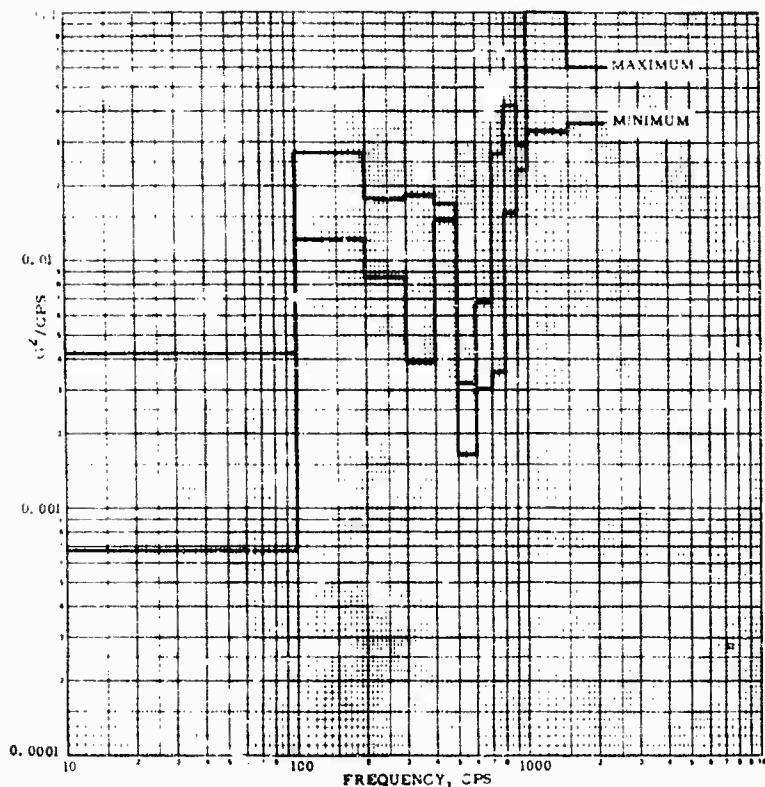


Fig. 61. Broad-band PSD analysis for measurement V2U02, base of P92, longitudinal axis

Fig. 62. Broad-band PSD analysis at umbilical disconnect for FTM 462, measurement V2U02

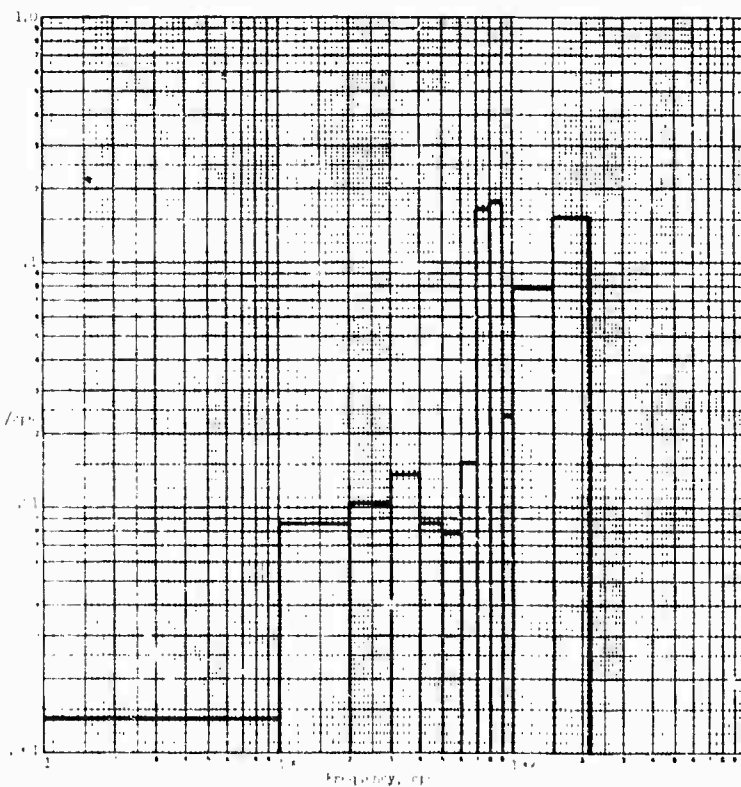


Fig. 63 Broad-band PSD analysis for measurement V2U03, base of P92, 90- to 270-deg lateral axis

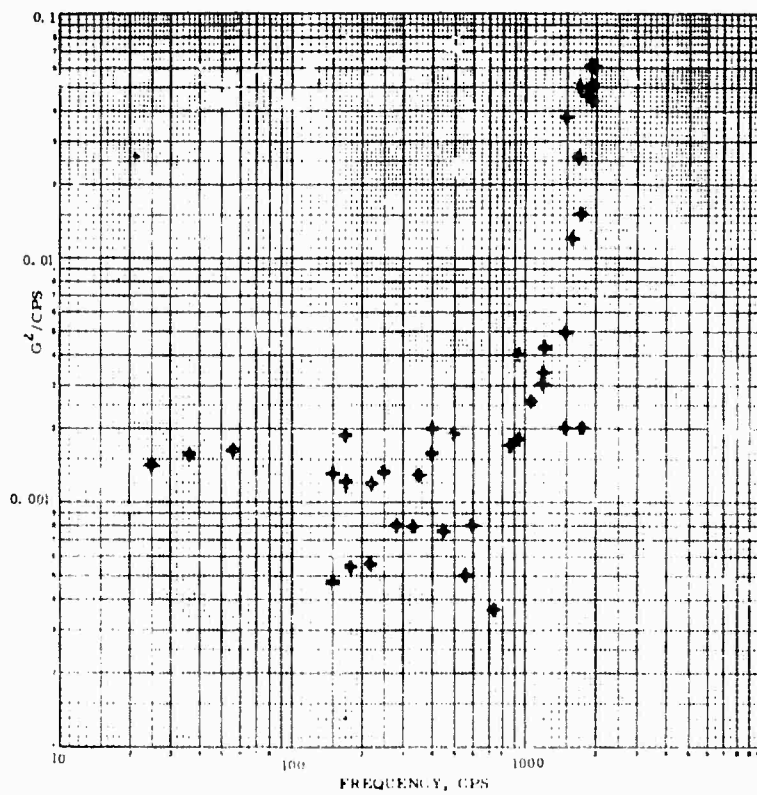
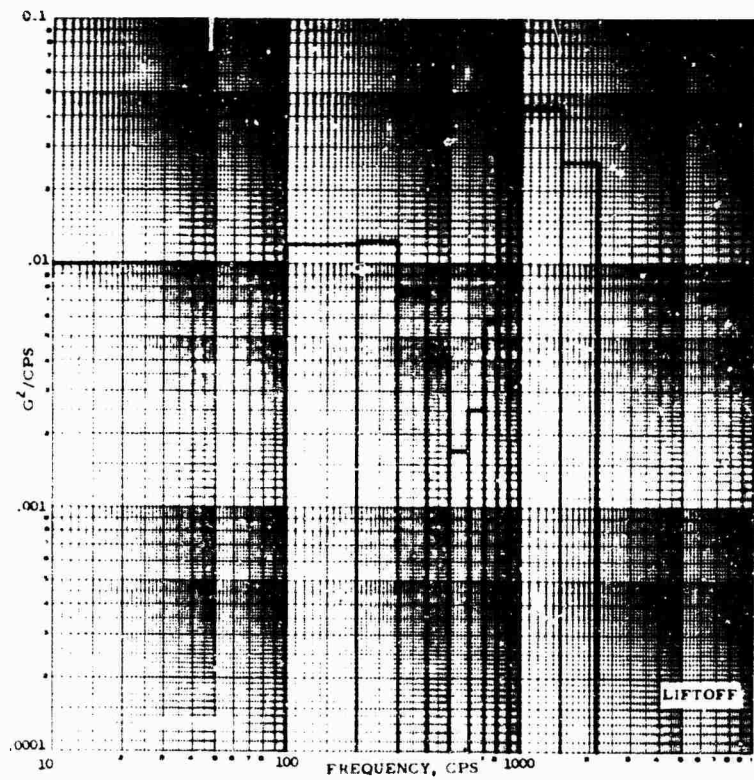


Fig. 64. Narrow-band (6 cps) PSD analysis for measurement V2U01, base of P92, 0- to 180-deg lateral axis



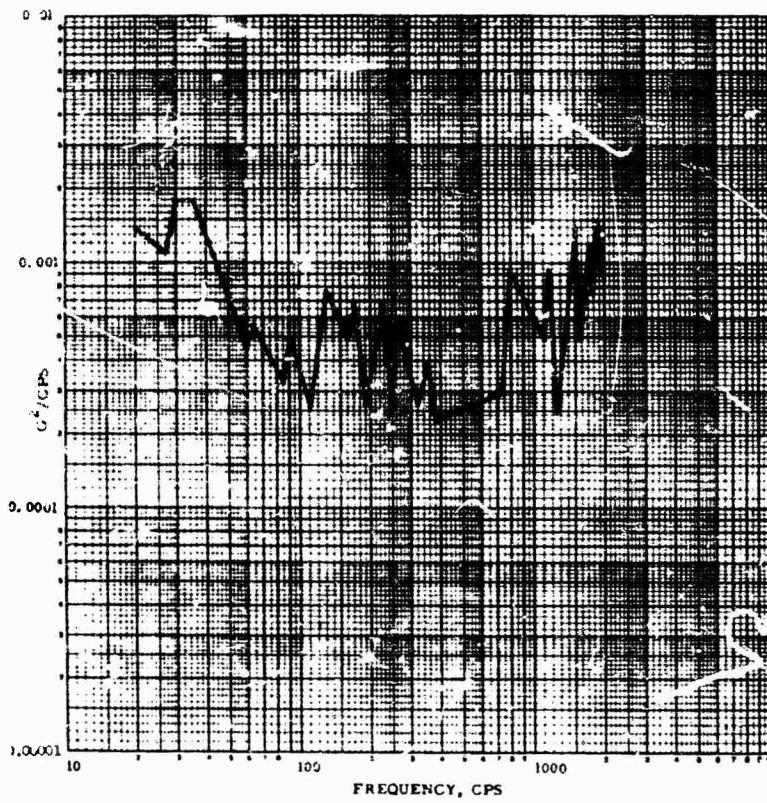


Fig. 65. Narrow-band (6 cps) PSD analysis for measurement V2U02, base of P92, longitudinal axis

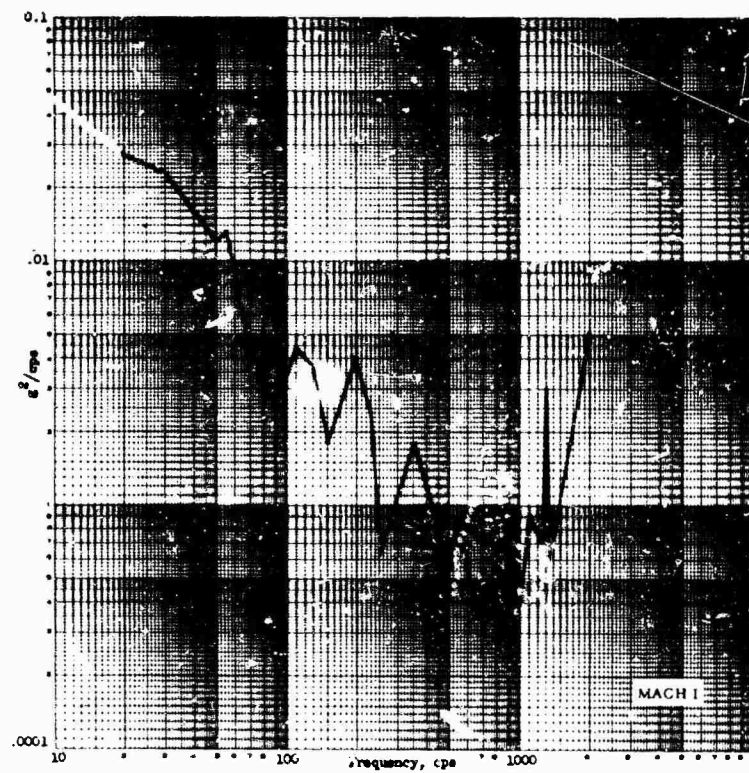


Fig. 66 Narrow-band (6 cps) PSD analysis for measurement V2U03, base of P92, 90- to 270-deg lateral axis

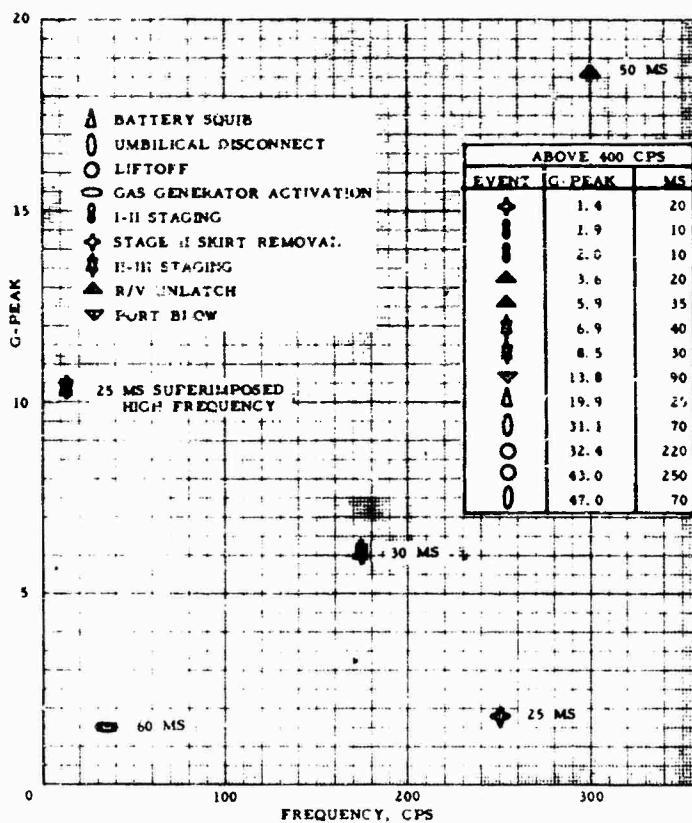


Fig. 67. Summary of decaying sinusoidal shock response data for measurement V2U01, IMU stable platform



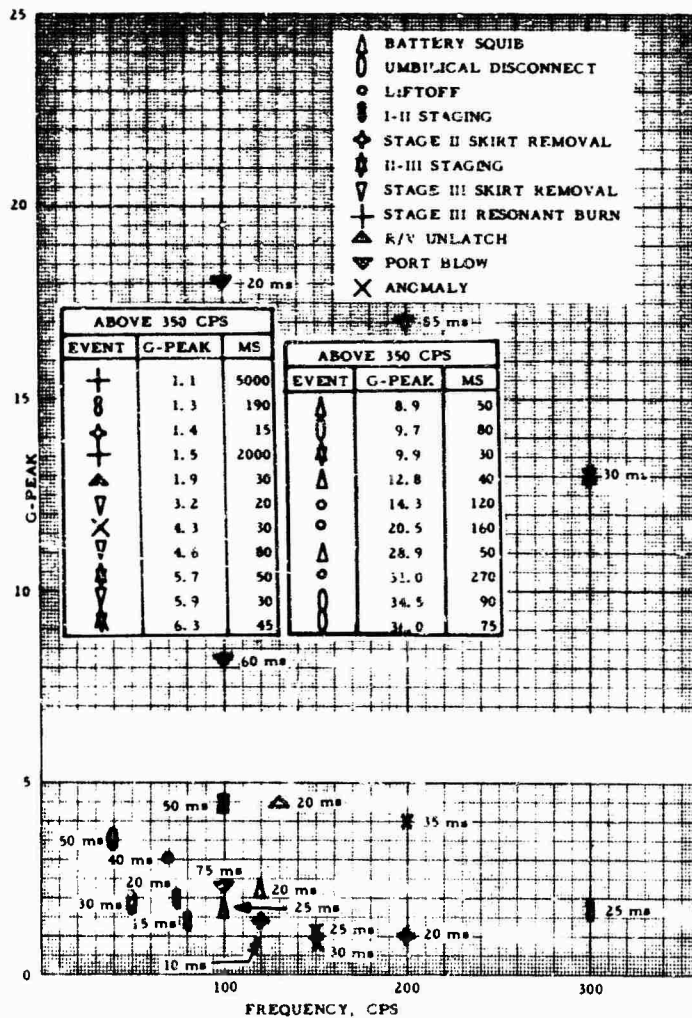


Fig. 68. Summary of decaying sinusoidal shock response data for measurement V2U02, IMU stable platform

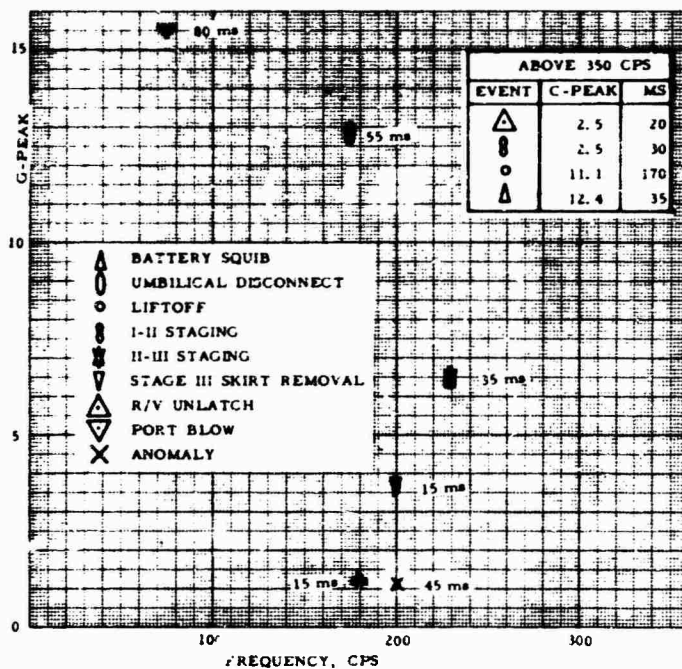


Fig. 69. Summary of decaying sinusoidal shock response data for measurement V2U03, IMU stable platform

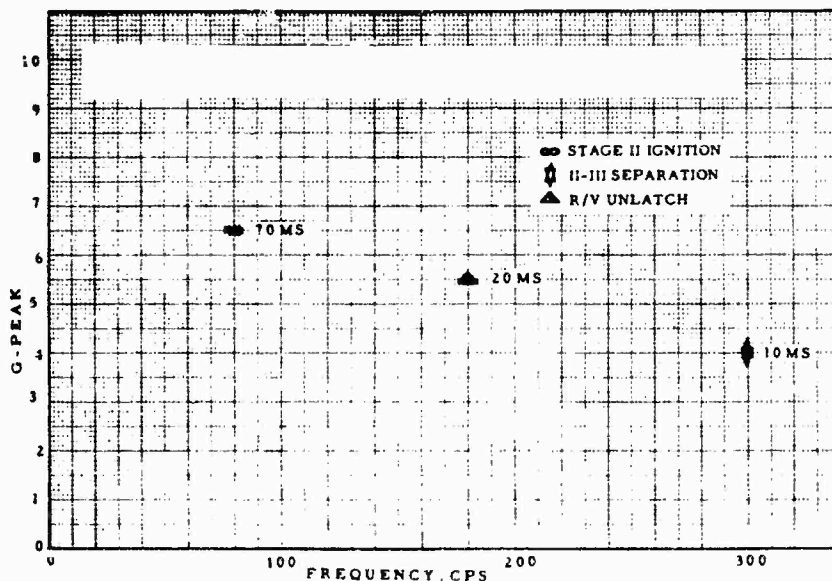


Fig. 70. Summary of decaying sinusoidal shock response data for measurement V4U01, Stage III NCU

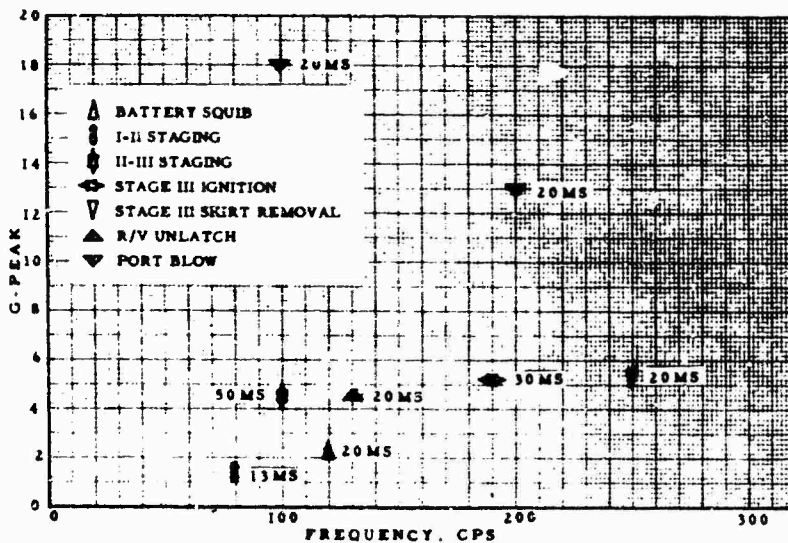


Fig. 71. Summary of decaying sinusoidal shock response data for measurement V4U02, Stage III NCU

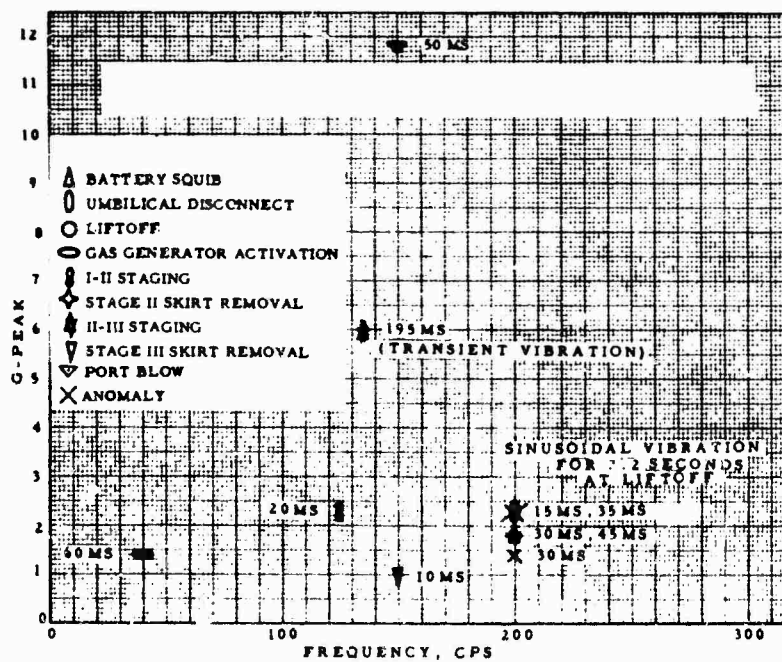


Fig. 72. Summary of decaying sinusoidal shock response data for measurement V4U03, Stage III NCU

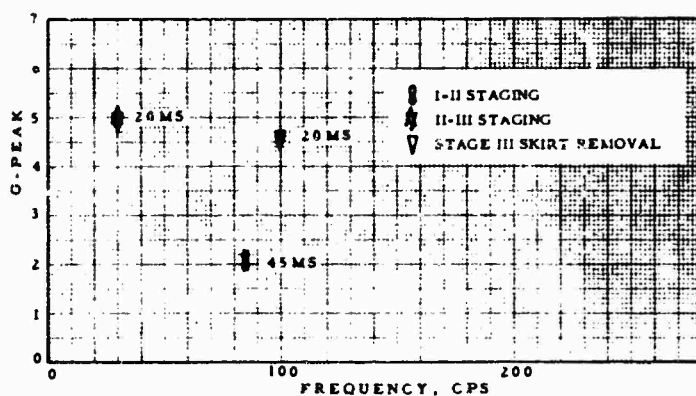


Fig. 73. Summary of decaying sinusoidal shock response data for measurement V4U04, Stage III NCU

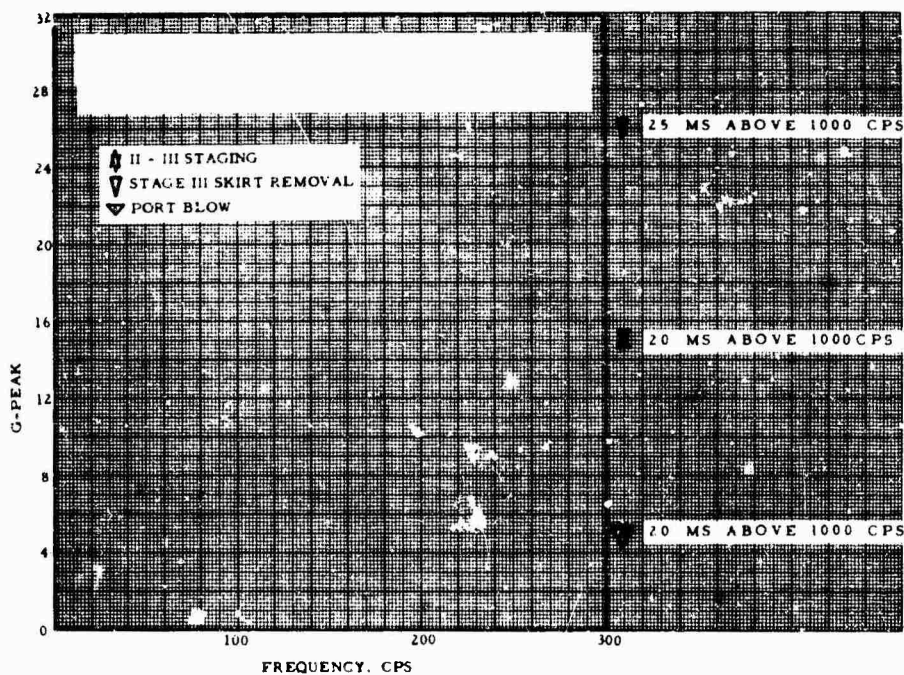


Fig. 74. Summary of decaying sinusoidal shock response data for measurement V4U05, Stage III NCU

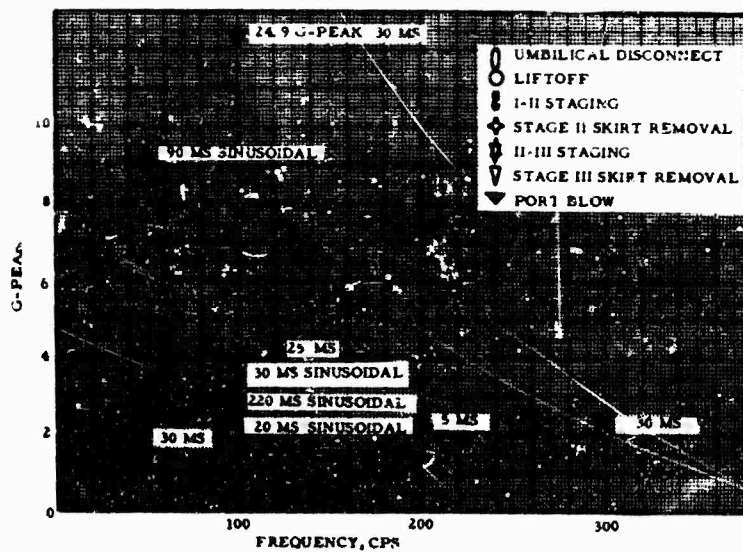


Fig. 75. Summary of decaying sinusoidal shock response data for measurement V4U06, Stage III NCU

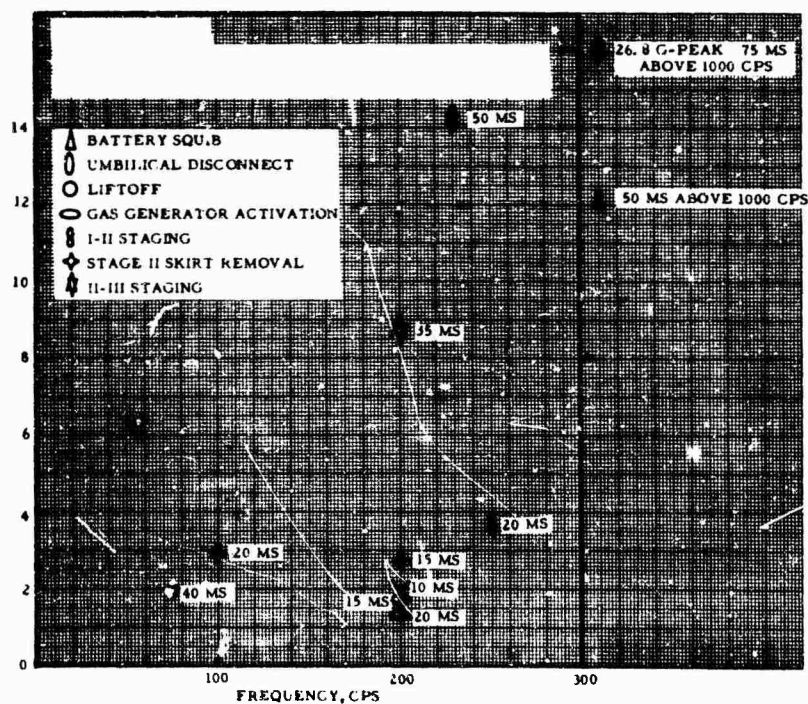


Fig. 76. Summary of decaying sinusoidal shock response data for measurement V5A02, II-III interstage

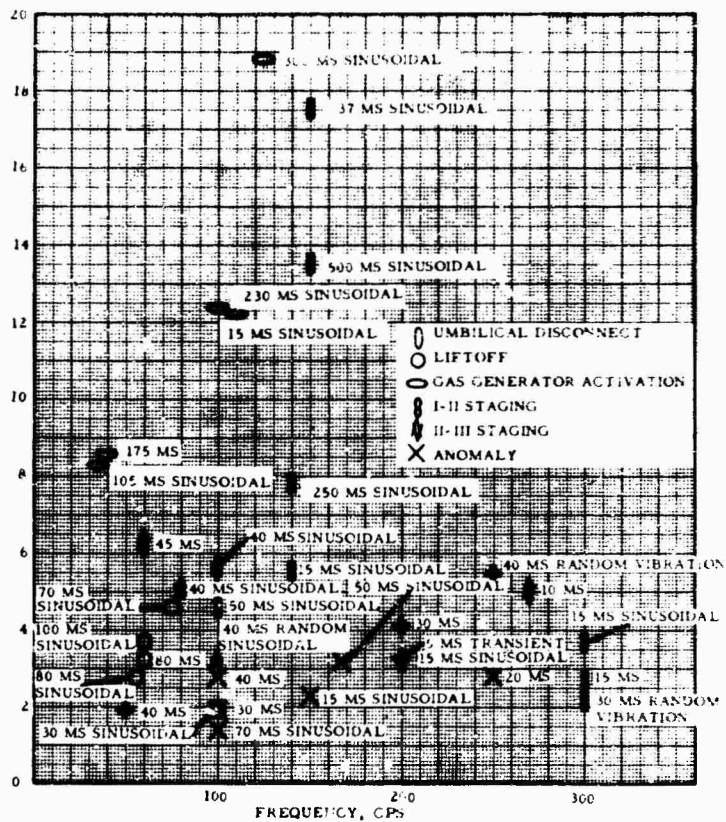


Fig. 77. Summary of decaying sinusoidal shock response data for measurement V6G01, LITVC gas generator

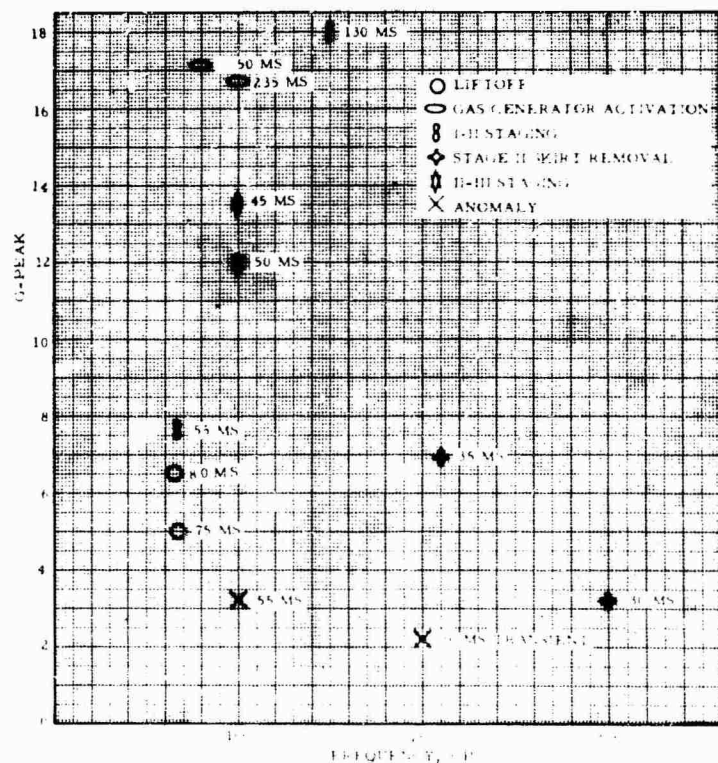


Fig. 78. Summary of decaying sinusoidal shock response data for measurement V6G02, LITVC gas generator



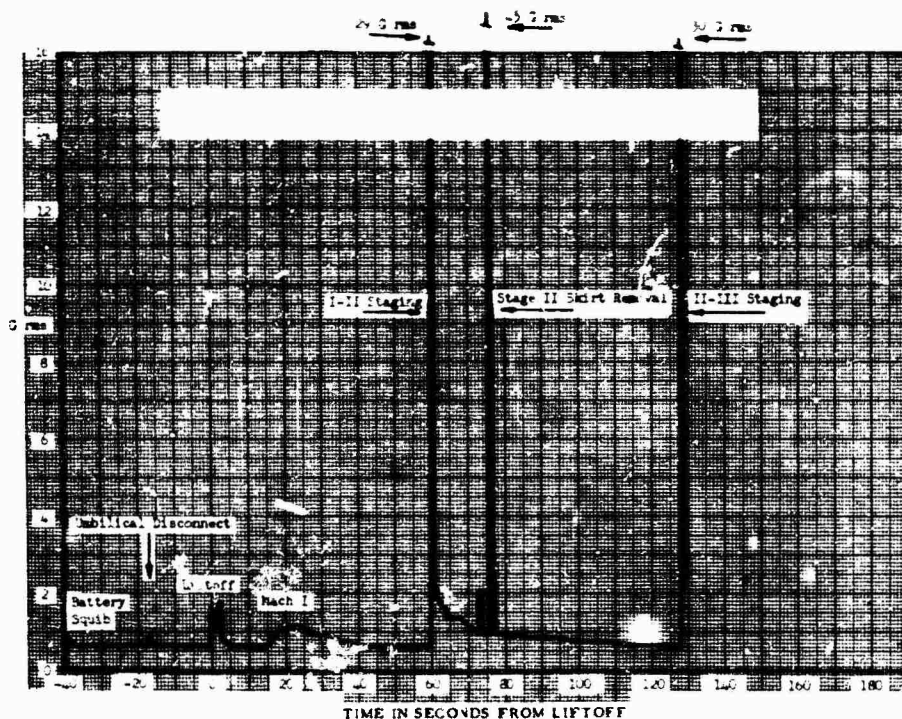


Fig. 79. Rms g vs flight time data for measurement V6T01, LITVC injector mount, longitudinal axis

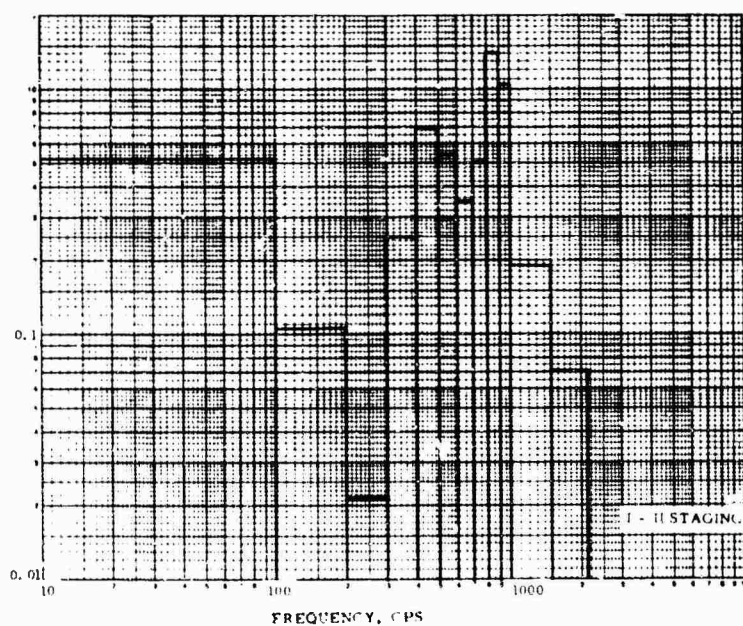


Fig. 80. Broad-band PSD analysis for measurement V6T01, LITVC injector mount, longitudinal axis

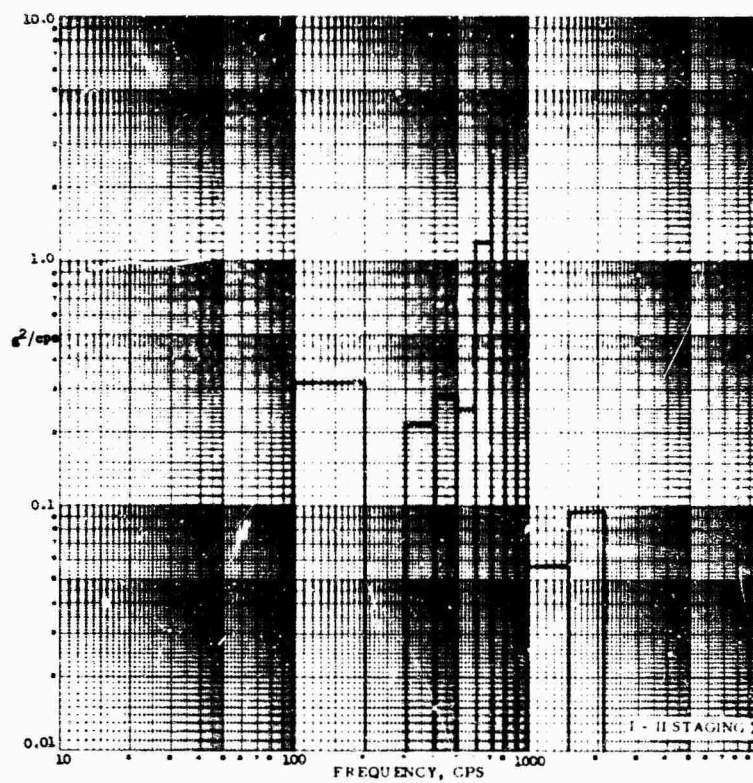


Fig. 81. Broad-band PSD analysis for measurement V6 T02, LITVC injector mount, 0- to 180-deg lateral axis



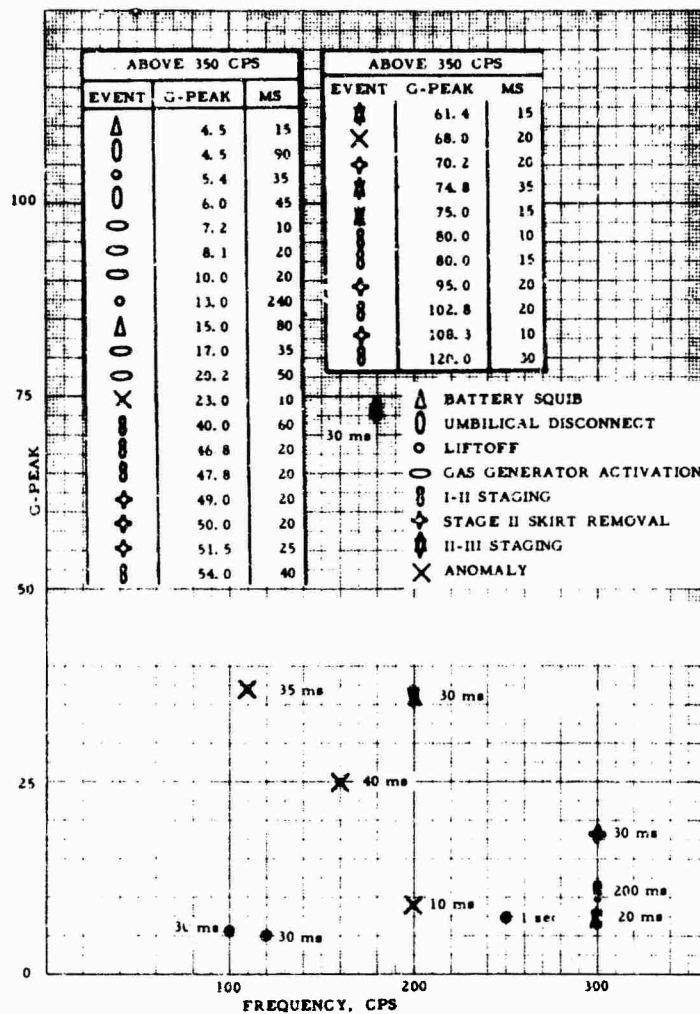


Fig. 82. Summary of decaying sinusoidal shock response data for measurement V6T01, LITVC injector mounting pad

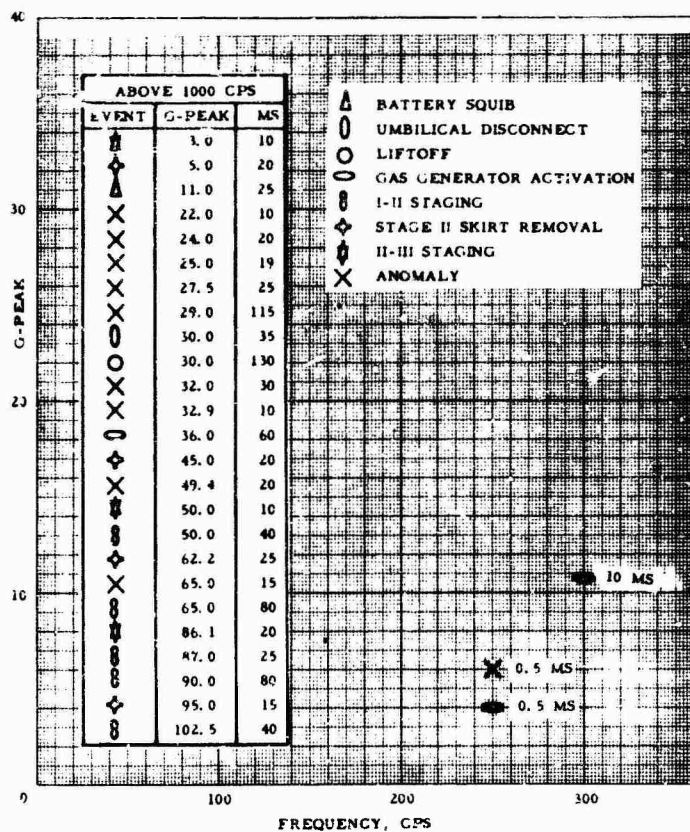


Fig. 83. Summary of decaying sinusoidal shock response data for measurement V6T02, LITVC injector mounting

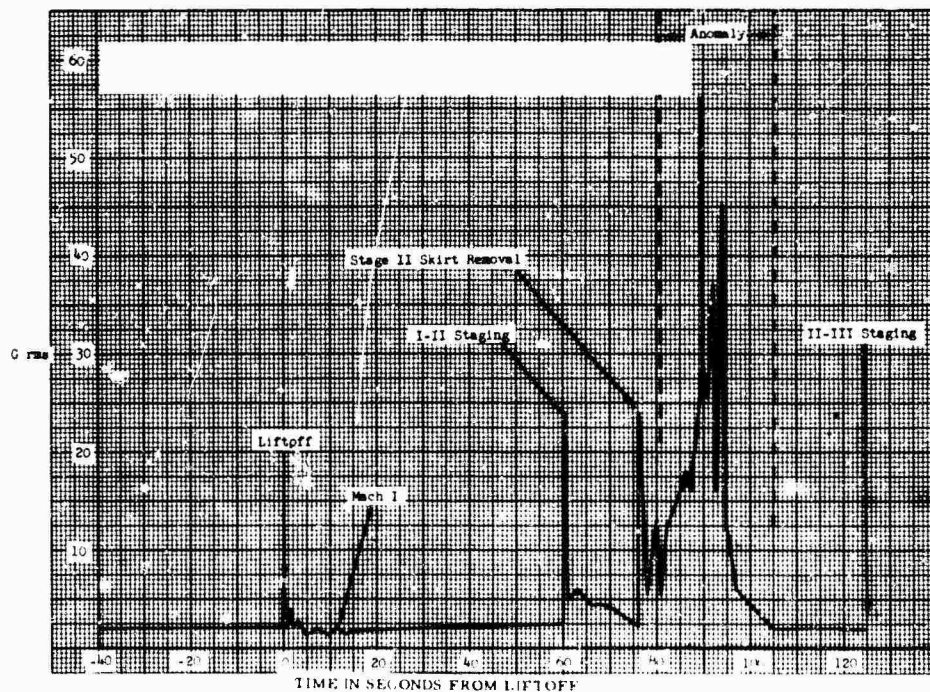


Fig. 84. Rms g vs flight time data for measurement V6T03, roll control valve, 17- to 197-deg lateral axis

Fig. 85. Broad-band PSD analysis for measurement V6T03, roll control valve, 17- to 197-deg lateral axis

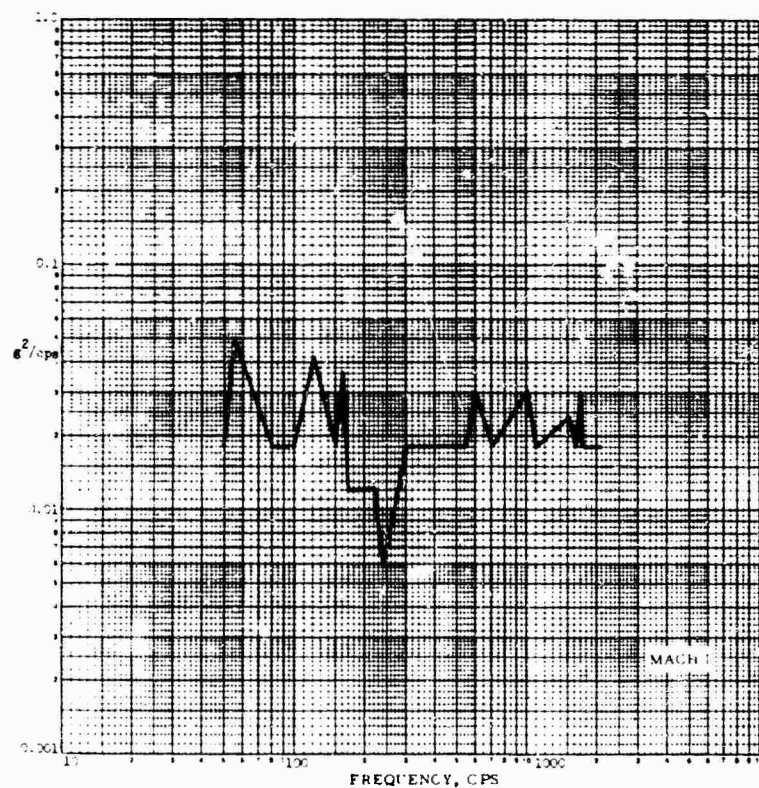
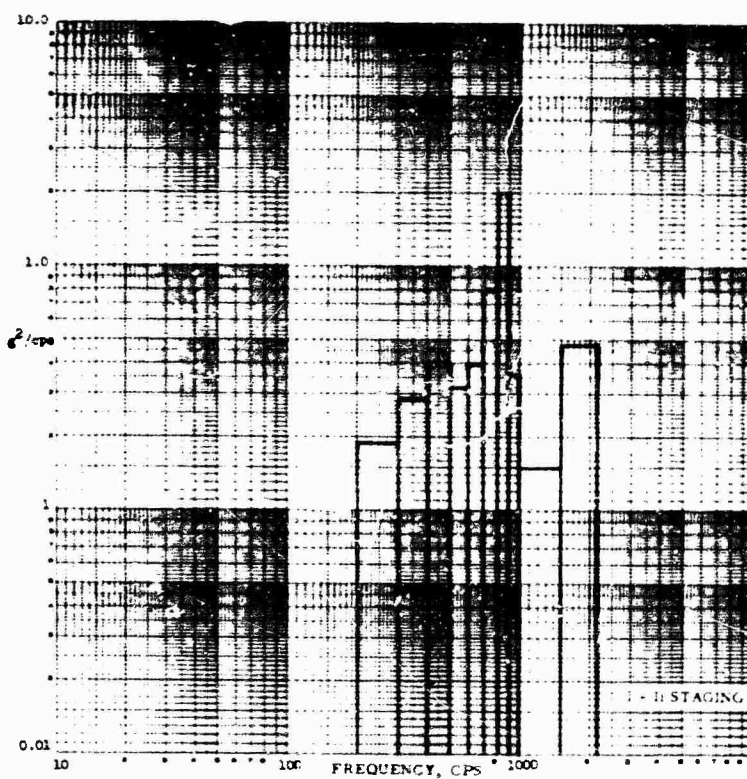


Fig. 86. Narrow-band (6 cps) PSD analysis for measurement V6T03, roll control valve, 17- to 197-deg lateral axis

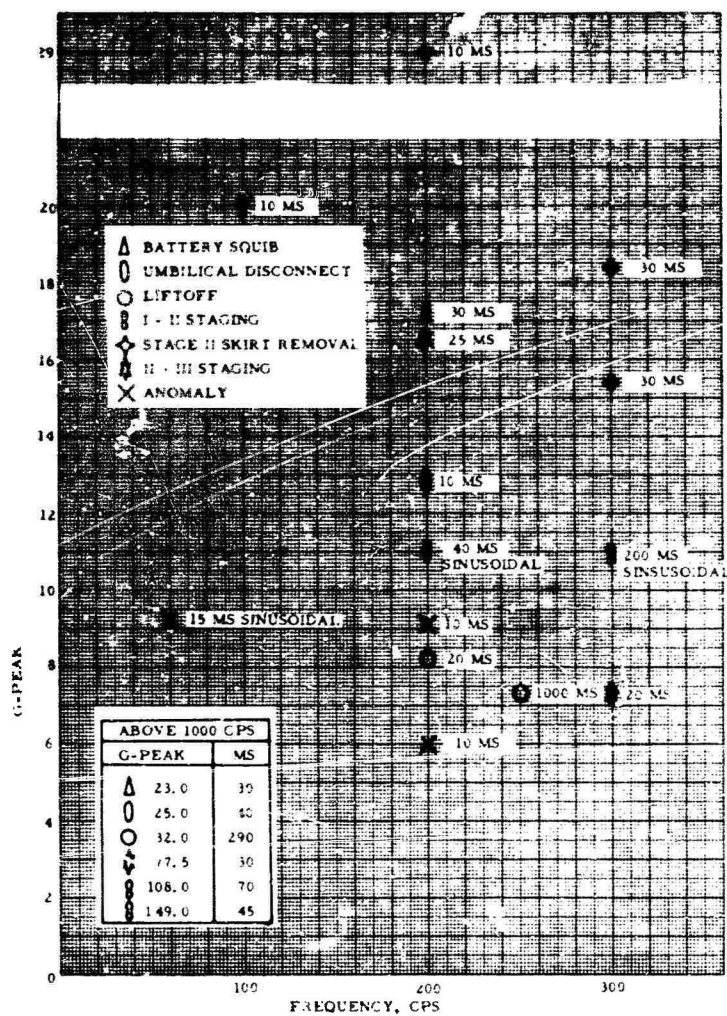


Fig. 87. Summary of decaying sinusoidal shock response data for measurement V6T03, roll control valve

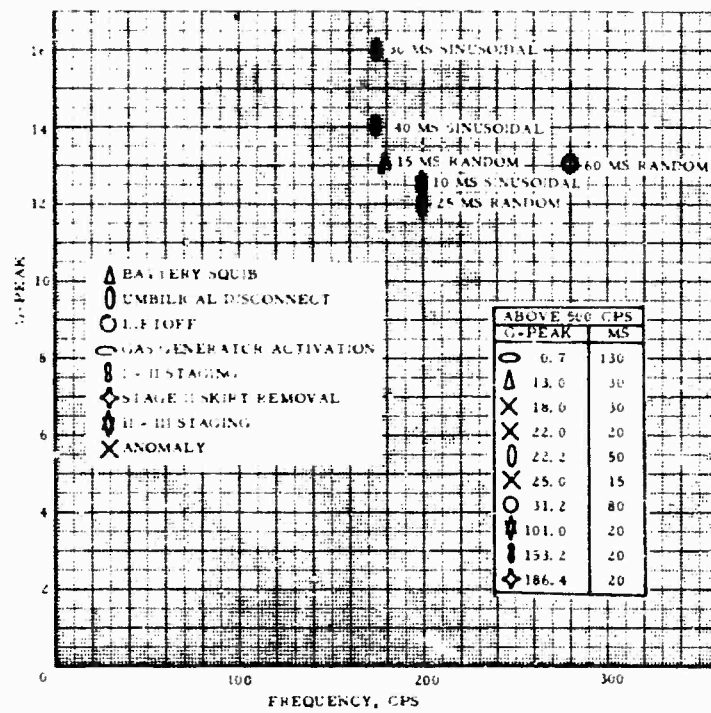


Fig. 88. Summary of decaying sinusoidal shock response data for measurement V6T04, roll control valve

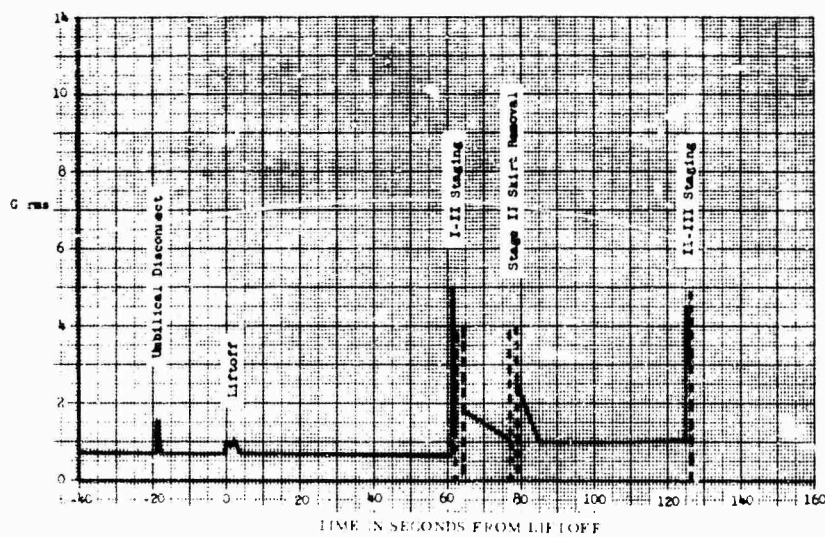


Fig. 89. Rms g vs flight time data for measurement V6T05, LITVC pressure relief valve, tangent

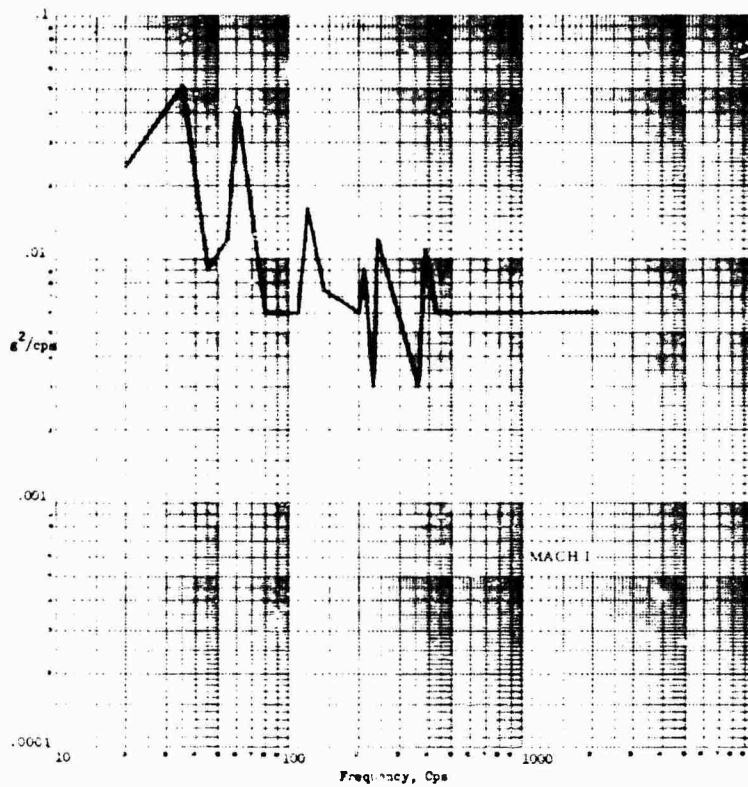


Fig. 90. Narrow-band (6 cps) PSD analysis for measurement V6T05 LITVC pressure relief valve, tangent



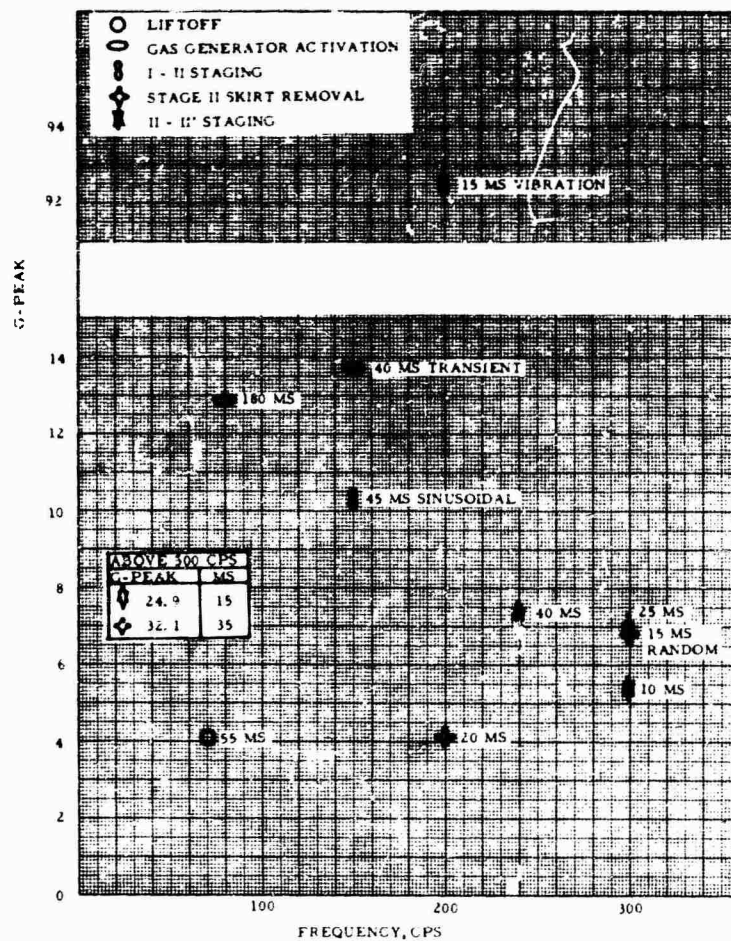


Fig. 91. Summary of decaying sinusoidal shock response data for measurement V6T05, LITVC pressure relief valve

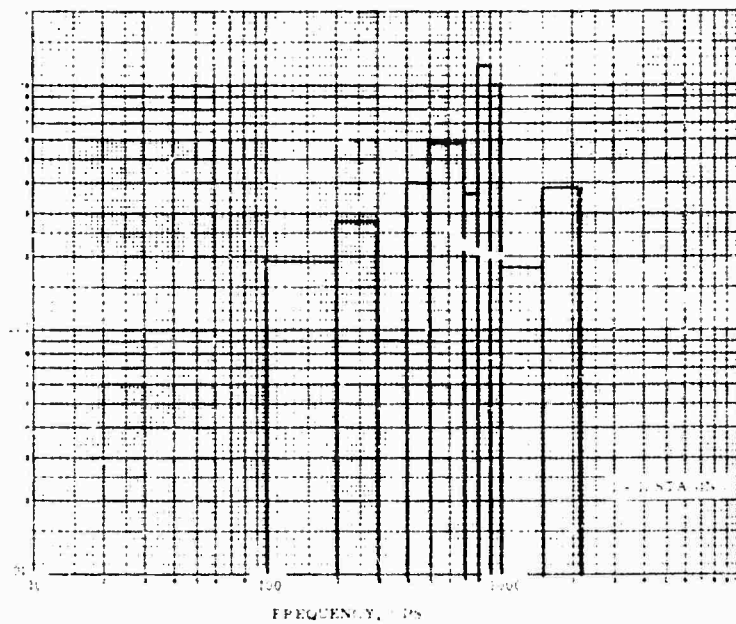


Fig. 92. Broad-band PSD analysis for measurement V6U02.  
ACI electronics base, 45- to 225-deg lateral axis

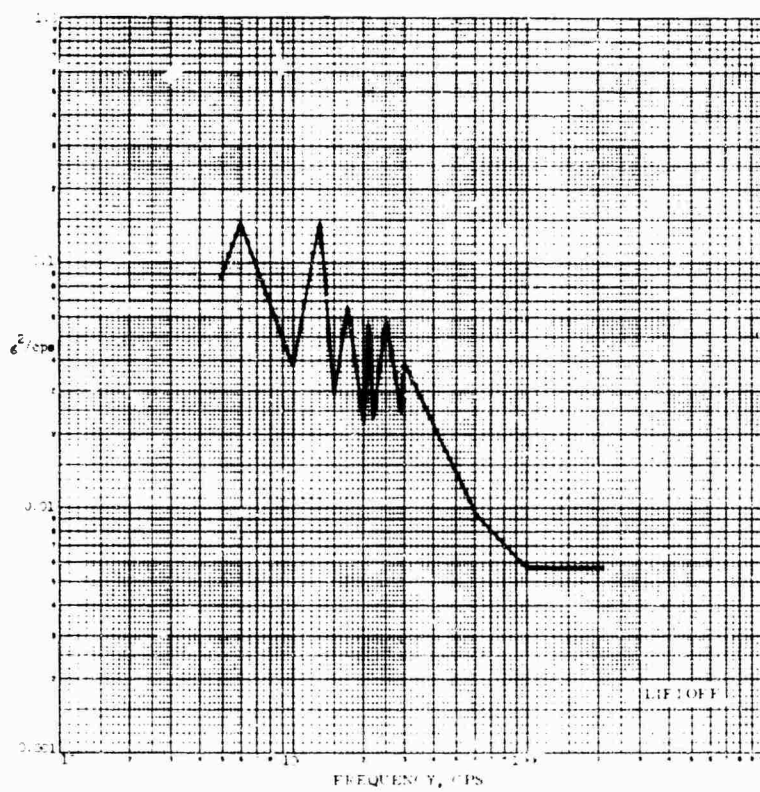


Fig. 93. Narrow-band (6 cps) PSD analysis for measurement  
V6U02, ACI electronics base, 45- to 225-deg lateral axis



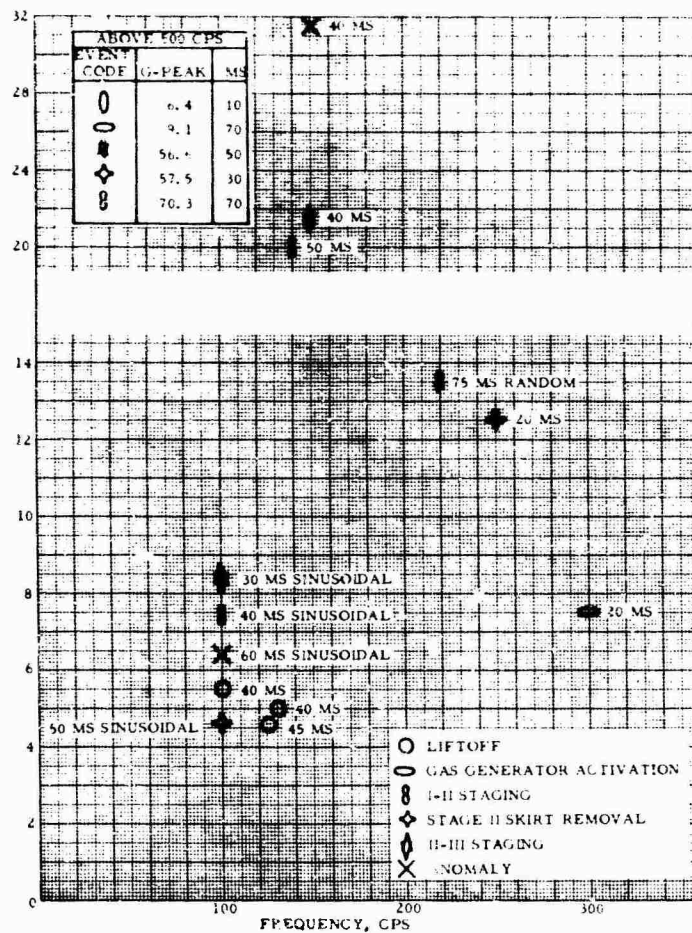


Fig. 94. Summary of decaying sinusoidal shock response data for measurement V6U01, ACI electronics base

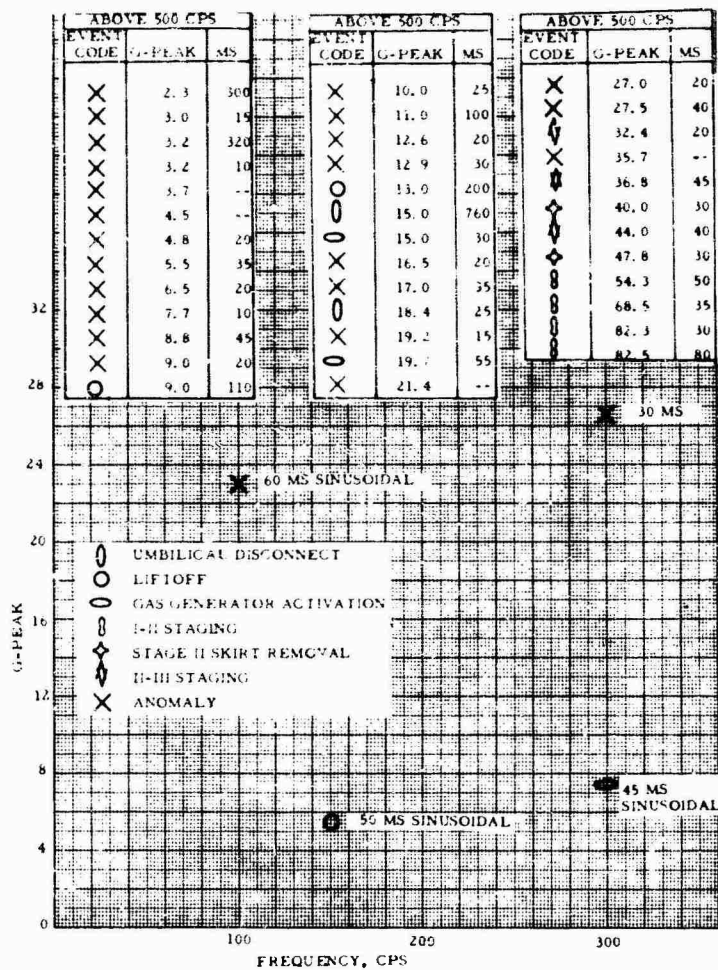


Fig. 95. Summary of decaying sinusoidal shock response data for measurement V6U02, ACI electronics base

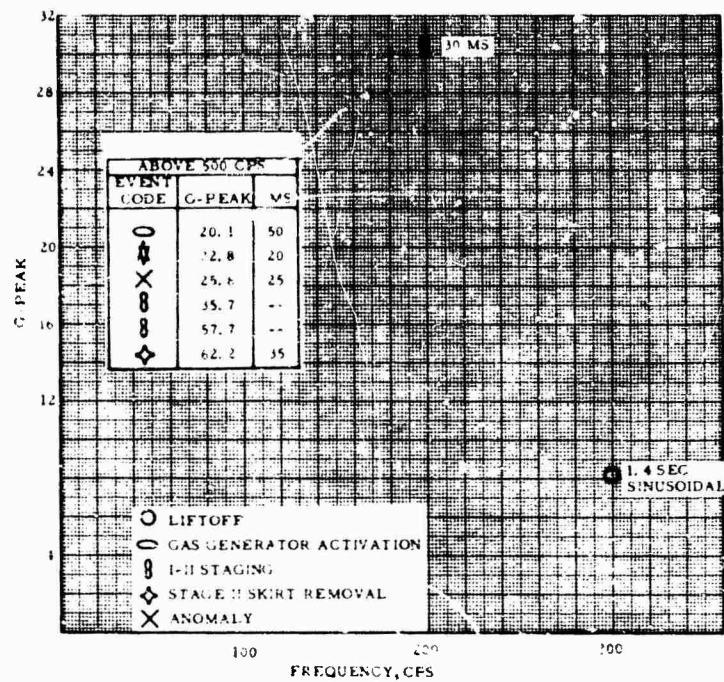


Fig. 96. Summary of decaying sinusoidal shock response data for measurement V6U03, ACI electronics base

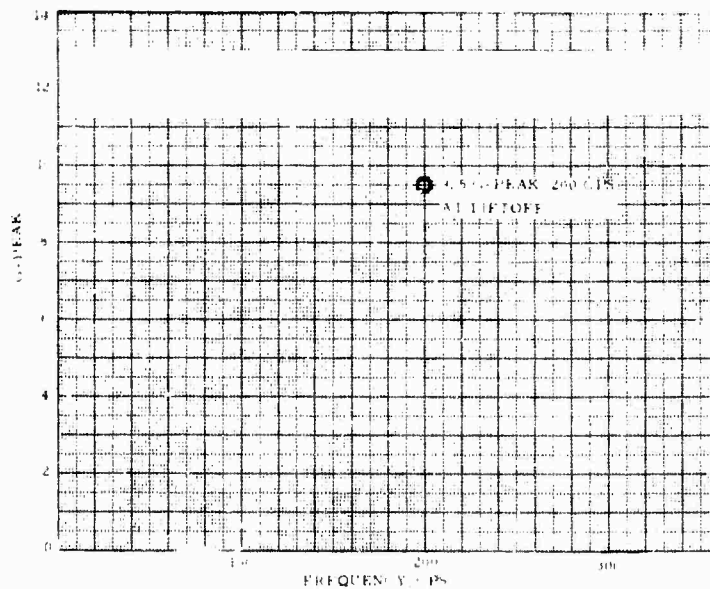


Fig. 97. Summary of decaying sinusoidal shock response data for measurement V8U01, Stage I NCU

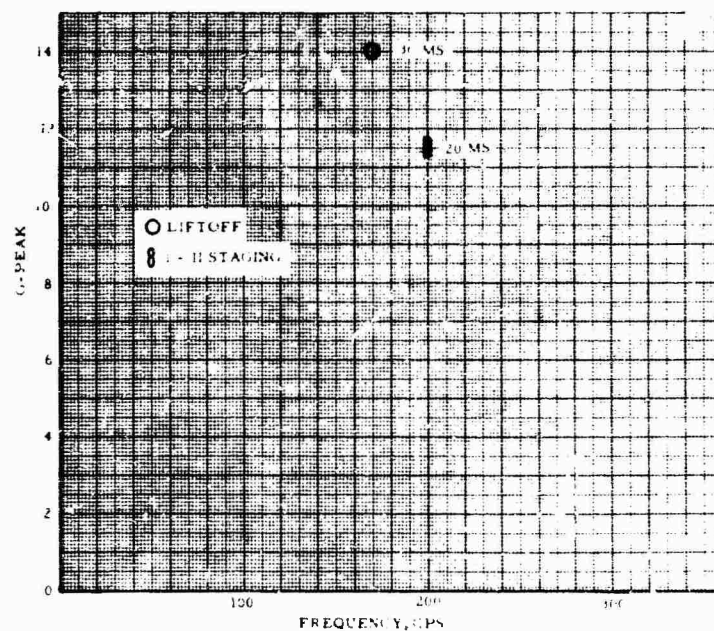


Fig. 98. Summary of decaying sinusoidal shock response data for measurement V8U02, Stage 1 NCU

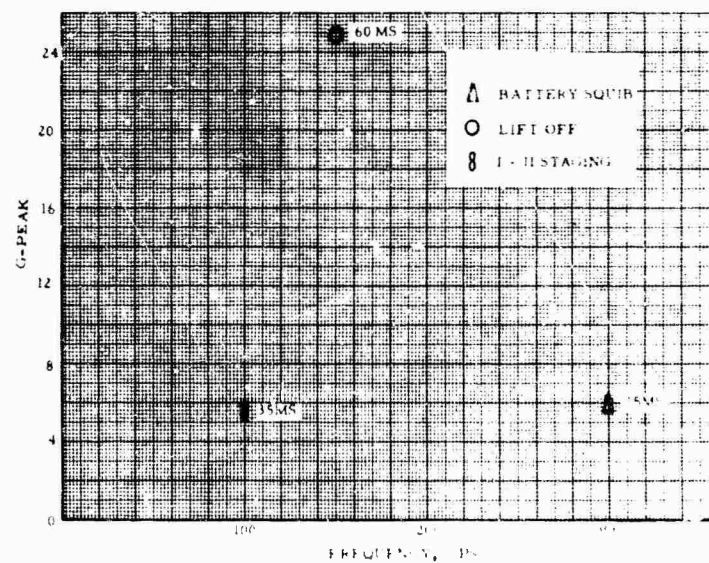


Fig. 99. Summary of decaying sinusoidal shock response data for measurement V8U03, Stage 1 NCU

## Appendix A

### MEASUREMENT LOCATIONS

This appendix presents pictorial data to illustrate the positioning of the various transducers employed in gathering the vibration data. Figures A-1 through A-14 are photographs and sketches showing the exact measurement locations.

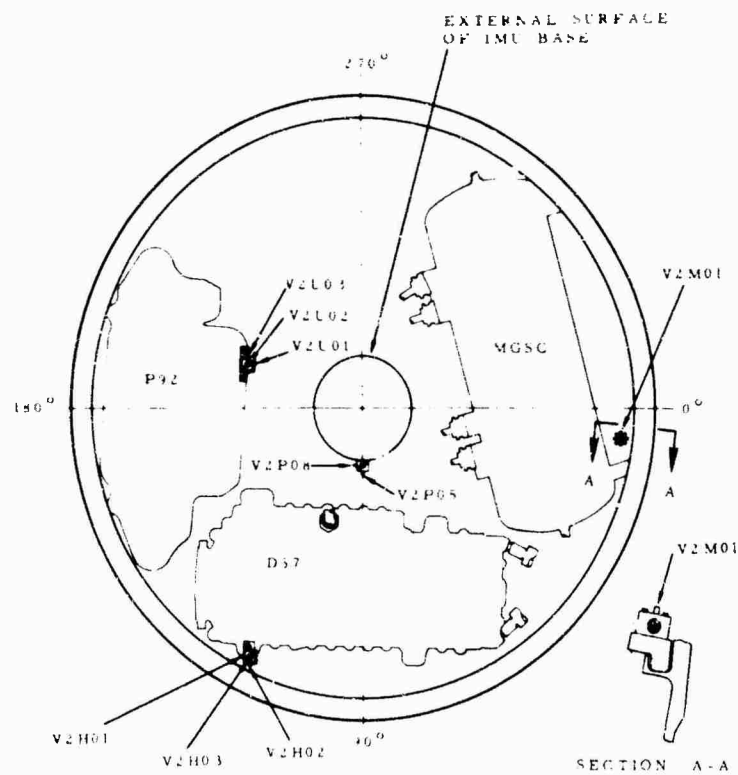


Fig. A-1. Measurements on the guidance and control equipment section

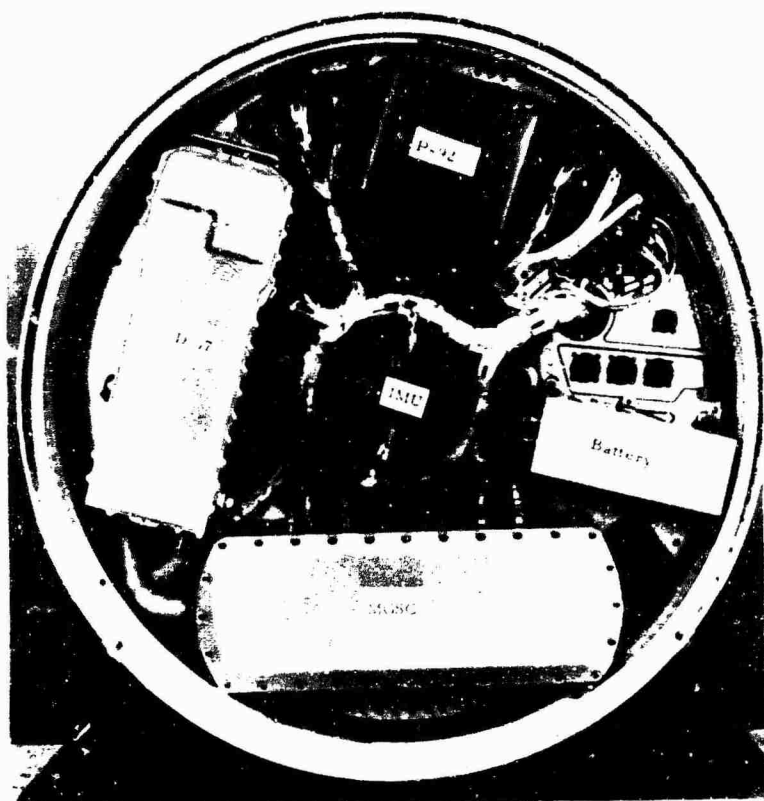


Fig. A-2. View looking forward, G and C section

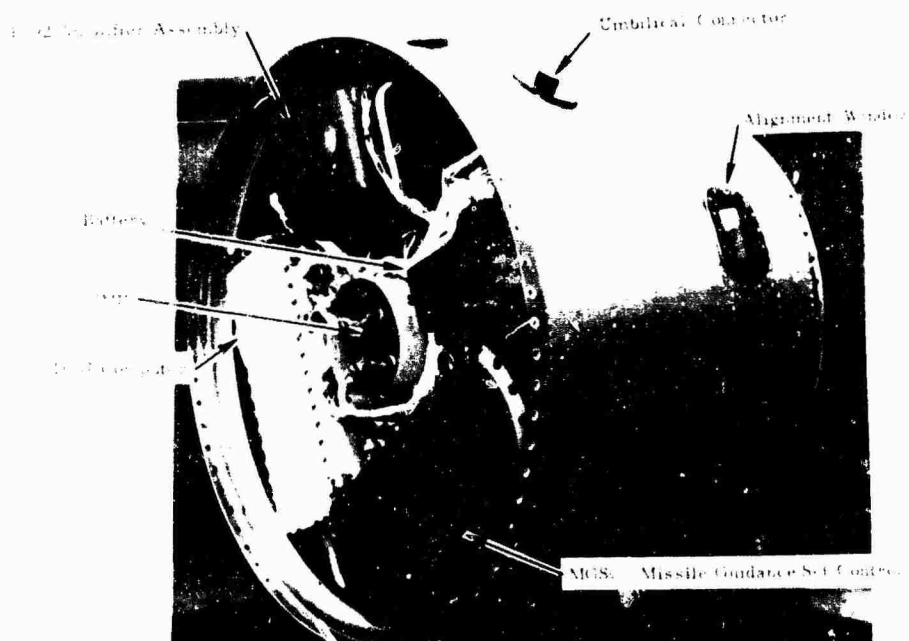


Fig. A-3. Bottom end view of NS17 mockup

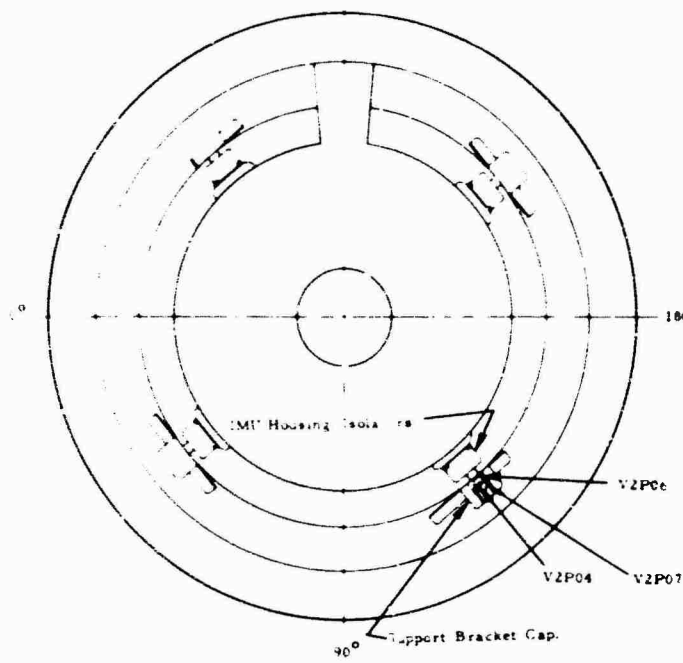


Fig. A-4. Measurement locations on IMU support bracket cap

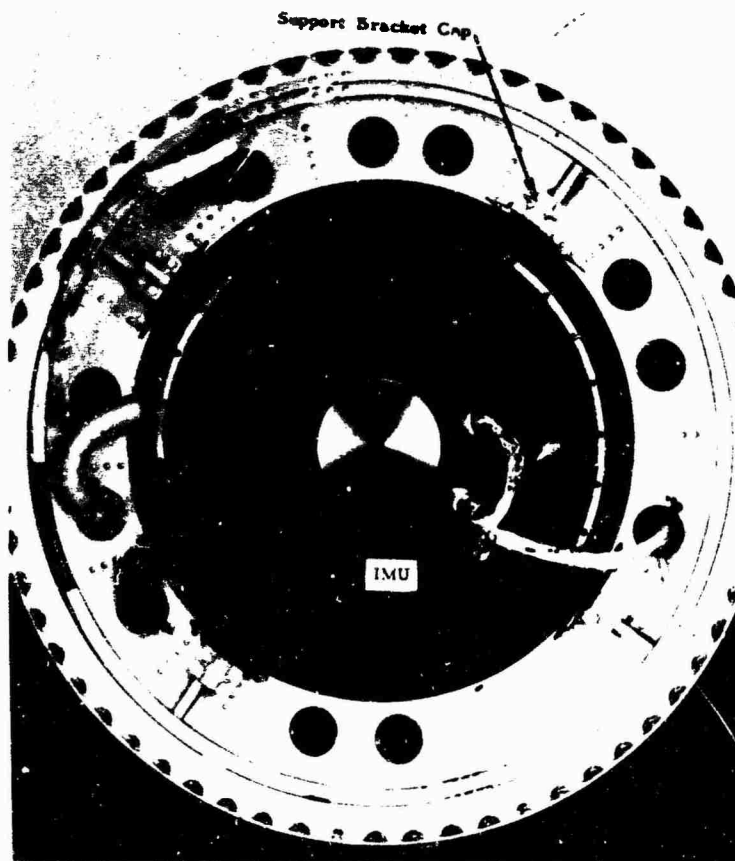


Fig. A-5. Top view of NS17 with IMU

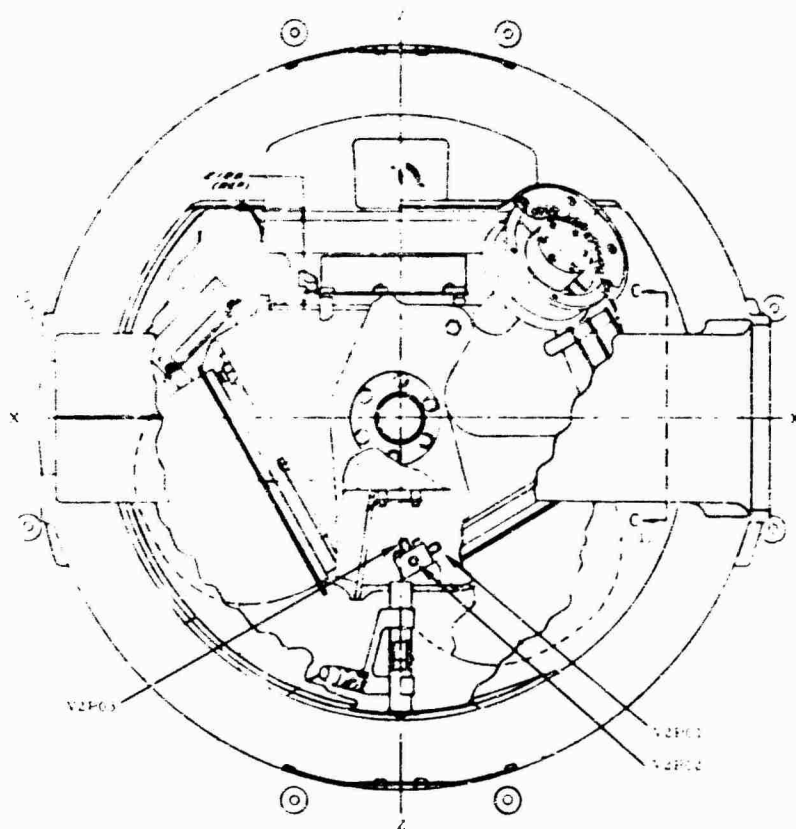


Fig. A-6. Measurements located on the G and C IMU platform (section 42)

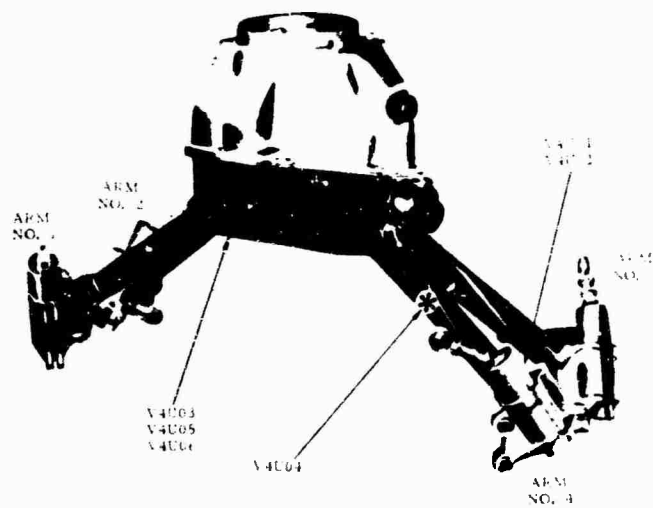


Fig. A-7. Stage III NCU measurement location



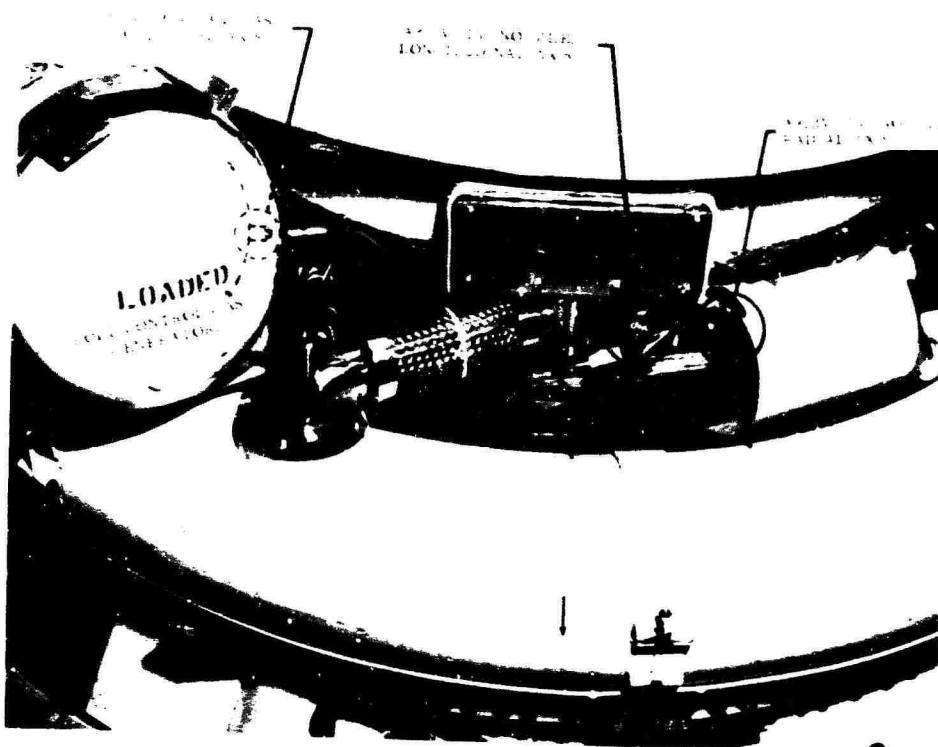


Fig. A-8. Measurements located on the LITVC equipment section

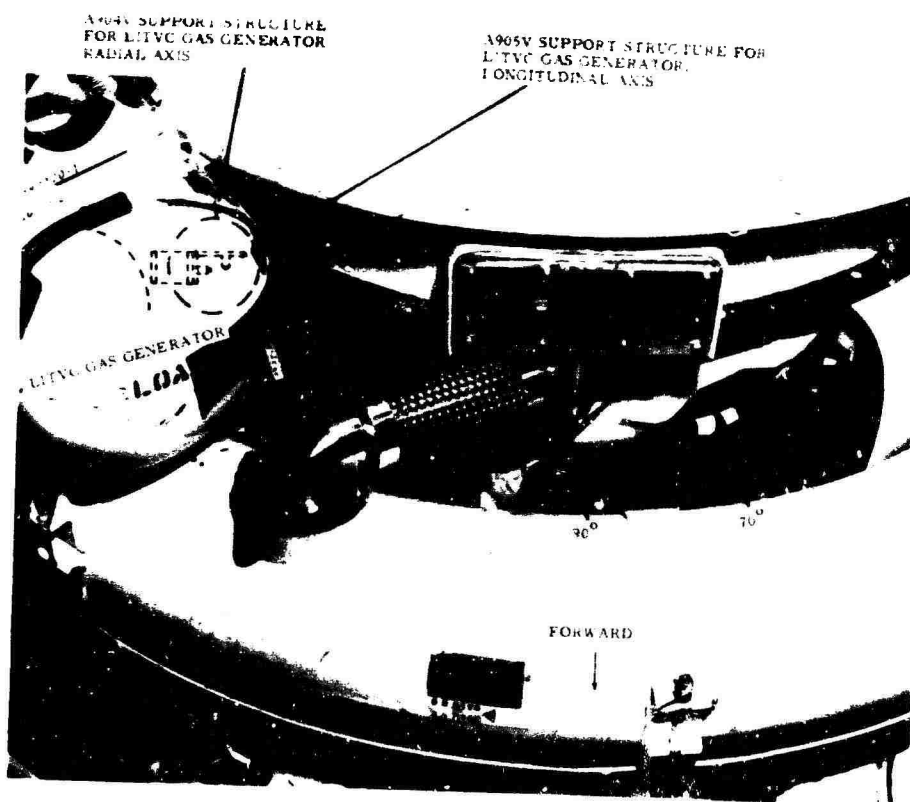


Fig. A-9. Accelerometer locations on Minuteman Fly-3 Stage II motor

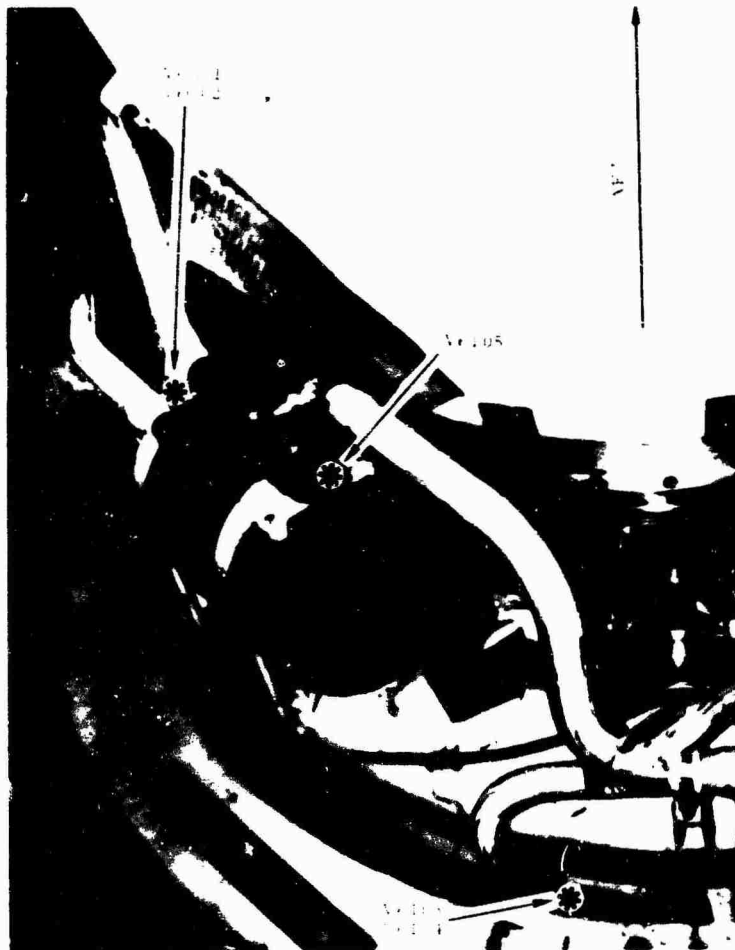


Fig. A-10. Measurements located on the gas generator

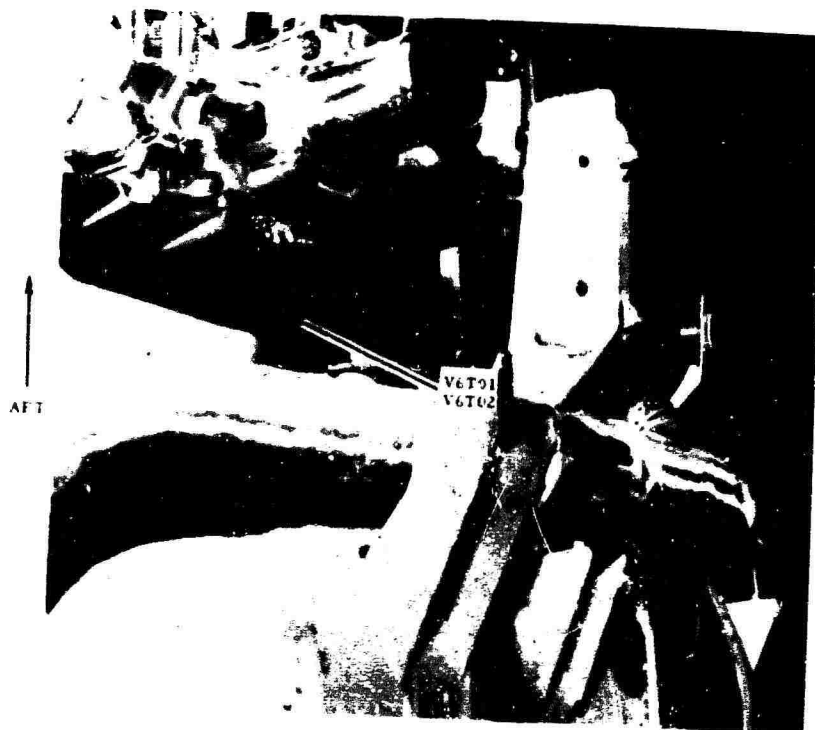


Fig. A-11. Measurement located on the LITVC injection mounting pad (section 46)

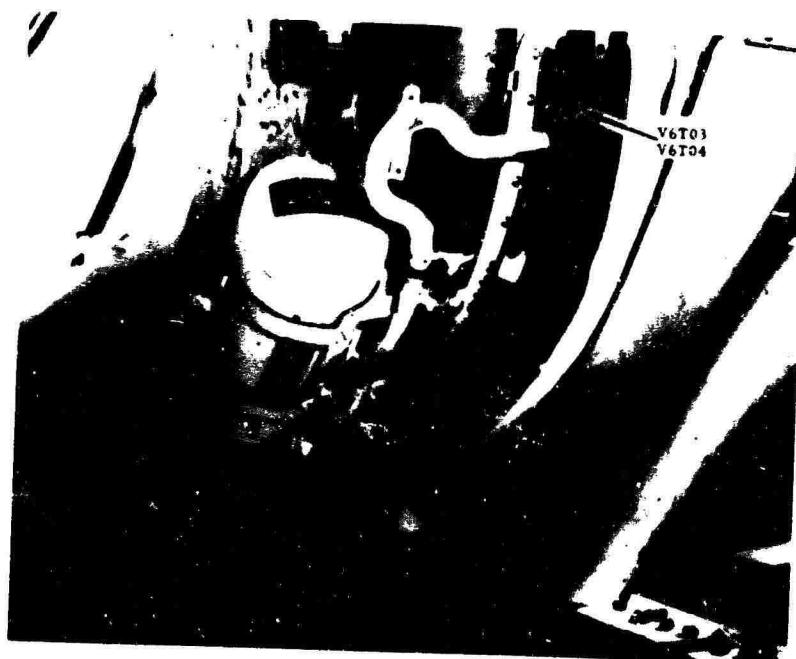


Fig. A-12. Measurements located on the roll control valve (section 46)

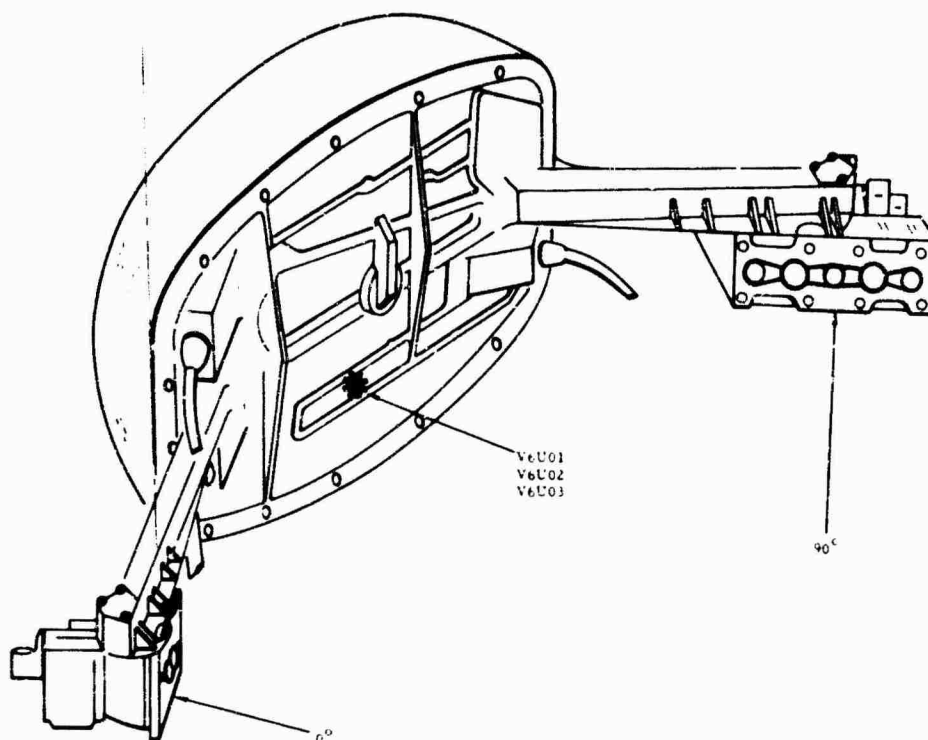


Fig. A-13. Measurements located on the ACI electronics base (section 46)

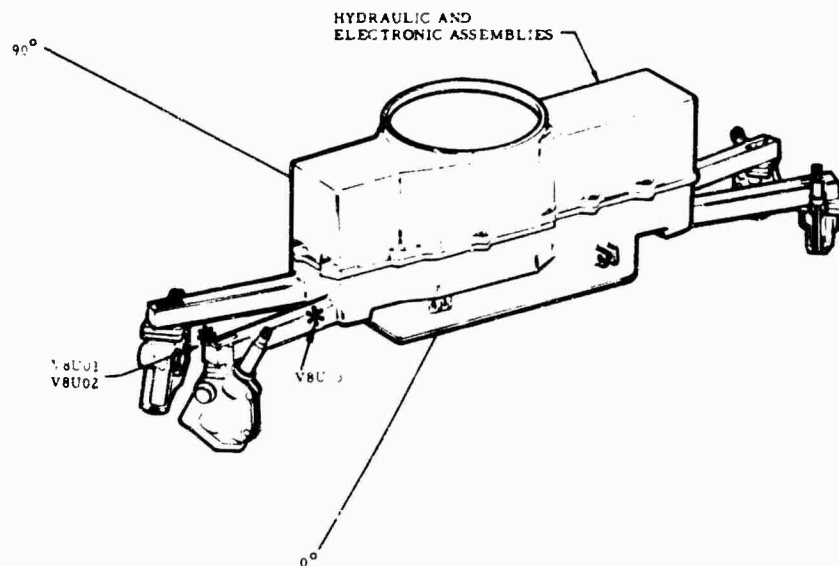


Fig. A-14. Stage I NCU (section 48)

Appendix B

BACK-UP DATA

The volume of data to be included in this appendix is too great for publication here. These back-up data may be obtained by request from the authors.

\* \* \*

## SPACECRAFT VIBRATION: A COMPARISON OF FLIGHT DATA AND GROUND TEST DATA

G. Kachadourian  
General Electric Company  
Philadelphia, Pennsylvania

There has been a continuing accumulation of flight vibration data throughout the industry from measurements on space flight systems. Comparison of these data and the vibration procedures used in qualification testing of systems and components has shown that these procedures generally do not duplicate flight conditions adequately and that overtesting and undertesting is encountered. The differences between flight vibration environments and ground test vibrations by the use of a specific space system are investigated to develop improved systems and component testing procedures. These results are extended to cover spacecraft in general.

Details of the flight measurements, including sensor mounting details, time histories, and power spectral densities, are presented. Nonstationarity of the data is discussed, and a method for correcting the PSD plots for nonstationarity is applied.

Details of ground test measurements on an identical system are presented, discussed, and compared with the flight data. The importance of sensor locations is graphically illustrated, and the importance of categorizing vibration data according to sensor location and mounting is emphasized.

### INTRODUCTION

This paper addresses the problem of defining the vibration environment within a spacecraft during booster-powered flight and the problem of reproducing these environments in ground testing. Although a specific spacecraft-booster combination is considered, the conclusions reached and the recommendations made are general and applicable to any system.

In a spacecraft, the significant vibration environments, which are experienced during booster-powered flight, result from the acoustic environments external to the spacecraft. The acoustics in turn have two basic sources: the noise of the booster rocket motors and the aerodynamic noise of transonic buffet and boundary-layer turbulence. First, the acoustic environments acting on the external surfaces of the spacecraft and booster cause these external surfaces to vibrate, and then the vibrations are transmitted into the spacecraft. The predominant vibrations are in the natural modes of the spacecraft, so that even though the external acoustics have relatively broad-band spectra, the vibration responses are usually narrow-band random.

Theoretical treatment in prediction of these acoustically induced vibrations has met with limited success. The two major obstacles are (a) inadequate description of the acoustic forcing function, space and time correlation characteristics in particular, and (b) the magnitude of the problem caused by the necessarily detailed mathematical model. It is felt that an empirical approach provides more accurate predictions in a fraction of the time and cost. Consequently, an empirical approach is used here and is recommended for general use. It is readily admitted, however, that the conclusion is debatable and that improvement of both theoretical and empirical predictions methods should be sought.

The empirical methods presently in use in the industry are invariably based on an accumulation of flight measured data compiled or transformed into a form which establishes a relationship between acoustic pressure, type of structure, and vibration response of that structure. For the empirical method to be accurate, however, there must be a sufficient degree of similarity between the new configuration and the configuration on which the data were gathered. Ideally, the spacecraft for which the vibration prediction is being made should be

structurally similar to the spacecraft on which the flight data were obtained, should use the same booster, and should fly the same general trajectory from the same launch pad. All variations in these factors should be factored into the prediction. Today there are generally sufficient applicable flight vibration data and successful vibration criteria to permit an accurate prediction of vibration environments for a new spacecraft by direct analogy.

There are two notable practices within the industry in establishing spacecraft vibration criteria. One is to define an external vibration environment acting at the spacecraft-booster interface. It is then incumbent on the spacecraft manufacturer to define the vibration responses to this interface environment by analysis, to verify the analysis by vibration test, and from this to define component vibration criteria. This approach has two distinct disadvantages. First, the internal vibration and component criteria thus established are not accurate representations of the vibration actually experienced in flight under acoustic excitation. The inaccuracy results from the fact that the spacecraft vibration responses to external acoustic loadings are not the same as the responses to a mechanical vibration applied at

the booster interface or any other point in the spacecraft. Second, severe scheduling problems are encountered because component criteria are not established until the spacecraft is built and tested.

The second practice for establishing spacecraft vibration criteria is to define the external and internal environments independently, but both on the basis of flight measurement data. This approach has the disadvantage that a component probably experiences vibration levels in the spacecraft vibration test which exceed the component qualifications levels.

This report reviews a specific spacecraft, comparing flight vibration measurements with measurements from ground vibration testing of the same spacecraft to expose the inaccuracies of the vibration criteria, and defining new criteria. A general approach for establishing vibration criteria for spacecraft is then defined.

## SPACECRAFT

The general configuration of the spacecraft is shown in Figs. 1 and 2. The spacecraft consists of a measurements' capsule with an

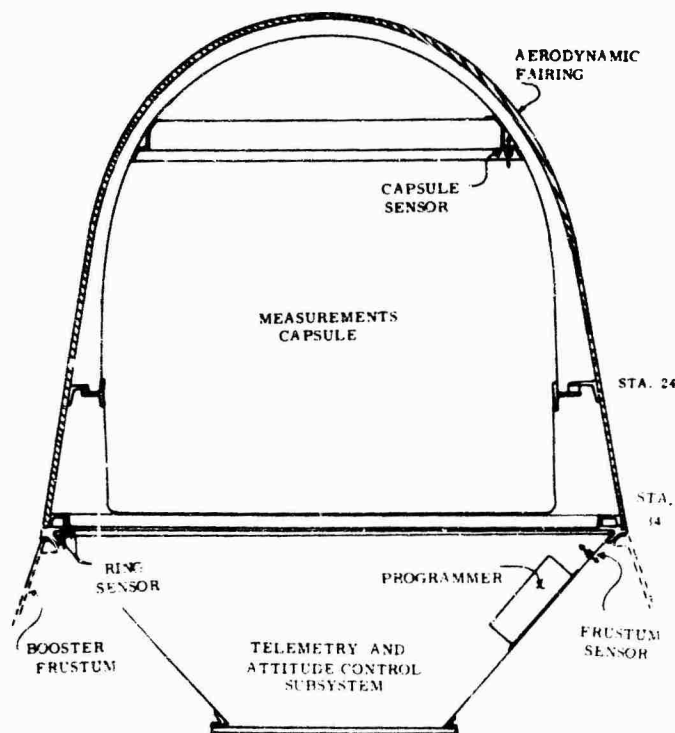


Fig. 1. Spacecraft general configuration with vibration sensor locations

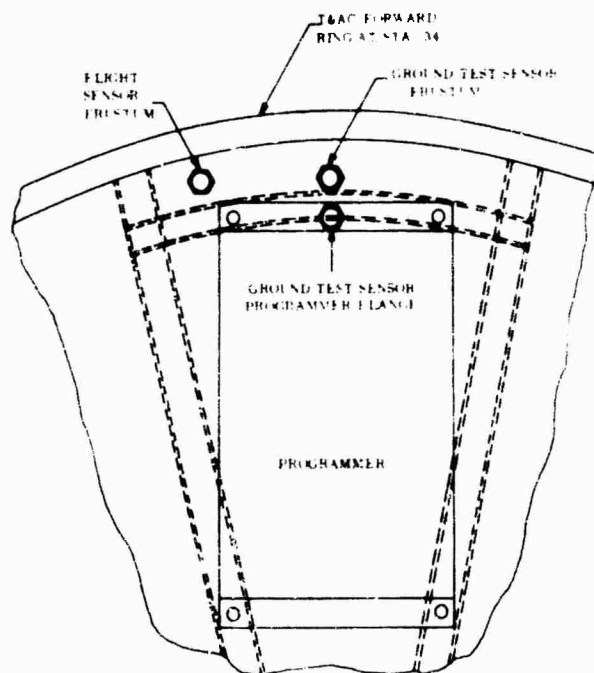


Fig. 2. Sensor locations for programmer and frustum

aerodynamic fairing and a telemetry and attitude control (T&AC) subsystem. Attachment to the booster is through mating conical rings with a two-point holddown.

The vibration criteria for the spacecraft consist of the vehicle qualification test requirement and component qualification test requirement

shown in Figs. 3 and 4. These requirements have been carried on from previous program requirements without change, primarily because of their excellent flight success record. It will be shown that these requirements are basically incompatible with each other and that the spacecraft test requirement is very conservative.

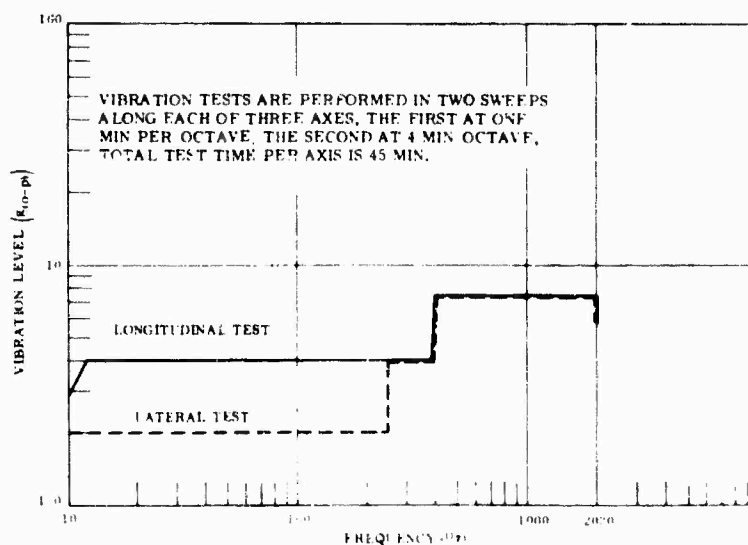


Fig. 3. System qualification vibration test input levels



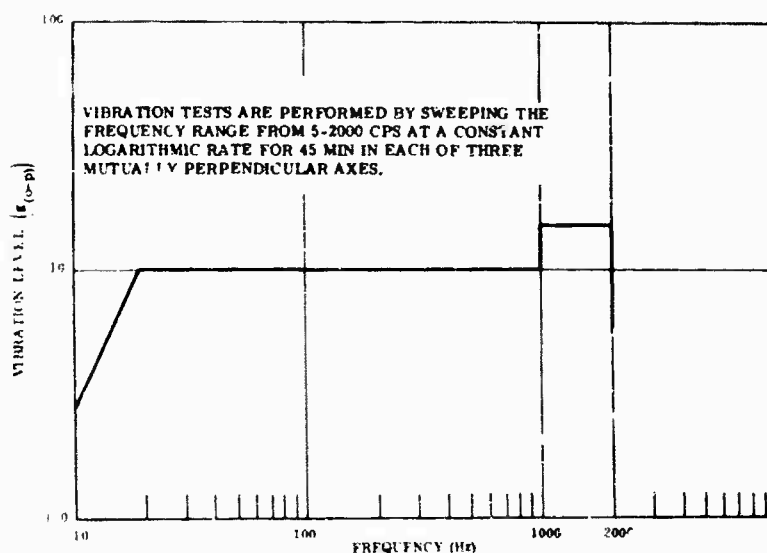


Fig. 4. Component qualification vibration test input levels

## SPACECRAFT VIBRATION TEST

The vibration qualification testing of the spacecraft consisted of imposing sinusoidal vibrations in frequency sweeps at the levels and times shown in Fig. 3 along each of the three major axes of the vehicle. The tests were performed by mounting the spacecraft on a vibration fixture and controlling the input vibration at the spacecraft-fixture interface. The fixture duplicated the booster side of the spacecraft-booster mating rings but was otherwise relatively stiff. For the longitudinal direction tests, the fixture and vehicle were mounted directly on an MB-C-126 electrodynamic exciter, with the dead weight of the fixture and vehicle supported by a low-frequency bungee suspension. In the lateral directions the fixture and vehicle were mounted on a team bearing system.

Six vibration sensors were used to monitor the input levels, and 44 sensors were used to measure the responses throughout the vehicle. All data were recorded on magnetic data tape and played back as x-y plots of vibration amplitude as a function of frequency. A Spectral Dynamics automatic mechanical impedance measuring system, model SD 1002A-49, produced these x-y plots, using a 5-Hz bandwidth sweeping filter. A Sangamo model 472RB magnetic tape recorder, having response characteristics to 350 kHz  $\pm 3$  db when operated at 60 ips in the direct mode, was the data recorder. Twelve of the recorder's 14 tracks were used for data recording. A multiplexer system was used in conjunction with the magnetic tape to

obtain the necessary data channels, with 4-kHz capability.

Typical data from the spacecraft vibration test are shown in Figs. 5 through 10 and are presented only to provide a general indication of the spacecraft vibration characteristics. Figures 5, 6, and 7 are measurements within the capsule and show major resonances in the 50- to 250-Hz frequency range. Figures 8, 9, and 10 are measurements on the T&AC subsystem and show its major resonances to be in the 40- to 300-Hz range.

## FLIGHT MEASUREMENTS

### Instrumentation

The flight instrumentation consisted of three piezoelectric vibration sensors and amplifiers, manufactured by the Columbia Research Laboratories and installed in the vehicle as shown in Figs. 1 and 2. The data were transmitted over the standard IRIG FM/FM telemetry subcarrier oscillator (SCO) bands 16, 17, and 18. These SCO's have center frequencies of 40, 52.5, and 70 kHz and frequency response ratings of 600, 790, and 1050 Hz, respectively. All sensors were bolted to the structure and sealed with Locktite thread sealant.

### Flight Data Analysis

The flight vibration data were first played back on oscillograph records typified by Figs.

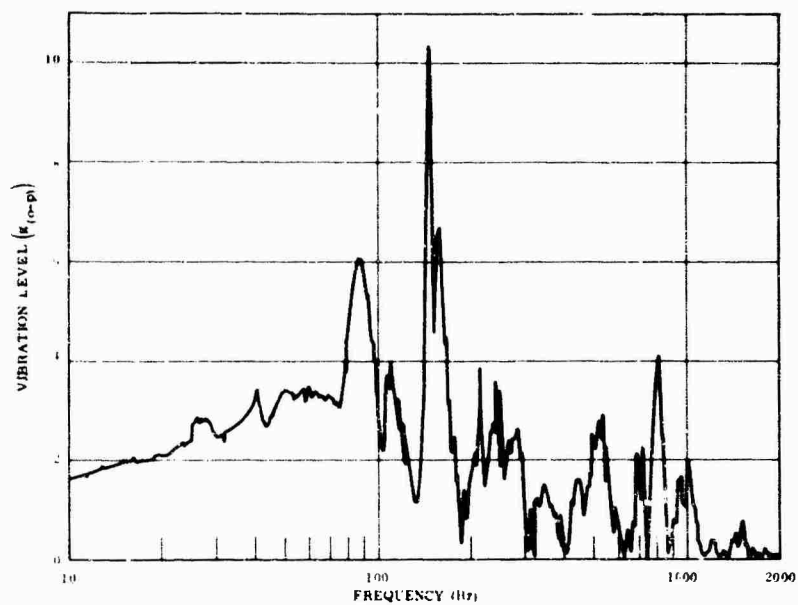


Fig. 5. Spacecraft pitch axis vibration test, capsule pitch axis response

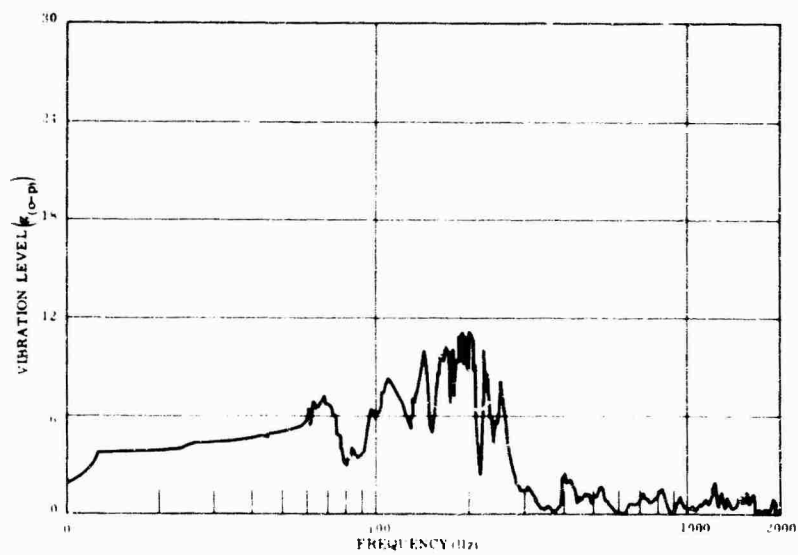


Fig. 6. Spacecraft roll axis vibration test, capsule roll axis response

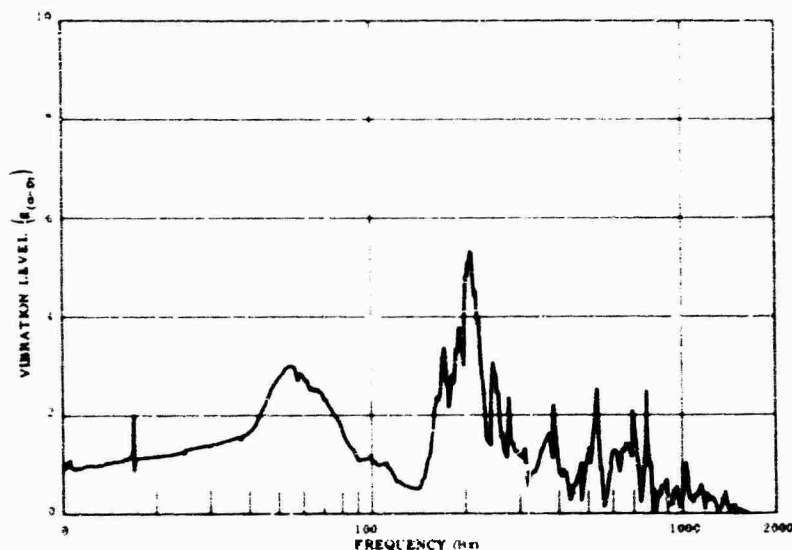


Fig. 7. Spacecraft yaw axis vibration test, capsule yaw axis response

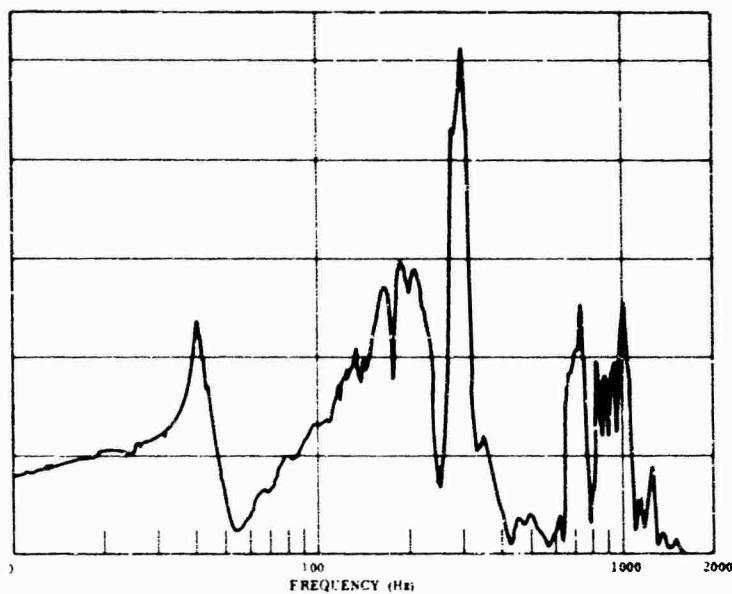


Fig. 8. Spacecraft pitch axis vibration test, T&AC package pitch axis response

11 through 14. From these the peak g vs flight time plot of Fig. 15 was developed, the peak g readings corresponding to  $3\sigma$  values.

From the oscillograph recordings it was apparent that there were three periods of flight where significant vibrations were generated: liftoff, transonic, and maximum dynamic pressure (max Q). Power spectral analyses were performed by dubbing magnetic tape records of

the period's of maximum vibration, splicing each recording to form tape loops, and performing analysis of these loops using a Spectral Dynamics analyzer. The resulting PSD plots are shown in Figs. 16 through 24.

It was necessary to make three types of corrections on these PSD plots. First, a correction was applied to the high-frequency levels to correct for the TM attenuation according to

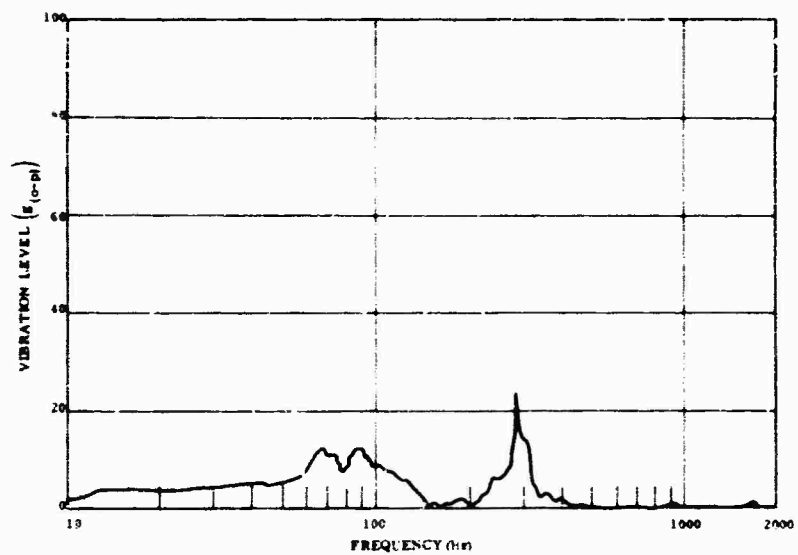


Fig. 9. Spacecraft roll axis vibration test, T&AC package roll axis response

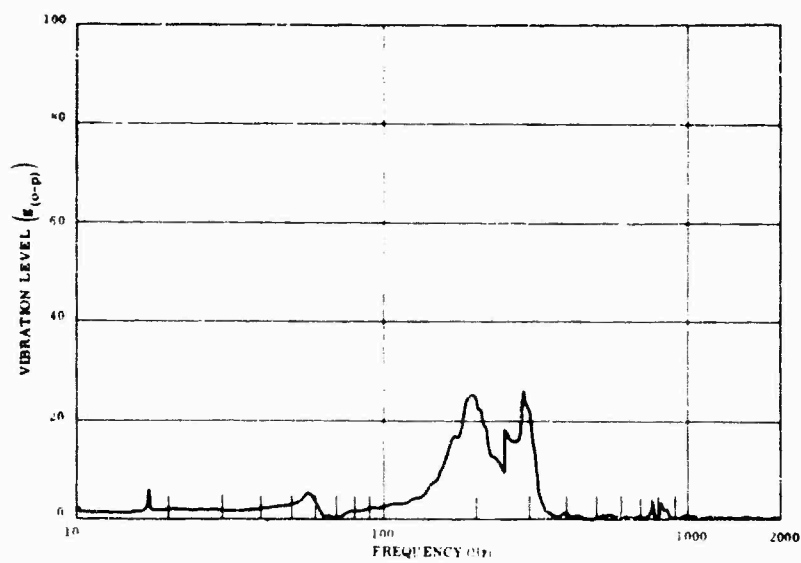


Fig. 10. Spacecraft yaw axis vibration test, T&AC package yaw axis response

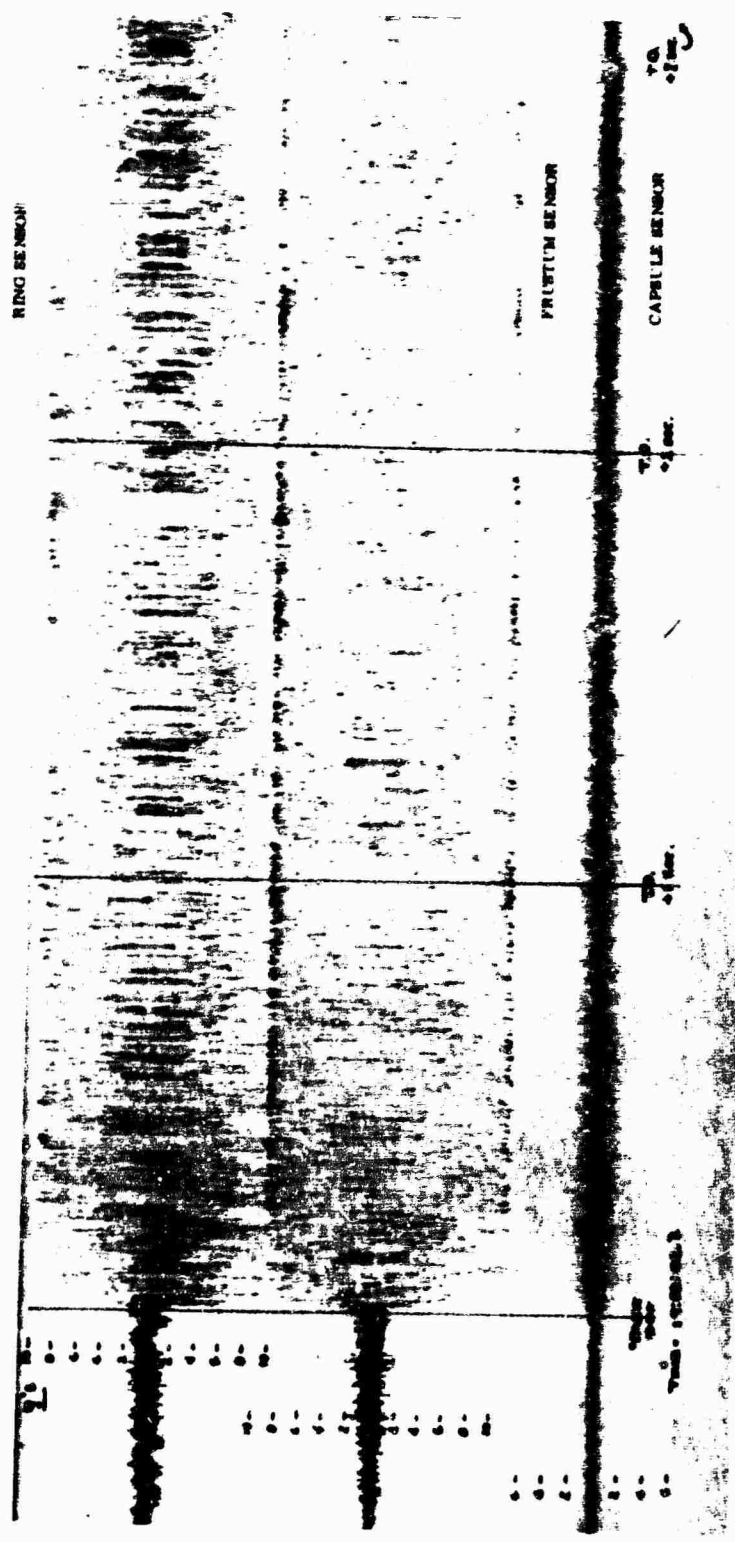


Fig. 11a. Time history of lift-off vibrations

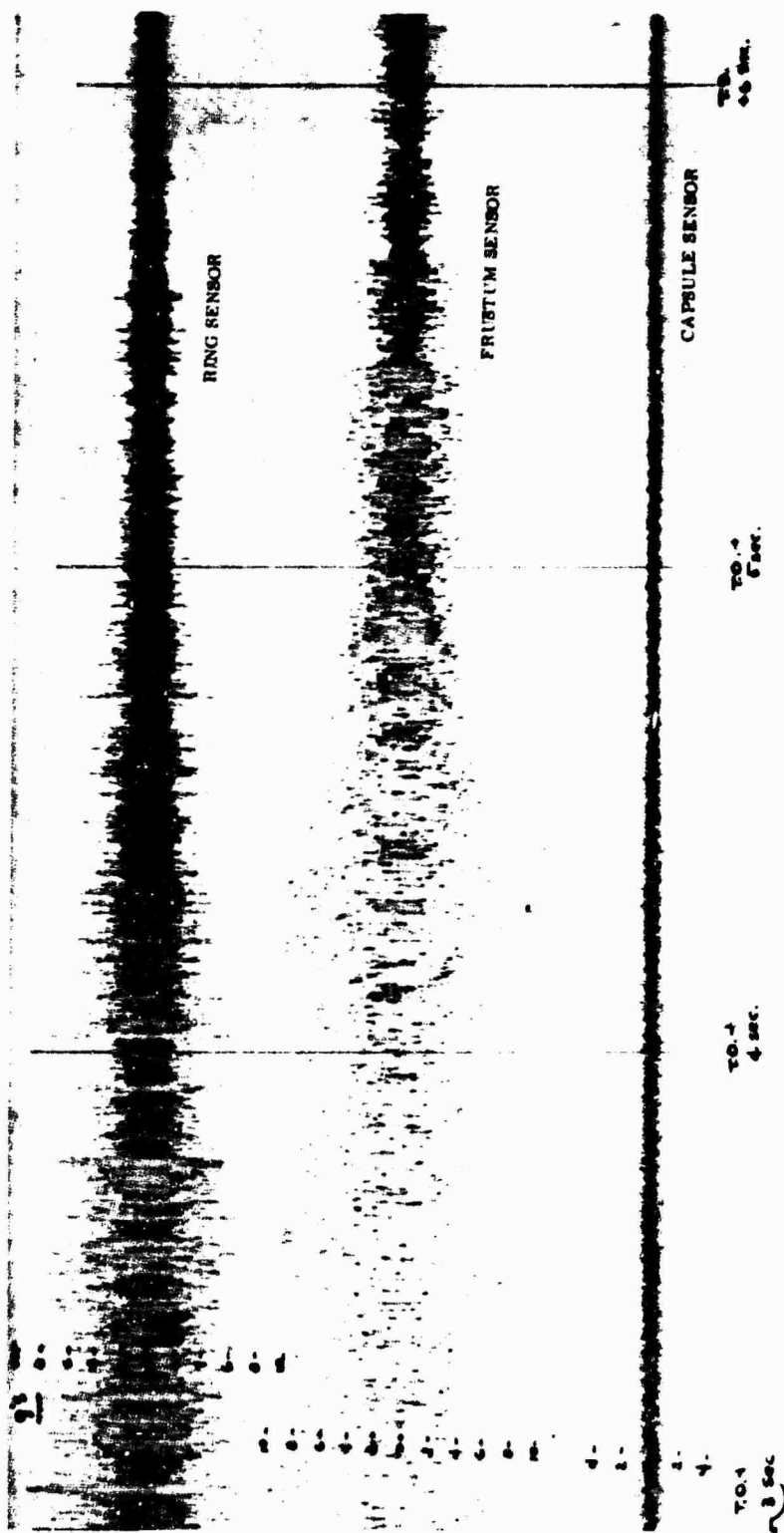


Fig. 11b. Time history of liftoff vibrations

the curves shown in Fig. 25. Second, where there was evidence of signal clipping, an estimate was made of the amount of clipping and correction factors were indicated. Finally, in the transonic region the vibration is at its maximum for too short a period of time to permit a reasonable loop length. For these cases a correction factor was established based on the ratio of  $1\sigma$  values indicated by the uncorrected PSD plot and by the oscillograph. For example, the ring sensor at Mach 1 was handled as follows:

1. From the oscillograph record the  $3\sigma$  peak values were measured at 8.0 g and the ratio of  $3\sigma$  to  $1\sigma$  was estimated at 3.6:1;  $1\sigma = 2.22$  g.
2. From the PSD plot the  $1\sigma$  is indicated to be 0.66 g.
3. The ratio of the two  $1\sigma$  values was assumed to result from the variation of the general vibration level during the time the PSD analysis was made. Thus the correction for the nonstationarity of the random vibration, applied to the PSD data of Fig. 9, is 3.33 for the g scale and 10 for the  $g^2/Hz$  scale.

There were a number of transient events during booster flight which were evidenced by the vibration sensors. Most of the transients indicated by the vibration sensors have been identified with specific flight events, as shown in Figs. 15 and 17. The unidentified transients probably originated in the booster and, as they were relatively mild, there was no attempt to obtain a positive identification.

The transients invariably show the major responses to be at relatively high frequencies and g levels. These high-frequency transient vibrations do not cause any significant structural loadings but may be of concern to equipment items. Unfortunately, the instrumentation sensitivity could not be set to obtain both the vibration data and the transient data. Proper sensitivity for the vibration data results in instrumentation saturation during the transient events. Proper sensitivity for the transients results in poor vibration data because of poor signal-to-noise ratio.

#### Flight Test Results

One of the first observations to be made on the flight vibration data is that each of the three measurements has significant differences from the other two. This leads to the conclusion, which is by now a well-established one, that the vibration at any point in a space vehicle is primarily dependent on the characteristics of the

local structure. The relationship between the measured vibration and the structural configuration is discussed below.

A second observation is that the highest responses can be attributed to resonant conditions of structure local to the vibration sensors, and the PSD's of these responses are almost two orders of magnitude greater than the general response level.

The differences between the vibration at the three locations are best illustrated in Fig. 26. The capsule sensor has the lowest level of vibration, never exceeding  $0.003 g^2/Hz$ . Referring to Fig. 1, this low level can be explained by the fact that this point in the structure is well removed from the acoustic excitation forces. The capsule is supported off the ring at station 24 with apparent resonant frequencies at 64 and 170 Hz as indicated by ground vibration results. The mass associated with these frequencies is the full mass of the capsule, approximately 120 lb, and, since response varies inversely with mass (from  $\ddot{x} = p/\gamma m$  for single degree of freedom at resonance), this response was low, as expected. The response of the capsule sensor at 930 Hz is a higher mode of vibration and represents motion local to the sensor location only.

The ring sensor is bolted to the flange of the station 24 ring, as shown in Fig. 1. This ring is the juncture of three conical sections (the booster adapter, forward frustum, and aft frustum), and it consequently has relatively high restraint to longitudinal, radial, and tangential motions. But the ring will twist fairly easily. The flight vibration data from this sensor are again as expected: the vibration levels are low, generally less than  $0.01 g^2/Hz$ , except in the 700- to 900-Hz range, where a maximum level of  $0.30 g^2/Hz$  is reached. The general low level is representative of a stiff structural juncture; the high-frequency response results from a twist mode of the station 34 ring and is representative only of motion local to the vibration sensor.

The vibration sensor on the T&AC frustum is located, as shown in Figs. 1 and 2, on the frustum skin between an attachment point of the programmer and the station 34 ring. The frustum is 0.020 aluminum skin with 0.032 bent-up channel stiffeners. There are stiffeners at the programmer attachment points, as shown in Fig. 2. The data from the ground vibration testing indicated resonant frequencies of 65, 90, and 110 Hz for the T&AC subsystem. Consequently, in this frequency range the frustum vibration sensor data are representative of

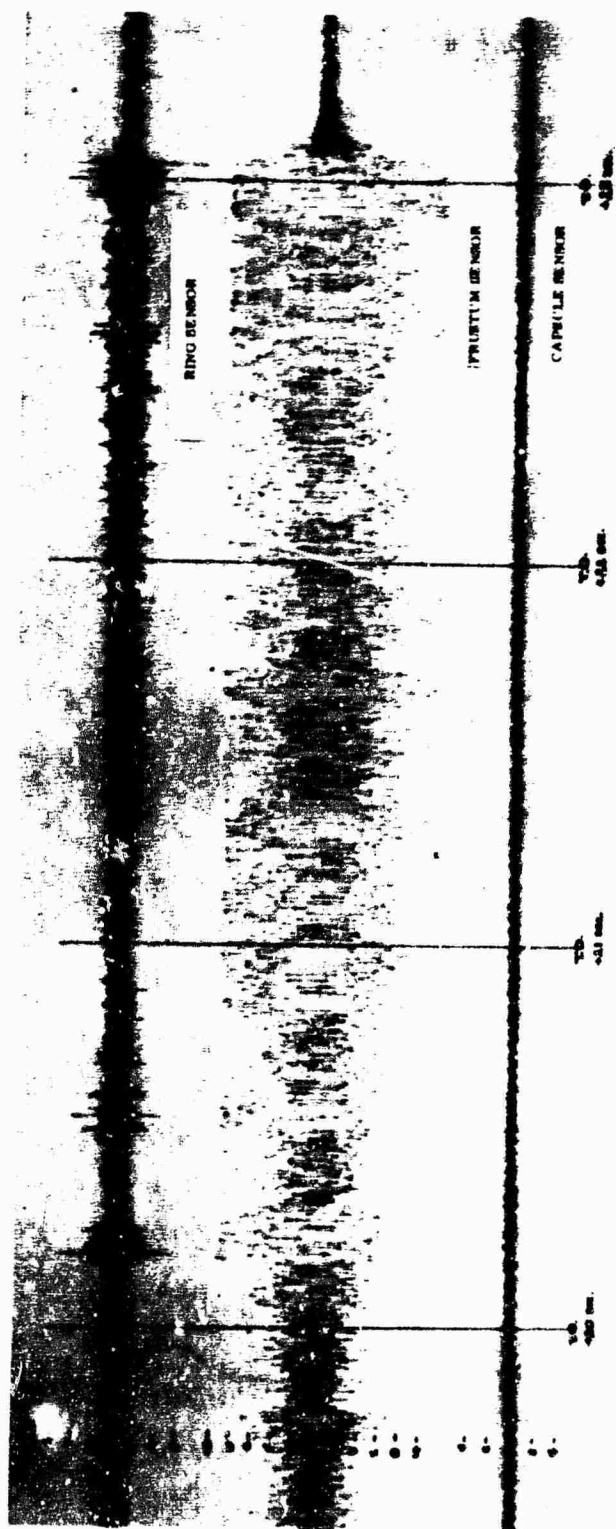


Fig. 12. Time history of transonic vibrations



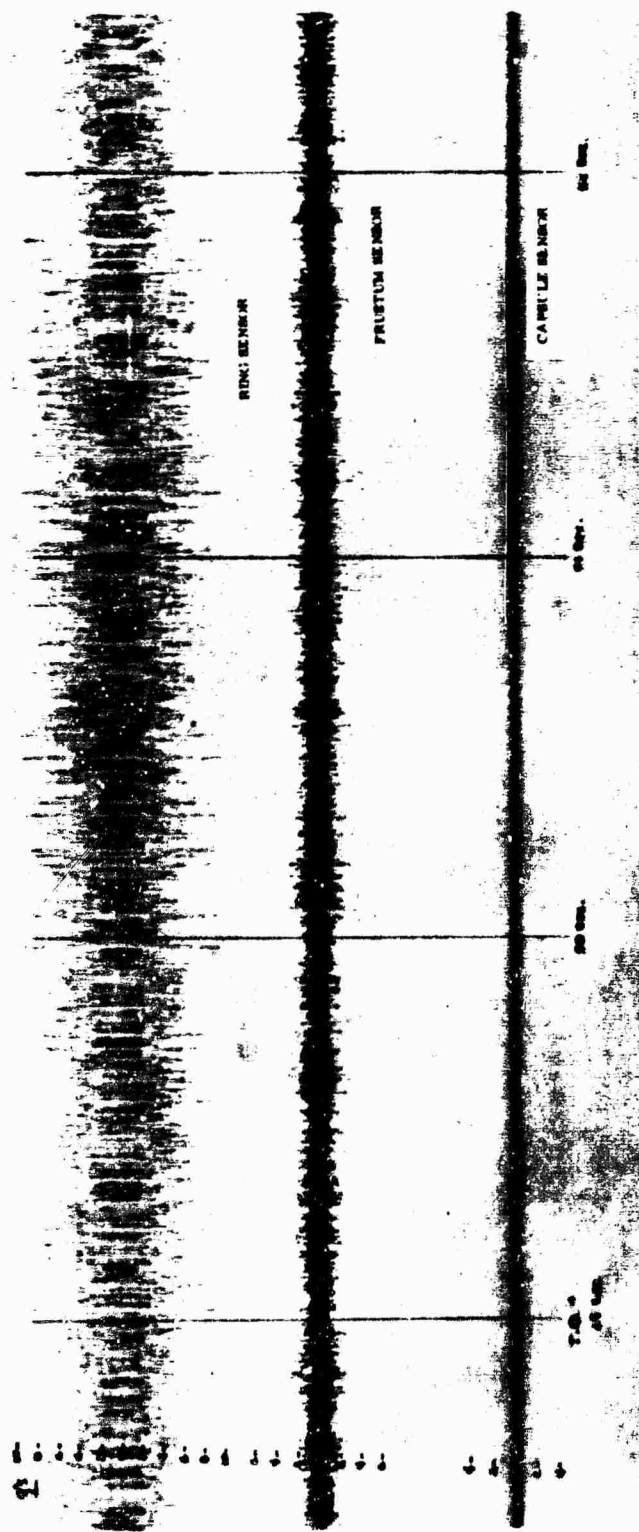


Fig. 13. Time history of max Q vibrations

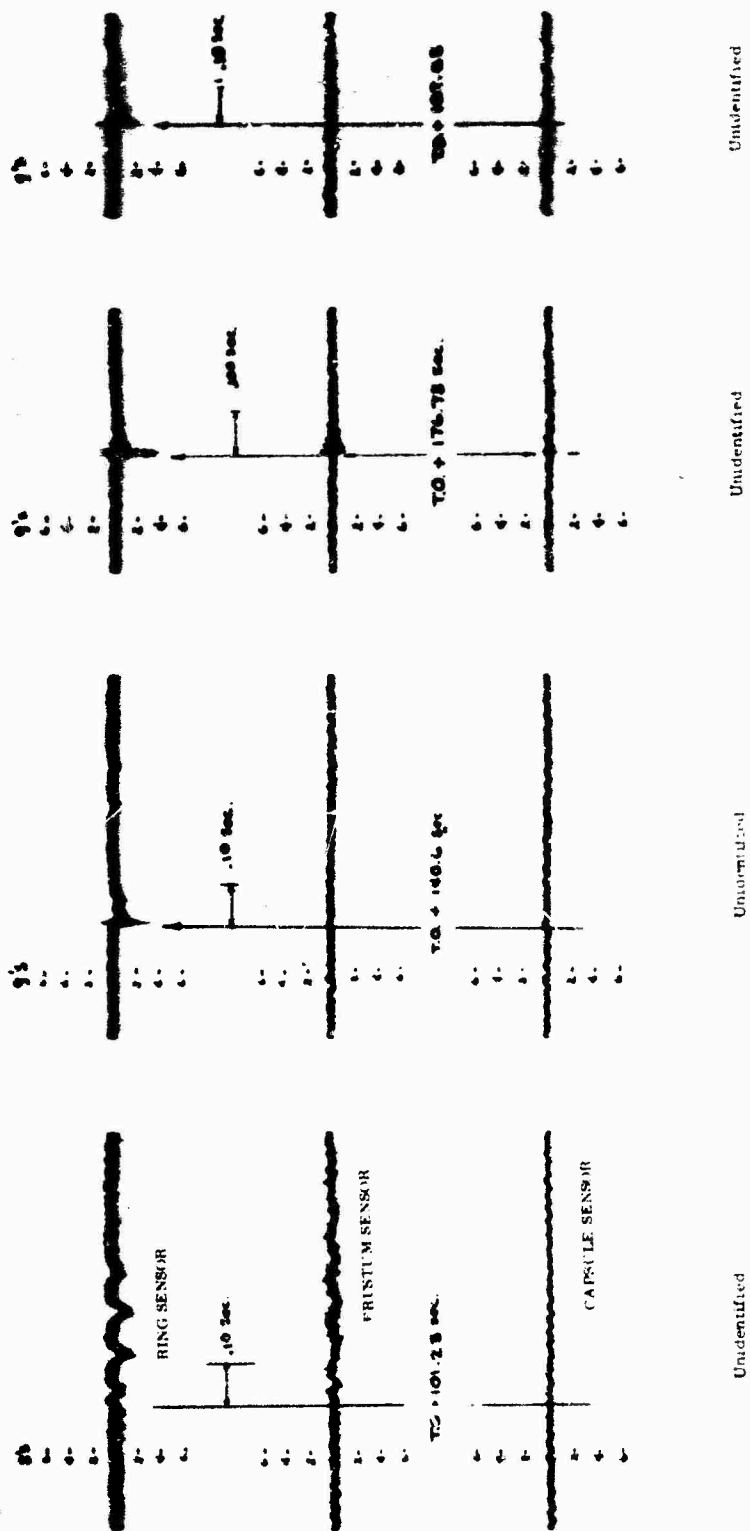
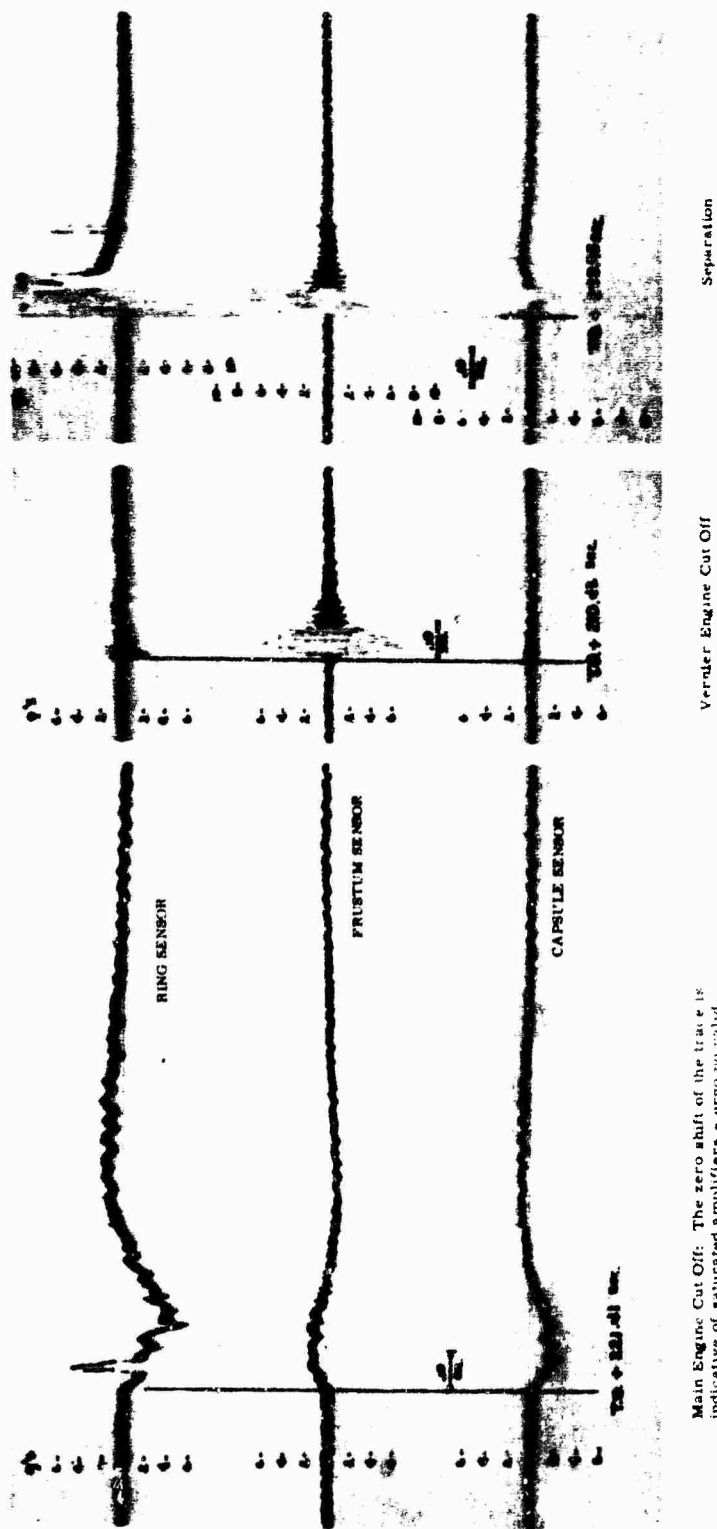


Fig. 14a. Transient events



Main Engine Cut Off: The zero shift of the trace is indicative of saturated amplifiers - ergo no valid data except that all sensors experienced well over 10 g.

Fig. 14b. Transient events

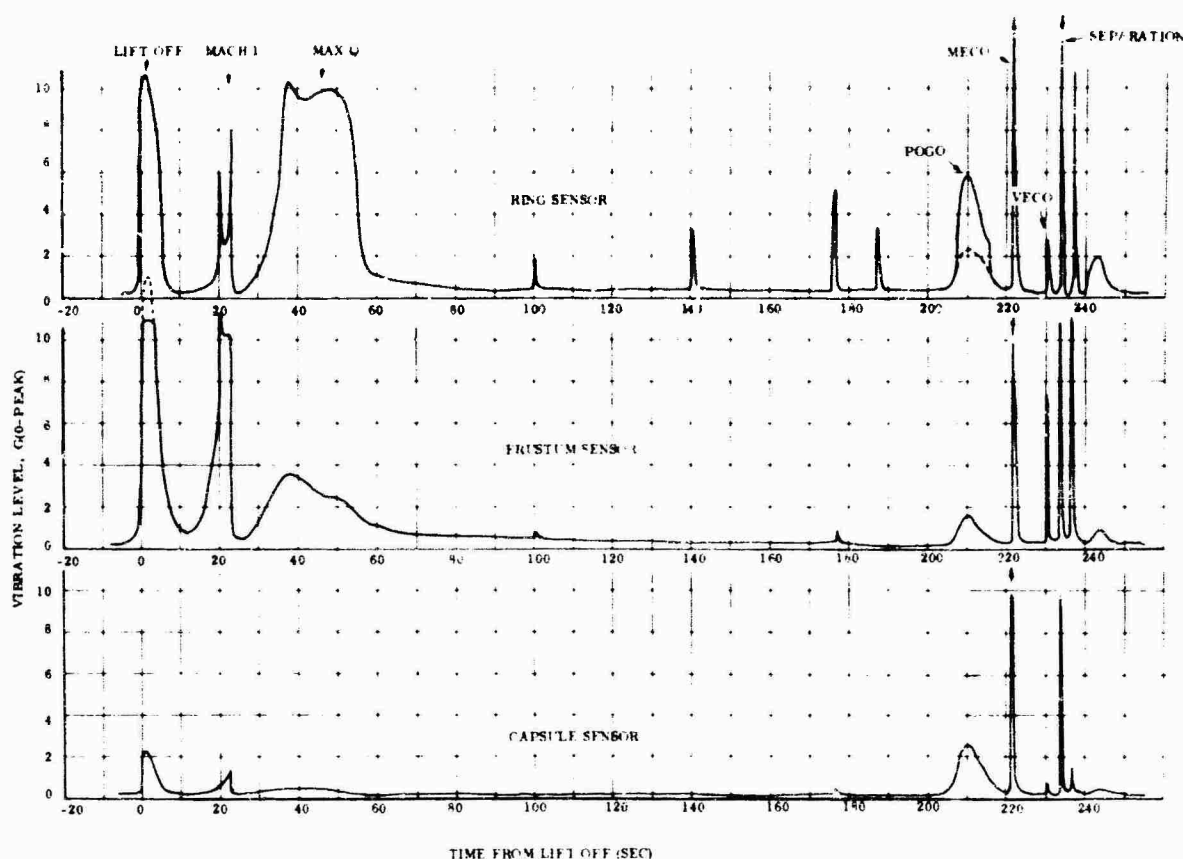


Fig. 15. Peak vibration levels, powered flight

programmer vibration. Above these frequencies, the programmer is for all practical purposes vibration isolated, and the vibration indicated by the frustum sensor is representative of the sensor motion only and not the programmer. Thus, the relatively high levels of vibration indicated by the flight sensor in the 150- to 450-Hz range result from resonances of the frustum skin local to the vibration sensor only.

Figure 26 is reconstructed in Fig. 27 in terms of  $3\sigma$  peak values to have the vibration in units comparable to the sinusoidal specifications applicable to this program. This was done by reading peak values of  $g^2/\text{Hz}$  from Fig. 26, multiplying by the half power frequency bandwidth of the associated peak, taking the square root to obtain the  $1\sigma$  rms value, and then multiplying this by 3 to obtain a  $3\sigma$  value. Normal distribution of peaks is assumed.

Internal environment envelopes, drawn on Figs. 26 and 27, envelop all values from the three sensors at the three periods of maximum vibration: liftoff, transonic, and max Q. The

peak vibration indications, which were shown to result from resonance effects of the vibration sensor attachment, were not included in these envelopes.

#### COMPARISON OF FLIGHT AND GROUND TEST VIBRATION

Comparisons of the flight data presented in this report and response data from ground vibration testing of the spacecraft are shown in Figs. 28, 29, and 30. The ground test data were from measurements at the same sensor location as the flight sensors, except for the frustum sensor. The difference in the locations of this sensor between ground test and flight test, shown in Fig. 2, is close enough to be comparable, with limitations.

One prominent conclusion which can be drawn from this comparison is that the qualification test requirements (Figs. 3 and 4) are extremely conservative. The most significant structural vibration load seen in flight is the

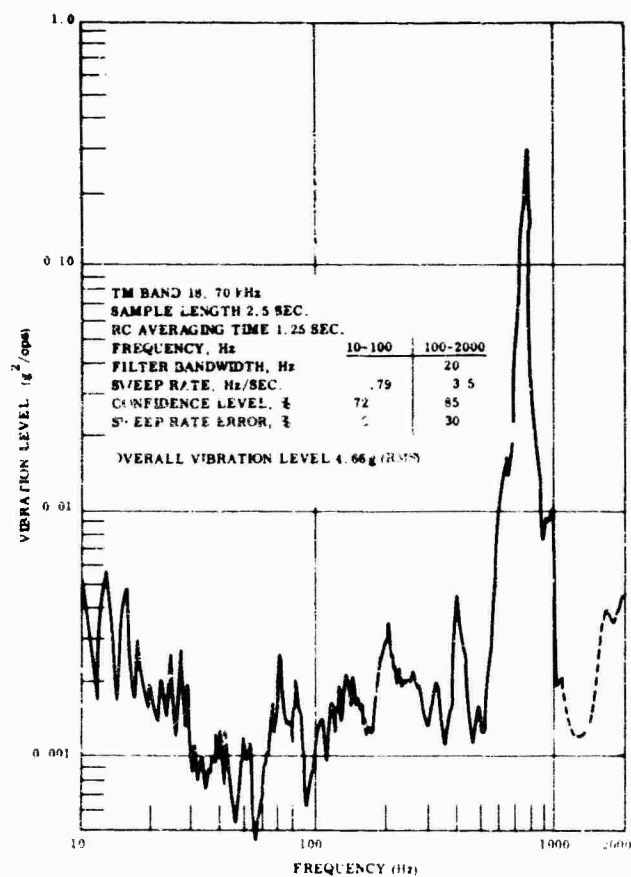


Fig. 16. Flight vibration data,  
ring sensor, liftoff

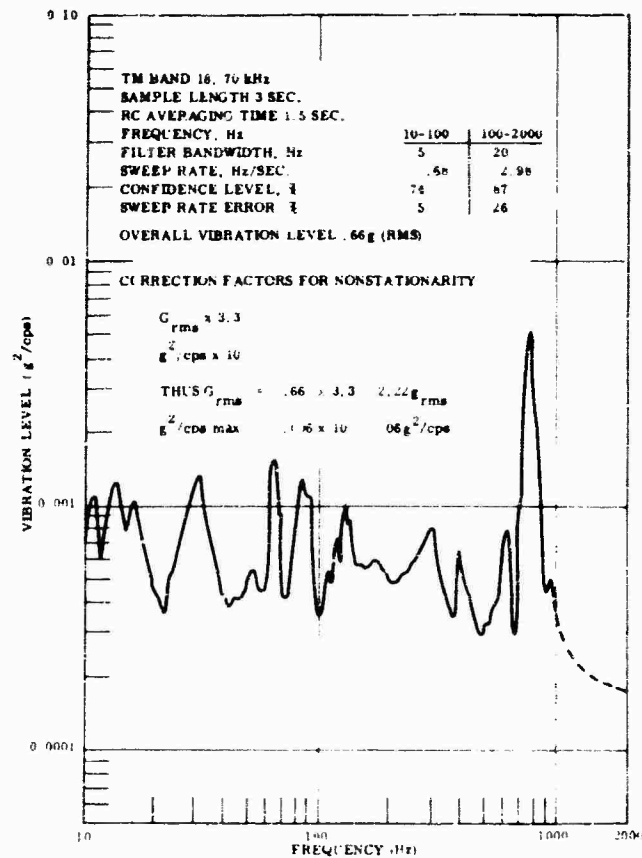


Fig. 17. Flight vibration data, ring sensor, Mach 1

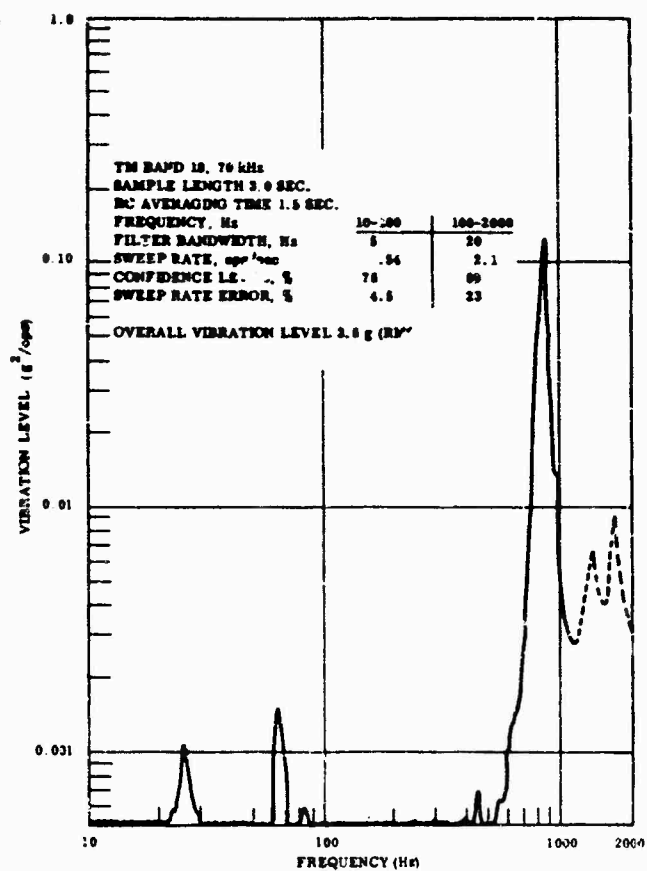


Fig. 18. Flight vibration data,  
ring sensor, max Q

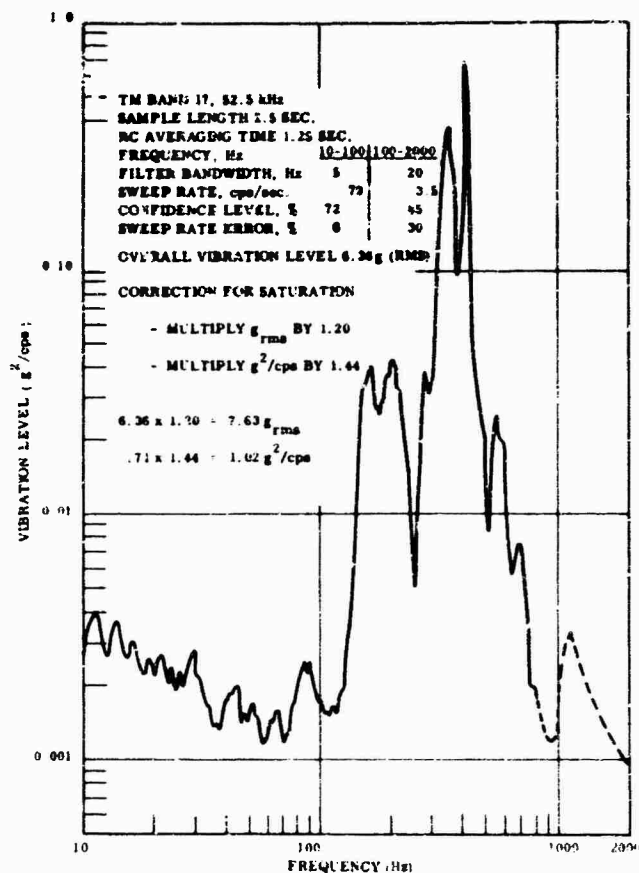


Fig. 19. Flight vibration data, frustum, liftoff

2.5-g "pogo" oscillation just before main engine cutoff. The most significant structural loads in the ground test are at the 60- and 110-Hz resonances, where load factors of up to 28 g are seen on the T&AC subsystem and up to 7 g in the capsule. The high-frequency responses are not directly applicable to structural loads or component environments, but they do show that the ground test responses exceed 100 g, compared to maximum flight measurement of 18 g.

#### CONCLUSIONS AND RECOMMENDATIONS FOR THE EXAMPLE SPACECRAFT

On the basis of the comparison of flight vibration responses and ground vibration test responses, the system qualification test requirements as shown in Fig. 3 are very conservative. The ground test loads are higher by factors of between 2.8 and 11.2. The ground test high-frequency responses are higher than the flight measurements by factors of up to 6.0.

Although reductions of system qualification test requirements could be made with relatively small loss in probability of flight success, the increased risk of failure in ground qualification testing is also small and is the preferred approach.

The internal vibration envelope (3.0 g max) shown in Fig. 19 reveals that there is also a high degree of conservatism in the component qualification requirements of 10 g (5-1000 Hz) and 15 g (1000-2000 Hz). However, as in the system test requirements, the recommendation is made not to reduce the requirements.

Although no change to the system and component vibration test requirements is recommended, improvement in the test can and should be made. The changes should be to a better simulation of actual flight vibration while maintaining the present high degree of conservatism. This would include system acoustic testing and random and sine vibration testing at both the system and the component levels.



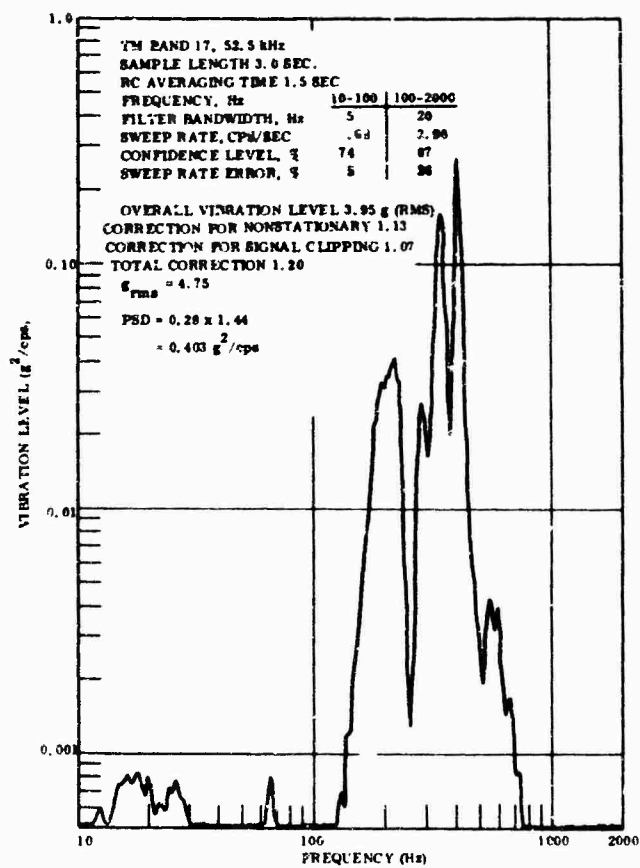


Fig. 20. Flight vibration data, frustum, Mach 1

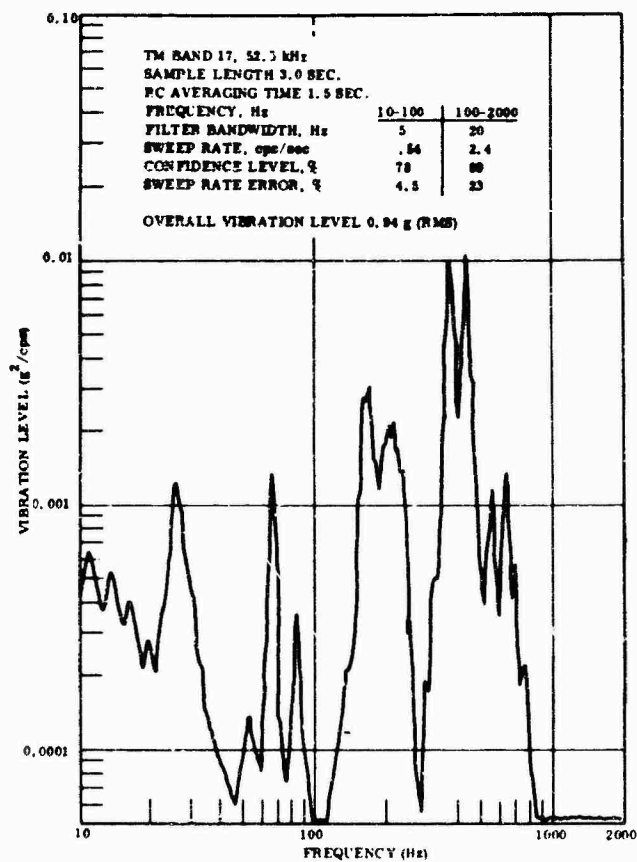


Fig. 21. Flight vibration data, frustum, max Q

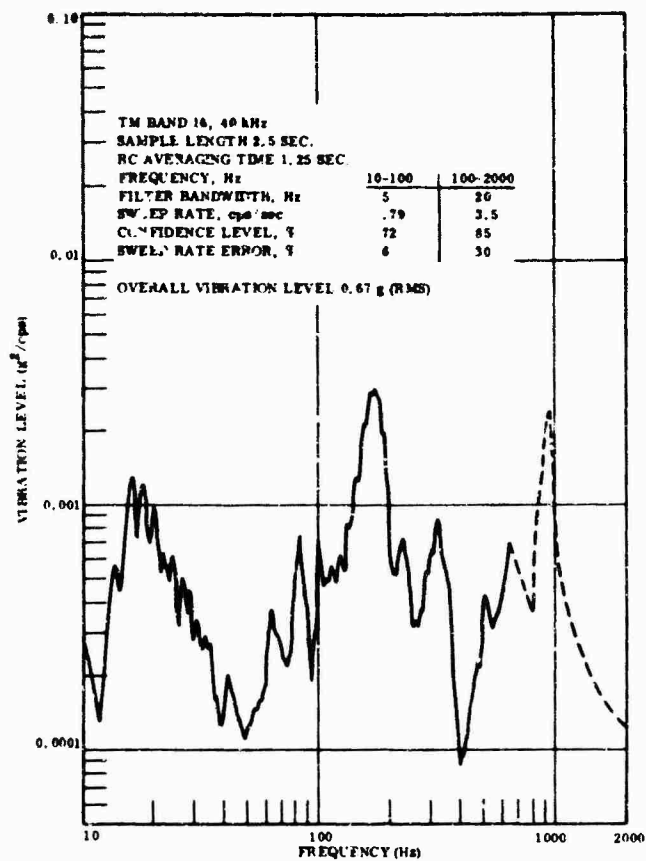


Fig. 22. Flight vibration data, capsule, liftoff

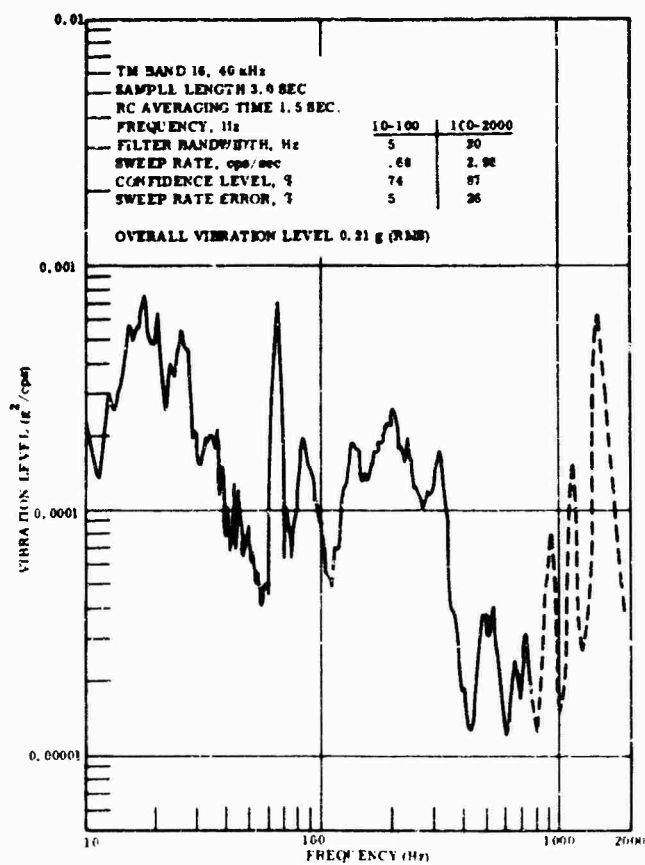


Fig. 23. Flight vibration data, capsule, Mach 1

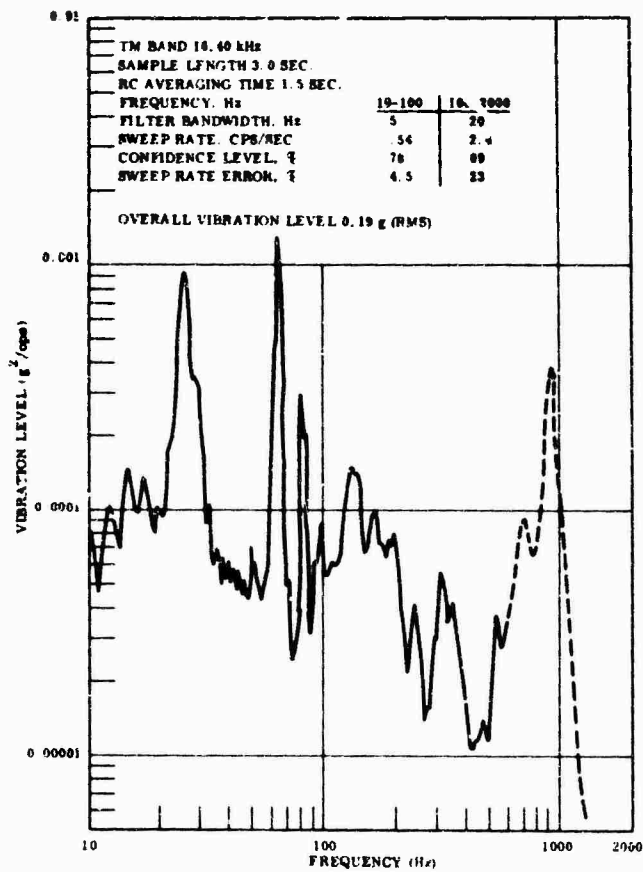


Fig. 24. Flight vibration data, capsule, max Q

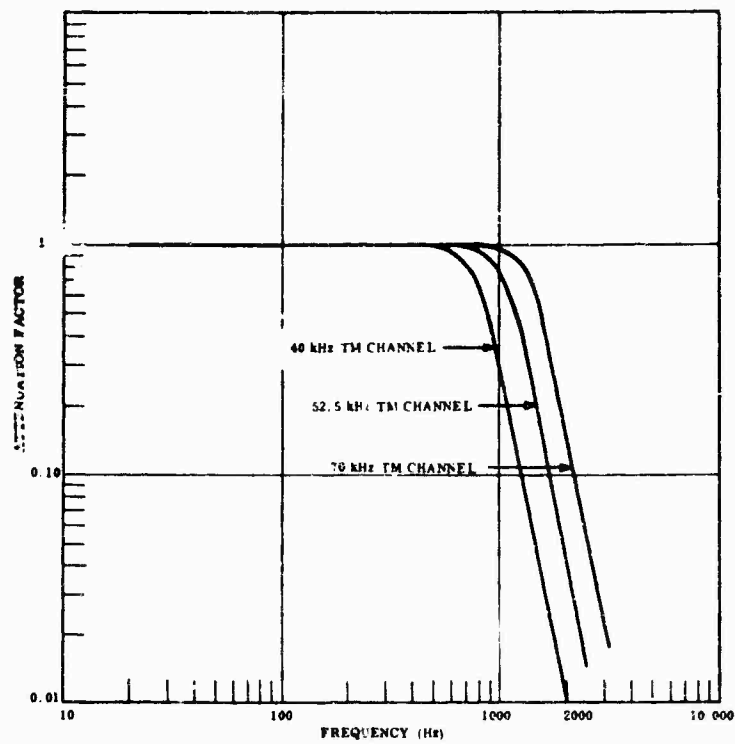


Fig. 25. Standard IRIG low-pass filter characteristics

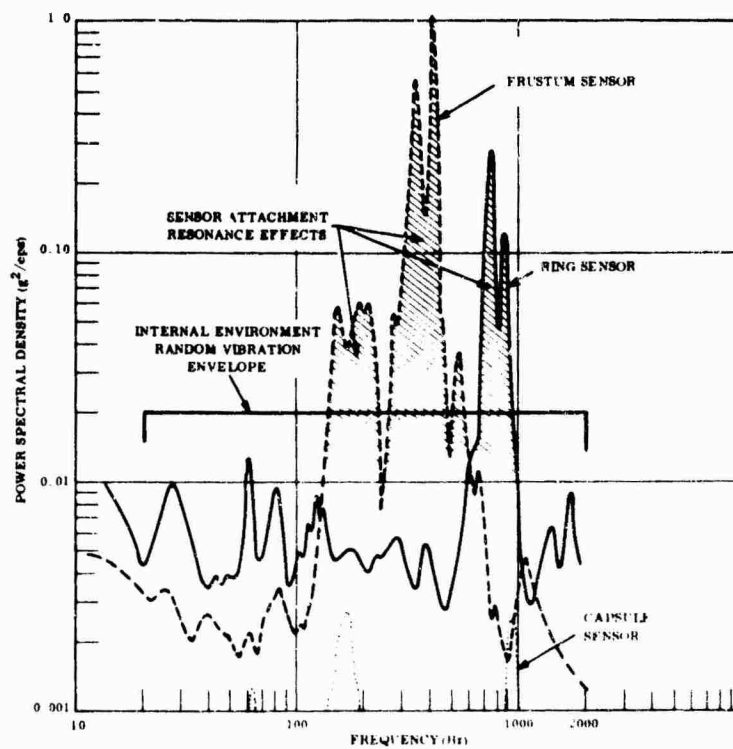


Fig. 26. Composite of flight vibration data obtained by enveloping liftoff, transonic, and max Q data

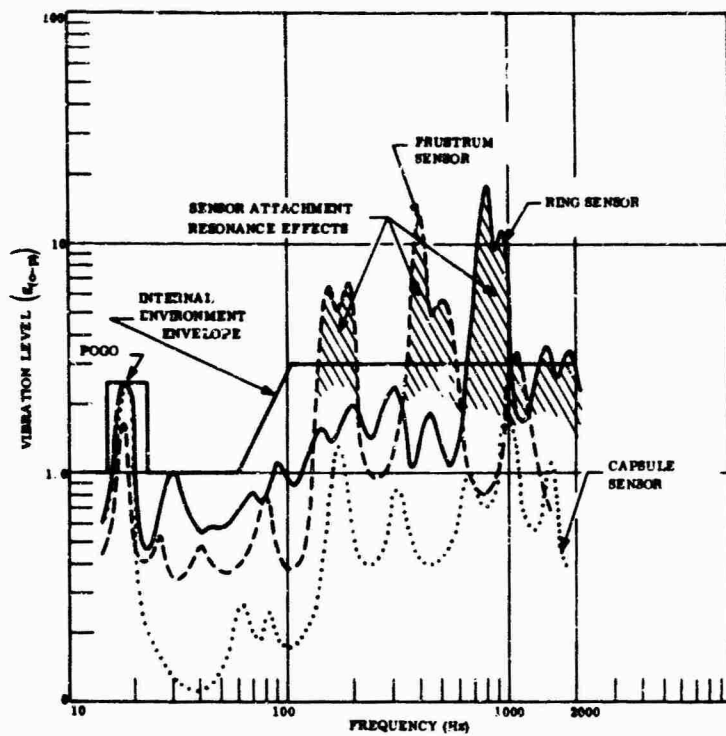


Fig. 27. Composite of flight vibration data,  $3\sigma$  levels

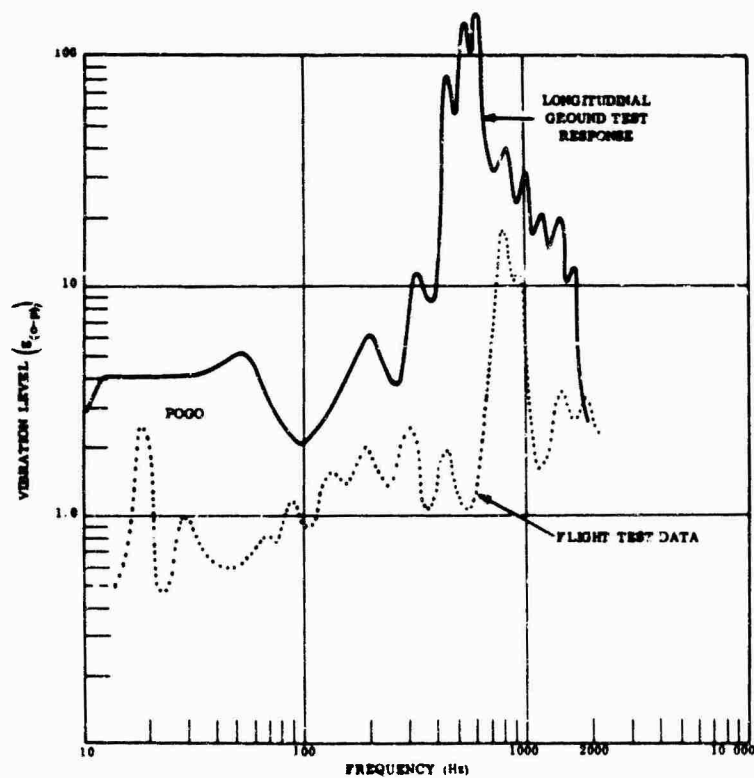


Fig. 28. Ground test and flight test measurements compared, ring sensor

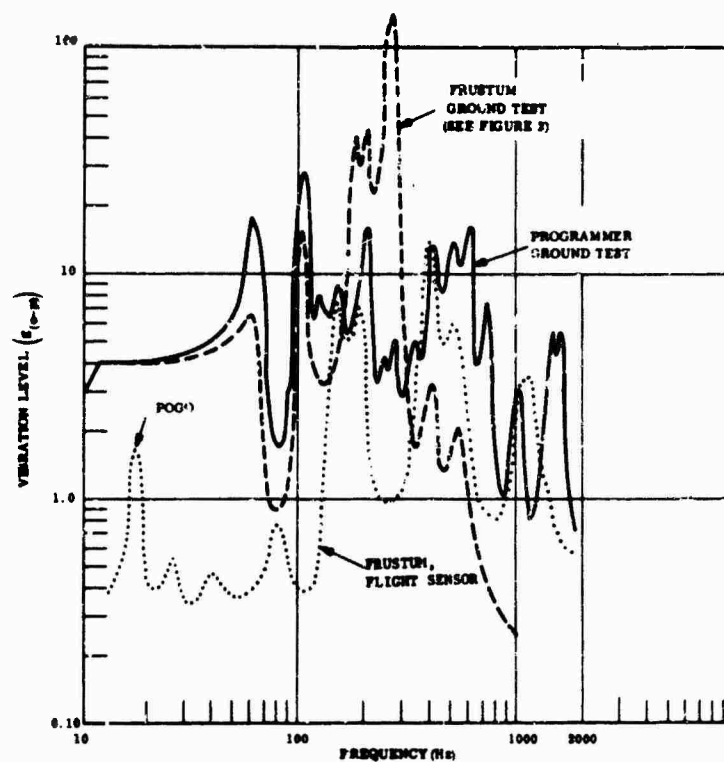


Fig. 29. Ground test and flight test data compared, frustum

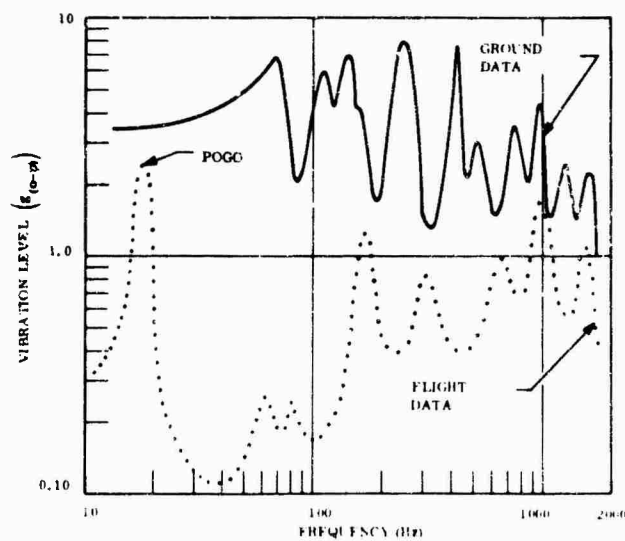


Fig. 30. Ground test and flight test data compared, capsule



On the basis of the random and sine environment envelopes shown in Figs. 26 and 27, the following component vibration qualification requirements would be recommended for future similar spacecraft:

1. Random-vibration qualification test: 20-2000 Hz,  $0.10 \text{ g}^2/\text{cps}$  applied for 4 min along each of three mutually perpendicular axes;
2. Sinusoidal-vibration qualification test: 10-2000 Hz, 6.0 g (0 peak) applied as a frequency sweep at the rate of 1 min/octave going up from 10 to 2000 Hz and back to 10 Hz, with amplitude limited by shaker capability, along each of three mutually perpendicular axes;
3. Both random and sine requirements are to be applied, but separately.

The system qualification vibration test can at best be a compromise, since a mechanical excitation will not generate the same vibration responses as an acoustic excitation and since the acoustic environment, including correlation characteristics, cannot be reproduced accurately in the test laboratory. For the subject spacecraft the following recommendation is made:

1. Sinusoidal vibration, 10-200 Hz: (a) constant-g sine sweep: 2.0 g (0 peak) longitudinal, 1.0 g (0 peak) lateral (2 axes); (b) constant-force sine sweep:  $F = 2W$  (spacecraft) longitudinal,  $F = W$  (spacecraft) lateral (2 axes) applied at a sweep rate of 1 min/octave up and back, 10-200-10 Hz, total test time 60 min.

2. Acoustic test: the spacecraft is to be mounted on a structurally similar section of the booster which is at least one booster diameter in length and placed in a reverberant acoustic chamber. The acoustic environment generated in the chamber shall have the same spectrum as the liftoff acoustic environment, but 6 db higher.

3. Random vibration (alternate for acoustic test): a frequency of 100- to 2000-Hz flat spectrum with input force = spacecraft weight (rms pounds) applied for 4 min in the longitudinal direction, and 0.5 spacecraft weight for 4 min in each of two mutually perpendicular lateral axes. Total random vibration test time is 12 min.

#### COMPONENT VIBRATION CRITERIA FOR THE GENERAL CASE

The empirical approach offered below is felt to be a practical and accurate means for

predicting the internal vibration environment for a new spacecraft. The approach recommended entails five steps.

#### Step 1 - Compilation of Flight Vibration Data from Similar Spacecraft

Similarity criteria are covered in steps 3 and 4 below.

#### Step 2 - Evaluation of Flight Data

As shown in the example spacecraft of this report, it is very important that the resonant peaks indicated by the flight data be identified with the three categories of resonance: booster and spacecraft overall structural, component mounting, and sensor mounting. This identification is easiest when accomplished during vibration tests prior to flight. Without these data a chart similar to Fig. 31 can be developed. The three frequency bands for spacecraft, component, and sensor resonances are shown as being very broad for the general case. For a specific spacecraft these frequency bands can be made narrower. Figure 31 indicates that any resonant peak which is above 800 Hz is very probably the result of a very localized resonance and should not be considered as component vibration environment. Resonant peaks in the 300- to 800-Hz range could be either component resonance (for a light component) or sensor mounting resonance.

Evaluation of the flight data should also categorize general location in the spacecraft, such as shell mounted, internally mounted (integral structure), or internally mounted (truss). A truss is defined as any relatively large massive structural assembly used primarily for the support of equipment, with high-impedance structural path to the outer shell. The output of this step is a definition of component vibration environments for the reference spacecraft.

#### Step 3 - Conversion Factors

Establish conversion factors relating new spacecraft to reference spacecraft for the following parameters:

**Component Location** - The applicable reference spacecraft data (shell mounted, truss mounted, etc.) would be used. However, if data for a location category are not available, factors relating the vibration for different locations should be established (for example,  $g_{\text{internal}} = 0.5 g_{\text{shell}}$  and  $g_{\text{truss}} = 0.25 g_{\text{shell}}$ , where  $g$  = vibration level in gravity units and where similar spectra are assumed).

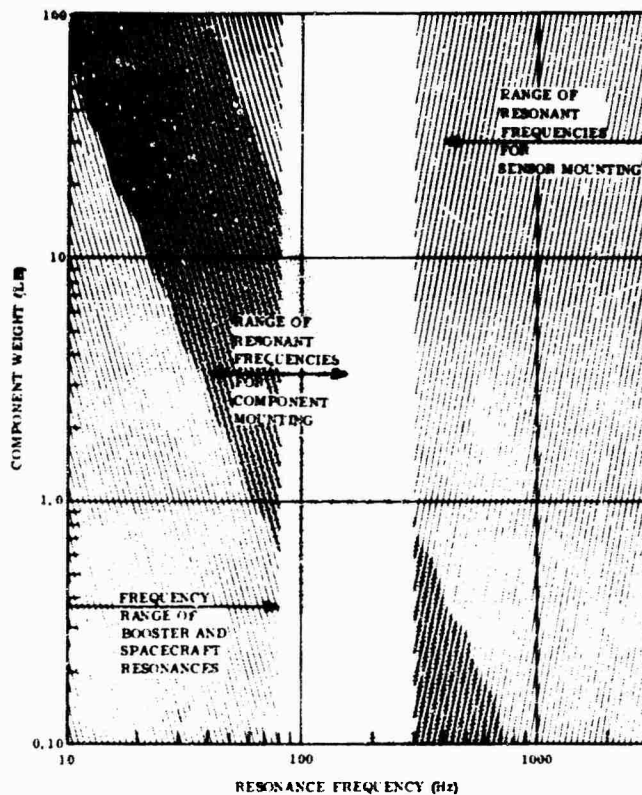


Fig. 31. Frequency bands of resonant frequencies for spacecraft in general

**Component Weight** — Adjust the vibration environment by the factor of 0.5 db (g level)/weight ratio. For example, an environment which causes a  $0.04 \text{ g}^2/\text{Hz}$  peak level for a 10-lb component will cause a  $0.04 \text{ g}^2/\text{Hz} + 5 \text{ db}$  or  $0.124 \text{ g}^2/\text{Hz}$  peak level for a 1-lb component.

**Spacecraft Density (in Terms of Weight per Unit Surface Area)** — Obtain this factor by dividing the total spacecraft weight by the spacecraft external surface area exposed to the acoustic environment. Use this in the relationship

$$\frac{g_{\text{new}}}{g_{\text{ref}}} = \frac{W_{\text{D ref}}}{W_{\text{D new}}}$$

**Spacecraft Structural Damping** — This factor can be applied only as an approximation since damping properties are not predictable with any degree of accuracy. Monocoque shells, large flat panels, welded joints, and generally simple structures will be lightly damped. Complex built-up structures with bolted or riveted joints and no plain, flat panels will be heavily damped. Corrections should be made if either the old

or the new spacecraft tends toward either extreme:

$$g_{\text{new}} \gamma_{\text{new}} = g_{\text{ref}} \gamma_{\text{ref}}$$

$$\gamma = \frac{c}{c_c}$$

**Sound Pressure Level of the Acoustic Environment** — The liftoff environment is generally more severe than transonic or max Q and is the main criterion. However, any sharp irregularities (hammer heads) in the external contours should be taken into consideration.

$$\frac{g_{\text{new}}}{\text{SPL}_{\text{new}}} = \frac{g_{\text{ref}}}{\text{SPL}_{\text{ref}}}$$

where SPL = sound pressure level, psf.

#### Step 4 — Prediction of New Spacecraft Internal Environment

This prediction is accomplished by combining steps 2 and 3.

#### Step 5 - Define Component Qualification Levels

It is usual practice to define component vibration qualification levels at 1.5 times the maximum environment levels. This is an artificial factor since the environment is never accurately definable at the time the qualification levels are established. Often the component qualification requirements are defined first, and the environment level is then defined as equal to 67 percent of the qualification levels.

If sufficient measured vibration data are available, a statistical analysis can be performed, and acceptance levels, flight environment levels, and qualification levels can be defined in terms of percentiles, confidence lines, or other terms, depending on the type of analysis performed. The approaches used throughout the industry vary, and unfortunately the qualification levels developed also vary.

If the approach recommended here is used, i.e., reducing the high-frequency peaks resulting from vibration sensor mounting resonance, a factor of 2 is recommended between the maximum vibration g level predicted and the qualification g level.

#### SPACECRAFT TESTING FOR THE GENERAL CASE

There are four basic reasons for performing vibration testing of the complete spacecraft:

1. Demonstrate structural integrity;
2. Demonstrate the adequacy of electrical wiring, tubing and ducting, and associated connectors and bracketry;
3. Verify the performance of equipment in the spacecraft;
4. Demonstrate that the total system will function properly and within specification limits during and after exposure to the flight vibration environments.

The actual flight vibrations can be divided into low frequency (below 100 Hz) vibrations, resulting from the total booster system vibration, and high-frequency vibrations resulting from the acoustic environment. The low-frequency vibrations can be faithfully reproduced in the system vibration test, but not the high-frequency acoustically induced vibrations. Ideally, a combined vibration and acoustic test would be performed. However, since the

significant structural loads result from the low-frequency vibrations and since the significant component vibration is in the high-frequency range, the separate performance of low-frequency vibration and acoustic tests is permissible.

The amplitude of excitation of the low-frequency vibration is determined most logically through analyses of booster dynamic response to determine spacecraft structural loads and analyses of spacecraft dynamic response to determine what excitation is needed to match these loads. Both constant-g sine testing and constant-force sine testing should be performed so that both low-impedance and high-impedance resonant modes are excited.

The acoustic test should be performed with the acoustic level higher than expected; a 6-db increase is recommended. A section of the booster, one diameter in length, should be attached to this spacecraft in the acoustic test.

If the performance of the acoustic test is not feasible, a random-vibration test may be substituted. However, the amplitude of excitation is difficult to define because of the inherent inaccuracy of this test approach, i.e., because of the use of a point application of a mechanical force to represent an acoustic excitation. It is recommended that a best estimate of the random excitation force be made, and this excitation be adjusted to give the predicted response internal to the spacecraft.

#### CONCLUSIONS

The conclusions reached in this report center on the three basic points summarized below. It is hoped that the data and arguments which have been presented have convinced the reader of the plausibility, not the validity of the conclusions reached, and that sufficient interest has been aroused for others to look for the data which will prove or disprove these conclusions for their case in hand.

Vibration testing of a complete spacecraft cannot be made to duplicate internal flight vibration environments satisfactorily. Because of this discrepancy, the system test results should not be used to define internal, or component, environments. Internal environments should be defined from flight vibration measurements on similar spacecraft. The system vibration test has its primary usefulness in demonstrating structural integrity and the adequacy of tubing, ducting, electrical wiring, and associated connectors and bracketry.

Flight vibration measurements must be frequency analyzed and identification made of the resonant peaks as to whether they are representative of component environment. Any narrow-band, high-level vibration above 300 Hz is open to question; peaks above 800 Hz should be ignored.

The margins between the flight vibration levels and the qualification levels of components

are held to be actually higher than usually assumed, because sensor mounting resonances are not usually corrected. Because of the many uncertainties involved with both the environment and the component capability, large margins are necessary. A minimum of 2:1 is recommended, and margins of up to 3:1 are preferred.

\* \* \*

# MEASUREMENT AND ANALYSIS OF GUN FIRING AND VIBRATION ENVIRONMENTS OF THE RIVER PATROL BOAT

R. S. Reed  
Naval Ordnance Laboratory  
Silver Spring, Maryland

The River Patrol Boat (PBR) is a 30-ft, dual-engine, fiber-glass boat which uses a pump propulsion system. The vibration environment was measured at seven locations, chosen because they were present or proposed weapon mounting locations or because they were logical storage locations. The measurements were made under conditions which included high speed, medium speed, bow slap (condition created by turning into the wake), and gun firing. The data were analyzed using a general purpose digital computer to determine power spectra, amplitude distribution, and shock spectra (when appropriate). In general, the analyses indicated that most of the vibration energy was below 400 Hz and that overall acceleration levels ranged from 0.07 to 0.86 g rms (excluding the firing data). The amplitude distributions had Gaussian forms. The transient firing data had peaks as high as 23 g; the major shock spectrum peaks occurred at 1500 Hz and were in the 50- to 100- $\gamma$  range.

## INTRODUCTION

The recent and extensive application of small craft for river patrol duty has created a need for a more thorough understanding of small craft vibration environments. Vibration measurements were made on the Patrol Boat, River (PBR) (Fig. 1). The analyses of these data are summarized in this paper. The interpretation of the results is left to the designers

and environmental engineers using the information.

So that an effective measurement and analysis program could be planned, preliminary measurements were made using hand-held vibration transducers and portable level meters. The measurements helped to determine to what extent the vibration environment was dependent on location, direction, and the speed of the boat.



Fig. 1. Patrol Boat, River

## INSTRUMENTATION AND ANALYSIS

Using the measurements and a certain amount of judgment, seven locations were chosen as representative of the vibration extremes found on the boat. The locations chosen are:

1. The carriage of the Mk 30 Mod 0 Twin 0.50-cal. machine gun (Fig. 2a). This location was chosen primarily to measure the transient created by the gun firing.

2. The storage area in the bow (Fig. 2b). This location was chosen because it is the most logical for storing munitions. The preliminary measurements had indicated that the levels were significant.

3. The rear armament mount (Fig. 2c). The mount was without a weapon during the test, which would indicate that more data would be necessary if meaningful estimates of the environment were needed for the loaded condition. The locations were at the deck below the mount and the top of the tripod mount itself.

4. The forward gun mounting ring, port and starboard (Fig. 2d). These locations were instrumented primarily because of the presence of the 0.50-cal. machine gun which was in place. The locations would also generate information which would be of use in evaluating lighting and sighting devices which might be used with the gun.

5. The gunwales (upper edge of a boat side) (Fig. 2e). These have been suggested as a possible location for the mounting of armament. Preliminary measurements indicated significant levels at this location.

6. The locations which were instrumented are shown schematically in Fig. 3. In addition to the obvious dependence on location and direction, it was assumed that the vibrations were dependent on boat condition. For this reason three conditions, in addition to gun firing, were chosen as typifying those found in service. The high-speed (24 knots at 2600 rpm) condition was chosen as representative of the craft when in pursuit or retreat. The medium-speed (20 knots at 2000 rpm) condition was chosen as

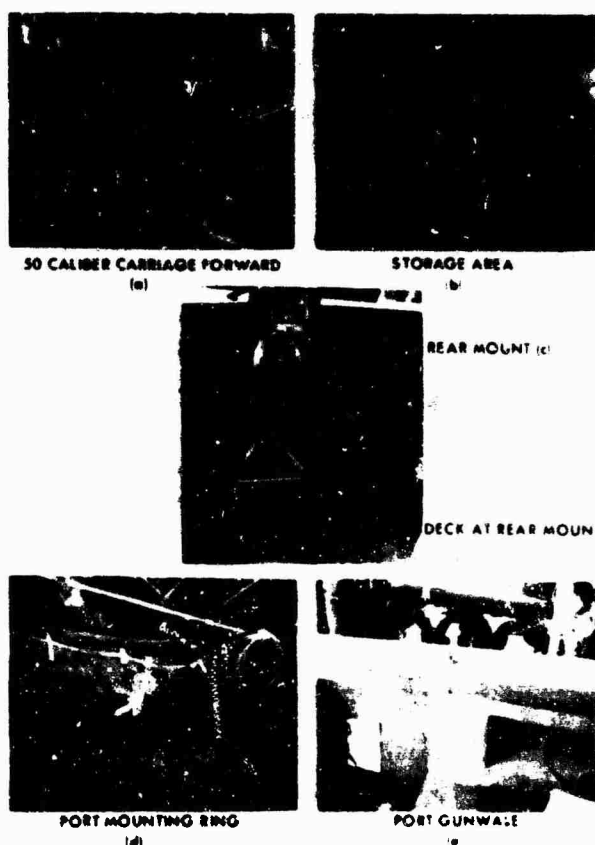


Fig. 2. Accelerometer locations

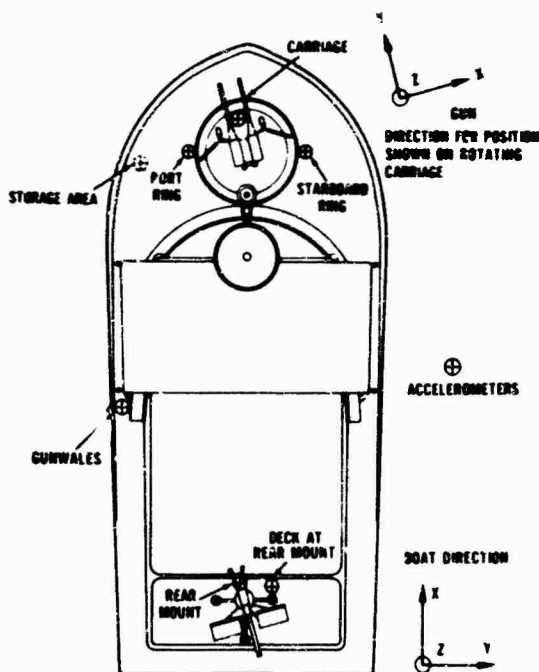


Fig. 3. Schematic diagram of accelerometer locations

representative of the boat during normal patrol. The final condition was bow slap, the condition created by turning the boat into its own wake at full speed (a maneuver which slowed the boat considerably). The gun firing or transient data were recorded with the boat at a speed which was just sufficient for holding its course. Because of mechanical difficulties, only a single gun was fired. The gun was fired to port.

To avoid problems which might be encountered in adapting instruments to operate on the boat's internal power, it was decided to devise instrumentation (Fig. 4) that could operate completely independently of the boat. Since the Honeywell 8100 recorder has facilities for operating on two 12-v batteries, this was chosen as the recorder, and two 12-v lead storage batteries were chosen as the power pack. A Terado 600-w inverter was used to produce 110-v, 60-cycle power for the remaining instrumentation gear. The transducers chosen were Endevco model 2272 piezoelectric accelerometers. The outputs of six accelerometers were recorded using Endevco model 2712A charge amplifiers for impedance and sensitivity requirements. The six data channels were periodically given

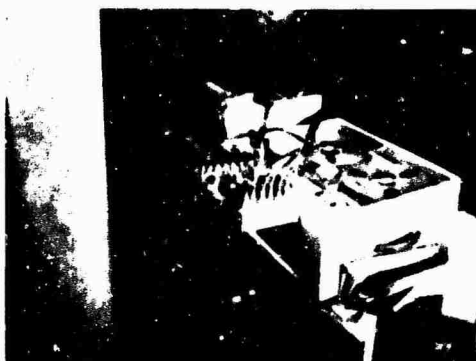
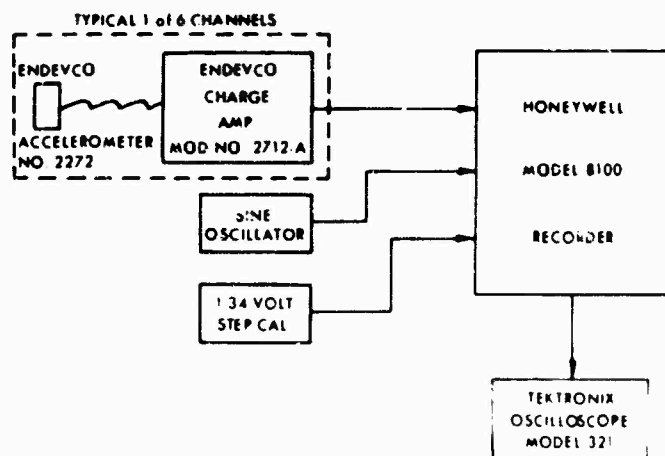


Fig. 4. Instrumentation

TABLE 1  
Overall Acceleration Levels (rms g)

Condition and Axis	50-Cal. Mounting Ring, Port	50-Cal. Mounting Ring, Starboard	Forward Below Deck Storage Area	Port Gunwale	Deck at Rear Mount	Rear Armament Mount
High speed, X	0.16	—	—	0.86	—	0.63
High speed, Y	0.11	0.12	0.12	0.75	0.64	0.83
High speed, Z	0.16	0.14	0.26	0.77	0.73	0.68
Bow slap, X	0.17	—	—	0.82	—	0.73
Bow slap, Y	—	0.11	0.12	0.83	0.73	0.83
Bow slap, Z	0.15	0.13	0.25	0.75	0.83	0.73
Medium speed, X	0.10	—	—	0.60	—	0.45
Medium speed, Y	0.09	0.14	0.08	0.36	0.29	0.40
Medium speed, Z	0.07	0.11	0.20	0.44	—	0.44

a 1.34-v step calibration signal. The seventh channel was used alternately for voice and an additional 500-Hz sinusoidal calibration. A Tektronix model 321 oscilloscope was used to check the data tapes.

#### Steady-State Analysis

Oscillograph playback and high-pass filters with meter readout indicated that the vibration levels were insignificant above 4 kHz for the nonfiring runs. Two-second portions of data were then digitized using an 8-kHz sampling rate. The firing run data, however, indicated that higher frequencies were present. For this reason the firing data were digitized at a 16-kHz sampling rate. The nonfiring data were analyzed for PSD (Blackman-Tukey method [1]) and amplitude distribution.

The overall levels of vibration are shown in Table 1, which shows that the acceleration levels were dependent on location, orientation, and boat conditions.

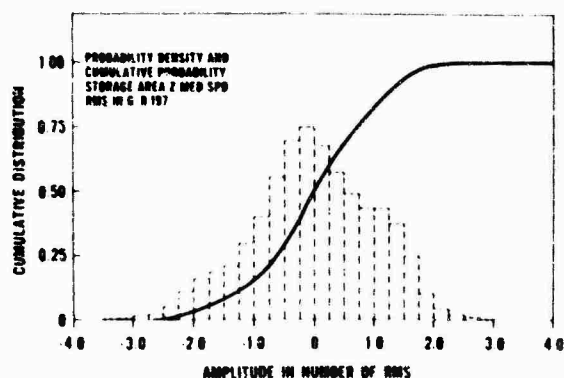


Fig. 5. Typical amplitude distribution

The amplitude distribution of the vibration data had a Gaussian form. A typical distribution is presented in Fig. 5. Table 2 shows the probability (for the conditions indicated) of the amplitude falling between  $\pm 1$  standard deviation. The probabilities again indicate the near-Gaussian shapes present in the amplitude distributions. This value for true Gaussian data is 0.682.

The power spectra shape (50-Hz resolution bandwidth) proved to be principally dependent on location and orientation and only slightly dependent on boat conditions. The high-speed and bow-slap conditions created almost identical spectral shapes. The medium-speed results varied from the other two by a slight shift in the frequency of the peak power spectral value. The frequency shifted up in some cases and down in others. The similarity in spectral shape could be caused by a broad-band driving force which is present in all three conditions. Table 3 shows the value and frequency of the PSD peaks.

The PSD results are presented in Tables 4 and 5 in terms of the cutoff frequencies for the accumulation of 50 and 90 percent of the vibratory energy. The 50 percent cutoff is, by some definitions, the data bandwidth. Table 4 reveals that the vibration at the deck, below the rear mount, had the largest bandwidth. Inspection of the power spectral plots indicates that this is true. Table 5 (the 90 percent cutoff frequency) shows that energy is present in the higher frequencies.

Figures 6 through 20 show the PSD and cumulative power (dotted) for six locations in three orientations. The PSD is shown for only one condition because of the independence of spectral shape with respect to boat condition.



**TABLE 2**  
Amplitude Probability Between Plus and Minus One Standard Deviation

Condition and Axis	50-Cal. Mounting Ring, Port	50-Cal. Mounting Ring, Starboard	Forward Below Deck Storage Area	Port Gunwale	Deck at Rear Mount	Rear Armament Mount
High speed, X	0.698	—	—	0.683	—	0.679
High speed, Y	0.684	0.702	0.686	0.667	0.669	0.714
High speed, Z	0.653	0.679	0.663	0.678	0.678	0.685
Bow slap, X	0.668	—	—	0.674	—	0.683
Bow slap, Y	—	0.671	0.668	0.655	0.687	0.672
Bow slap, Z	0.658	0.669	0.668	0.666	0.682	0.686
Medium speed, X	0.682	—	—	0.668	—	0.514
Medium speed, Y	0.662	0.721	0.679	0.670	0.679	0.688
Medium speed, Z	0.659	0.641	0.666	0.649	—	0.634

**TABLE 3**  
Peak Power Spectral Density Values

Condition and Axis	50-Cal. Mounting Ring Port		50-Cal. Mounting Ring, Starboard		Forward Below Deck Storage Area		Port Gunwale		Deck at Rear Mount		Rear Armament Mount	
	g	Hz	g	Hz	g	Hz	g	Hz	g	Hz	g	Hz
High speed, X	0.00020	124	—	—	—	—	0.00347	223	—	—	0.00195	124
High speed, Y	0.00006	136	0.00007	99	0.00005	149	0.00583	124	0.00194	124	0.00638	173
High speed, Z	0.00025	124	0.00010	124	0.00053	124	0.00317	124	0.00340	124	0.00494	224
Bow slap, X	0.00031	124	—	—	—	—	0.00333	223	—	—	0.00342	124
Bow slap, Y	—	—	0.00006	173	0.00011	99	0.00839	124	0.00151	124	0.00425	174
Bow slap, Z	0.00029	124	0.00019	124	0.00050	124	0.00431	124	0.00660	124	0.00278	223
Medium speed, X	0.00010	173	—	—	—	—	0.00497	198	—	—	0.00312	223
Medium speed, Y	0.00007	149	0.00025	174	0.00008	198	0.00101	198	0.00021	198	0.00119	223
Medium speed, Z	0.00004	173	0.00016	198	0.00054	200	0.00183	198	—	—	0.00267	223

**TABLE 4**  
50 Percent Energy Cutoff Frequency (Hz)

Condition and Axis	50-Cal. Mounting Ring, Port	50-Cal. Mounting Ring, Starboard	Forward Below Deck Storage Area	Port Gunwale	Deck at Rear Mount	Rear Armament Mount
High speed, X	124	—	—	770	—	198
High speed, Y	198	173	164	161	819	185
High speed, Z	124	124	173	241	223	229
Bow slap, X	149	—	—	521	—	173
Bow slap, Y	—	198	136	149	919	189
Bow slap, Z	136	142	173	210	198	231
Medium speed, X	161	—	—	198	—	226
Medium speed, Y	173	173	206	223	670	206
Medium speed, Z	157	185	203	210	—	235

TABLE 5  
90 Percent Energy Cutoff Frequency (Hz)

Boat Condition and Orientation	50-Cal. Mounting Ring, Port	50-Cal. Mounting Ring, Starboard	Forward Below Deck Storage Area	Port Gunwale	Deck at Rear Mount	Rear Armament Mount
High speed, X	248	—	—	993	—	695
High speed, Y	1093	1316	844	795	1739	372
High speed, Z	273	695	447	1714	—	2459 <sup>a</sup>
Bow slap, X	248	—	—	993	2459 <sup>b</sup>	944
Bow slap, Y	—	1316	919	770	1763	745
Bow slap, Z	347	447	372	1664	2459 <sup>c</sup>	2459 <sup>d</sup>
Medium speed, X	223	—	—	770	—	273
Medium speed, Y	322	223	720	819	1689	596
Medium speed, Z	472	223	273	1639	—	844

<sup>a</sup>88.7 percent.

<sup>b</sup>87.3 percent.

<sup>c</sup>88.5 percent.

<sup>d</sup>85.2 percent.

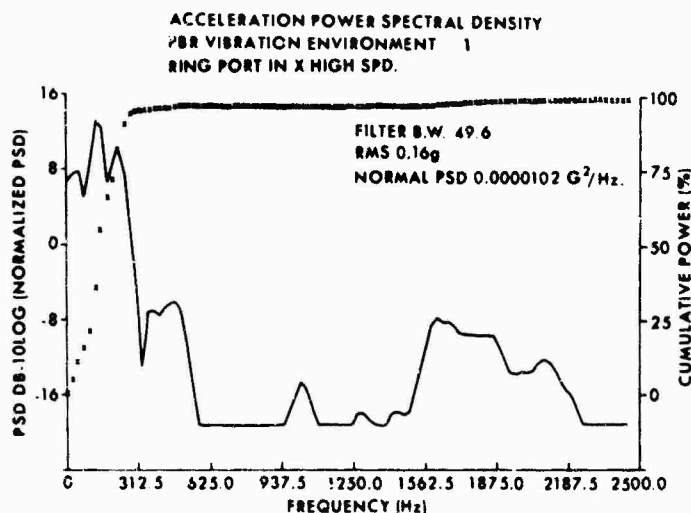


Fig. 6. PSD, ring, port, X axis, high speed

#### Transient Analysis

The gun-firing transients were analyzed using shock spectral techniques as defined in Ref. [2]. A transient was not always separable from the steady-state vibration in some locations. For this reason, no spectra were calculated for these locations. The peak accelerations found in the actual transients are shown in Table 6. Shock spectra for all three orientations were calculated for the carriage and port mounting ring, and are shown in Figs. 21 and 22. The shock spectra for additional locations are shown, in part, in Fig. 23. The

transients, in general, had a duration of 200 msec. The interval between transients was approximately 274 msec. The fact that this interval exceeds the transient duration means that no buildup occurred as a function at the firing duration.

#### Summary

The rms levels ranged from 0.07 to 0.86 g. The data bandwidth found in the PSD computation was, in most cases, below 400 Hz. The exceptions to this were the data obtained at the

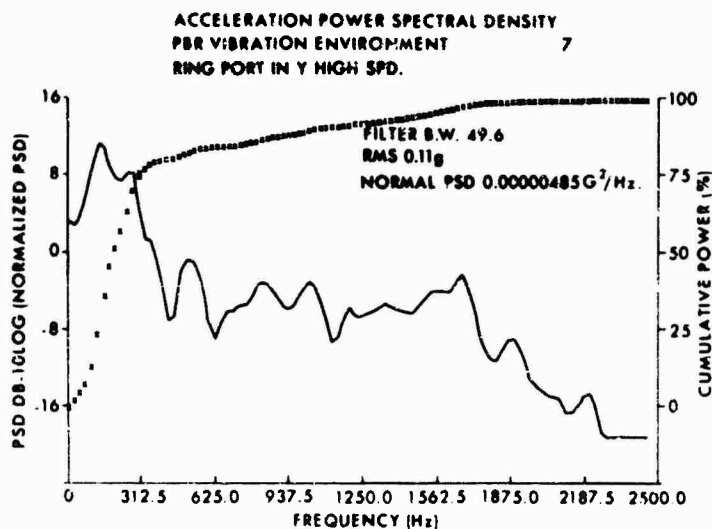


Fig. 7. PSD, ring, port, Y axis, high speed

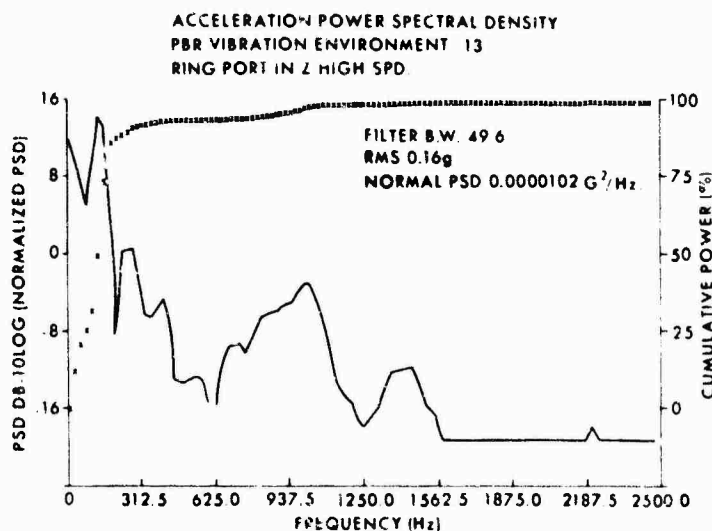


Fig. 8. PSD, ring, port, Z axis, high speed

gunwale and deck (at the rear mounts). The amplitude distributions were Gaussian in form; peaks as high as four times the rms level were found. The gun-firing transients were as high as 23 g at locations on the gun mount. Shock spectral values were approximately 80 g at 1500 Hz.

#### CONCLUSIONS

The vibration data found on the PBR were not excessively high. The levels found would

not ordinarily be destructive for short periods of exposure. It should be kept in mind that these craft are used for patrol duty, and therefore weapons used on these craft are subjected to the environment for long periods of time. The levels of the shock may not be considered destructive in a single occurrence; however, the transients occur eight times a second during gun firing. Here again the severity of this environment should be judged with the long durations of the environment in mind.

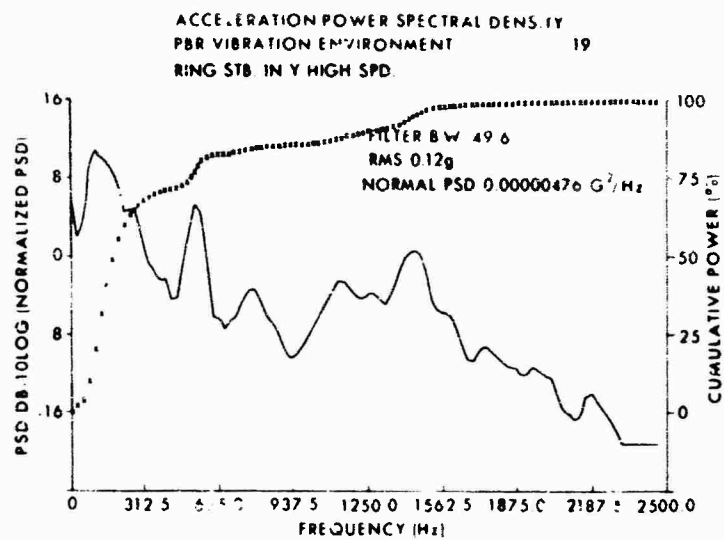


Fig. 9. PSD, ring, starboard, Y axis, high speed

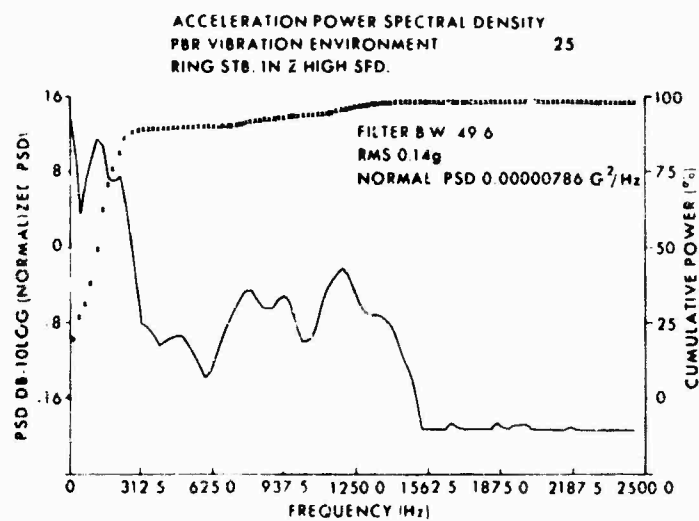


Fig. 10. PSD, ring, starboard, Z axis, high speed

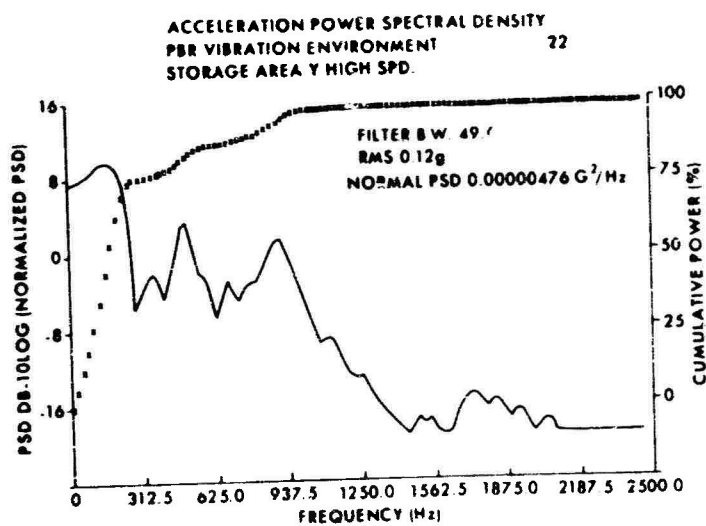


Fig. 11. PSD, storage area, Y axis, high speed

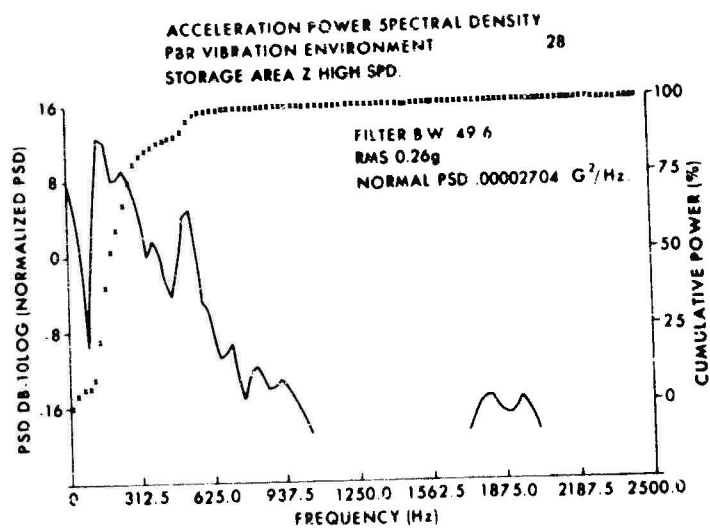


Fig. 12. PSD, storage area, Z axis, high speed

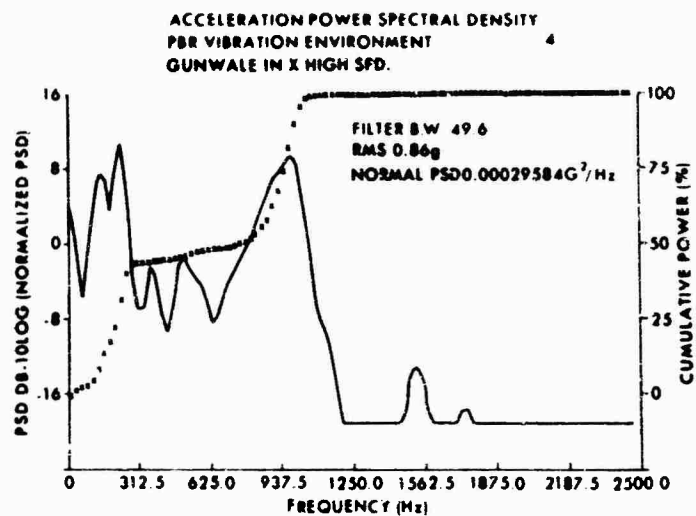


Fig. 13. PSD, gunwale, X axis, high speed

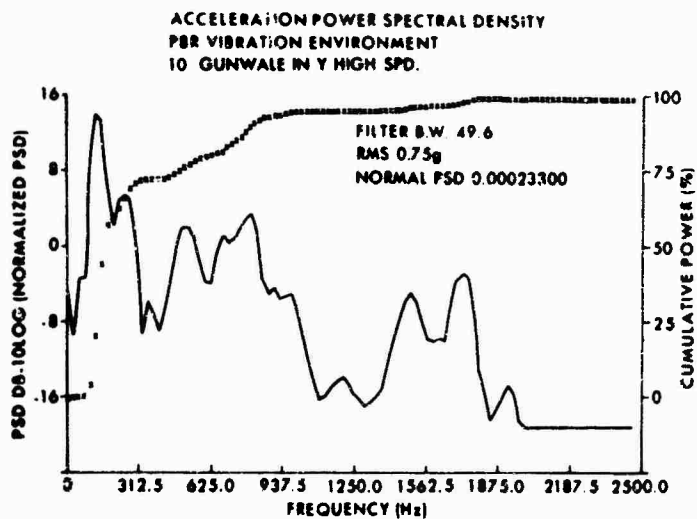


Fig. 14. PSD, gunwale, Y axis, high speed

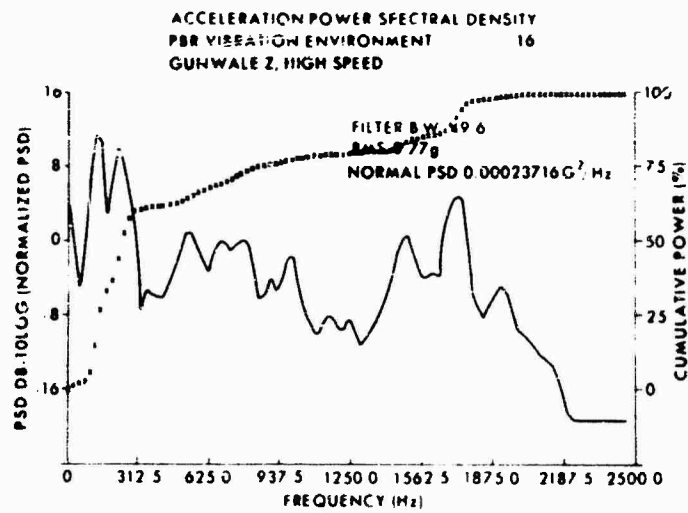


Fig. 15. PSD, gunwale, Z axis, high speed

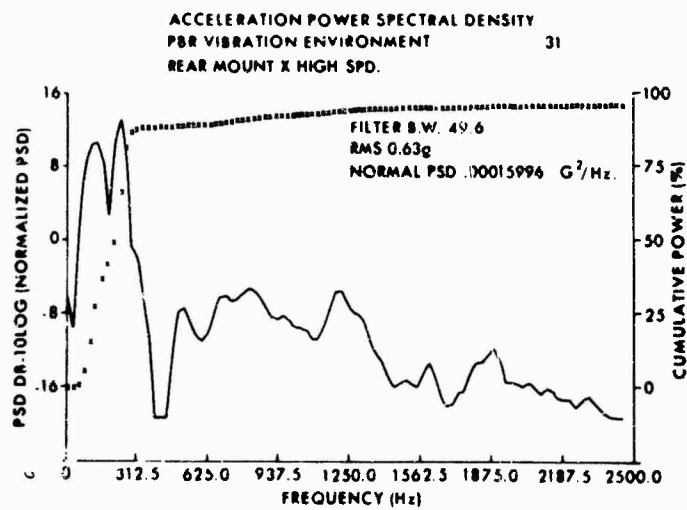


Fig. 16. PSD, rear mount, X axis, high speed

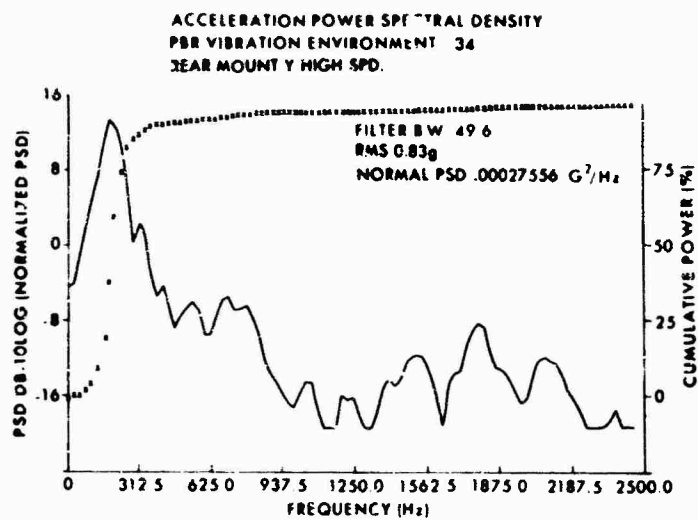


Fig. 17. PSD, rear mount, Y axis, high speed

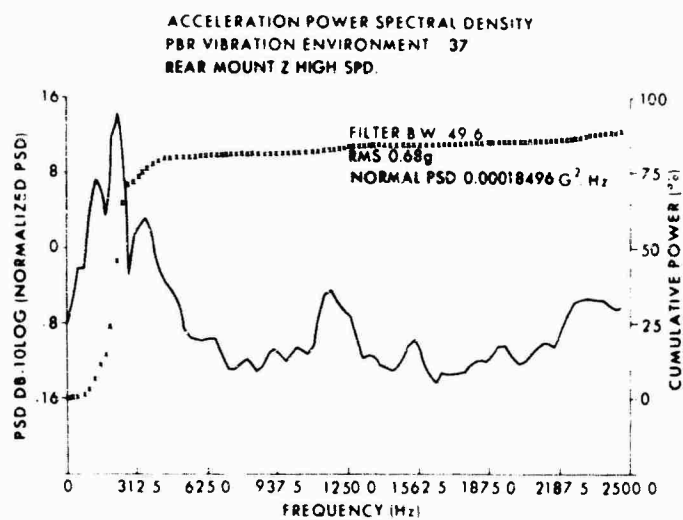


Fig. 18. PSD, rear mount, Z axis, high speed



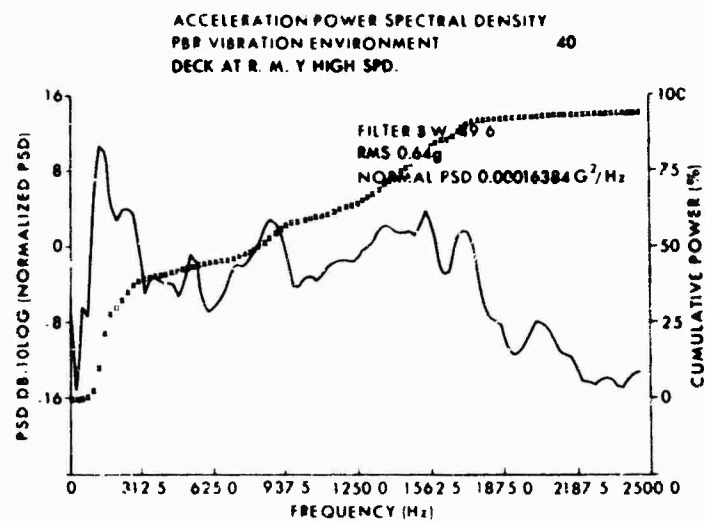


Fig. 19. PSD, deck at rear mount, Y axis, high speed

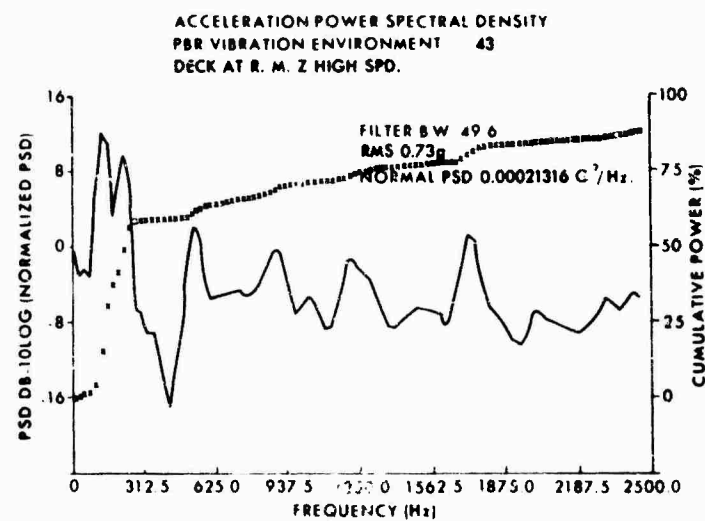


Fig. 20. PSD, deck at rear mount, Z axis, high speed

TABLE 6  
Peak Acceleration (g)

Axis	Carriage Mk 36 Mod 0 Mount	Forward Mounting Ring	Forward Below Deck Storage Area	Gunwale	Deck at Rear Mount
Fore-Aft	13.0	21.0	12.0	2.5	2.0
Abeam	13.0	23.0	10.0	—	3.5
Vertical	20.0	23.0	10.0	8.0	4.0

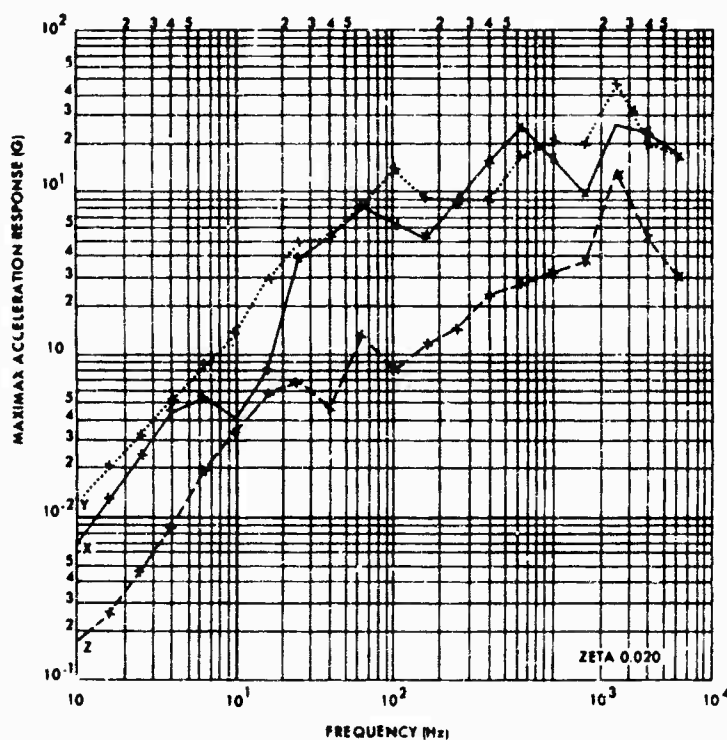
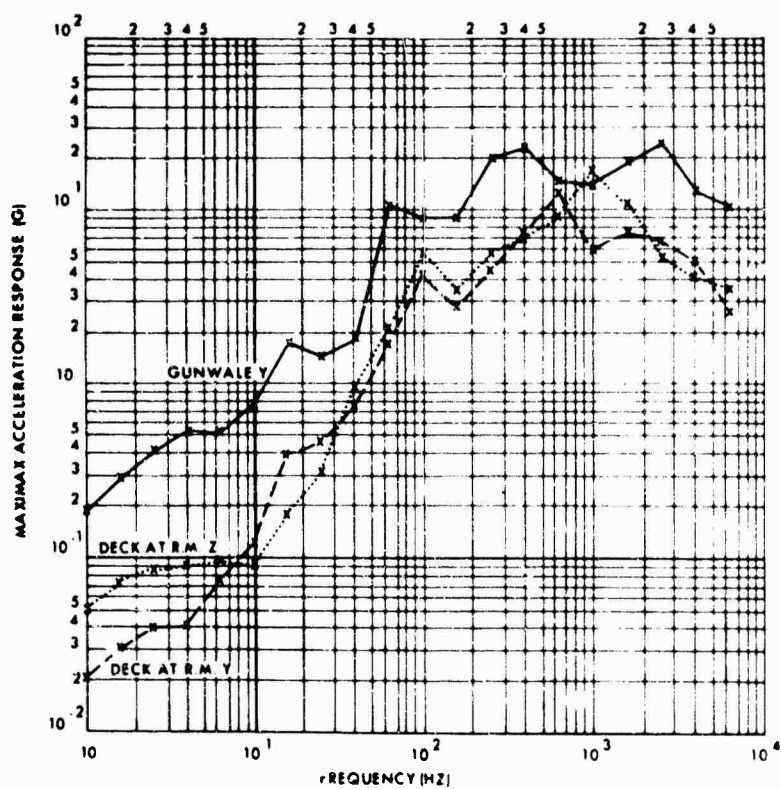
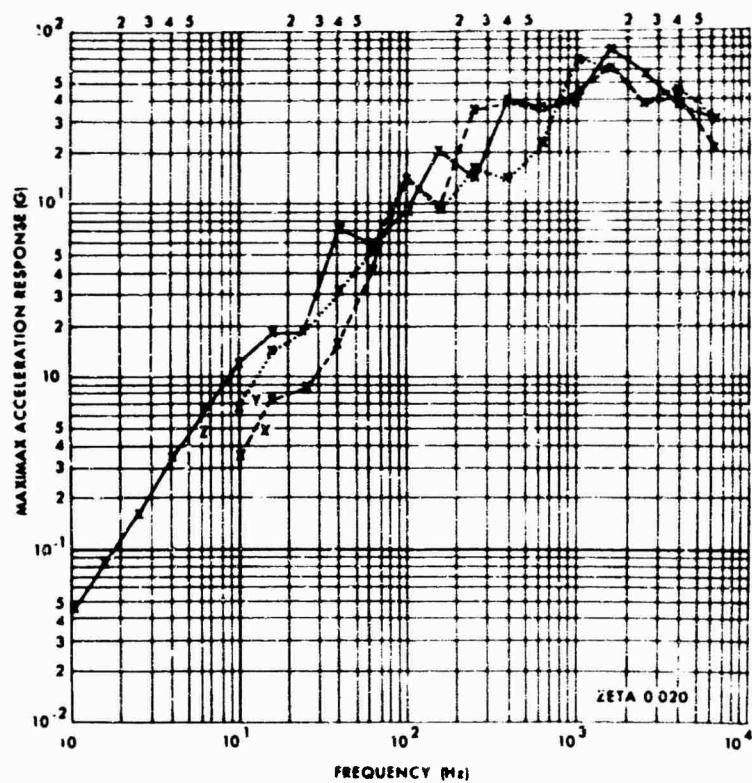


Fig. 21. Shock spectra for carriage



#### REFERENCES

1. J. S. Bendat and A. G. Piersol, Measurement and Analysis of Random Data (Wiley, New York), 1966
2. William T. Thomson, Vibration Theory and Applications (Prentice-Hall, Englewood Cliffs, N.J.), 1965

\* \* \*

## SCALE-MODEL WIND-TUNNEL ACOUSTIC DATA\*

John R. Baratono and Frank A. Smith  
Martin-Marietta Corporation  
Denver, Colorado

Boundary-layer acoustic noise data were measured on numerous 7 percent scale-model vehicle configurations during wind-tunnel tests at the AEDC facility. Sound pressure levels (SPL) were obtained over a Mach range of 0.6 to 1.2 for each of six vehicle configurations over a range of tunnel conditions. For each configuration, from 6 to 10 microphones were installed flush to the external skin surface. These microphone locations were chosen on the basis of both maximum turbulent regions (separated flow) and applicable full-scale equipment locations.

The data are presented in the form of one-third octave band SPL's for the various tunnel test conditions: Mach number, dynamic pressure, angle of attack, and vehicle configuration. Approximately 1500 acoustic plots are presented, permitting a detailed evaluation of boundary-layer noise for a wide range of conditions.

The test model was a 7 percent aeroelastic Titan III booster with six payload configurations: (a) configuration 31, similar to that used in the Titan III HST launch at Cape Kennedy; (b) Titan III with 15-deg half-angle conical nose; (c) configuration 41, similar to that used in the Titan III HST launch at Cape Kennedy (except without protuberances); (d) Titan III with two-man SV-5 orbital vehicle; (e) Titan III with 13-ft-diam, 40-ft cylinder Apollo with launch escape system; (f) Titan III with 13-ft-diam, 20-ft cylinder and Apollo with launch escape system.

The microphones used to measure the pressure oscillations were model 714 Photocons; scale-model one-third octave plots cover the frequency range from 160 to 31,500 Hz.

### INTRODUCTION

This report is concerned primarily with disseminating boundary-layer acoustic noise data on 7 percent scale-model vehicle configurations during wind-tunnel tests at the AEDC facility. The models consisted of a dynamically similar model of the Titan III booster and solid rocket motors together with a number of various payloads and upper stages. A description of the various payloads and upper stages is as follows: a 15-deg half-angle conical nose, a two-man SV-5 orbital vehicle, a 13-ft-diam, 40-ft cylinder and Apollo with launch escape system, a 13-ft-diam, 20-ft cylinder and Apollo with launch escape system, configuration 31, which is similar to that used in the Titan III HST launch at Cape Kennedy, and finally a configuration similar to 31, except that it has no protuberances.

Sound pressure levels were measured at several selected locations along each of the six model configurations. The data were reduced in the form of one-third octave band analyses and overall SPL's. Because each configuration

yielded approximately 30 pages of one-third octave band analyses, only one configuration (31) was selected for presentation here. The one-third octave band spectra for the other configurations are included in the Martin Marietta Corporation report to the Air Force [1].

### TEST DESCRIPTION

#### Test Facility

The tests were conducted in the transonic (16T) wind-tunnel circuit of the propulsion wind tunnel (PWT) at the AEDC. The 16T tunnel is a continuous flow, closed-circuit wind tunnel capable of operation from a stagnation pressure level of 40 to 4000 psfa. The test section measures 16 by 16 by 40 ft and is lined with perforated plates to allow continuous operation with minimum wall interference in the Mach number range of 0.5 to 1.6. Basically, the transonic tunnel Mach number range for the acoustic data acquisition tests was from 0.6 to 1.2.

The nominal (100 percent) test conditions for each configuration were:

\*This paper was not presented at the Symposium.

Mach No.	Dynamic Pressure (psf)
0.6	384
0.7	479
0.8	567
0.9	651
1.0	722
1.1	783
1.2	837
1.3	879
1.4	911

These figures should be used in conjunction with the Mach number and dynamic pressure values indicated on the data sheets presented below to determine actual dynamic pressures experienced during the particular tunnel test.

#### Model

This section defines the pertinent model parameters with those of the full-scale vehicle that are necessary in applying the data contained herein. The model was a sting-mounted aeroelastic 7 percent geometrically scaled model of the booster vehicle and various payload combinations. Elastic simulation applied for the all-metal core, the SRM's, and up to but excluding the actual payloads. The conical payload and the SV-5 can be considered rigid because in their fabrication only the mass and center of gravity were scaled. The model was designed to simulate the free-free bending modes in both pitch and yaw planes.

Various parameters of the model (m) and the full-scale vehicle (p) are indicated below for ready reference:

Scale factor	$n = 0.07 = m/p$
Length	$L_m = nL_p = 0.07 L_p$
Strouhal frequency	$f_m = (1/n)f_p$
Mach number	$M_m = M_p$
Pitch angle	$\theta_m = \theta_p$
Dynamic pressure	$q_m = q_p$

#### Instrumentation

The transonic wind-tunnel microphone data were recorded on a 14-channel Ampex E.S. 100 direct record magnetic tape recorder. A tape speed of 15 ips was used during data acquisition. A maximum of 10 model 714 Photocon microphones was used to obtain the fluctuating

pressure data. The microphones were connected by 60 ft of cable to Photocon model PS 310 power supplies and line drivers in the tunnel plenum chamber. Approximately 400 ft of twisted shielded pair cables connected the Photocon power supplies to the tape recorder.

System verification checks were performed prior to, during, and following each configuration test run in the wind tunnel. Prior to and upon completion of each model configuration tunnel test, the microphones and associated instrumentation systems were calibrated by the stimulus method. These calibrations were performed using a 1000-cps acoustic source at SPL's of 150 and 160 db. A system frequency calibration was also performed prior to initiation of the model tests. Each microphone channel was frequency calibrated over the range of 50 to 31,500 Hz. The voltage insertion method was used, with the input applied into each microphone in place of the diaphragm. A linearity check was also performed by stimulating each microphone at three given input SPL's, all at a frequency of 1000 Hz. A secondary standard was used as the known reference source to confirm calibration levels.

#### Vehicle Configurations

The six models each consisted of a common three-body (Titan III) booster, with different upper stage and payload configurations. Microphone locations are shown on the data sheets below.

The configurations are defined as follows:

1. Configuration 31: similar to that used by the Titan III HST launch at Cape Kennedy;
2. Configuration 32: Titan III with 15-deg half-angle conical nose;
3. Configuration 41: similar to that used in the Titan III HST launch at Cape Kennedy, except without protuberances;
4. Configuration 34: Titan III with two-man SV-5 orbital vehicle;
5. Configuration 36: Titan III with 13-ft diam, 40-ft cylinder and Apollo with launch escape system;
6. Configuration 36: Titan III with 13-ft diam, 20-ft cylinder and Apollo with launch escape system.

(The detailed acoustic data for configurations 32, 41, 34, and 36 are contained in Ref. [1] and are not a part of this report.)

#### Microphone Locations

All microphones were flush mounted to within  $\pm 0.002$  in. of the model surface. Their locations are given in Table 1, while the orientation of the microphones, for use in applying the data in Table 1, is indicated in Fig. 1.

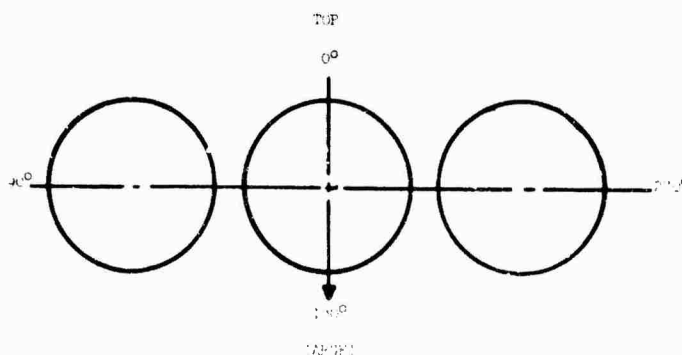
Microphones 1 through 6 are at the same locations for all configurations, while microphones 7 through 10 vary.

Figure 2 is a sketch showing the approximate location of the microphones; however, Table 1 should be used whenever location accuracy is required. Because of security requirements, Table 1 must be used in conjunction with Ref. [1] to determine specific microphone locations for each configuration.

TABLE 1  
Microphone Locations: Full-Scale and Model Stations

Microphone Number	Model Station (in.)	Configuration and Full-Scale Stations and Orientations				
		31	32	41	36	37
1	24.4	349.0" 15.8°	349.0" 15.8°	349.0" 15.8°	349.0" 15.8°	349.0" 15.8°
2	24.4	349.0" 111.8°	349.0" 111.8°	349.0" 111.8°	349.0" 111.8°	349.0" 111.8°
3	20.4	292.0" 111.8°	292.0" 111.8°	292.0" 111.8°	292.0" 111.8°	292.0" 111.8°
4	18.3	261.0" 111.8°	261.0" 111.8°	261.0" 111.8°	261.0" 111.8°	261.0" 111.8°
5	17.0	242.0" 15.8°	242.0" 15.8°	242.0" 15.8°	242.0" 15.8°	242.0" 15.8°
6	16.2	231.0" 111.8°	231.0" 111.8°	231.0" 111.8°	231.0" 111.8°	231.0" 111.8°
7	12.2	175.0" 91.7°	175.0" 91.7°	175.0" 91.7°	—	—
8	-14.1	—	-201.0" 99.55°	-201.0" 99.55°	—	—
9	-28.7	-410.0" 91.7°	-410.0" 91.7°	-410.0" 91.7°	—	—
10	-30.8	-440.0" 91.7°	—	—	—	—

Fig. 1. Vehicle orientation for locating microphones; view looking toward aft end of model



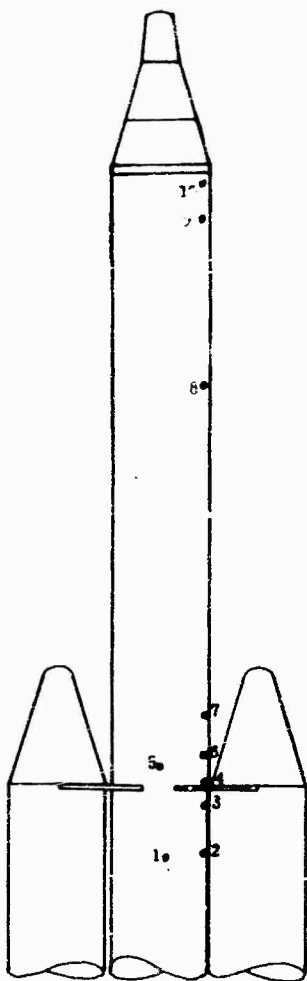


Fig. 2. Configuration 31, similar to that used in the Titan III HST launch at Cape Kennedy

## DATA REDUCTION

An Ampex FR-600 magnetic tape recorder, set at 15 ips, was used to reduce the data. No speed shift occurred during the data playback. Data reduction involved the use of an Ampex tape loop machine and a Bruel and Kjaer third-octave spectrum analyzer. During playback the data were monitored on an oscilloscope and were recorded on a Consolidated Electrodynamics Corporation type 5-119 oscillograph to assist in verification of the data. During actual reduction of the data on the spectrum analyzer, a 150-Hz high-pass filter was used to filter and remove the low-frequency system noise, thereby maintaining quality data.

Tolerance on the data reduction system was  $\pm 1.0$  db, excluding frequency response effects. Frequency response checks indicate that the data are within  $\pm 3.0$  db from 200- to approximately 4000 Hz. Above this frequency range, corrections to the data should be made in accord with the values contained in Table 2. The overall SPL's were also determined with the spectrum analyzer in the "linear" (no filtering) mode.

## DATA PRESENTATION

To assist in rapid evaluation of the data, the overall SPL's for four of the six configurations and tunnel test conditions are presented in Tables 3 through 6. These overall levels are identical to the levels indicated in the upper right-hand corner of each plot presented below.

The reduced microphone data of configuration 31 is presented in Figs. 3 through 8. These plots are SPL's in decibels (re.  $0.0002 \mu\text{bar}$ ) vs one-third octave band midfrequencies (Hz).

It is emphasized that all acoustic data presented here are in terms of scale-model parameters. To apply the data to full-scale size, only the abscissa (frequency axis) must be modified; i.e., multiply the abscissa by 0.07.

## CONCLUSIONS

The maximum overall SPL's measured on configuration 31 occurred on microphone 6 at Mach 0.95 and at an angle of attack of  $1.0^\circ$ . The maximum level measured on the configuration 31 payload region occurred on microphone 9 at Mach 0.80 and at an angle of attack of  $0^\circ$ . The dynamic pressure was 80 percent of nominal in the first case and 100 percent of nominal in the second case. The overall levels were 167.5 and 161.9 db, respectively.

A cursory analysis of the full-scale acoustic spectral shapes for all six configurations indicates that a majority of the data peaks in the 35- to 500-Hz range. This conclusion appears consistent with transonic model acoustic data obtained from Refs. [2], [3], and [4]. In addition, the peak frequency tends to increase with increasing Mach number for a majority of the spectrum plots. Additional acoustic data interpretation applicable to this report is included in Ref. [1].



TABLE 2  
Frequency Response Correction Factors --  
Model Microphone Frequency Response

Frequency (Hz)	Microphone 1			Microphone 2			Microphone 3			Microphone 4			Microphone 5		
	150 db	160 db	170 db	150 db	160 db	170 db	150 db	160 db	170 db	150 db	160 db	170 db	150 db	160 db	170 db
160	-3	-3.8	-3	-3	-4	-4	-4	-4	-4	-4	-4.5	-4	-3	-3.5	-3
200	-1	-1.5	-1	-1	-2	-1	-1	-1	-1	-1	-1	-1.7	-1	-1.5	-1
250	+1.5	+0.5	+1.5	+2	+1	+2	+2	+0.5	+1	+2	+1	+1.5	+2	+1	+1
315	+1	0	+1	+1	0	+1	+1	0	0	+1	0	+0.5	+1	0	0
400	-1	-1	-1	-0.5	-1	-1	-1	-1	-1	0	-1	-1	-0.5	-1	-1
500	-1.5	-2	-1.5	-1	-2	-2	-2	-2	-2	-1	-2	-1.5	-2	-2	-2
630	-1	-1	0	-1	-1	-1.8	-1.8	-1.3	0	-1	-1	0	-1	-1	-2
800	-0.5	-0.5	-0.5	-0.5	-0.5	-0.5	-0.5	-0.5	-0.5	0	-0.5	-0.5	0	-0.5	-0.5
1000	0	-0.5	0	0	-0.8	0	0	-0.8	-0.8	0	-0.8	0	✓	-1	0
1250	-1	-1.5	-1	-1	-1.5	-1	-1	-1	-1	-0.5	-0.5	-0.5	-1	✓	-1
1600	-1	-1.5	-1	-1	-1	-1.5	-1	-1.5	-1	-1	-2	-1.4	-1.3	-2.5	-1.7
2000	-2	-1.5	-1.5	-1.5	-1.5	-2.2	-2	-2.5	-2.5	-1.5	-2.5	-0.9	-2	-2.5	-2.5
2500	-1.8	-0.3	-2.3	-1.3	-1.3	-1.3	-1.8	-2.8	-2.3	-1.3	-2.3	-0.8	-1.8	-3.3	-2.3
3150	-2	+2	-2.5	-2	-1	-3	-2	-3	-3	-2	-2.8	-2.5	-2	-3.5	-3
4000	-2	-2.7	-2.5	-2	-1	-2.8	-2	-3.5	-3	-1.5	-3	-2.5	-2	-4	-3
5000	-3	-4.5	-3.5	-3	-2	-3.6	-3.5	-4.7	-4	-3	-4	-3	-4	-5	-4
6300	-3.2	-3.2	-3.2	-3.2	-3.2	-3.8	-3.7	-3.7	-3.7	-3.2	-3.2	-3.2	-4.2	-4.2	-4.2
8000	-3.2	-4.7	-3.7	-2.7	-2.2	-3.2	-3.7	-4.2	-4.2	-2.7	-4.2	-2.7	-3.7	-5.2	-4.2
10000	-4	-5.5	-4	-3.8	-3	-4	-4.5	-5.5	-5	-3.5	-5	-3.5	-5	-6	-5
12500	-3.5	-5	-4	-2.5	-3	-3	-3.5	-5	-4	-2.5	-4	-3	-4	-6	-5
16000	-4.5	-6	-5	-3	-4	-3.7	-4	-6	-5	-3.5	-4	-3.5	-4	-7	-6
20000	-5.5	-7	-5.5	-4	-5	-5	-5.5	-7.5	-6.5	-4.5	-5	-5	-6	-7	-8

(Continued)

TABLE 2 (Cont.)  
Frequency Response Correction Factors --  
Model Microphone Frequency Response

Frequency (Hz)	Microphone 6			Microphone 7			Microphone 8			Microphone 9			Microphone 10		
	150 db	160 db	170 db	150 db	160 db	170 db	150 db	160 db	170 db	150 db	160 db	170 db	150 db	160 db	170 db
160	-5.5	-5	+0.5	-3	-4	-4	-3	-4	-3.5	-3	-4	-3.5	-3	-4.5	-3.5
200	-2	-1	+3.5	-1	-1.5	-1	-1	-1.5	-1	-1	-1.5	-1	-1	-1.4	-0.6
250	+2	+2	+6	+2	+1	+1.5	+2	+1	+1.5	+2	+1	+1.5	+0.4	+1.5	+2
315	+1	+1	+5	+1	+0.5	+1	+1	+0.5	+1	+1	0	+1	0	0	+1
400	-1	-1	+3.5	0	-1	-0.5	0	-1	-0.5	0	-1	0	0	-1	-0.2
500	-1	-1.5	+3	-1	-2	-2	-1	-2	-1.5	-1.5	-2	-1.5	-1.4	-2	-1
630	-1	-1	+5	-1	-1	0	-1	-1	+0.4	-1	-1	-1.5	-1	-1	-0.5
800	-0.5	-0.5	+4.5	-0.5	-0.5	-0.5	0	-0.5	0	-0.5	-0.5	-1	0	-0.5	0
1000	0	-0.5	+4.5	0	-1	0	0	-0.6	0	0	0	-0.5	0	-1	+0.5
1250	-1	-1	+3.5	-1	-1.5	-0.5	-0.4	-1.5	-1	-0.5	-1.8	0	-1	-1.8	-1
1600	-1.5	-1.5	+3	-1	-2	-1.5	-1	-2	-1.5	-1	-2	-1	-1	-2.5	-1
2000	-1.5	-2	+2.5	-1.5	-2.5	-1.5	-1.5	-2.5	-1.5	-1.5	-2.5	-1.8	-1.5	-3	-1.5
2500	-1.8	-2.3	+2.7	-1.3	-2.3	-2.3	-1.3	-2.8	-2.3	-2.3	-2.8	-2	-1.3	-3.3	-1.8
3150	-2	-2.5	+2	-2	-3	-2.5	-1.5	-3	-2.5	-2	-3	-2.3	-2	-4	-2
4000	-2	-3	+2	-2	-3	-3	-1.5	-3	-2	-2	-3.5	-2.5	-2	-4	-2
5000	-3	-4	+2	-3	-4.5	-4	-2.5	-4	-3	-3	-5	-4	-2.5	-5.5	-4
6300	-3.2	-3.2	+1.3	-3.2	-3.2	-3.2	-2.2	-4.2	-3.2	-3.2	-4.7	-4.2	-2.7	-5.2	-3.2
8000	-3.2	-3.7	+0.8	-2.7	-4.2	-3.2	-2.2	-4.2	-2.7	-3.2	-4.7	-4.2	-2.7	-5.2	-2.7
10000	-4	-5	0	-4.5	-5	-4	-2.5	-5	-3	-5	-6	-5	-4	-6	-4
12500	-3.5	-4	+0.5	-3	-4.5	-4	-1.5	-4	-2.5	-4	-5.5	-4.5	-3	-3	-5.5
16000	-4	-5	0	-4.5	-5.5	-4.5	-2	-5	-3	-5	-6.5	5.5	-4	-5	-4
20000	-5	-5	-2	-5	-5	-5	-3.5	-6.5	-4	-6.5	-8.5	-7	-4.7	-6.5	-5

**TABLE 3**  
**Overall Sound Pressure Levels**  
(in decibels re. 0.0002  $\mu$ bar): Configuration 31

Mach Number	Microphone								
	1	2	3	4	5	6	7	9	10
q (psf) = 100 percent of nominal; angle of attack = 0 deg									
0.6	149.5	153.5	155	147.5	146	150	149.5	159	147.5
0.7	152	154.5	156.3	150	148.3	153	152	161.8	150.5
0.75	153	154.6	156.5	151.3	147.8	154.5	152.5	161.8	158.3
0.8	153	155	157.5	152	147	155	152.7	161.9	148
0.85	153	154.2	158	153.2	147	—	153.8	161	151
0.9	146	149	152	151	144	157	148.5	153.3	150
0.925	153.3	154.5	159.2	157.9	N/A	159	155.6	150	148
1.0	151	151	159	163.8	152.2	N/A	152	161.5	149.8
1.2	152	152	160	165	154	N/A	156	160.5	150.2
q (psf) = 80 percent of nominal; angle of attack = 1 deg									
0.85	155.3	154.5	157.8	154.3	144.2	165	152	158	149.8
0.9	155	154.2	158	155.6	145	162.5	152.4	159	146
0.95	154.5	154.6	157	157.7	146.5	167.5	154	158	145
1.0	152	151	156.5	158	147	159	156	158.6	146
q (psf) = 100 percent of nominal; angle of attack = 1 deg									
0.8	157.5	155	158	155.5	147.8	161	154	161	151
0.85	156.7	155.3	158.3	156.5	147.2	166	155.4	159.8	152.8
0.9	158	155.8	158	158.3	147.8	158	156	160	149

TABLE 4  
Overall Sound Pressure Levels  
(in decibels re. 0.0002  $\mu$ bar): Configuration 41

Mach Number	Microphone								
	1	2	3	4	5	6	7	8	9
q (psf) = 100 percent of nominal; angle of attack = 0 deg									
0.6	148	154	154.3	147.5	145	149	150	147.5	152
0.7	151	154	156	150	147.5	151	156	156	160
0.75	151	153.5	156	151	148	152	157.5	157.5	159.5
0.8	151	153.5	158	152	146.5	152	158	158	160
0.85	151.5	153	157	152.7	147	152	159	158	159
0.9	151.3	153	158.5	157	147	154	160	159	159
0.925	151	153	158	155.5	148	155	160	160	159
0.95	151.3	152	159	157	149	155.5	161	162	157
0.975	150	150	158.5	157	148.5	156.5	160	161.5	156
1.0	150	149	158	157	149	157	160.5	162	157.5
1.1	148	149	158	158	149.7	137 <sup>a</sup>	N/A	160.5	159
1.2	148	149.5	158	161	141.5	152	161	158.5	156
q (psf) = 80 percent of nominal; angle of attack = 0 deg									
0.7	154	155.5	159	151	148.5	153.5	153	161	158
0.75	154	155.5	159.5	152	148	153.5	154	160.5	158
0.8	151	153	154.5	151.5	145	154	154	158	157
0.85	151	153	157	152	145	154	155.5	157.5	156.5
0.9	151	153	157	153	146.5	155.5	157.5	158.5	156.5
0.925	151.5	153	159	155	147	156.5	159	159	158
0.95	152	152	159	153	147	157	158.5	160	156.5
1.0	150	149	158	155.5	148	158	158.5	155	156
1.1	150	150	158	158	148.5	160	160	159	157.5
1.18	146.5	148	157	155.5	148	155.5	162	157.5	157
q (psf) = 80 percent of nominal; angle of attack = 1 deg									
0.8	152	153.5	156.5	152	145.5	154	156	158	156.5
0.85	152	152.6	158	152.5	145.5	154	157	154.5	N.G.
0.9	152	153	157.5	153.5	145.5	155	158	159	157.5
0.925	152	152.5	157	156	146.5	156	159.5	160	158.5
0.95	151.5	153	158	155.5	146.5	156.5	157.5	160	157
0.975	150.5	150	157	153.3	146	156.5	158	161	156
1.0	150	148	156.5	153	147	157.5	158	161	156

<sup>a</sup>Questionable.

**TABLE 5**  
**Overall Sound Pressure Levels**  
(in decibels re. 0.0002  $\mu$ bar): Configuration 36

Mach Number	Microphone								
	1	2	3	4	5	6	7	8	9
q (psf) = 100 percent of nominal; angle of attack = 0 deg									
0.6	150	155	161	162.5	161	156.5	—	—	—
0.7	153 <sup>a</sup>	155.5 <sup>a</sup>	162 <sup>a</sup>	165.5 <sup>a</sup>	163 <sup>a</sup>	157 <sup>a</sup>	— <sup>a</sup>	— <sup>a</sup>	— <sup>a</sup>
0.8	152	155.5	162	164.5	163.5	158	—	—	—
0.85	152.5	152.5	161	163	162.5	159.5	—	—	—
0.9	147.5	152.5	160	165	163.5	157	—	—	—
0.925	149.5	152.5	160	164.5	163.5	157	—	—	—
0.95	150	152.5	160	165	164.5	157.5	—	—	—
0.975	151	152	159.5	165	166	158	—	—	—
1.0	151	152	161	166	167.5	159	—	—	—
1.1	150	153	162	165	168.5	161	—	—	—
1.2	157	155.5	163	166	166	160	—	—	—
q (psf) = 80 percent of nominal; angle of attack = 0 deg									
0.8	152	153	160	165.5	165.5	156	—	—	—
0.85	149	152	157.5	164.5	161	156	—	—	—
0.9	149	152	156	164.5	161	155	—	—	—
0.925	150	151	156.5	162	161.5	155	—	—	—
0.95	147	150	156	166	163	155	—	—	—
0.975	146	150	158	165.5	164	156.5	—	—	—
1.0	148	150	159	165	166	156.5	—	—	—
1.1	149	151	158.5	165	168	160	—	—	—
q (psf) = 100 percent of nominal; angle of attack = 1 deg									
0.8	152.5	155.5	161	162.5	163	165	—	—	—
0.85	152.5	154	160	165	163	161.5	—	—	—
0.9	152.5	152	158	163.5	163	159.5	—	—	—
0.925	152	153.5	158	163.5	163	160	—	—	—
0.95	151.5	151	158	164	163.5	161	—	—	—
0.975	151	150	158.5	163.5	166.5	161	—	—	—
1.0	150	149	158.5	163.5	166	161	—	—	—
1.1	153	151	160.5	163.5	167	162	—	—	—
1.2	156	154	163	165	166.5	161.7	—	—	—
q (psf) = 120 percent of nominal; angle of attack = 0 deg									
0.8	152.5	N/A	161.5	166	165	161	—	—	—
0.85	152	N/A	161.5	166	164	161	—	—	—
0.9	152	N/A	160	165	164	160	—	—	—
0.925	151	N/A	159	164.5	165	160	—	—	—
0.95	151	151	159.5	166.5	166.5	160	—	—	—
0.975	150.5 <sup>b</sup>	151 <sup>b</sup>	159.5 <sup>b</sup>	166 <sup>b</sup>	169.5 <sup>b</sup>	160 <sup>b</sup>	— <sup>b</sup>	— <sup>b</sup>	— <sup>b</sup>
1.0	151.5	151	160	165	170	160.5	—	—	—
1.1	152.5	151.5	162	165	171	161	—	—	—

<sup>a</sup>q (psf) = 110 percent of nominal.

<sup>b</sup>q (psf) = 160 percent of nominal.

TABLE 6  
Overall Sound Pressure Levels  
(in decibels re. 0.0002  $\mu$ bar): Configuration 37

Mach Number	Microphone								
	1	2	3	4	5	6	7	8	9
q (psf) = 80 percent of nominal; angle of attack = 0 deg									
0.8	150	—	161.5	165	159.5	162	—	—	—
0.85	151	—	161.5	165.5	160.5	162	—	—	—
0.9	151	—	160	168	160.5	161	—	—	—
0.925	150.5	—	160	168	161	160.5	—	—	—
0.95	150	—	160	169	162	161	—	—	—
0.975	149.5	—	159	169.5	163	161	—	—	—
1.0	150	—	160	169.5	164	161	—	—	—
1.1	150	—	161	161	167.5	161	—	—	—
q (psf) = 100 percent of nominal; angle of attack = 1 deg									
0.8	149.5	—	162	166.5	161.5	164.5	—	—	—
0.85	151	—	161.5	168	162	164	—	—	—
0.9	150	—	160	172	162	163.5	—	—	—
0.925	151.5	—	159	173	163	163.5	—	—	—
0.95	152	—	159	173.5	164.5	164	—	—	—
0.975	152	—	159	174.5	166	164	—	—	—
1.0	150.5	—	159	173	167	164.5	—	—	—
1.1	152.5	—	161	176	168.5	165	—	—	—
q (psf) = 100 percent of nominal; angle of attack = 0 deg									
0.6	150	—	162	162.5	160	164	—	—	—
0.7	154	—	164	165	163	164	—	—	—
0.8	150	—	163	166.5	164	165	—	—	—
0.85	150	—	162	168	163	163	—	—	—
0.9	152	—	161.5	168	162.5	162	—	—	—
0.925	151.5	—	161	168	163	162	—	—	—
0.95	151	—	161	171	163.5	162	—	—	—
0.975	150.5	—	160	170	166	162.5	—	—	—
1.0	150.5	—	160	170	167	163	—	—	—
1.1	152.5	—	162	173.5	170	163	—	—	—
1.2	151	—	161.5	172	168.5	162	—	—	—
q (psf) = 120 percent of nominal; angle of attack = 0 deg									
0.8	N/A	—	N/A	N/A	N/A	N/A	—	—	—
0.85	N/A	—	N/A	N/A	N/A	N/A	—	—	—
0.9	N/A	—	N/A	N/A	N/A	N/A	—	—	—
0.925	153.5	—	160.5	173.5	165.5	163	—	—	—
0.95	153.5	—	160.5	174	167	163	—	—	—
0.975	152.5	—	160	175	168	163	—	—	—
1.0	152	—	161	175.5	169	163	—	—	—
1.1	153	—	162	172.5	170	163	—	—	—

$\alpha = 0^\circ, \beta = 0^\circ, \gamma = 100\%$  of Nominal

March 0.7

March 0.7

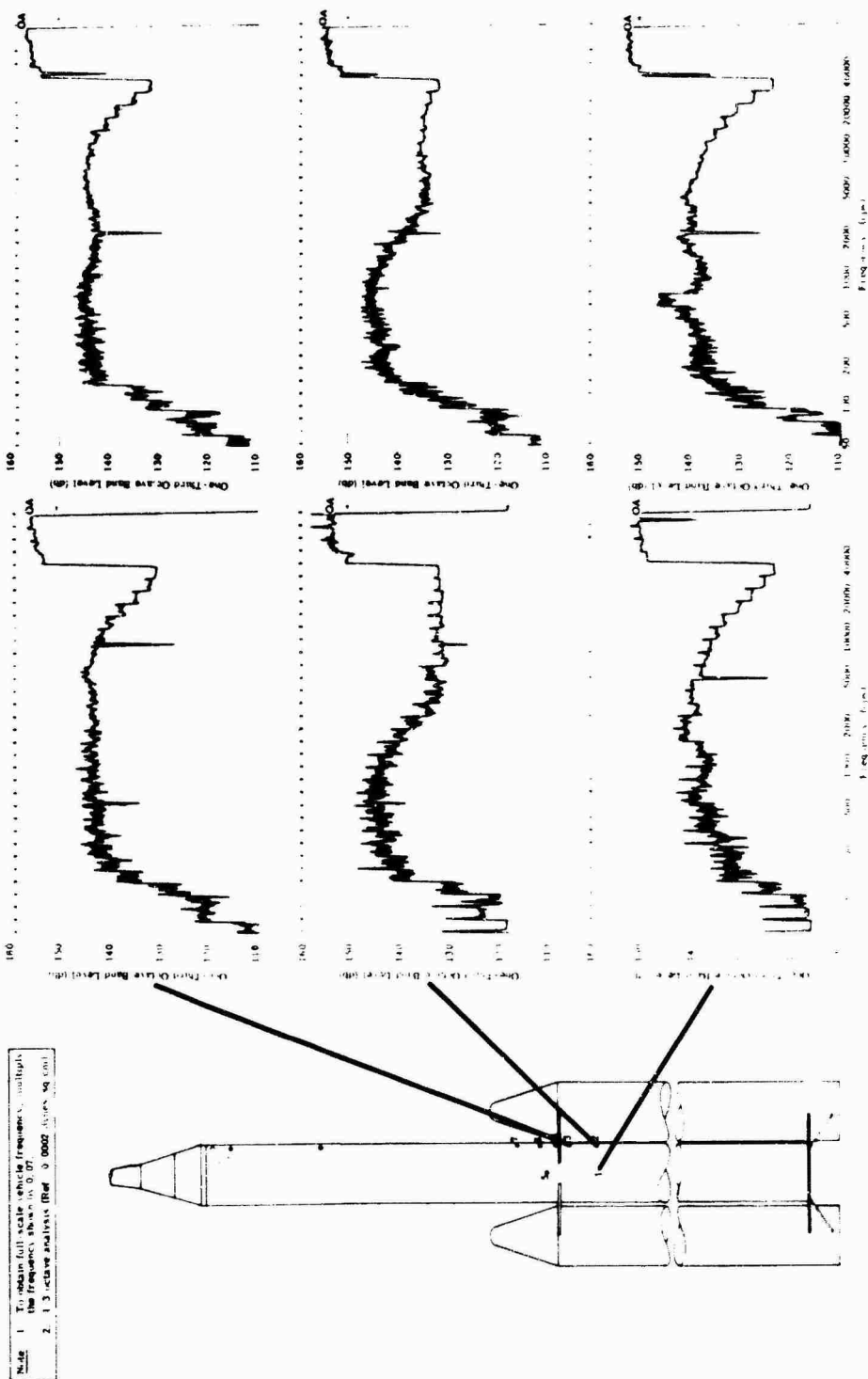


Fig. 3(a). Configuration 31 model transonic SPL's at microphones 1, 2, and 3

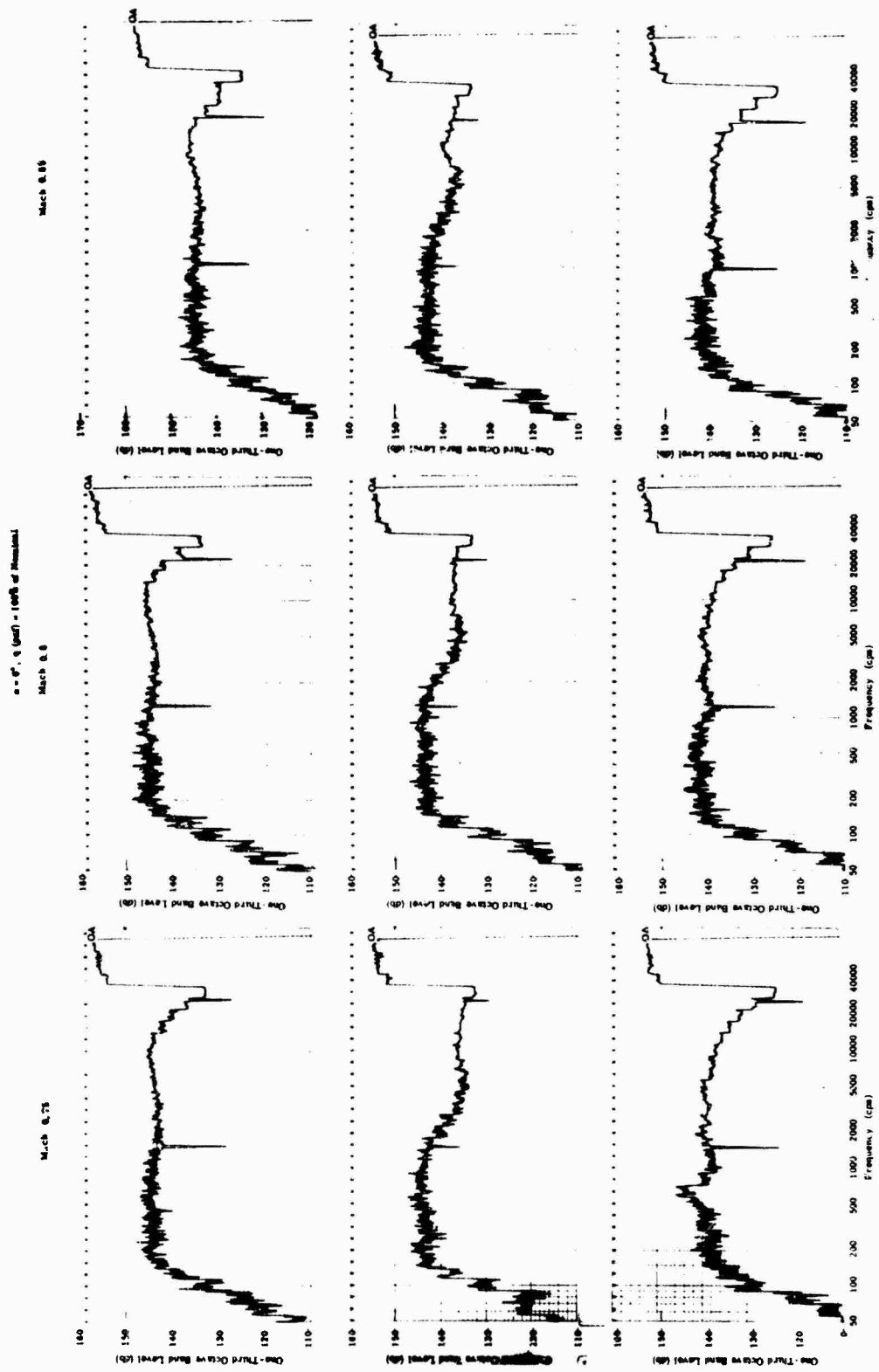


Fig. 3(b). Configuration 31 model transonic SPL's at microphones 1, 2, and 3



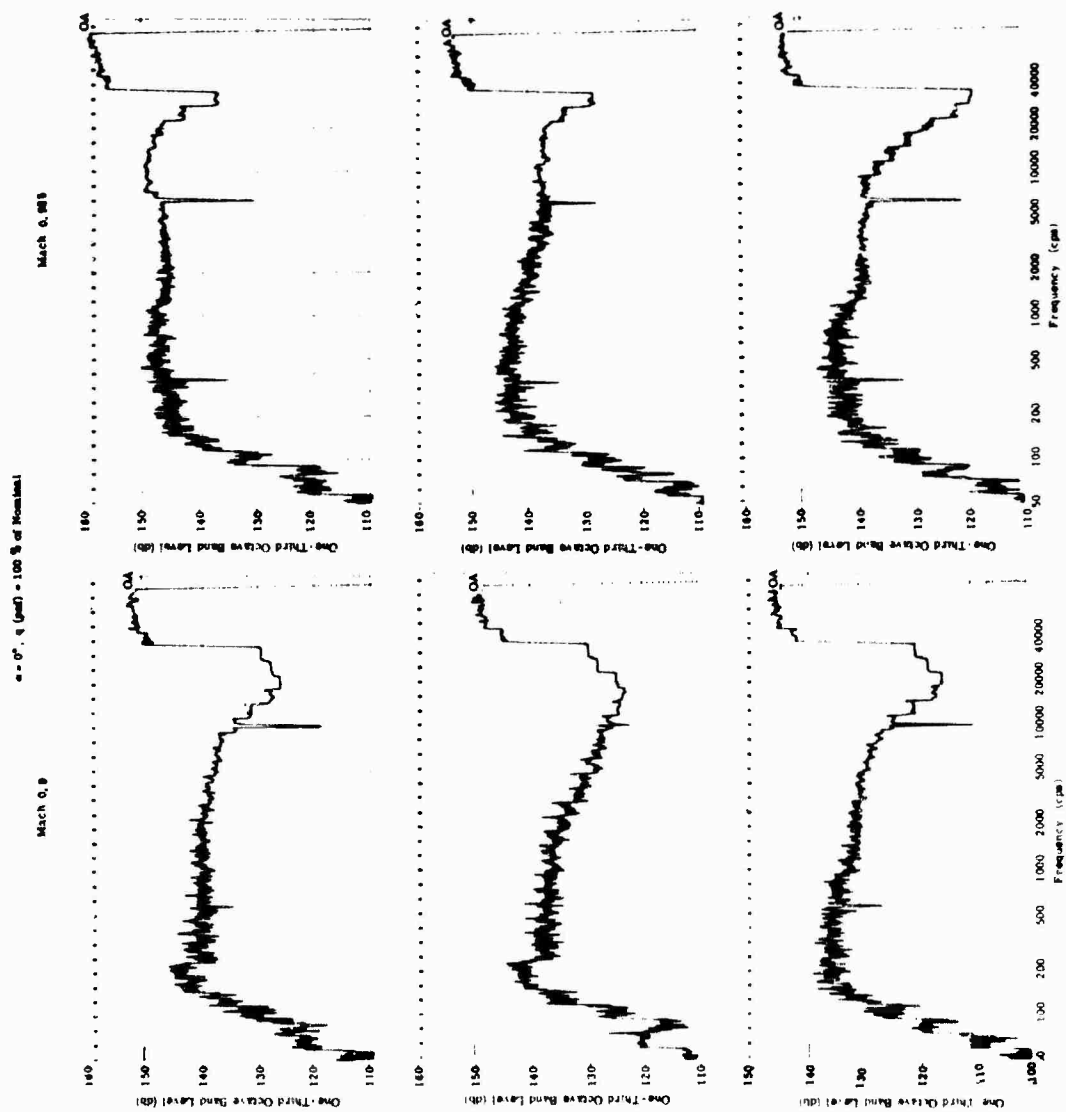


Fig. 3(c). Configuration 31 model transonic SPL's at microphones 1, 2, and 3

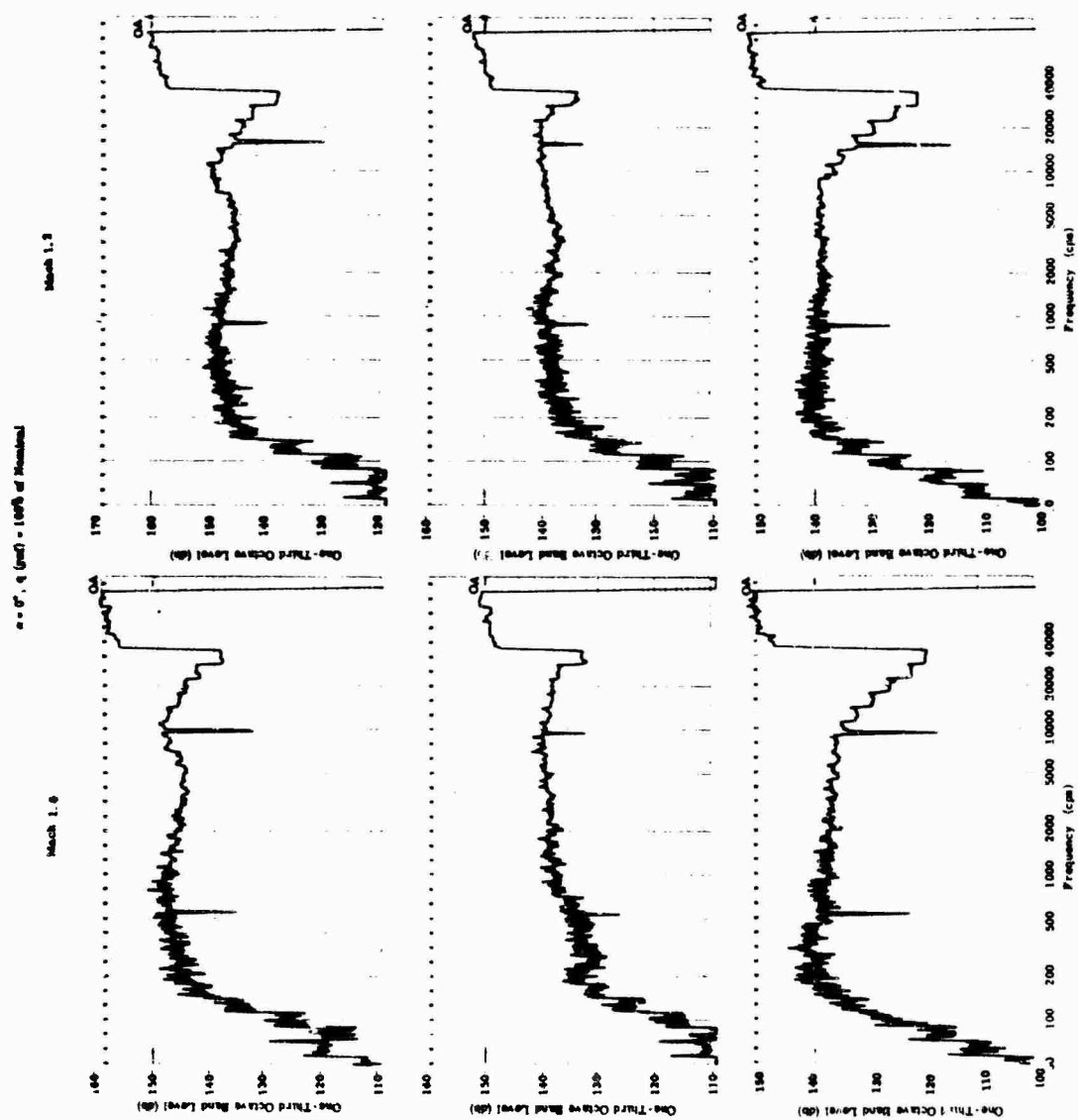


Fig. 3(d). Configuration 31 model transonic SPL's at microphones 1, 2, and 3

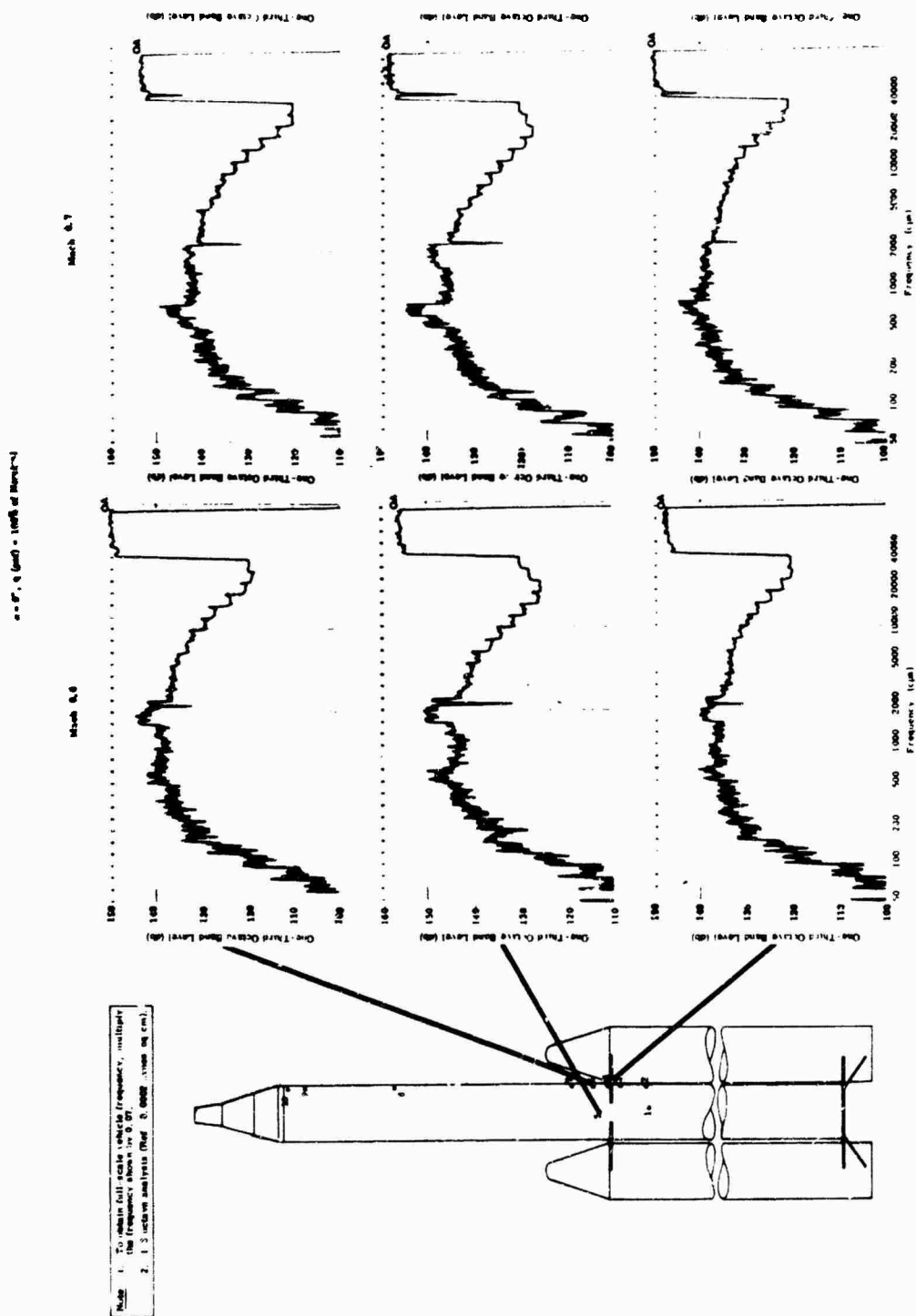


Fig. 4(a). Configuration 31 model transonic SPL's at microphones 4, 5, and 6

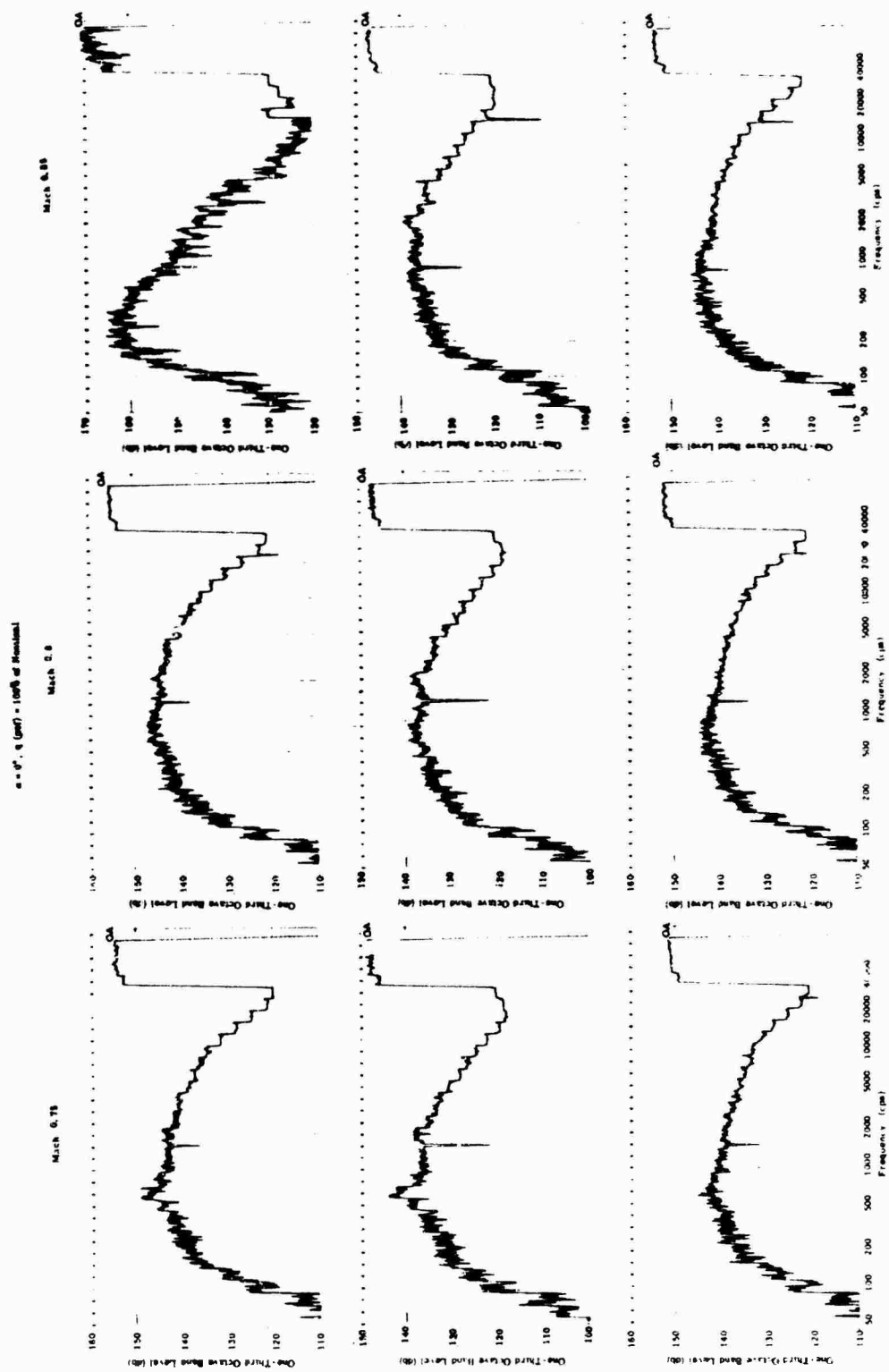


Fig. 4(b). Configuration 31 model transonic SPL's at microphones 4, 5, and 6

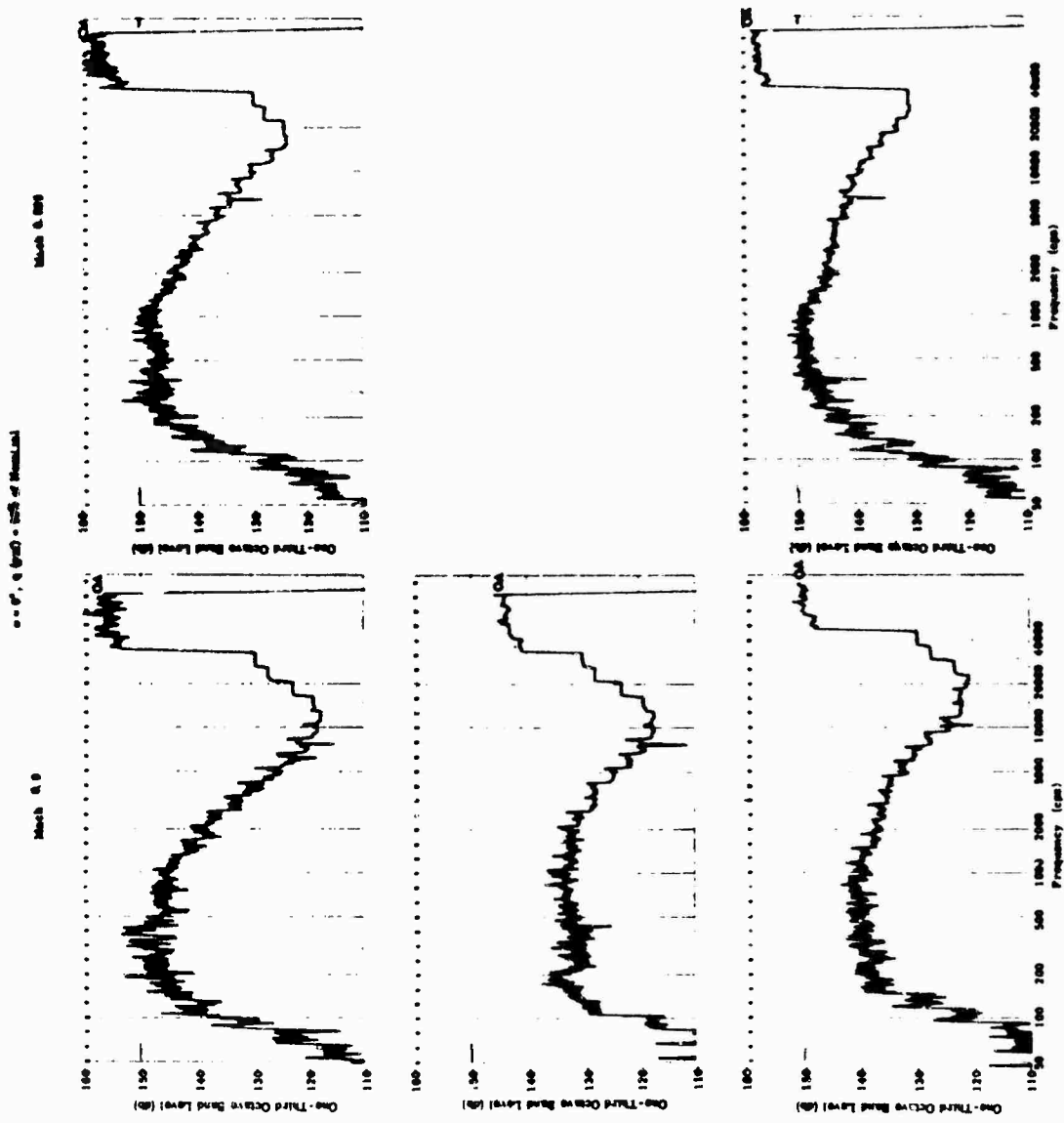


Fig. 4(c). Configuration 31 model transonic SPL's at microphones 4, 5, and 6

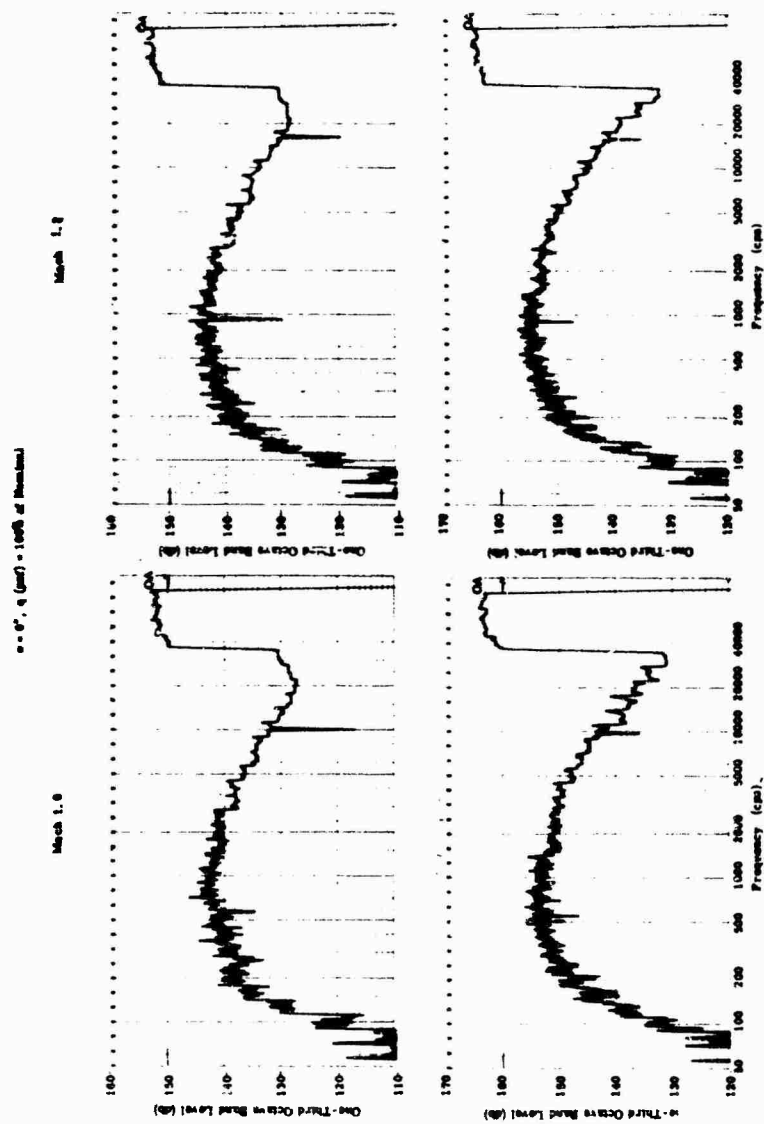


Fig. 4(d). Configuration 31 model transonic SPL's at microphones 4, 5, and 6



$\alpha = 0.7, 0.9, \text{ and } 1.0$  (dB at 1000 Hz)

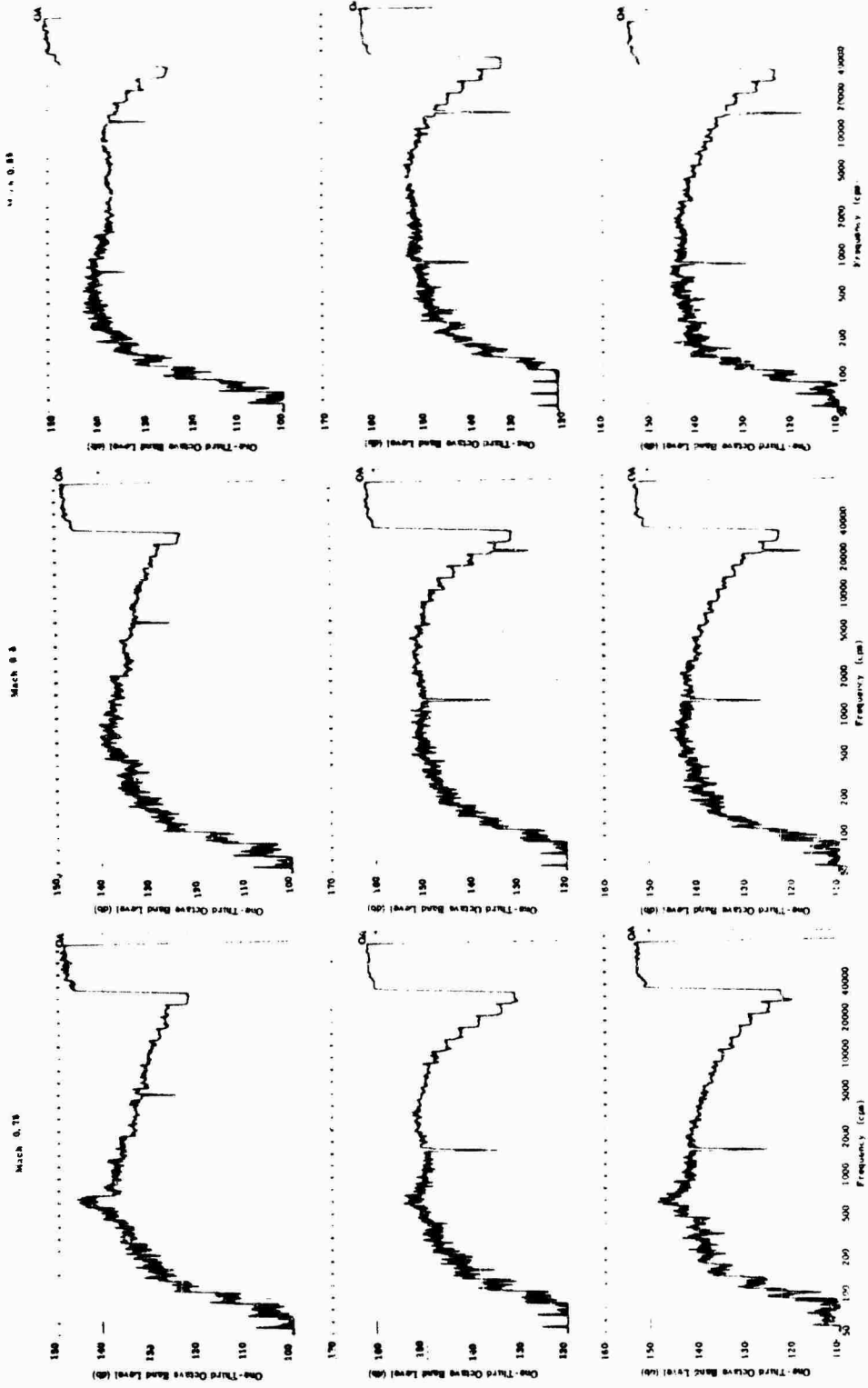


Fig. 5(b). Configuration 31 model transonic SPL's at microphones 7, 9, and 10



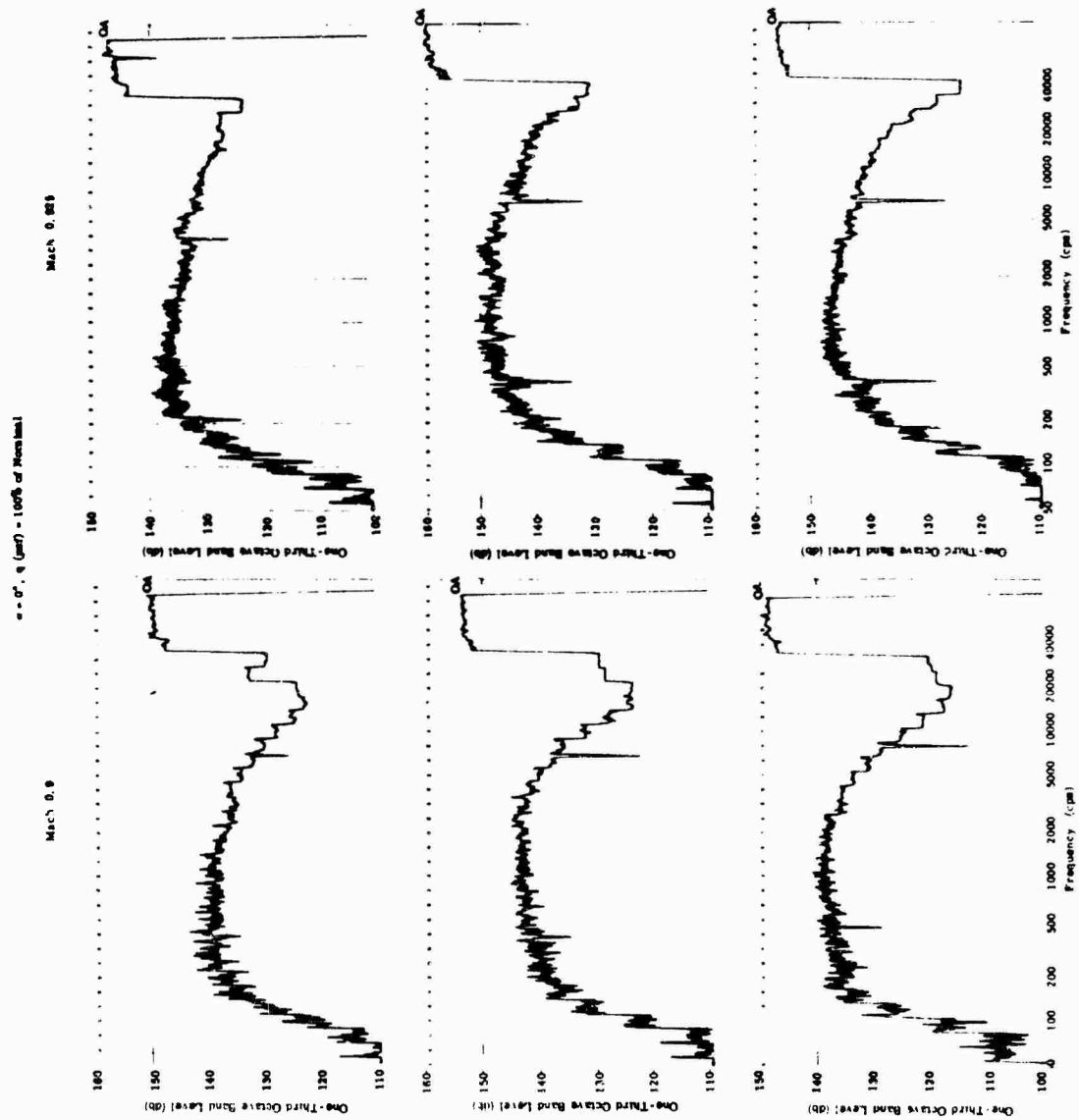


Fig. 5(c). Configuration 31 model transonic SPL's at microphones 7, 9, and 10

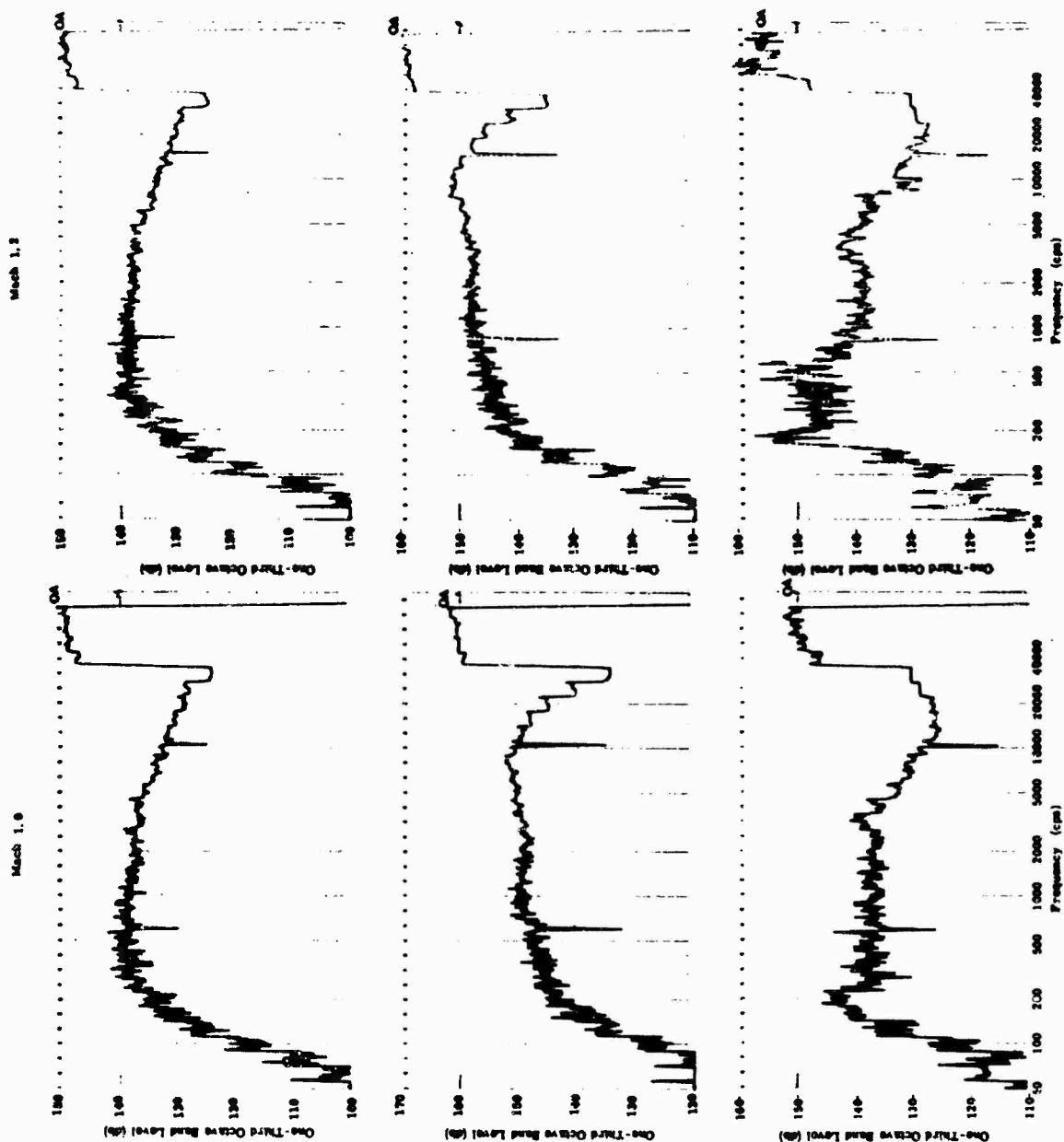


Fig. 5(d). Configuration 31 model transonic SPL's at microphones 7, 9, and 10

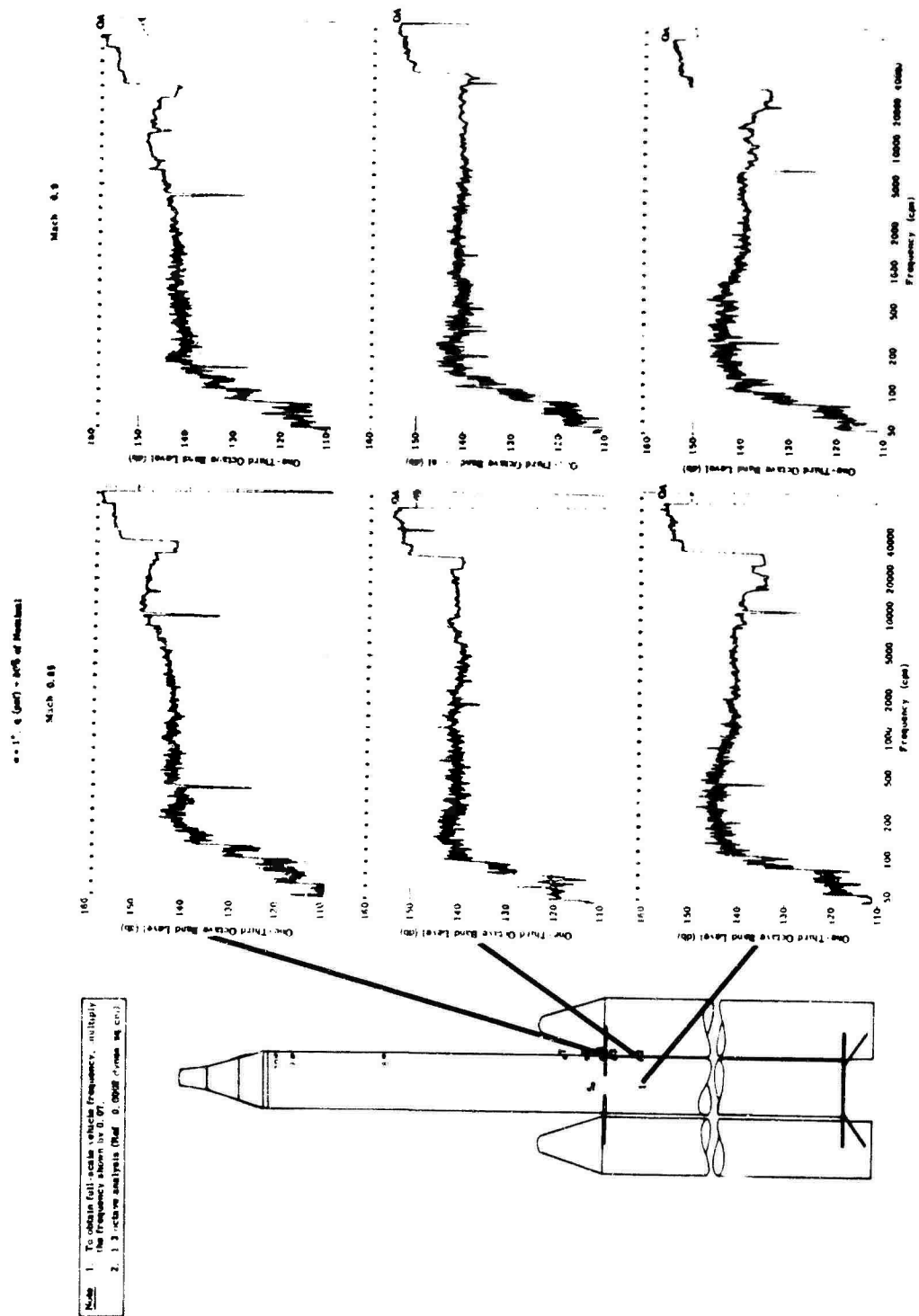


Fig. 6(a). Configuration 31 model transonic SPL's at microphones 1, 2, and 3

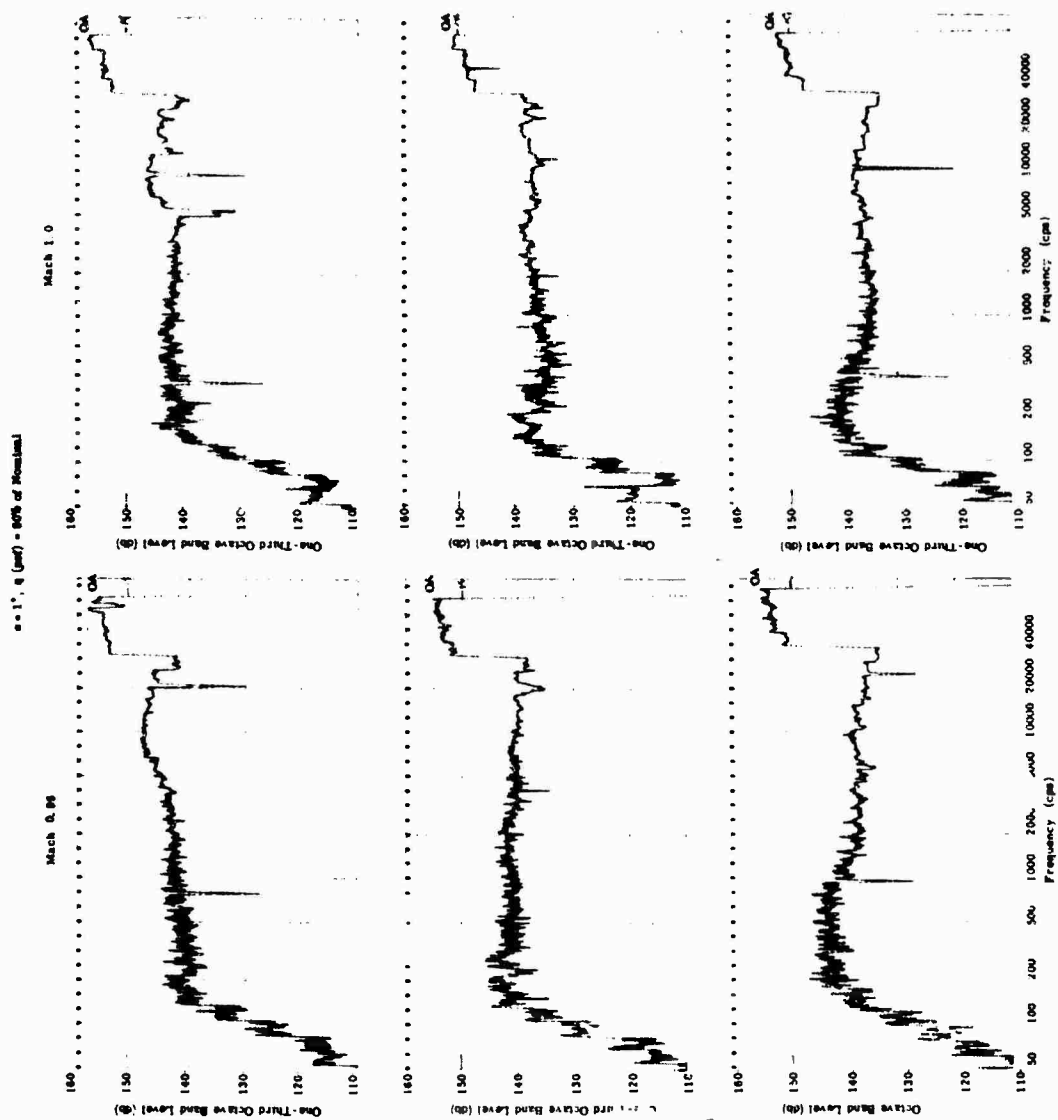


Fig. 6(b). Configuration 31 model transonic SPL's at microphones 1, 2, and 3

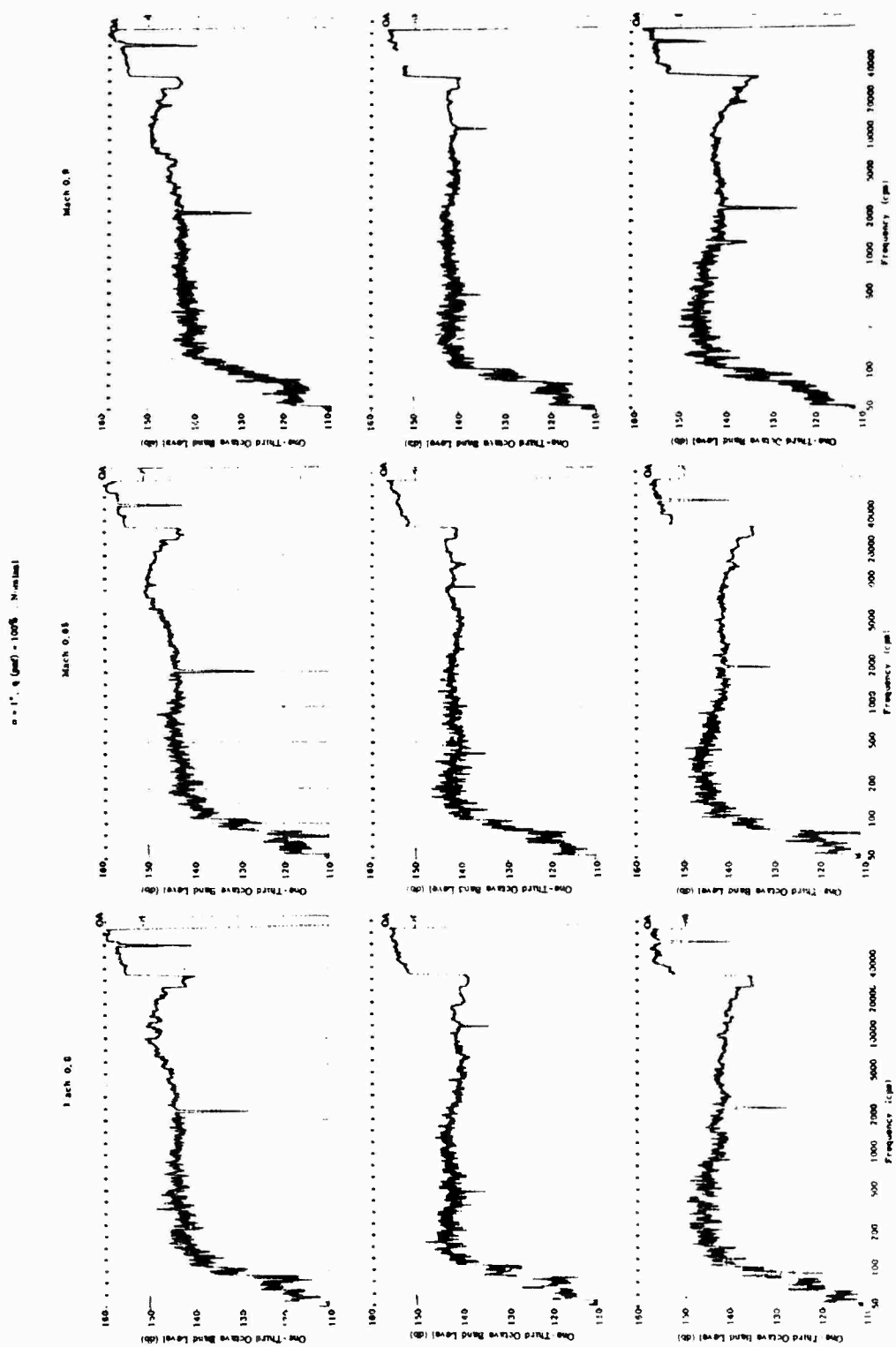


Fig. 6(c). Configuration 31 model transonic S L's at microphones 1, 2, and 3

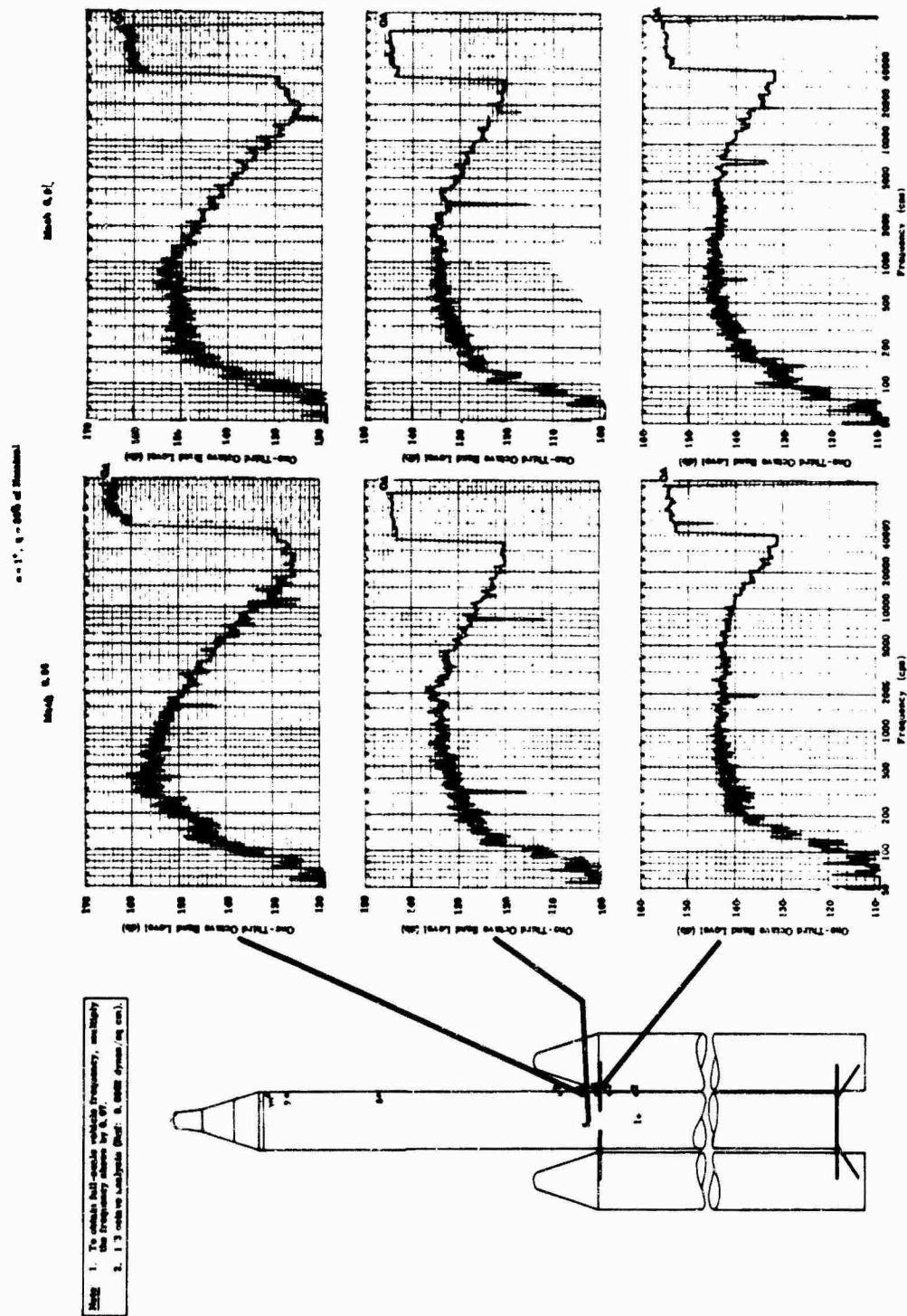


Fig. 7(a). Configuration 31 model transonic SPL's at microphones 4, 5, and 6

$\alpha = 1.5 \times 10^{-3}$  (cm) = 0.0015 of thickness

March 6, 1965

March 1, 1967

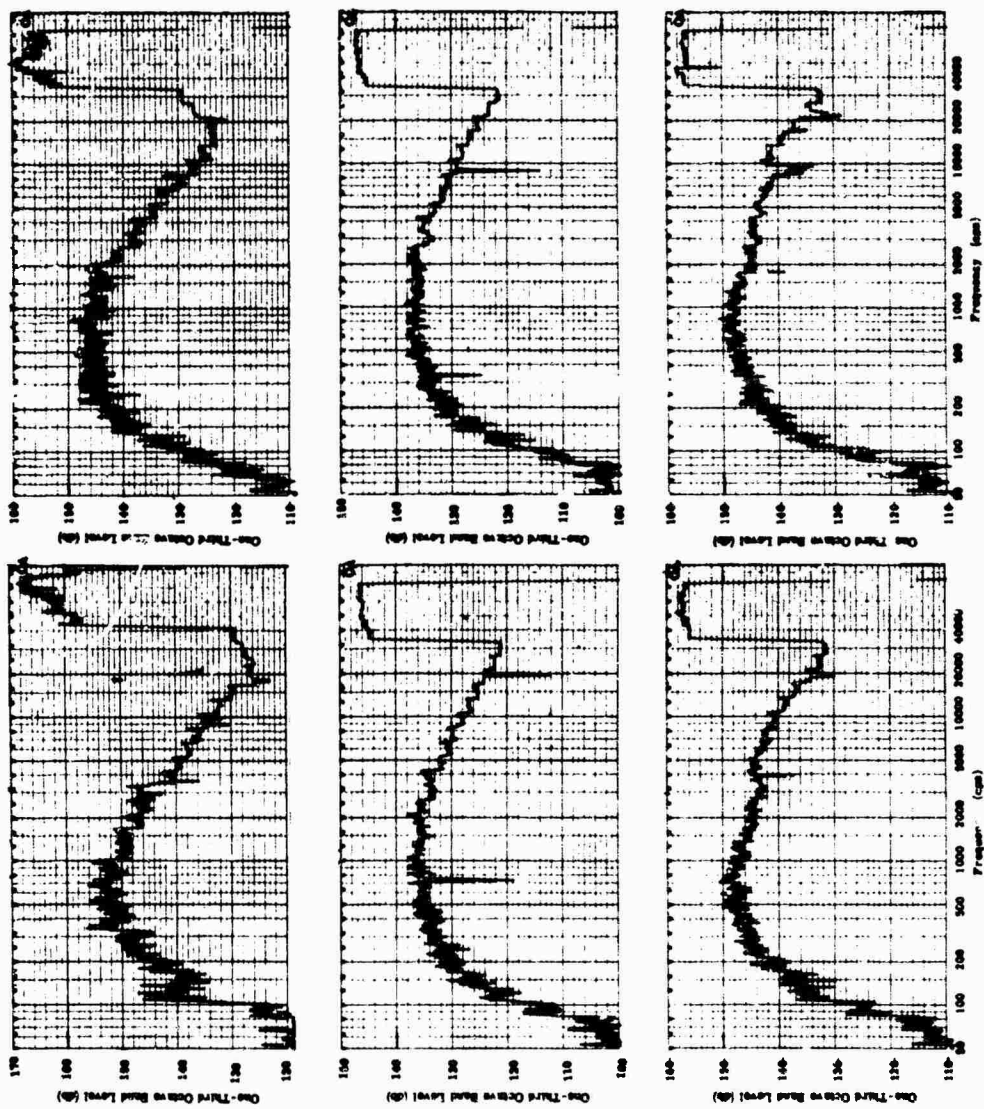


Fig. 7(b). Configuration 31 model transonic SPL's at microphones 4, 5, and 6

$\sigma = 1^\circ$ ,  $q = 100\%$  of Nominal

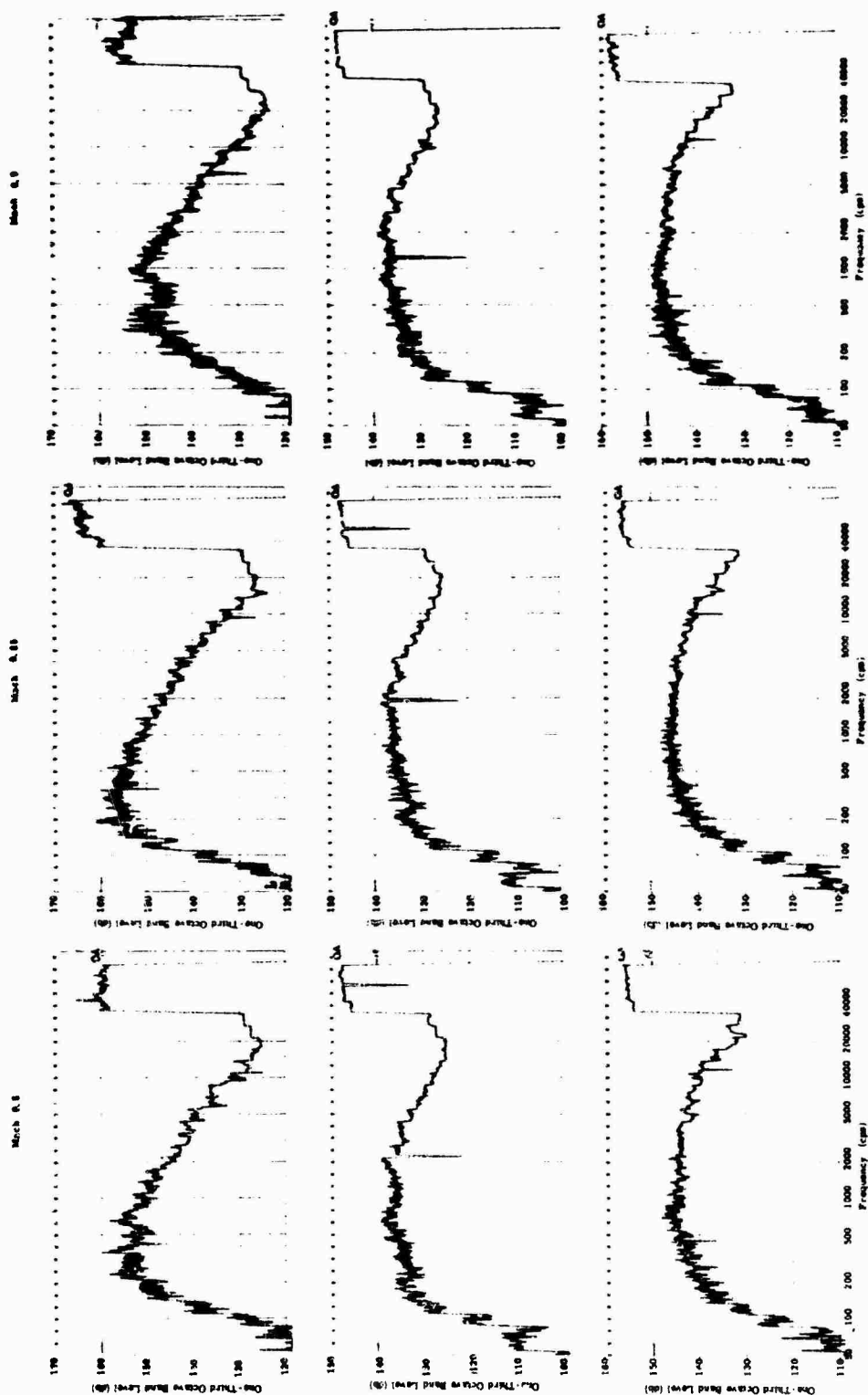


Fig. 7(c). Configuration 31 model transonic SPL's at microphones 4, 5, and 6





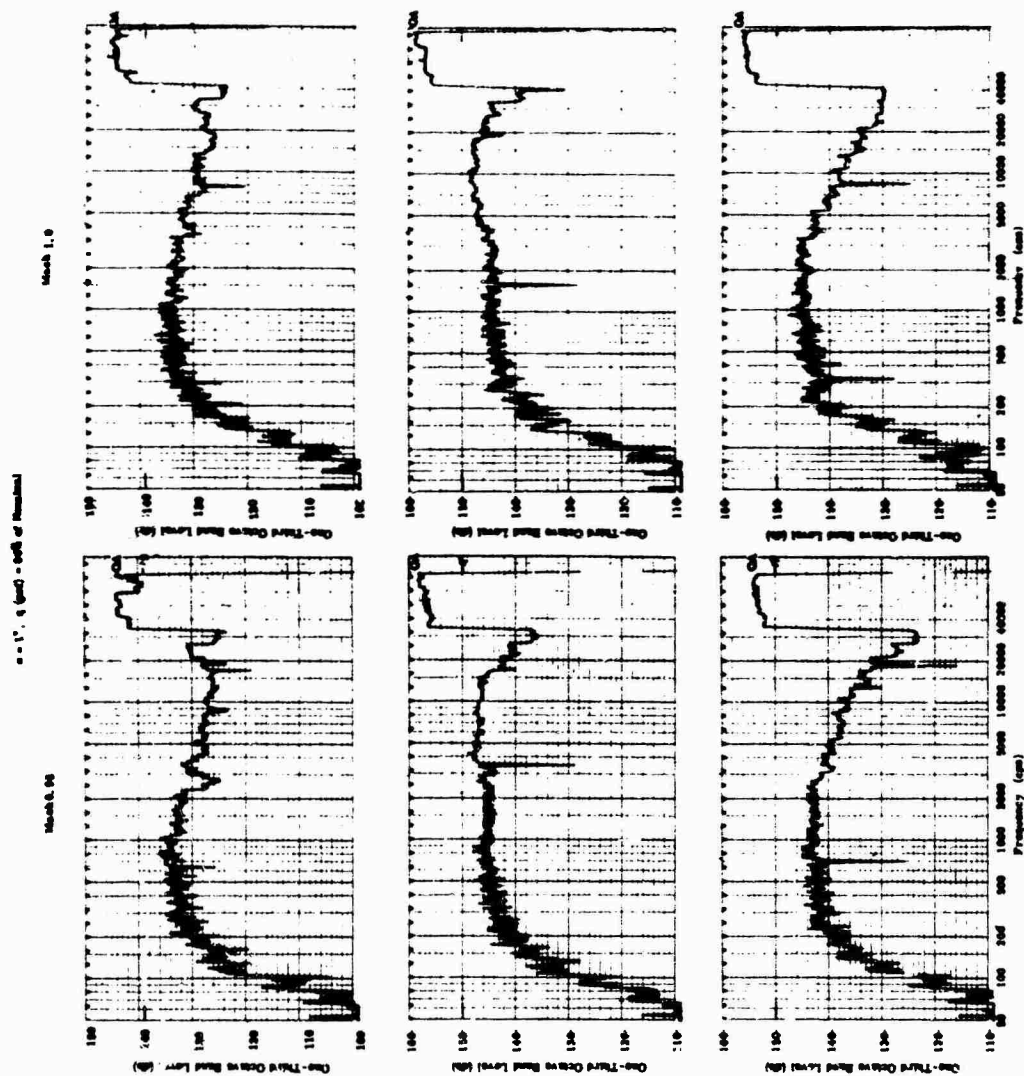


Fig. 8(u). Configuration 31 model transonic SPL's at microphones 7, 9, and 10

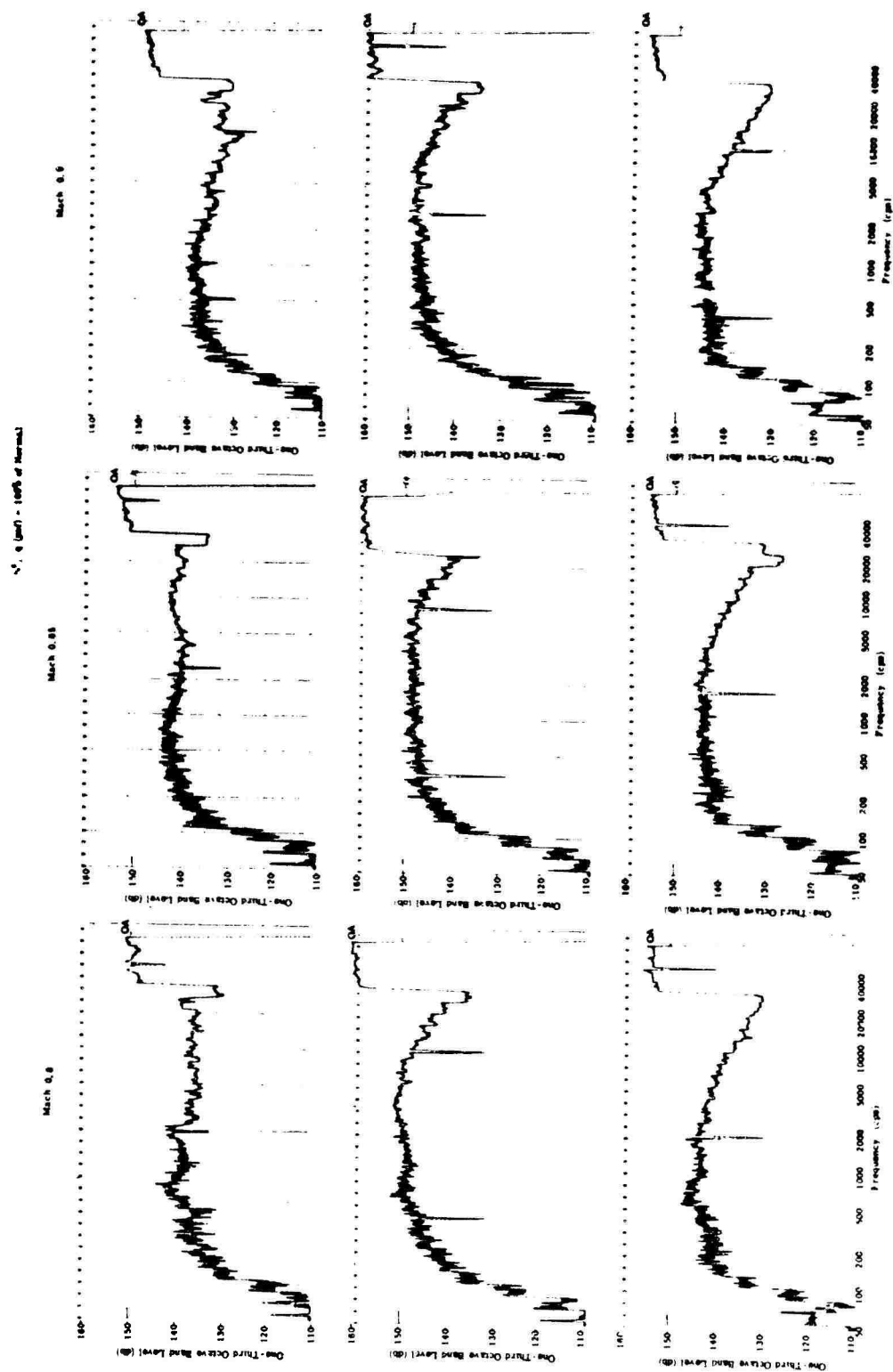


Fig. 8(c). Configuration 31 model transonic SPL's at microphones 7, 9, and 10

## REFERENCES

1. Anon., "Final Post-Test Report on Phase II 7% Transonic Buffet Model Test for Various Titan III Configurations, Martin Marietta Corp., Denver, Colo., MCR-67-311, 1967
2. M. Lankston, "Aerodynamic Model Test Report, Titan IIIM Final Post-Test Report, 5.35% Force and Pressure Test," Martin Marietta Corp., Denver, Colo., SSD-CR-66-683, Dec. 1966
3. J. Marcantonio and O. M. Hanner, Jr., "Aerodynamic Test, Post-Test Report (Wind Tunnel Test Data, Final)," Martin Marietta Corp., Denver, Colo., SSD-CR-65-230, Jan. 1966
4. D. R. Wiley and M. G. Seidl, "Aerodynamic Noise Tests on X-20 Scale Models," Boeing Co., Seattle, Wash., AFFDL-TR-65-192, Vol. 2, Nov. 1965

## BIBLIOGRAPHY

- Anon., "Final Post-Test Report on 7% Transonic Buffet Model Test for Various Titan III Configurations (Phase II)," Martin Marietta Corp., Denver, Colo., SSD-CR-66-563, Jan. 1966
- Anon., Propulsion Wind Tunnel Facility, Vol. 5. Test Facilities Handbook (6th ed.) (AEDC, Tullahoma, Tenn.), Nov. 1966
- Anon., "Applications - Final Report on 7% Transonic Buffet Model Test for Various Titan III Configurations," Martin Marietta Corp., Denver, Colo., MCR-67-5, Feb. 1967
- Anon., "Buffet Response of Aeroelastically Scaled Titan III Missile Configurations at Transonic Mach Numbers," AEDC, Tullahoma, Tenn., AEDC-TR-67-33, Mar. 1967
- Anon., "Applications - Final Report on Phase III 7% Transonic Buffet Model Test for Various Titan III Configurations," Martin Marietta Corp., Denver, Colo., MCR-67-312, 1967
- J. Uchiyama and F. Peters, "Buffet Response Measurements of a 7 Percent Aeroelastically Scaled Model of Various Titan III Configurations," Shock and Vibration Bull. No. 37, Part 3, Jan. 1968

\* \* \*